ISSN : 0075-5168 Volume 53 : July 2022

Karnataka University Journal of Science

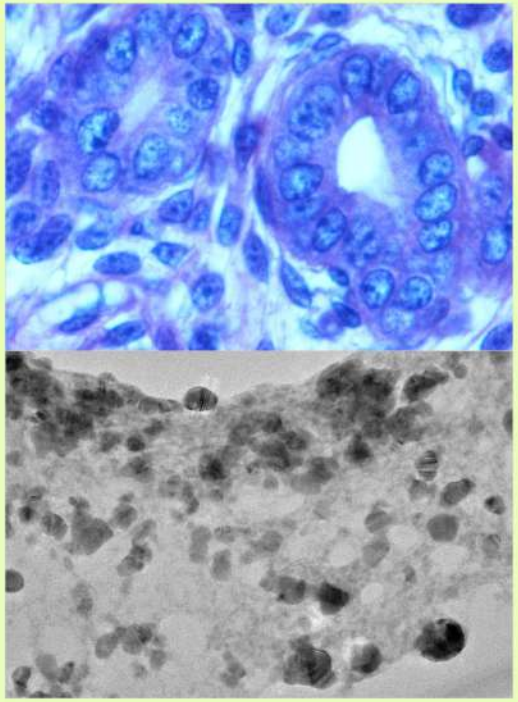

Full text available at: https://www.kud.ac.in

Chief Editor
Dr. Sanjeev R. Inamdar F.R.S.C. (UK)
Fellow, Karnataka Science & TechnologyAcademy

JOURNALS OF THE UNIVERSITY

1. Karnatak University Journal of Science
2. Karnatak University Journal of Social Science
3. Karnatak University Journal of Humanities
4. Karnatak Bharati (Kannada)
5. Vidyarthi Bharati (Kannada)

Rates of Annual Subscriptions

Social Science	: Rs. 300=00
Humanities	: Rs. 300=00
Science	: Rs. 300=00
Karnatak Bharati	: Rs. 075=00
Vidyarthi Bharati	: Rs. 050=00

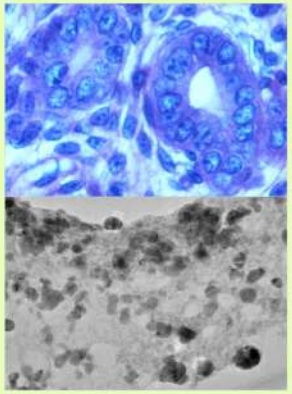

Cover : Impact of chronic administration of anabolic-androgenic steroid on histoarchitecture of uterus and adrenal in mice, Mus musculus by Praveenkumar S. Kondaguli and Laxmi S. Inamdar

Cover : Size controlled Thiol Capped Silver Nanoparticles by - V.S. Patil, et. al.,

Price 300/- **ISSN : 0075-5168**

Publisher : Director, Prasaranga, Karnatak University, Dharwad-580 003

Karnatak University

Journal of Science

Vol. 53, July 2022

Publisher

Director

Prasaranga, Karnatak University, Dharwad-580003.

The journal is published annually in order to disseminate new knowledge and research findings of the faculty and students of Karnatak University and other academic institutions belonging to various disciplines in the area of Science. The journal also encourages interdisciplinary research.

ISSN: 0075-5168

Annual subscription: Rs. 300/-

Research articles and books for review should be addressed to: Publisher
Director
Prasaranga
Karnatak University, Dharwad
Pavate Nagar, Dharwad-580 003, INDIA

Printer:
Director,
Karnatak University, Printing Press,
Dharwad.

Journal in exchange may be sent to:
Librarian
Professor S. S. Basavanal Library
Karnatak University, Dharwad
Pavate Nagar, Dharwad-580 003, INDIA

Editorial Board

FOREWORD

The Karnatak University Journal of Science (KUJS) is a peer reviewed journal and is publishing articles on recent advances in science research from all over India. I am indeed very happy to present this fifty-third volume to the readers. I am glad to note that the researchers from premier institutes of India are publishing their research outcomes in our journal. Just as in its preceding two volumes, the articles have been classified as Science Articles of general interest and Research Articles, with topics of current trends in scientific research in chemistry, physics, mathematics and life sciences. I appreciate the commendable efforts of Chief Editor, Prof. Sanjeev R. Inamdar and the entire Editorial Board comprising of National and International researchers of eminence who have done a wonderful job to maintain the status of the journal. All the publishing ethics on par with International publishers are being followed. I am sure; their efforts will take our journal to the next level. Certainly, this volume is a trend setter for future volumes to come.

Prof. K. B. Gudasi
Hon. Fellow, KSTA
Vice Chancellor
Karnatak University, Dharwad

From Editor's Desk

With immense pleasure, I present this 53rd volume of Karnatak University Journal of Science -third in the series since Vol.51 (2020) published by this Editorial Board. Tremendous efforts have gone into realizing these three volumes and elevate the status of this journal on par with international journals. We have exercised care to choose good articles from outside and within Karnatak University, screen for plagiarism and to get them peer reviewed before publishing. Thus these three volumes contain articles authored by researchers from institutes/universities outside Karnatak University and from other states.

The present volume includes two invited articles that highlight the importance of light in science and in our lives, with special emphasis on exciting applications. One article describes effective use of sunlight for purification of water using semiconductor thin films, a very innovative method that addresses the societal needs. This is much more relevant in the present times as potable water is becoming scarce. The second article hovers around the optical tweezer, related to Arthur Ashkin's Nobel winning work on Optical Trapping and Manipulation of Neutral Particles using Lasers. The author discusses the optical confinement of nanoparticles based on this novel topic. Both these articles describe potential applications of light for the benefit of mankind. Thus, it's time we orient our students towards research in photonics-science of light. Karnatak University is doing its bit through SPIE (USA)-Karnatak University Student Chapter established by Laser Spectroscopy Program in 2019 (see details on *page 119*) conducting regular talks on advances in photonics, outreach activities on optics and photonics for school/college students.

I express my heartfelt gratitude to the esteemed members of the Editorial Board for their valuable contribution in bringing out this volume. My special thanks are due to our Vice Chancellor Prof. K.B. Gudasi who has extended full support and encouragement all through. Very importantly, I am grateful to my students Dr. Mallikarjun K. Patil, Dr. Manjunath N. Wari, Mr. Tilakraj and Mr. Vikram Pujari who have done their best in bringing in elegance in all the three volumes 51-53 by exercising utmost care in neat typesetting, cover page design, arrangement of articles, etc. It really has been an enjoyable experience working with them.

Hope you enjoy the issue….

Dr. Sanjeev R. Inamdar *FRSC, FKSTA*

Chief Editor

CONTENTS

INVITED ARTICLES

REGULAR ARTICLES

Karnatak University Journal of Science 53 (2022) 01-04

Karnatak University Journal of Science

ISSN: 0075-5168

Optical Confinement of Nanoparticles: Going beyond the Diffraction Limit

Naveena C.S and Sharath Ananthamurthy *
School of Physics, University of Hyderabad Hyderabad 500046-India
***Corresponding author:** *sasp@uohyd.ac.in*

ARTICLE INFO

Article history:
Received: 5 June 2022;
Accepted: 8 June 2022;

ABSTRACT

With the discovery in the mid-eighties that laser light when tightly focused can result in optically confining particles that have dielectric properties, led to major scientific developments that profoundly impacted almost all areas of the hard sciences. The so-called optical tweezer, an invention of Ashkin has led to the extraordinary ability to confine and manipulate microscopic objects without actually having to mechanically hold them through the electromagnetic forces. However the finite wavelength dimension of the optical fields precludes our ability to confine objects smaller than the typical wavelengths used in such experiments, which is in the range of a micron, due to diffraction limits. This limitation in size of objects was overcome too, nearly two decades ago, with the advent of the field of Plasmonics and the use of plasmonic structures in optical tweezing. Here, we will provide and brief review of plasmonic trapping.

When the laser was invented in the early sixties, like many other innovative tools that have been invented, this one too was received with some amount of uncertainty: " This is a solution that is in search of a problem", is apparently what was remarked about this tool by it's American inventor T.H. Maiman! This search never lasted too long for the almost instantaneous flood gates that opened with all kinds of problems/technologies that imply seemed waiting in the sides for the laser! A coherent nearly monochromatic powerful beam of photons is employable in all kinds of areas, from precision laser cutting of hard materials, precision tissue ablation in laser surgery, high fidelity signal transmission and communication technology, the music industry, you name it! The momentum carried by the photons in such beams can serve to efficiently transfer this momentum to other objects. Many of the applications stated here are those that involve large momentum transfer resulting in heat absorption by the material. In the other extreme, a low power laser beam can be used when tightly focused, resulting in small forces imparted by the photons of the beam, and result in moving small objects of microscopic and lesser sizes. A. Ashkin exploited this regime of force transduction when he invented the Optical Tweezer (OT) setup [1]. Today, OTs have been applied in practically every area of science and technology that requires the manipulation of

microscopic sized entities. The force applied through the tweezer fields are also comparable to the interaction forces between macromolecules like DNA, proteins and also are of the order of the forces generated within the cells for the movement of organelles through molecular motor mechanisms.[2,3,4] Thus, OT is a powerful tool used in measuring these forces.

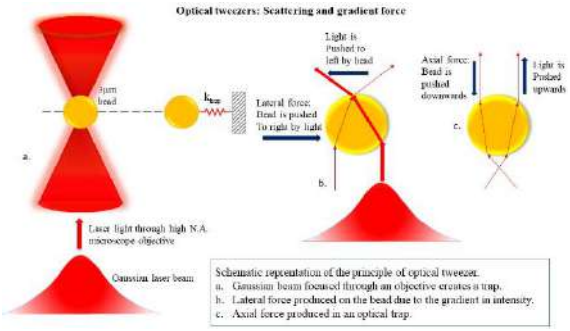

Figure 1: Illustration of the principle behind optical trapping. (a) shows a Gaussian beam focused with a high numerical aperture objective. In (b) and (c) the ray optics approach illustrates the way in which momentum is transferred to the bead in the laser beam.

Figure 1 illustrates the principle behind optical tweezing. A micron sized bead with refractive index slightly greater than the surrounding fluid in which it is trapped, experiences a net force directed in a radial direction towards the centre, of a sharply focused laser beam. The Numerical Aperture (NA) of the microscope objective lens decides the sharpness of the focus. The NA is a measure of the amount of bending of the light rays at the edges of the entrance of the objective lens. As illustrated in Fig. 1, the optically trapped object can be thought to be held by a harmonic spring force acting towards the centre of the tightly focused laser beam.

Next, we turn our attention to how small we may go down in size of particle that is to be trapped. To address this question, we need to see the regime of length scales where optical diffraction effects become important. The wavelengths being considered here are in the visible region ie 400-700nm. If our goal is to work with biological cells and tissue then the wavelengths that cause minimal absorption in the material and hence, minimally damage thermally, must be considered. Ideal wavelengths are in the infrared region (around 1micron radiation). However, at optical wavelengths diffraction effects of trapping objects whose sizes are much smaller than micron limit us. Imaging such objects is also a problem due to diffraction. The resolution of two diffraction-limited images is given by the Rayleigh criterion (Fig.2):

$\theta = 1.22\lambda / D$

where, θ is the resolving angle, D, the size of the aperture and λ is the wavelength, where D is much larger than the wavelength. In terms of the numerical aperture of the lens, NA, the Rayleigh criterion, for a resolution, R, can be written as:

$R = 0.61\lambda / NA$

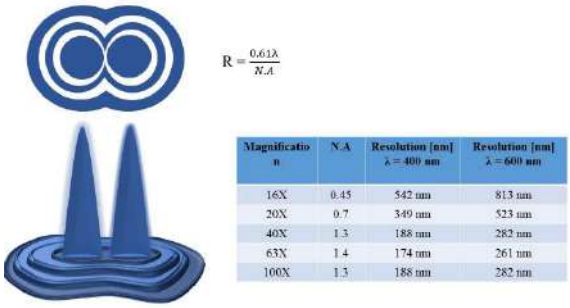

Magnification	N.A	Resolution [nm] λ = 400 nm	Resolution [nm] λ = 600 nm
16X	0.45	542 nm	813 nm
20X	0.7	349 nm	523 nm
40X	1.3	188 nm	282 nm
63X	1.4	174 nm	261 nm
100X	1.3	188 nm	282 nm

Figure 2: Illustration of the Rayleigh criterion for resolving two images that are close to each other. Table 1 in the inset shows R for different NA of the objective lens and for different wavelengths

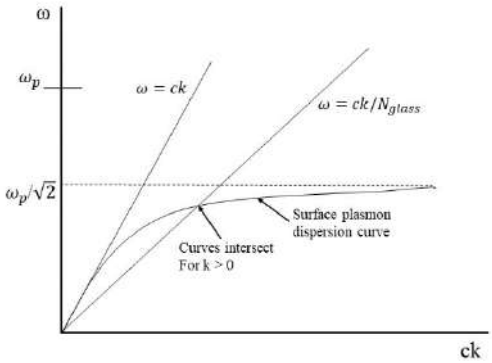

Figure 3: Dispersion relations for light propagating in air, in a glass surface and the dispersion relation for a surface plasmon. Note the intersection of the curves for propagation in glass with that of the surface plasmon

Table 1 shows the resolution achievable for a given NA and wavelength. We can see from the table that at 1000nm wavelength, for NA=1.3, the resolution is no better than 470nm. This diffraction limitation also comes in the way in creating a well defined optical potential well for confining a particle whose sizes are much less than a micron.

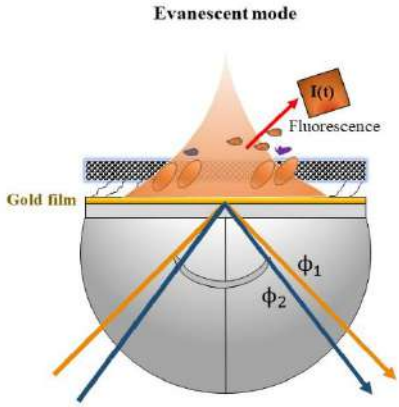

Figure 4: Illustration of an evanescent mode generated at a metal-glass interface by total internal reflection of light

Plasmonics to the rescue: The trick to achieving sub micron particle trapping then lies in the creation of oscillating fields whose wavelengths are smaller than the optical wavelengths normally used in trapping. Such fields are highly localized and arise due to oscillations in the local density, such as those of free electrons in a metal. They are called Plasmons and are the collective oscillations of the free electrons in a metal. These oscillations can be made to resonate with external fields under certain conditions. The plasmon frequency is, $\omega_p \propto \sqrt{n}$, where, n is the number density of the oscillating electrons. Thus, as the number density of the oscillating electrons goes up so does the corresponding electron plasmon frequency. Thus, n, serves as a quantity analogous to determining the "spring constant" of the oscillating plasmon. Coupling light energy to create plasmon oscillations, is however not that straightforward. For one, bulk plasmon oscillations are longitudinal, ie along the propagation direction, whereas, photon oscillations are transverse. The dispersion curves in Fig.3 show that free air propagation cannot result in coupling electromagnetic energy to generate plasmon oscillations. A modified dispersion relation from a metal-coated glass, on the other hand intersects for a value of k (the momentum) corresponding to the surface plasmon dispersion curve.

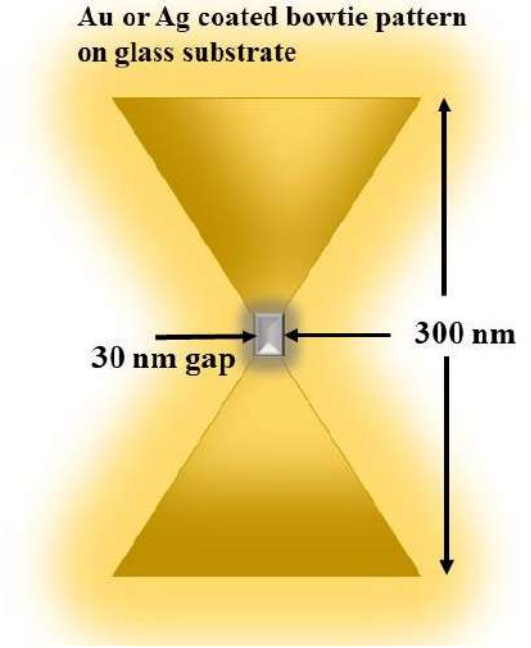

Figure 5: Bow tie patterned gold or silver structure on a substrate. The gap at the centre is a region wherein a plasmonic field potential minimum may be created.

A way of overcoming the problem of coupling photon momentum to that of the plasmons is to rely on surface plasmons, ie oscillations created at surfaces of thin metallic coatings or metal nanostructures deposited on dielectric materials like glass substrates. A method to couple photons and surface plasmons is to use attenuated total reflection at a metal coated glass surface. The exponentially damped or evanescent wave escaping from the glass can be matched to the surface (thin film) plasmon generated in the coating as in Fig.4. This technique that uses evanescent wave properties has also found applications in biosensing [5].

Plasmonic Tweezers: The design and creation of specialized shapes of metallic nanostructures, nanopillars, and different shaped

thin coatings that create localized plasmonic fields upon excitation by laser light is a big enterprise in itself [6] . The so-called Metamaterials are designed in different shapes and metals, alloys and mixtures are all tried out to create efficient ways of coupling laser excitation to plasmonic excitations. Fig. 5 shows a gold "bow tie" structure with sub micron sized gap between the pointed ends where a plasmonic excitation is created [7]. The fields created are highly localized. Potential minima that can help confine particles much smaller than those sizes, limited by the conventional tweezers that use optical range wavelengths Fig.6 shows a computed potential energy landscape for a given local plasmon field at a nanostructured material [8].

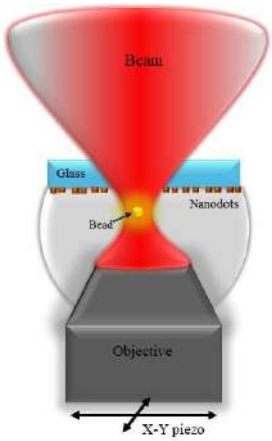

Fig.6 (a)

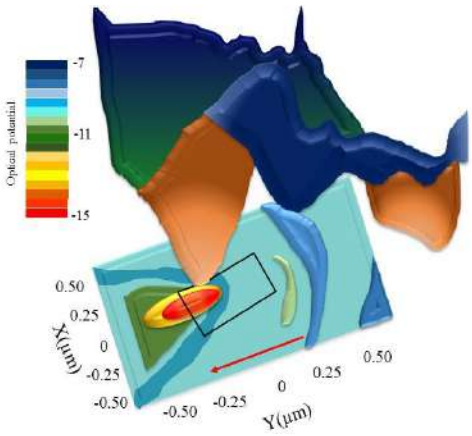

Fig.6 (b)

Figure 6(a) is a schematic of a plasmonic tweezer, with the required field created near the Nano dots. Fig. 6(b) is a representation of the computed field potential in such a tweezer.

Imaging at sub micron scales would also need to rely on near-field imaging techniques that get around diffraction-limited imaged planes. These are achievable with near field optical microscopes that also rely on the evanescent fields close to the material that is to be imaged. Integrating a plasmonic tweezer on a platform that allows for near field imaging, offers thus, tremendous advantages in micromanipulation of microscopic objects with capability of sub micron level imaging. The future is indeed bright, for micromanipulation, control and imaging of nanosized objects!

References:

1. Observation of a single-beam gradient force optical trap for dielectric particles, A.Ashkin et al., Opt. Lett. (11), No.5, 288-290, (1986)
2. Stretching DNA with optical tweezers, Wang MD, Yin H, Landick R et al. Biophys.J. 72(3):1335, (1997).
3. Direct Observation of kinesin stepping by optical trapping interferometry, Svoboda, K, Schmidt, C. F., Schnapp, B., and Block, S. M., Nature, 365, 6448, 721–727, (1993).
4. Microrheology with Optical Tweezers: Principles and Applications, Ed. Manlio Tassieri, Pan Stanford Publishing Pvt. Ltd., (2016).
5. Plasmonic tweezers for optical manipulation and biomedical applications, H. Tan et al. Analyst, DOI: 10.1039/d0an00577k5. (2020).
6. Plasmonic optical tweezers based on nanostructures: fundamentals, advances and prospects, Domna G. Kotsifaki and Sile Nic Chormaic, Nanophotonics, 8(7): 1227–1245 (2019).
7. Optical Trapping of a Single Protein, Y. Pang and R. Gordon, NanoLett. 2012, 12, 402−406 doi.org/10.1021/nl203719v (2011)
8. Plasmonic tweezers: for nanoscale optical trapping and beyond, Yuquan Zhang et al., Light: Science and Applications, https://doi.org/10.1038/s41377-021-00474-0, (2021)

Karnatak University Journal of Science 53 (2022) 5-7

Karnatak University Journal of Science

ISSN: 0075-5168

Solar Energy Assisted Purification of Water using Semiconductor Thin Films

C. H. Bhosale*

Energy Technology, Department of Technology, Shivaji University, Kolhapur- 416 004, India

***Corresponding author:** *chbhosale@gmail.com*

ARTICLE INFO

Article history:

Received: 5 July 2022

Accepted: 7 July 2022

ABSTRACT

Radiant energy from the Sun is abundant for life on our planet. One of the most important problems affecting people throughout the world is inadequate access to potable water. Over one billion people are exposed to unsafe drinking water due to poor source water quality and lack of adequate water treatment, a problem expected to grow worse in the coming decades. Water scarcity is occurring globally, even in regions currently considered water rich. The problem is particularly significant in developing countries and in arid areas where water sources are scarce. It was estimated that more than 50,000 tons of dyes are discharged from dyeing and coloration industries every year. Physical treatment such as boiling, distillation, reverse osmosis and UV irradiation require considerable energy input. One alternative for drinking water treatment method that has been proposed is solar photocatalysts purification. Wide band gap semiconducting transition metal oxide photocatalysts have been shown to decompose organic compounds, bacteria and other impurities present in water. The most prominent, widely studied photocatalyst is WO, TiO2, upon irradiation of a semiconductor with photons of energy higher than the band gap, charge carriers are generated, which lead to redox reactions at respective electrodes.

Radiant energy from the sun is vital for life on our planet. It determines the surface temperature of the earth as well as supplying virtually all the energy for natural processes both on the earth and in the atmosphere. One of the most important problems affecting people throughout the world is inadequate access to potable water. Over one billion people are exposed to unsafe drinking water due to poor source water quality and lack of adequate water treatment, a problem expected to grow worse in the coming decades, with water scarcity occurring globally, even in regions currently considered water rich. The problem is particularly significant in developing countries and in arid areas where water sources are scarce. This is a continually growing problem due to rising population and increasing demands for source of waters. Moreover, with rapid industrialization, many pollutants such as various dyes, sulphates and toxic compounds are dumped into the water. It was estimated that more than 50,000 tons of dyes are discharged from dyeing and coloration industries every year. Since azo dyes are intentionally designed to resist degradation, it is very difficult to degrade them by conventional wastewater treatment methods. In addition, the toxicity, mutagenicity and carcinogenicity of azo-dye degradation byproducts are of great

environmental concern. Chemical disinfection options such as chlorine and iodine treatment, ozonization, flocculation and filtering require additives and are also not cost-effective. Physical treatment such as boiling, distillation, reverse osmosis and UV irradiation require considerable energy input. One alternative for drinking water treatment method that has been proposed is solar photocatalytic purification, a process that could be utilized in countries that receive abundant sunlight. Wide band gap semiconducting transition metal oxide photocatalysts have been shown to decompose organic compounds, bacteria and other impurities present in water. The most prominent, widely studied photocatalyst is WO_3/TiO_2. Upon irradiation of a semiconductor with photons of energy higher than the band gap, charge carriers are generated. Those which are not lost by recombination can carry out electron transfer reactions at the interface between the semiconductor and a liquid containing an oxidizable or a reducible species. In the case of an n-type oxide semiconductor, valence band holes (h^+) lead either directly, or via OH^- radicals, to the oxidation of the solute (D), while conduction band electrons (e^-) lead to reduction of dissolved oxygen, if present, forming superoxide radical anions, O_2^-, and OH radicals, if not participating in the degradation process, finally lead to the formation of water and oxygen, respectively. Recombination of photogenerated positive holes and electrons inside the semiconductor are responsible for a rather low quantum yield of the photocatalytic degradation. A way of increasing electron– hole separation and consequently enhancing quantum yield is the use of transition stratified metal oxide semiconductor thin films and an application of electrical bias, which is possible when the photocatalyst is deposited on an electrically conducting substrate. Here, the working point of the photoelectrochemical reaction can be shifted to the potential range where photon flux limited (plateau) currents flow. Due to backside illumination through the transparent conducting substrate, direct photolysis is avoided and even strongly colored solutions can be treated, as actinic light is encountering the semiconducting layer first. Electrons are drawn away from the interface, and reduction reaction occurs at the counter electrode. Oxygen is available in sufficient quantity as a depolarizer for the counter electrode, firstly due to rapid recirculation of the solution through a reservoir in contact with air and, secondly, due to water oxidation by reaction steps initiated by valence band holes. As to the organic molecules which can be oxidized in this way, azo-dyes are of special interest, as mentioned above. Different methods have been explored for the removal of azo-dyes from solution. Bourikas et al. investigated the adsorption of a textile azodye, acid orange 7 (AO7), on the surface of WO_3/TiO_2 in aqueous suspensions in the range of 0.1–1 mM at pH values between 2 and 10. Liu et al. studied degradation of AO7 quite differently, using a Fe/granular activated carbon system in the presence of ultrasound. Fernandes et al. studied the electrochemical degradation of AO7 on a boron doped diamond electrode (BDD) and obtained 98% and 77% color and chemical oxygen demand (COD) removal, respectively. AO7 photofading by a photocatalytic method using WO_3 /TiO_2 nanotubes was also reported. Here photoelectrochemical degradation of organic compounds by TiO_2, taking AO7 as a model compound. The main aspects studied are (i) the use of electrical bias, (ii) the use of large catalyst surfaces, and (iii) the possibility of using solar light.

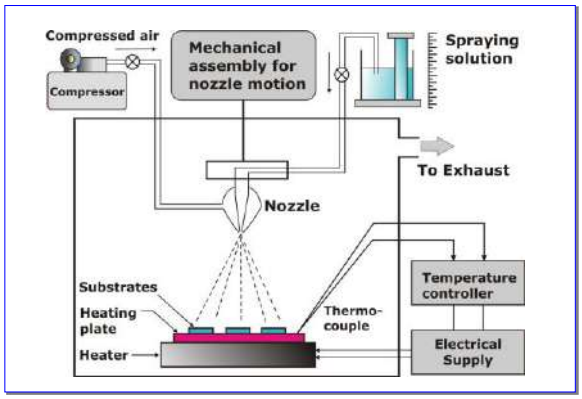

Fig 1. Schematic diagram of the Spray Pyrolysis Technique

Large area thin films of F:SnO_2 and TiO_2 and other oxide semiconductor thin films can be prepared by the above mentioned technique.

Out of 100% water on the earth, there is 97 % saline water, + 0.5 % polar ice + 2.5 % surface water. Out of 2.5%, 80 % water is polluted due to human activities. It is estimated that about 2 million human deaths per year occur due polluted water. Out of 2.5 % 70 % are used for agriculture, 20 % for industry and 10 % for private house hold.

Therefore purification of water is of paramount importance.

There are varieties of techniques to produce semiconducting thin films. The spray pyrolysis technique shown in the following figure works on the principle of pyrolytic decomposition.

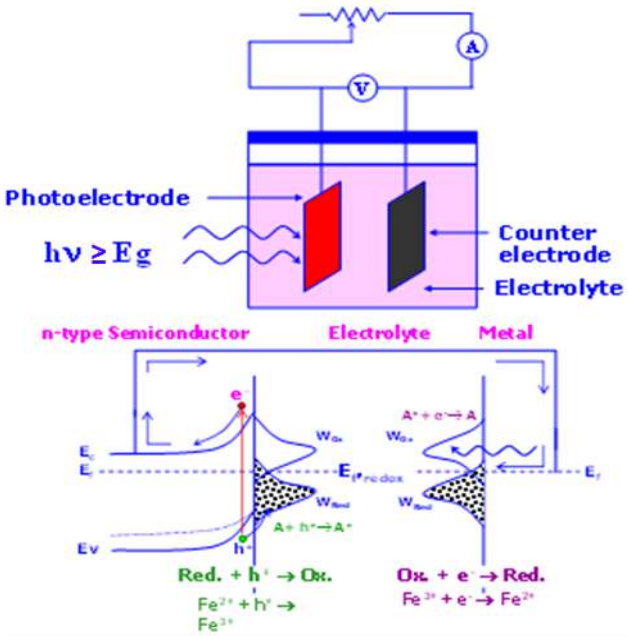

Fig 2. Principle of water purification with energy band diagram

Only photons having energy equal to or greater than the band gap energy (Eg) of a semiconductor can be absorbed by the semiconductor. This absorption leads to the creation of an electron - hole pair which is separated by the local electric field present across the junction. If the photon energy is less than that of the band gap energy the photon just passes through the semiconductor. Thus the absorption of photons of the solar spectrum in the photo electrode depends upon the band gap energy of the stratified layers. To have effective absorption of photons of the solar spectrum by the stratified layers, semiconductors with decreasing order of band gap energies are coated onto the transparent conducting substrates that helps to enhance the efficiency of the process. The capture of a hole by a reduced species is equivalent to oxidation and the capture of an electron by oxidized species is reduction as shown in the fig. 2. Purification of water is carried out by of red ox reactions. For n-type semiconductors, oxidation of pollutants occurs at the surface of the semiconductor and reduction of oxidized species occurs at the surface of the counter electrode as shown in the figure 2.

A nine cell reactor developed at SUK/Kolhapur is shown in the Fig. 3.

Fig 3. Nine Cell Reactor for purification of water.

This is a device that removes dyes present in water. Bacteria can also be killed just by keeping this reactor under sunlight. A peristaltic pump is being used to circulate impure water with a desired flow rate. The flow rate plays a vital role in influencing the efficiency of the process.

Karnatak University Journal of Science 53 (2022) 8-19

Karnatak University Journal of Science

ISSN: 0075-5168

Coordination behaviour of (*E*)-N'-(2,4-dihydroxybenzylidene)-2-benzamidobenzohydrazide towards transition metals

Umashri Kendur[a,b*], Geeta H. Chimmalagi[a], Mahantesh B.Budri[a], Sunil M. Patil [a], Ramesh S. Vadavi[a], Kalagouda B. Gudasi [a*]

[a] Department of Studies in Chemistry, Karnatak University, Dharwad, 580003, Karnataka, India

[b]P. G. Department of Studies in Chemistry, S. B. Arts and K. C. P Science College, Vijayapura, 586003, Karnataka, India

***Corresponding authors:** kbgudasi@gmail.com; drumashridr@gmail.com*

ARTICLE INFO

Article history:
Received: 30 May 2022;
Revised: 20 June 2022;
Accepted: 22 June 2022

Keywords:
Transition metals,
Square planar geometry,
Octahedral geometry,
Co-ordination complexes

ABSTRACT

Air and moisture stable coordination compounds of late first row transition metal ions, *viz.*, Co(II), Ni(II) and Cu(II) with a newly designed ligand, (*E*)-*N*'-(2,4-dihydroxybenzylidene)-2-benzamidobenzohydrazide (H_2L2) were prepared and extensively characterized using various spectro-analytical techniques. The ligand acts both in mono as well as doubly deprotonated manner. The ligand to metal stoichiometry was found to be 1:2 in case of complexes using chloride salts. The octahedral geometry was assigned for Co(II) and Ni(II) complexes, square planar geometry was assigned for Cu(II) complex.

1. Introduction

+Coordination chemistry is one of the most advanced and active research fields in inorganic chemistry. This branch of chemistry received much attention and offered fruitful results and hence this has become extremely attractive field of research [1].

Metals play a very important role in biological life kingdom. It will not be an exaggeration to say that metal complexes have vital role in modern scientific age to achieve advancement in the field of agriculture, plant nutrition and biological activity of living beings, industries and in medicine.

Metal ions are generally positively charged and act as electrophiles, seeking the possibility of sharing electron pairs with other atoms so that a bond or charge-charge interaction can be formed. Metal ions, however, often have positive charges greater one, and have a larger ionic volume so that they can accommodate many ligands around them at the same time [2].

Coordination compounds have been studied extensively because of their diverse molecular structure and chemical bonding as well as varied biological properties. The nature of the coordination compounds depends upon the metal ion, donor atom,structure of ligand and the metal ligand interaction. The metal ion function as the Lewis acid and range of Lewis base (electron pair donor) can include almost any species that has one or more unshared pair of electron [3].

Many of the properties of transition metal complexes are dictated by their electronic structures. The electronic structure can be described by a relatively ionic model that ascribes formal charges to the metals and ligands. This approach is the essence of crystal field theory (CFT) which treats all interactions in a complex as ionic and assumes that the ligands can be approximated by negative point charges [4-6].

Metal coordination complex have a wide variety of technological and industrial application ranging from catalysis to anticancer drugs. In these compounds the metal atom itself may have a number of roles, based on its coordination geometry, oxidation state and magnetic electronic and photochemical behavior. Schiff bases are an important class of ligand in coordination chemistry and their complexing ability containing different donor atoms are widely reported [7].

Hydrazones are a class of organic compounds which possess the structure $R_1R_2C=NNH_2$. They are related to ketone and aldehyde in which oxygen has been replaced with $-NNH_2$ group. Hydrazones are formed by the reaction of hydrazine or hydrazide with aldehydes and ketones. The C=N double bond in hydrazones are important compounds in drug design as they act as ligands for metal complexes, organo catalysis and synthesis of organic compounds. The C=N bond of hydrazone and terminal nitrogen atom containing a lone pair of electron is responsible for the physical and chemical properties. The C-atom in hydrazone has both electrophilic and nucleophilic character and both the N-atoms are nucleophilic although the amino type nitrogenis more reactive. Due to these properties hydrazones are widely used in organic synthesis [9-11].

2. Experimental

2.1. Materials and Methods

Purified solvents were used for the synthesis of ligands and complexes. Cobalt chloride,Nickel chloride andCopper chloride were purchased from S. D. fine chemical Ltd. Hydrazine hydrate, 4-hydroxy salicylaldehyde were purchased fromSpectrochem Pvt. Ltd. The aluminum pre-coated silica gel plates for TLC were obtained from S.D. fine chemicals.

2.2. Physical measurements

2.2.1. Thin Layer Chromatography (TLC)

Progress of the reaction and purity of the compounds prepared in each of the reactions were checked by TLC on pre-coated silica gel plates using different eluent systems.

2.2.2. Melting point

Melting points were determined in an open capillary on a gallenkamp melting point apparatus supplied by Sheetal Scientific Instruments and are uncorrected.

2.4. Fourier Transform Infrared spectral studies

Infrared spectra of ligand and complexes were recorded in KBr discs in the region 400-4000cm^{-1} on a Nicolet 170SX FT-IR spectrometer. IR spectra were recorded at University of Scientific Instrumentation Center, KarnatakUniversity Dharwad.

2.5. Nuclear Magnetic Resonance spectral studies

^{1}H NMR and ^{13}C NMR spectra of ligand were recorded in DMSO-d_6 on JEOL- 400 MHz FT-NMR spectrometer using tetramethysilane (TMS) as internal standard at University Scientific Instrumentation Center, Karnatak University, Dharwad.

2.6. Conductance measurements

The molar conductance made on ELICO conductivity bridge type CM-82 provided with a dip type conductivity cell fitted with platinum electrode. The cell constant was determined by measuring the conductance. The conductance values of the complexes were determined by using 10^{-3} M solution in DMF. The molar conductance is calculated as follows.

Λ_M = 1000 × k ×observed conductance (in mhos)/C

where, Λ_M = Molar conductance, k = cell constant, C = Molar concentration (10^{-3})

2.7. Electronic spectral studies (UV-Visible)

The UV-Visible spectra compounds were recorded (in DMF) on JASCO V-670UV-Visible spectrometer,University Scientific Instrumentation Center, KarnatakUniversity, Dharwad.

2.8. Mass spectrometry

Mass spectra of the ligand was recorded on GCMS2010S, USIC, Karnatak University, Dharwad and LCMS mass spectrum of copper complex was recorded on Waters UPLC-TQD Mass spectrometer SAIF, CDRI Lucknow.

2.9. Thermal studies

TGA of ligand and complexes was recorded using TGA instrument in the range of 25-1000^{o}Cfrom University Scientific Instrumentation Centre Karnatak University, Dharwad.

2.10. Synthesis of H_2L2 and its metal complexes

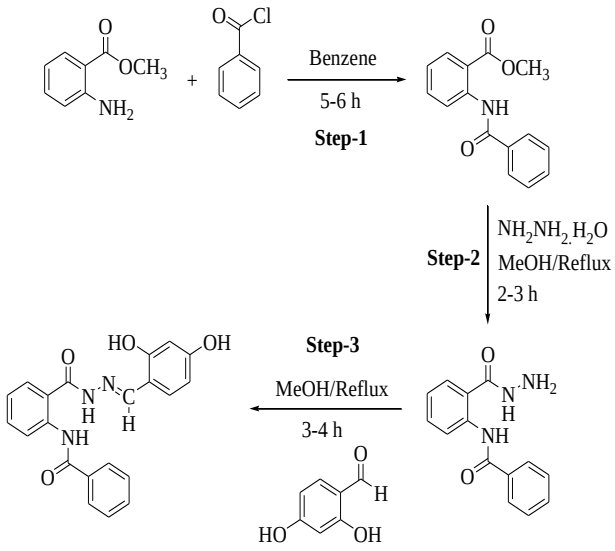

Scheme: Synthetic route for the ligand (H_2L2)

2.10.1. Synthesis of ligand involves following steps:-

Step 1: Preparation of methyl 2-benzamidobenzoate

Benzoyl chloride(10g,36.5 mmol) was dissolved in benzene and methanolic solution of methyl 2-aminobenzoatewas added drop by drop with constant stirring. The reactionmixture was refluxed on oil bath for 5-6 h.The progress of the reaction was monitored by TLC.After the completion of reaction the solvent was evaporated and the obtained white solid was filtered,washed with methanol, dried and weighed.

Yield: 79 % MP: 120-122ºC

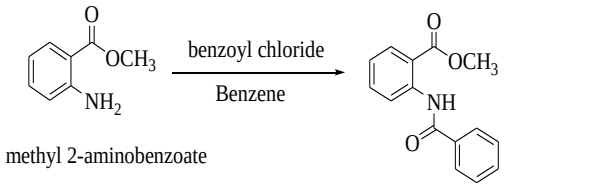

methyl 2-aminobenzoate

methyl 2-(benzamido)benzoate

Step 2:

Synthesis of 2-benzamidobenzohydrazide

To themethanolic solution of methyl 2-benzamido benzoate (10g, 36.5 mmol), hydrazine hydride (5.489 g, 109.6 mmol) was added and refluxed for 2-3 h. The progress of the reaction was monitored by TLC.After the completion of reaction the solvent was evaporated and the obtained white solid was filtered, washed with methanol, dried and weighed.

Yield: 81 % MP: 236-238ºC

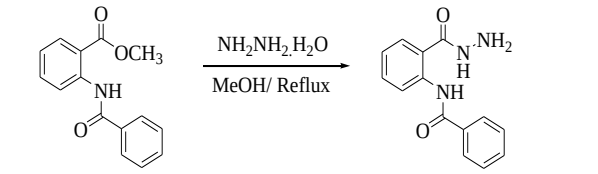

methyl 2-(benzamido)benzoate

2-(benzamido)benzohydrazide

Step 3: Synthesis of (*E*)-*N'*-(2, 4-dihydroxybenzylidene)-2-benzamidobenzohydrazide

To the methanolic solution of 2-benzamidobenzohydrazide (3g, 11.7 mmol), 4-hydroxy salicylaldehyde (1.623g, 11.75 mmol) was added and refluxed for 3-4 h.The progress of the reaction was monitored by TLC.After the completion of reaction the solvent was evaporated and the obtained white solid was filtered,washed with MeOH, dried and weighed.

Yield:81% MP: 272°C

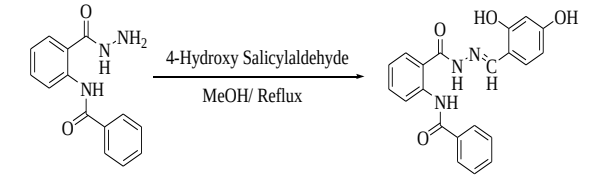

2-(benzamido)benzohydrazide

(*E*)-*N*'-(2,4-dihydroxybenzylidene)-2-(benzamido)benzohydrazide

2.10.2. Preparation of complexes

2.10.2.1. Preparation of cobalt complex (C1)

Methanolic solution of cobalt chloride (0.38g, 1.59 mmol), was added to methanolic suspension of ligand (0.6g, 1.59 mmol) with stirring. The solution was refluxed for 5-6 h and precipitate obtained was filtered,washed with methanol,dried and weighed.

Yield: 76 %

2.10.2.2. Preparation of nickel complex (C2)

Methanolic solution of nickel chloride (0.3802g, 1.59mmol) was added to methanolic suspension of ligand (0.6g, 1.59mmol) with stirring. The solution was refluxed for 4-5 h and precipitate obtained was filtered,washed with methanol,dried and weighed.

Yield: 72%

2.10.2.3. Preparation of copper complex (C3)

Methanolic solution of copper chloride (0.2726g, 1.59mmol), was added to methanolic suspension of ligand (0.6g, 1.59mmol) with stirring. The solution was stirred for 2-3 h and precipitate obtained was filtered,washed with methanol,dried and weighed.

Yield:78%

3. Results and Discussion

Metal complexes obtained in the present study were amorphous solid. The metal complexes were soluble in DMF, and DMSO whereas, insoluble in water, ethanol, methanol, carbon tetrachloride and chloroform solvents. The composition and structure of these complexes have been established based on various spectral studies and physico-chemical measurements. Physico-chemical data of the complexes are compiled in **Table 1**. The low molar conductance values suggest the non-electrolytic nature of these complexes. [12].

3.1. IR spectral studies

The diagnostic IR bands are given in **Table 2**and the spectra of ligand and its complexes are depicted in **Figures 2-5**,respectively. In the spectrum of the ligand a broad band at 3456 $cm^{-1}$is assigned to ν(OH) which is disappeared

Table 1. Analytical, molar conductance and electronic spectral data of $H_2L2$and its complexes

Sample Code	Empirical Formula	Metal (%)	Determination	Molar Conductance (ohm^{-1} cm^2mol^{-1})	λ_{max}(nm)		
		Calculated	Experimental		$\pi \rightarrow \pi^*$, $n \rightarrow \pi^*$	CT	d-d
H_2L2	$C_{21}H_{17}N_3O_4$	---	---	---	272,345	---	---
C1	$[Co(C_{21}H_{16}N_3O_4)_2]$	7.30	6.69	4.98	271,398	398	---
C2	$[Ni(C_{21}H_{16}N_3O_4)_2]$	7.27	8.76	7.67	271,402	402	977
C3	$[Cu(C_{21}H_{16}N_3O_4)Cl]$	13.42	13.78	1.37	271,391	391	628

Table 2. Diagnostic IR band in H_2L2 and its metal complexes (in cm^{-1})

Compound Code	$\nu(C^7=O)$	$\nu(C^{14}=O)$	ν(C=N)	ν(OH)	ν(C-O)
H_2L2	1661	1631	1604	3456	1168
C1	1672	1621	1588	---	1184
C2	1654	1618	1589	---	1189
C3	1647	1614	1591	---	1178

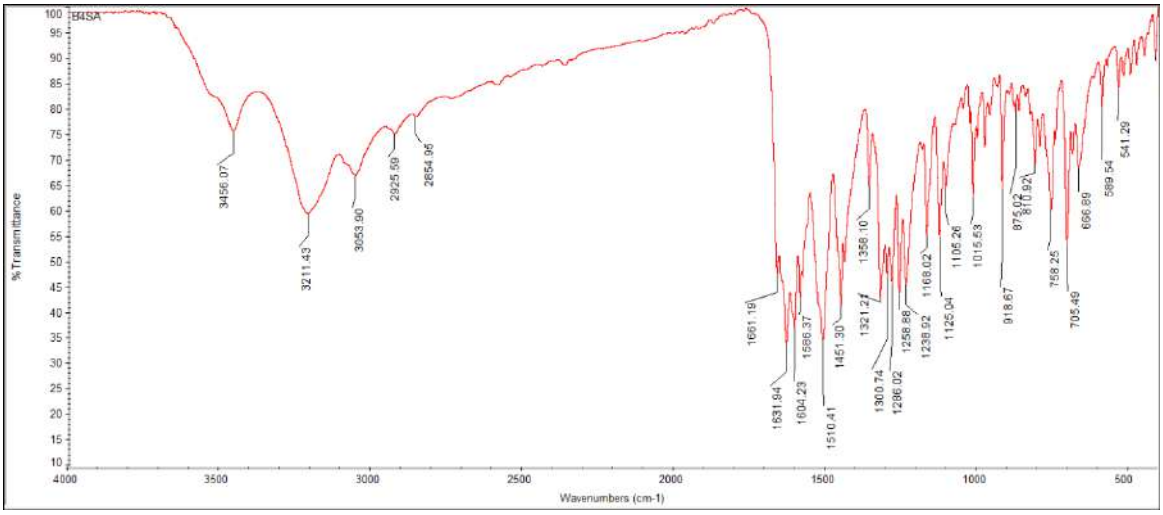

Figure 2. IR spectrum of H_2L2

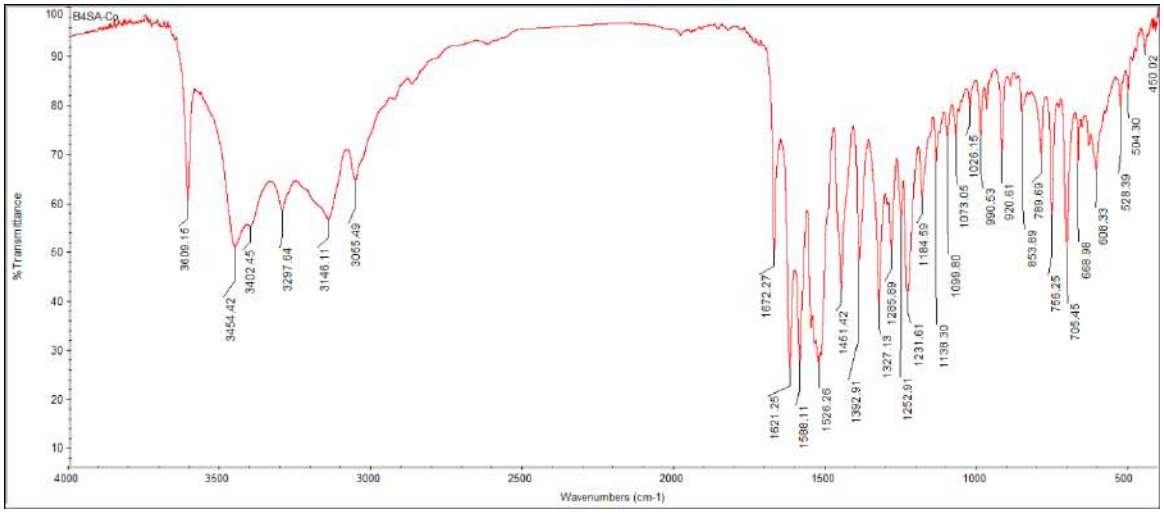

Figure 3. IR spectrum of C1

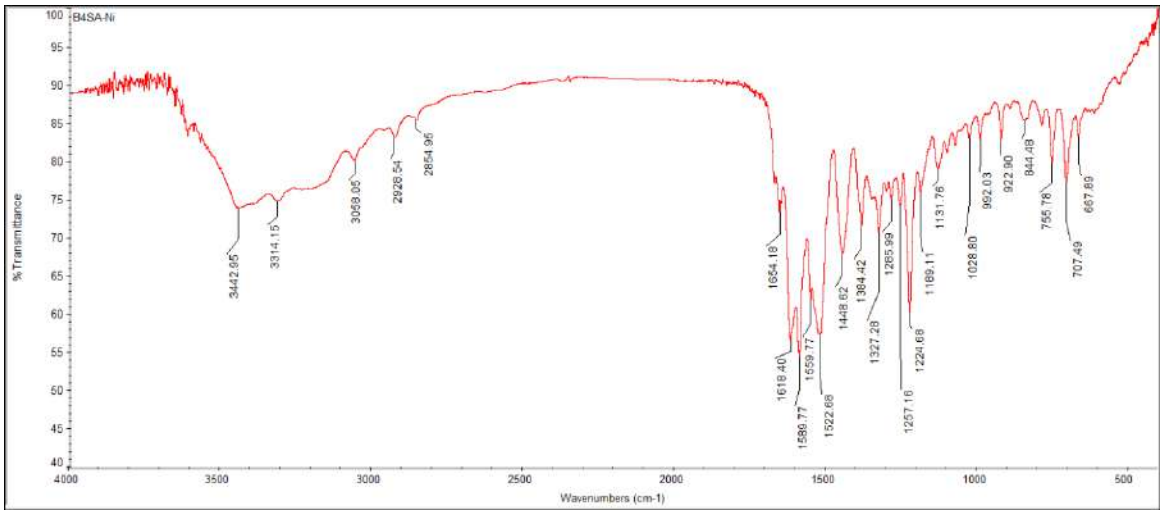

Figure 4. IR spectrum of C2

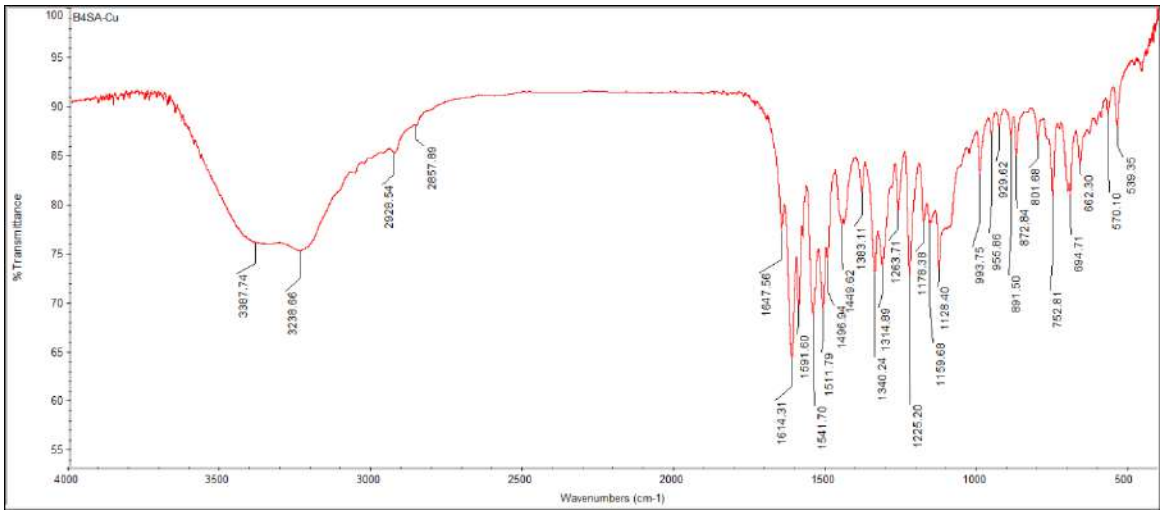

Figure 5. IR spectrum of C3

in all the complexes indicating its coordination to metal ion *via*deprotonation. In addition, the ν(C-O) band observed at 1168 cm^{-1} in H_2L2 shows a red shift in the complexes, indicates the coordination of phenolic oxygen *via*deprotonation to the metal ion. A band at 1661 cm^{-1}assigned to ν(C^7=O), shows no significant change in all the complexes indicates its non-involvement in coordination [13]. The strong band at 1631 cm^{-1} is attributed to ν(C^{14}=O) of H_2L2 has shifted to lower frequencies by 9 to 16 cm^{-1} in C1, C2, and C3 complexes, clearly indicates the involvement of oxygen of C^{14}=O group in coordination on the metal ion. Theazomethine group ν(C=N)observed at 1604 cm^{-1}in the free ligand is shifted to 1588, 1589, and 1591 cm^{-1}in Co(II), Ni(II), and Cu(II) complexes, respectively, indicating the participation of azomethine nitrogen in coordination to the metal ion [14]

3.2. NMR Spectral studies

Numbering pattern followed for the assignment of carbons and protons is shown in **Figure 1** and ^{1}H and ^{13}C NMR spectral data of H_2L2 is given in **Table 3**.

Table 3.^{1}H and ^{13}CNMR spectral data of H_2L2(in ppm)

Positions	H_2L2	
	^{1}H	^{13}C
C^1& C^5	7.547-7.612 (m,4H)	127.5
C^2 & C^4	7.547-7.612 (m,4H)	129.5
C^3	7.244 (t,1H, J=7.6 Hz)	132.6
C^6	---	134.9
C^7	---	165.1
C^8	---	139.8
C^9	7.913(dd,1H, J=7.6, 2.4Hz)	120.7
C^{10}	7.341 (d,1H, J=8.4)	133.1
C^{11}	7.865 (d,1H, J=3.6Hz)	123.7
C^{12}	8.513 (dd,1H,J=8.4,4Hz)	129.1
C^{13}	---	121.5
C^{14}	---	164.8
C^{15}	8.534 (s, 1H)	150.2
C^{16}	---	111.0
C^{17}	6.338 (d,1H, J=2Hz)	131.5
C^{18}	6.317 (1H, J=2Hz)	108.3
C^{19}	---	160.0
C^{20}	6.287 (1H, J=2.4)	103.7
C^{21}	---	161.5
N^1	11.95 (s,1H)	---
N^2	11.28 (s,1H)	---
O^3	12.13 (s,1H)	---
O^4	10.00 (s,1H)	---

Ligand showssinglets at 12.13, 11.95, and 11.28 ppm are assignable to O^3H, N^1H and N^2H protons, respectively. The C^{15}H proton has appeared as singlet at 8.53 ppm. All the aromatic protons have resonated in the range 6.32–8.51 ppm.The ^{1}H NMR spectrum of $H_2L2$is presented in **Figure 6.**

In the ^{13}C NMR spectrum of H_2L2clearly resolved signals were observed for all the carbon atoms are presented in **Figure 7.** Carbon signals due to two carbonylcarbons (C^7) and (C^{14}) are observed at 165.1, and 164.8 ppm, respectively. Signals for azomethine carbon(C^{15})andcarbons ($C^{19}$and C^{21}) attached to two hydroxyl groups are observed at 150.2, 160.0, and 161.5 ppm, respectively. Remaining all the carbon signals have resonated in their expected region. [15]. The detailed assignments of the ^{1}H and ^{13}C NMR spectra are compiled in **Table 3**.

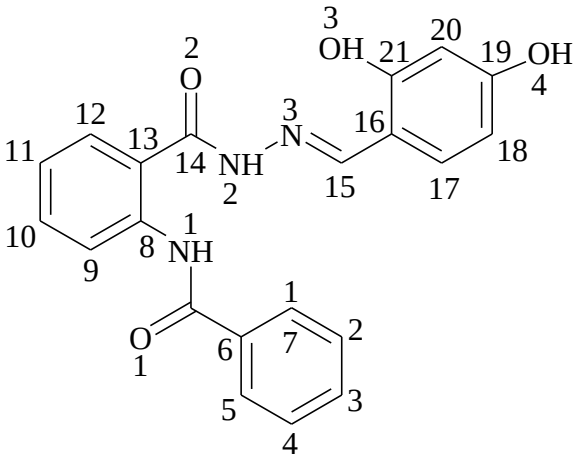

Figure 1. The numbering scheme for H_2L2

3.3. Mass spectral data

The mass spectrum of a H_2L2(**Figure 8**) shows molecular ion peak at 375 corresponds to its molecular weight. The LCMS of C3 (**Figure 9**) shows molecular ion peak observed at 497 corresponds to $[M+Na]^+$.

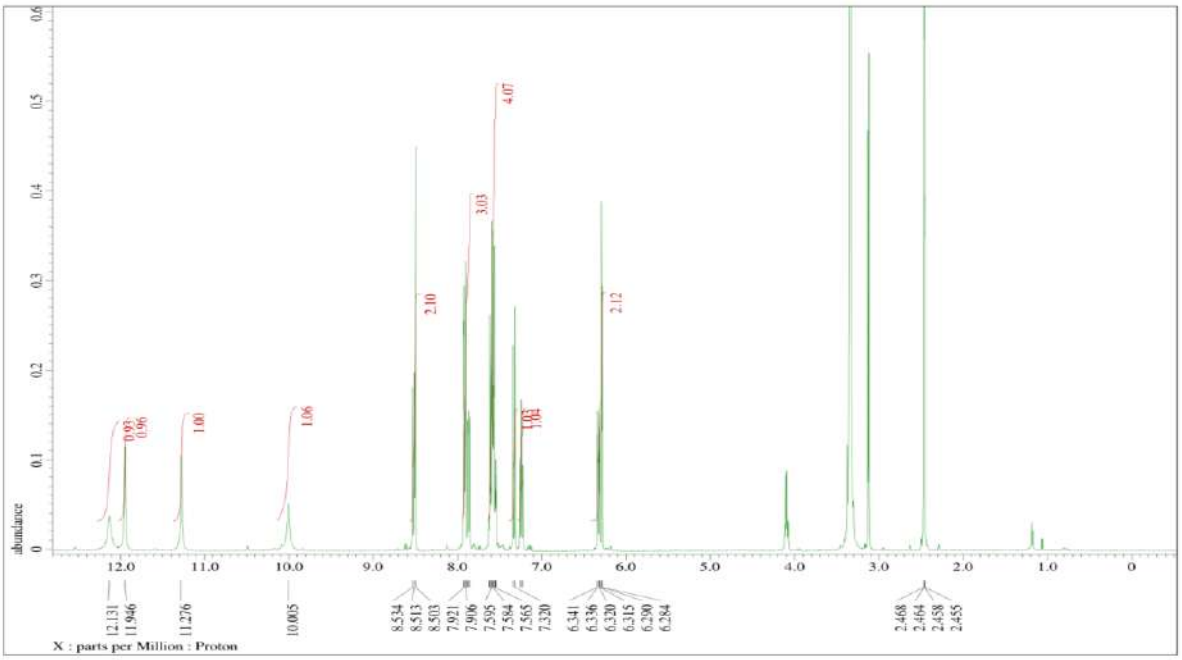

(b)

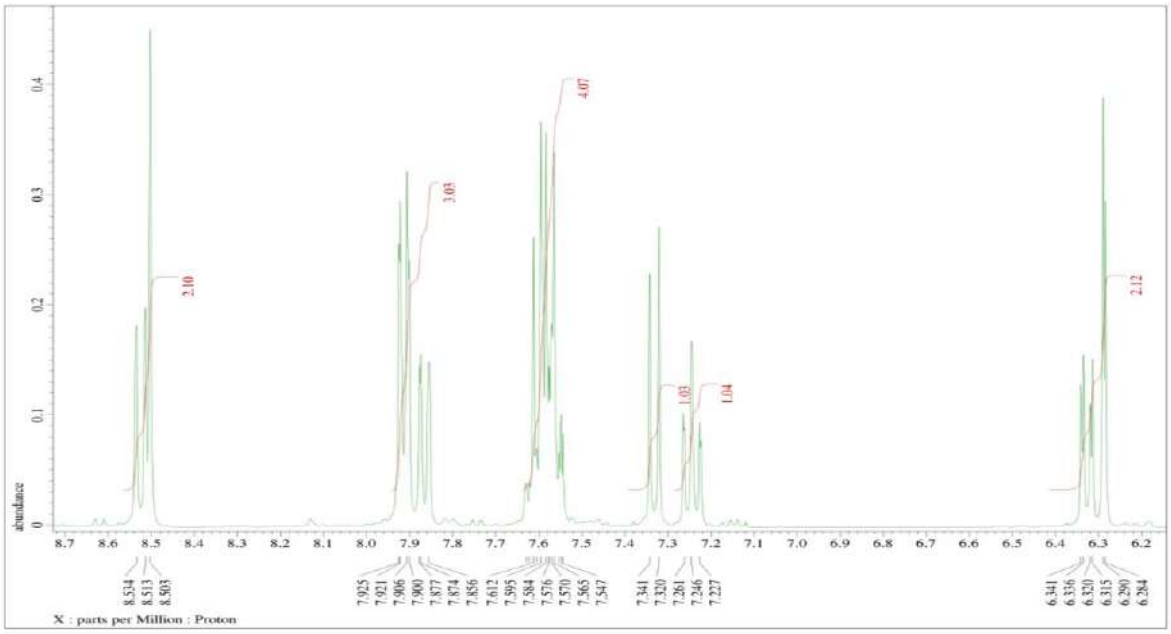

(a)

Figure 6. ^{1}H NMR spectrum of H_2L2 (a) 0-12 ppm (b) 6.2-8.7 ppm

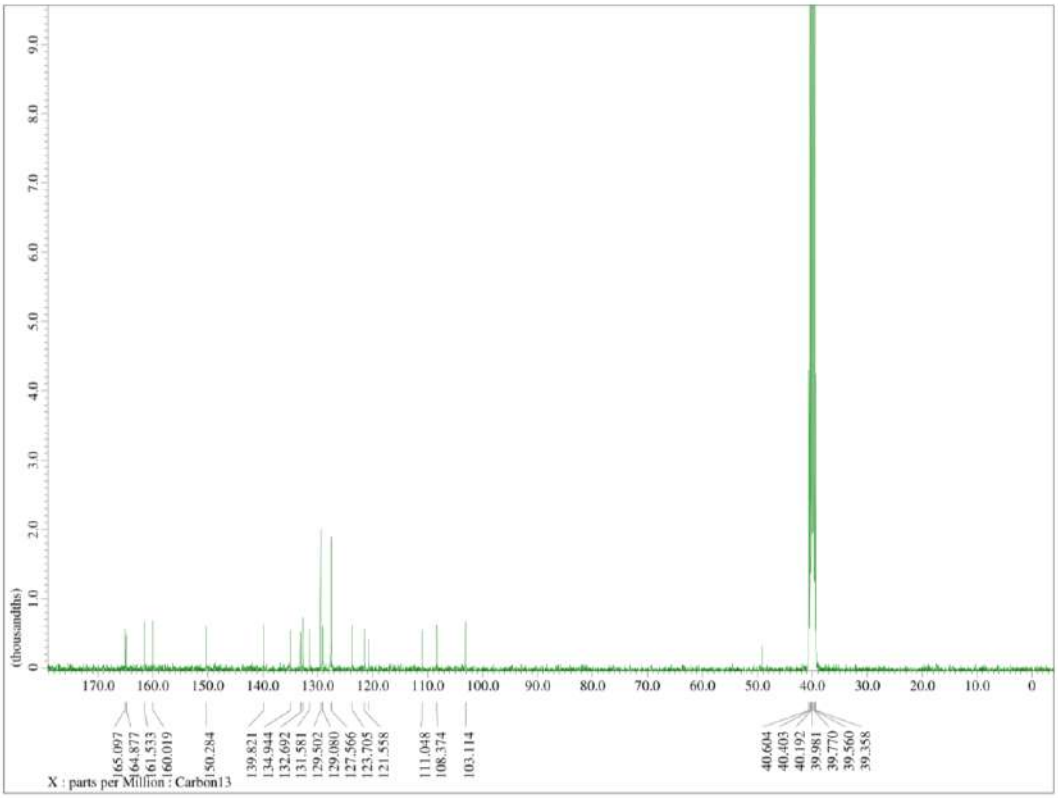

Figure 7. ^{13}C NMR spectrum of H_2L2

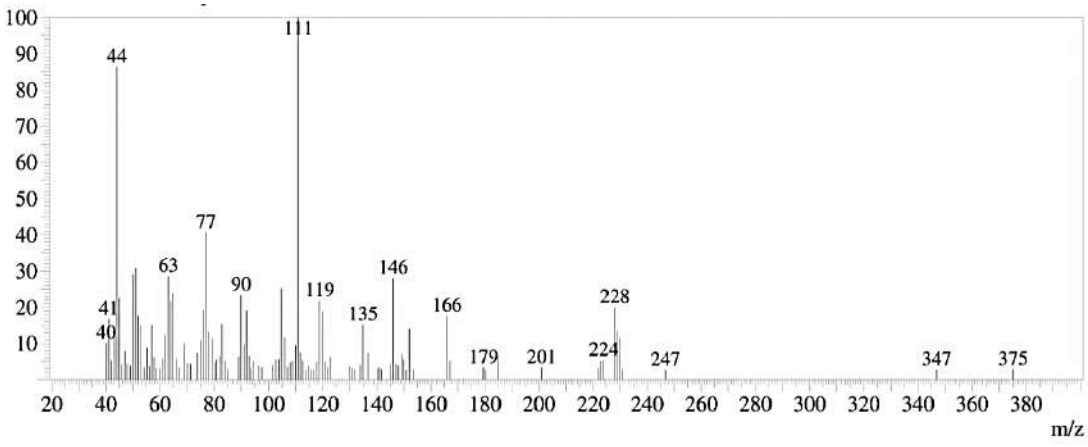

Figure 8. Mass spectrum of H_2L2

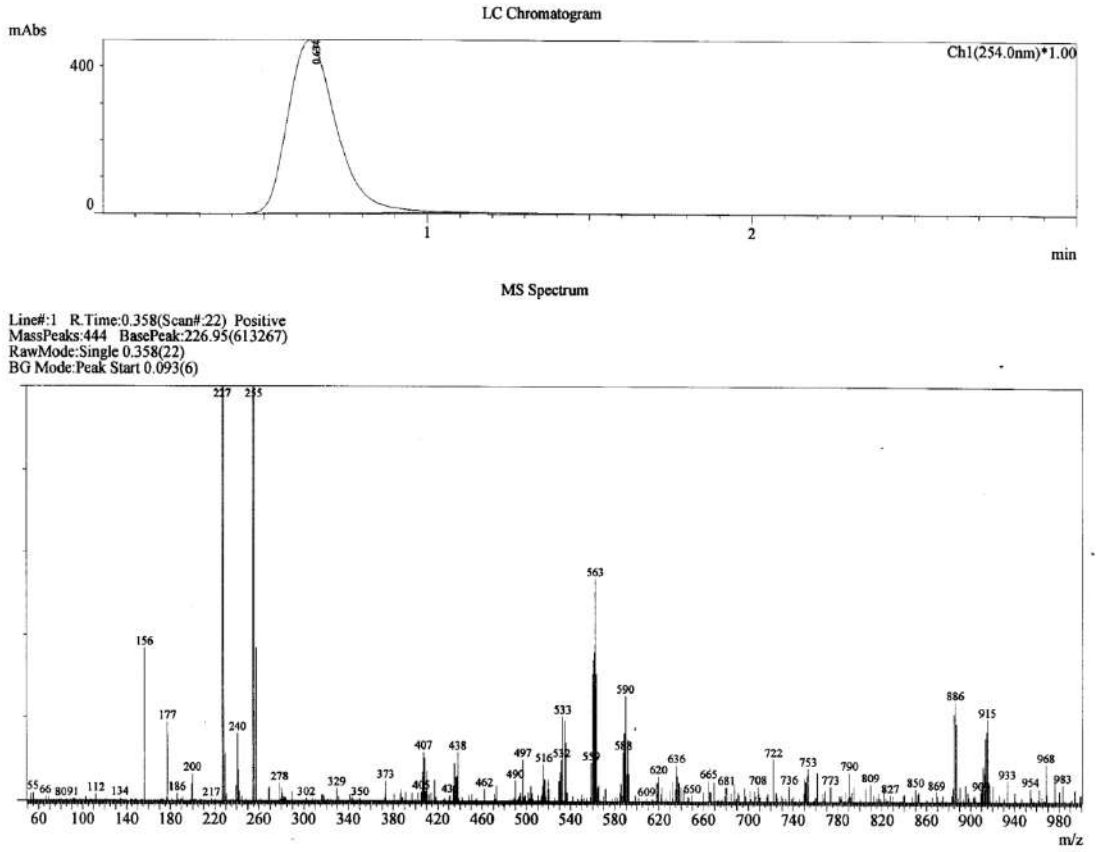

Figure 9. LCMS spectrum of C3

3.4. Electronic spectral studies

Electronic spectra of the compounds in DMF were scanned in the 200-1000 nm region. Electronic spectra of $H_2L2$and its complexes (C1-C3) are depicted in **Figure 10.**

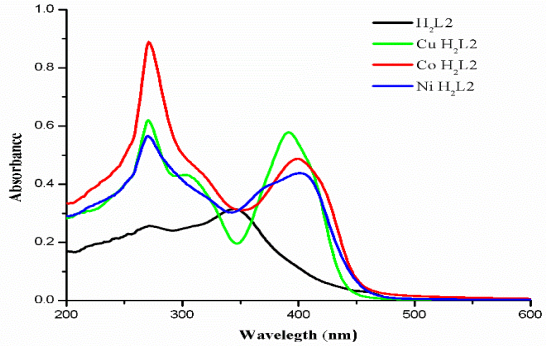

Figure 10. Electronic spectra of $H_2L2$and its Complexes

The ligand exhibit two absorption bands in the UV–visible region around 272 and 345 nm. The first intense band around 272 nm is assigned to a ligand $\pi \rightarrow \pi^*$ transition. This bandremains almost unchanged in the spectra of all the complexes. The second broad band around 345 nm assigned to $n\rightarrow\pi^*$ transition, has suffered bathochromic shift by 46-57 nm upon complexation indicating the coordination of azomethine nitrogen to the metal centre.The estimated weak d-d transitions for the paramagnetic complex C1 in the visible region cannot be detected even with concentrated solution. It may be lost in the low energy tail of the charge transfer [16]. All the complexes have shown an intense band in the region 391-402 nm, which can be assigned to charge transfer (CT) transition has merged with$n\rightarrow\pi^*$ transition peak. The electronic spectrumof the C2shows bandat977 nm, is attributable to$^3A_{2g}(F) \rightarrow {}^3T_{2g}(F)$ transition suggesting an octahedral geometry for C2 [17]. A broad band in the visible region for C3 with λ_{max} at 628 nm is assigned to the combination of $^2B_{1g} \rightarrow {}^2A_{1g}$ and $^2B_{1g} \rightarrow {}^2E_g$ transition and this transition indicates square planar geometry around Cu (II) ion.

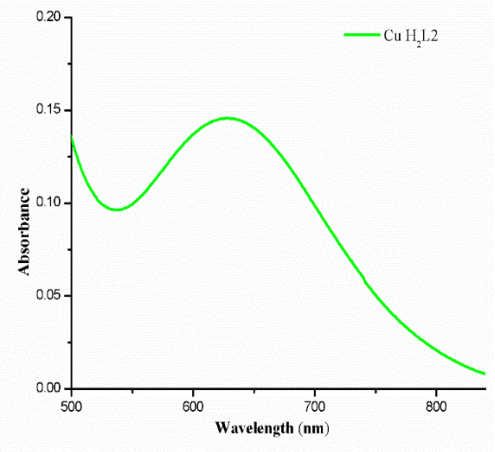

Figure 11. Electronic spectra of metal complexes showing d-d transitions.

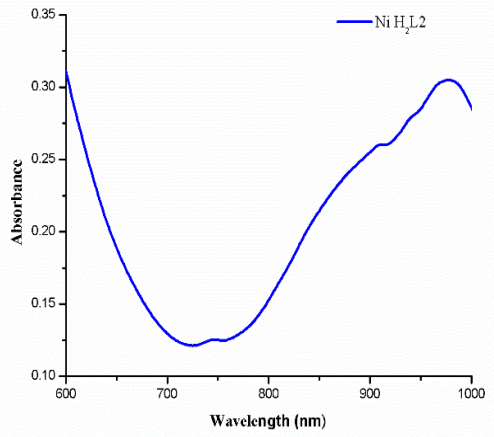

3.5 Thermal studies

Thermogravimetric study of cobalt complex have been undertaken toknow the presence/absence of coordinated/lattice held solvent/water molecules, to confirm its composition and to understand the thermal stability. The thermogram of C1 showeda weight loss of 4.22% (calc. 4.26%) between the temperature range 52-120°C, indicating thepresence of two lattice held water molecules.This is clearly evidenced in DTA curve in the formof an exothermic peak at 75°C. Weight loss of 87.04% (Calc. 87.09%) around 250-675°C corresponds to the loss of two coordinated ligand molecules and plateau obtained after heating 675˚C corresponds to the formation of stable CoO. Thermogram of C1 is shown in **Figure 12.**

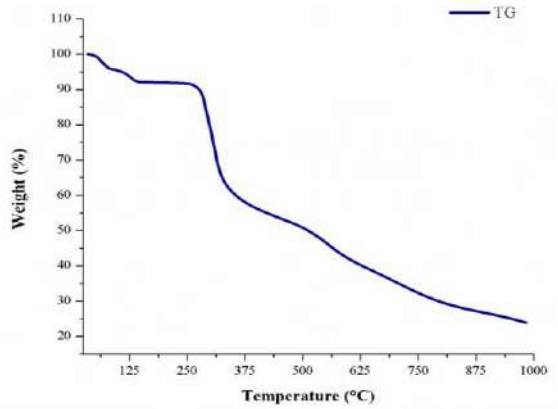

Figure 12. Thermogram of C1 complex

4. Conclusion

The new ligand (*E*)-*N*'-(2,4-dihydroxybenzylidene)-2-benzamidobenzohydrazide (H_2L2) and its Co(II), Ni(II), and Cu(II) complexes were synthesized and characterized. The composition and structures of the synthesized compounds were confirmed based on various spectro-analytical techniques. H_2L2 acts as a monobasic tridentate ligand in case of all the complexes. Theoctahedral geometry was assigned forCo(II) and Ni(II) complexes,square planar geometrywas assigned forCu(II) complex. On the basis of all the observations, tentatively assigned structures for the C1-C3 complexes are shown in **Figure 13.**

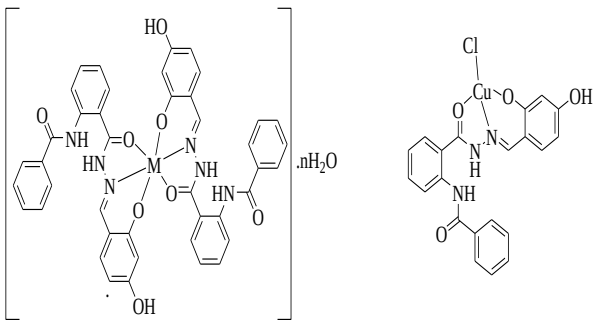

Figure 13. Tentative structures for C1-C3 complexes

References

[1] R. S. Nyholm, Proc. Chem. Soc., 273, (1961).

[2] N.N. Greenwood and A. Earnshaw, Chemistry of the elements, 2nd edition. Butterworth-Heinemann, Oxford, UK, 224, (1997).
[3] X. Shen, Q. L. C Yang and Y. Xie, Synth. React. Inorg. Met.-Org Chem., 26, 1135, (1996).
[4]J.C. Kotz, K.F. Purcell, Chemical and Chemical Reactivity Saunders New York, 106-112, (1987).
[5] R. H. Prince, Comprehensive Coordination Chemistry, Pergamone, Oxford, 5, 926, (1987).
[6] J. Hanas, D. J. Hazuda, D. F. Bogenhagen, J. H. Wu and C. W. Wu, J. Bio .Chem., 258, 14120, (1983).
[7] M. M. T. Khan and A. E. Martell, Homogeneous Catalysis of metal complexes, Academic Press, New York, 1, (1974) 545-552
[8] P. W. Blower and J. R. Dilworth, Coord. Chem. Rev., 121, 76, (1987).
[9] FB. Abdel-Wahab, AEG. Awad, and AF. Badria, Synthesis, antimicrobial, antioxidant, anti-hemolytic and cytotoxic evaluation of new imidazole-based heterocycles, Eur. J. Med. Chem., 46, 1505-151, (2011).
[10] M. Emami, H. Shahroosvand, R. Bikas, T. Lis, C. Daneluik, and M. Pilkington, Synthesis, Study, and Application of Pd(II) Hydrazone Complexes as the Emissive Components of Single-Layer Light-Emitting Electrochemical Cells, Inorg. Chem., 60, 2, 982–994, (2021).
[11] N. Stevanović, M. Zlatar, I. Novaković, A. Pevec, D. Radanović, I. Z. Matić, M. ĐorđićCrnogorac, T. Stanojković, M. Vujčić, M. Gruden, D. Sladić, K. Anđelković, I. Turel, and B. Čobeljić, Cu(II), Mn(II) and Zn(II) complexes of hydrazones with a quaternary ammonium moiety: synthesis, experimental and theoretical characterization and cytotoxic activity, Dalton Trans., 51, 185-196, (2022).
[12] UmashriKendur, Geeta H. Chimmalagi, Sunil M. Patil, Kalagouda B. Gudasi, Christopher S. Frampton. Applied Organometallic Chemistry 32, 4278, (2018).
[13] UmashriKendur, Geeta H. Chimmalagi, Sunil M. Patil, Kalagouda B. Gudasi, Christopher S. Frampton, Chandrashekhar V. Mangannavar, Iranna S. Muchchandi, Journal of Molecular Structure 1153, 299-310, (2018).
[14] Geeta H. Chimmalagi, UmashriKendur, Sunil M. Patil, Kalagouda B. Gudasi, Christopher S. Frampton, Mahantesh B. Budri, Chandrashekhar V. Mangannavar, Iranna S. Muchchandi.
Applied Organometallic Chemistry 32, 4337, (2018).
[15] Geeta H. Chimmalagi, UmashriKendur, Sunil M. Patil, Christopher S. Frampton, Kalagouda B. Gudasi, Delicia A. Barretto, Chandrashekhar V. Mangannavar, Iranna S. Muchchandi.
Applied Organometallic Chemistry 32, 4557, (2018).
[16] Yueqin Li, Zhiavei. Yang, Minya Zhou, Yun.Li, Jing He, Xuehengwang, Zhengfong Lin, RSC Adv., 7, 41527, (2017).
[17] Sunil M Patil, Ramesh S Vadavi, SuneelDodamani, UmashriKendur, GeetaChimmalagi, Sunil Jalalpure, Christopher S Frampton, Kalagouda B Gudasi. Transition Metal Chemistry 43, 65-72, (2018).

Karnataka University Journal of Science 53 (2022) 20-28

Karnataka University Journal of Science

ISSN: 0075-5168

Insight into the impact of neutron irradiation on optical parameters of poly (methyl methacrylate) (PMMA) loaded with methyl red (MR)

Soumya S Bulla[a,b], Rajashekhar F Bhajantri[a]*, Chetan Chavan[a]

[a]Department of Studies in Physics, Karnataka University, Dharwad - 580 003, Karnataka, India

[b]Department of Studies in Physics, Davangere University, Shivagangotri, Davangere -577 007 Karnataka, India

***Corresponding author:** rfbhajantri@gmail.com, rfbhajantri@kud.ac.in*

ARTICLE INFO

Article history:
Received: 30 March 2022;
Revised: 27 April 2022;
Accepted: 30 June 2022;

Keywords:
Optical constants;
polymethylmethacrylate;
neutron irradiation;
polymer composites;

ABSTRACT

The solution casting method was used to prepare PMMA/Methyl Red dye doped polymer composites using THF as a solvent, which were then cured in S-line petri dish and dried in hot air oven at 60 ℃. The prepared samples were exposed to neutron irradiation for seven days with neutron flux of 10^5 n/cm^{2}s. When PMMA and MR/PMMA subjected for neutron irradiation, the change in optical absorbance occurs due to the interaction of neutron with C=O group of PMMA. These findings demonstrate that the composites exhibit a high degree of optical transparency in visible region. Aside from optical absorption and extinction coefficients, the transmission data is also used to calculate the optical refractive index(n), real (ε_r) and imaginary (ε_i) dielectric constant, optical conductivity (σ_{opt}) and skin depth(χ).

1. Introduction

Polymers find the potential uses in many domains of science and technology, notably in opto-electronics, photonics and planetary science. In recent years, polymer scientists have focused their attention on electron, neutron or ion beam radiation in order to tune the physical properties of polymers [1]. There are several varieties of synthetic dyes, such as azo, vat, nitro, indigo, and others, that are extensively utilised for a wide range of applications in the paper and pulp industry, as well as in printing and textile manufacturing [2,3]. Methyl red (MR) is another example of a dye that has been frequently employed [4]. Methyl red (MR) is a photosensitive organic azobenzene chemical. The structure of azobenzene is marked by N=N bond. Due to dynamic photo-chemical feature of the structure, azobenzene may readily undergo trans and cis conformational change under irradiation period, a process known as photoisomerization. Certain azobenzene research have shown that trans-cis configuration transitions are an efficient mechanism for generating substantial optical nonlinear effects, which is favourable for applications and innovation [5,6]. According to Jaeyoung Lee et al. the diffusion of MR was significantly more hindered in a toluene solution of polyvinyl acetate (PVAc) than in polystyrene. The rationale for the slower diffusion in the presence of a PVAc matrix was attributed to hydrogen bonding between the probe and the polymer. The MR diffusion behaves similarly in a PMMA/toluene mix. This discovery completely supports the hypothesis that the slowed diffusion is induced by a particular interaction between MR and the carbonyl group in these polymers [4,7]. It is well understood that significant chemical changes occur in polymers during irradiation, including gas evolution, the formation of new double bonds, the creation of vacancy clusters, primary crosslinks (C=C bond scission), cross-linking and others [8]. Among these chemical alterations, cross-linking and chain scission are perhaps the most kinds of reactions in irradiated polymers [9].

Exploration of optical transitions and evaluation of the band structure and optical energy band gap of materials is aided by optical absorption investigations. Polymer nanocomposites provide the potential of a new era of lightweight composite materials with a wide range of uses in a variety of industries including automotive, general industry, and industrial applications. It has the potential to be used as radiation shielding materials in place of typical materials, among other things. Because of the high kinetic energy of neutrons, they are capable of penetrating through most materials and interacting with the atoms of the target substance shortly after impact [10]. Neutrons are typically employed in nuclear power plants for the generation of nuclear energy, and personnel in these facilities are exposed to neutrons on a regular basis. Aside from them, aircraft crew members are at risk of being exposed to neutrons. Exposure to neutrons is regarded crucial due to the negative impact they have on the human body as a result of the fact that they form considerably denser ion pathways while storing their energy [11]. This motivation provoked interest in understanding more about the influence of neutron irradiation on dye doped polymers. The current article focuses on investigating the optical characteristics of Poly (methyl methacrylate) (PMMA) and Methyl red doped PMMA (MR-PMMA) polymer composites, which were prepared using solution casting technique. It is important to investigate the changes in optical properties that are induced by neutron irradiation on PMMA (N-PMMA) and MR/PMMA (N-MR-PMMA) composites. UV-Visible spectroscopy was used to examine these changes in the optical characteristics such as transparency, Urbach energy, refractive index, extension coefficient, optical dielectric properties, and activation energy of neutron irradiated PMMA and MR/PMMA.

2. Materials and Methods

2.1. Reagents

Tetrahydrofuran (THF) is procured in liquid form from S D Fine Chemical Limited (SDFCL), Mumbai-30, with a molecular weight of 72.11 and a boiling temperature of 65-67 ℃. Methyl red (MR) ($C_{15}H_{15}N_3O_2$) is an azo dye made up of benzoic acid with a 4-[(dimethyl amino)phenyl] diazenyl group substituted at position two by a dimethylaminophenyl group with a molar mass of 269.3 g/mol procured from Sigma-Aldrich.

2.2. Preparation of PMMA/MR Films

Solution casting technique was used to produce thin films of a PMMA/MR dye combination utilizing THF as a solvent. Initially, 400mg of pure PMMA was dissolved entirely in THF solvent to make a homogenous solution using a magnetic stirrer at 300rpm to ensure thorough dissolution. This solution was held aside until it became viscous. 40 mg of Methyl Red was added to the pure PMMA (PMMA) solution in order to produce Methyl Red doped PMMA (MR-PMMA) at a concentration of 1 wt.% The solution was then carefully poured into a clean and dry petri dish. The viscous solution is then allowed to evaporate the solvent at room temperature in hot air oven. Films were carefully removed from Petri plates and afterwards stored in vacuum desiccators for future investigation. Thickness of the prepared films varies from 150-186 μm.

Measurements

Ultraviolet-visible (UV-Vis) spectra in the absorbance mode were recorded using Jasco - 750 equipped with deuterium lamp in the wavelength range of 200 – 800 nm at a scan rate of 10 nm min^{-1} to study the bandgap variation with the incorporation of the Methyl Red.

3. Result and Discussion

The scanned absorption graphs [12] were used to determine the optical parameters such as optical refractive index (n), real (ε_r) and imaginary (ε_i) dielectric constant, optical conductivity (σ_{opt}), and skin depth (χ).

3.1. Optical transmittance studies

The UV–Visible transmittance spectra of PMMA and its polymer composites before and after neutron irradiation were used to determine their optical transparency as shown in Figure 1. Investigated the optical performance of composite materials in the (200–800 nm) wavelength range in order to better understand their optical transmission. Transmittance at 780 nm was used to evaluate the visual transparency. It was noted that the composite material's transparency varied by ~2.7 when the azo dye (MR) was added to the PMMA matrix.

Table 1. Transparency of the prepared azo dye doped PMMA with and without neutron irradiation.

Sample code	**Transmittance (%) at different wavelength**					
	UV-Region (nm)			**Visible-Region (nm)**		
	300	**336**	**360**	**560**	**580**	**780**
PMMA	53.3	59.2	60.5	67.4	68.0	74.2
MR-PMMA	25.9	35.5	37.6	41.3	46.0	51.6
N-PMMA	56.5	61.7	63.3	70.8	71.4	76.9
N-MR-PMMA	23.2	36.1	40.0	44.9	52.1	59.9

Table 1 summarizes the computed values for the composites (PMMA, MR-PMMA with and without irradiation) in comparison to pristine PMMA. These findings demonstrate that all composite materials exhibit a high degree of optical transparency in the visible region [13].

It is observed (Table 1) that the optical transparency in the UV-region (300, 336 and 360 nm) and visible region (560, 580 and 780 nm) for PMMA and methyl red doped PMMA(MR-PMMA) is decreased for all wavelengths of the spectrum. However, after

Figure 1. Transmittance spectra of pure PMMA and MR dye-doped PMMA with and without irradiation.

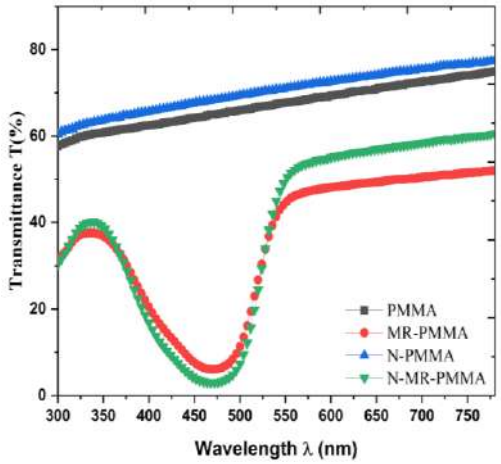

neutron irradiation, the optical transparency is increased both in UV and Visible region. For MR-PMMA the transmittance decreases due to the fact that the azo dye consists of electrons in its outer orbits, these electrons acquire the electromagnetic energy of the incoming light. Consequently, electrons are excited to higher energy levels and this process is not accompanied by radiation emission because the electrons that moved to higher levels have occupied vacant positions of energy bands, and thus part of the incident light is absorbed by the Polymer nanocomposites (PNCs) are emitted. Pure PMMA has a high transmittance due to the absence of free electrons (i.e., electrons are strongly bound to their atoms via covalent bonds), which means that breaking the electron linkage and switching to the conduction band requires a photon with a high energy [14].

Unlike electrons, neutrons are not charged and it interact with the target material's atomic nuclei rather than electrons. They end up losing energy as a result of nuclear interaction, which results in the release of secondary charged particles, fragmentation of the target (N-PMMA and N-MR-PMMA) nucleus, or retention of the incident neutron by the target atoms' atomic nucleus [15]. So, these secondary charge particles may be responsible for change in optical transparency of prepared PNCs.

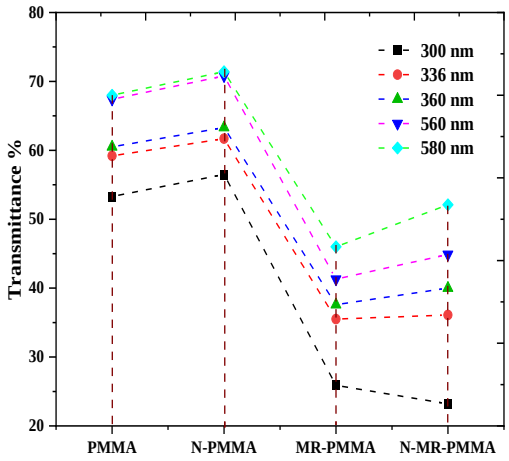

Figure 2. Transmittance with comparison to certain ultraviolet (UV) wavelengths

Figure 2 illustrates the transmittance of pure PMMA and MR-PMMA with and without irradiation at specific ultraviolet wavelengths. For different UV-wavelengths 300, 336, and 360 nm, the prepared PCs PMMA displays transmittance of 53.3, 59.2 ,60.5% respectively. The transmittance in azo dye doped PMMA (MR-PMMA) is 25.9, 35.5, 37.6% corresponding to wavelengths 300, 336, and 360 nm respectively. With neutron irradiation the transmittance values for N-PMMA are 56.5, 61,7, 63.3%, and in the case of N-MR-PMMA the values are 23.2, 36.1, 40.0% respectively. From these data, it is concluded that the transmittance of neutron irradiated PCs N-PMMA is increased by 3.2, 2.5, 2.8% compared to unirradiated sample (PMMA). Moreover, the optical transparency of N-MR-PMMA is modified by -2.7, 0.6, 2.4% compared to pure samples.

Thus, N-PMMA and N-MR-PMMA composites exhibit high UV absorption at wavelengths 300, 336, 360nm. In view of these results N-PMMA and N-MR-PMMA may can be considered as potential UV-shielding materials when compared to pure PMMA and MR-PMMA.

3.2. Urbach energy studies

The Urbach diagrams for pure PMMA and MR-PMMA composites with and without irradiation are shown in Figure 3. The Urbach energy (E_u) can be used to find out if the sample is amorphous or crystallised after it has been doped. In disordered and amorphous materials, Urbach tail can be observed, which is important in order to understand their electron transport properties. Table 2 summarises the calculated Urbach energies for Polymer composites (PCs) with and without irradiation. The band tail states in the amorphous portions of the composite material is caused by the strain in the PMMA backbone chain that generates local energy states into the forbidden energy gap [13]. In addition, as the band gap closes, the band tails decay exponentially. The Urbach energy is figured out using Urbach formula:

$$\alpha = \alpha_0 exp\left(\frac{\hbar\upsilon}{E_a}\right) \qquad (1)$$

Where α_0=constant E_a=activation energy or Urbach energy.

The inverse slope of the straight lines representing ln (α) versus photon energy (hυ) is used to determine the values of E_u. After doping with methyl red (MR), the Urbach energy of PMMA is increased from 0.17 eV to 0.37 eV. Further, when these sample are irradiated with neutrons the Urbach energies are figured out for N-PMMA (0.18 eV) and N-MR-PMMA (0.35 eV).

Table 2. Urbach energy of pristine PMMA and MR-PMMA with and without neutron irradiation

Sample code	Urbach energy (eV)
PMMA	0.17
MR-PMMA	0.37
N-PMMA	0.18
N-MR-PMMA	0.35

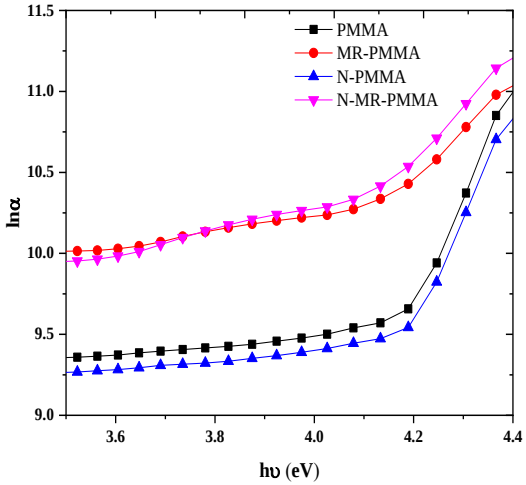

Figure 3. Urbach plots of PMMA and MR-PMMA as a function of photon energy with and without neutron irradiation.

Urbach energy was seen to rise, which means that the amorphous nature of these composite materials becomes more noticeable. This can be explained by an increase/decrease in crystallinity as a result of neutron irradiation. Irradiation improves crystallinity because energy is deposited during the irradiation, which is similar to thermal annealing. It can also be interpreted as a decrease in defect density, which causes a release in strain.

3.3. Refractive index and extinction coefficient curves

Extinction coefficient, refractive index(n), and dielectric constant are essential optical characteristics that must be analysed in attempt to comprehend the polarizability of composites and their applications. Figure 4 depicts the variation of refractive index of PMMA, N-PMMA, MR-PMMA and N-MR-PMMA composites. The refractive index is calculated using the Fresnel equation [16].

$$n = \frac{(1+R)}{(1-R)} + \sqrt{\frac{4R}{(1+R)^2} - k^2} \;\&\; k = \alpha\lambda/4\pi \qquad (2)$$

The refractive index increases as the chromophore is doped, but decreases as the wavelength increases, pointing to the fact that the longest wavelength transmits most light. This behaviour of increasing the refractive index of polymers owing to the inclusion of azo dye has been described elsewhere in the

literature as well [17]. The rising trend in refractive index by doping of azo dye may be explained in terms of intermolecular interactions between azo dye and the adjacent ion of PMMA polymer matrix, which culminates the thin films to dense and, as a result, higher refractive indices can be produced, as per well-known Clausius–Mossotti relation. After irradiation, PMMA and MR-PMMA shows an increasing trend of refractive index and decrease with increase in wavelength. This phenomenon occurs because of the resonance interaction between the electrons in the MR-PMMA film and the photons incident beam. The interaction induces the electric field to oscillate as a consequence of the coupling of electrons in the MR-PMMA film, which results in the retardation of the propagation of EM waves in the polymer matrix. It is vital to calculate the extinction coefficient *k*, because it is correlated to both the real and imaginary components of the dielectric constant, and it reflects the amount of energy dissipated as a consequence of the absorption and scattering by the composite materials molecules. Figure 5 depicts the variation of the extinction coefficient *k* with wavelength of polymer composites. The values of *k* grow gradually for PMMA and N-PMMA films, but the values of extinction coefficient *k* decrease abruptly for MR-PMMA and N-MR-PMMA composites within the wavelength range 528 nm to 572 nm due to absorption and scattering by polymer matrix molecules. The value of extinction coefficient *k* for MR-PMMA composites reduces abruptly between the wavelength range of 528 nm to 572 nm and grows steadily within the wavelength range of 573 nm to 800 nm. Increase in the value of extinction coefficient *k* indicate an increase in the absorption and scattering of light by PMMA, N-PMMA, MR-PMMA, and N-MR-PMMA molecules, while decrease in *k* indicate a reduction in the scattering and absorption of light by polymer composite molecules [18].

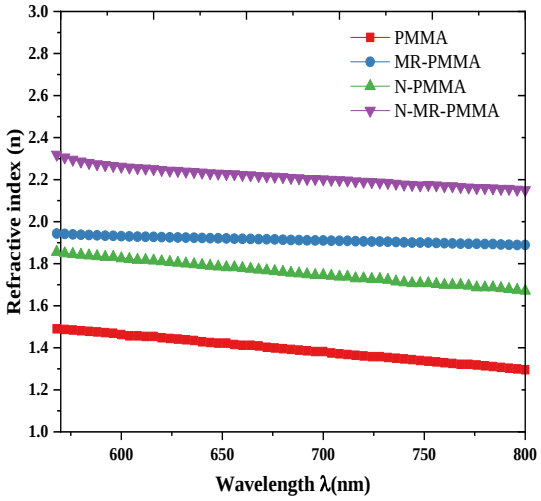

Figure 4. Variation of Refractive index of the PMMA, N-PMMA, MR-PMMA and N-MR-PMMA composites.

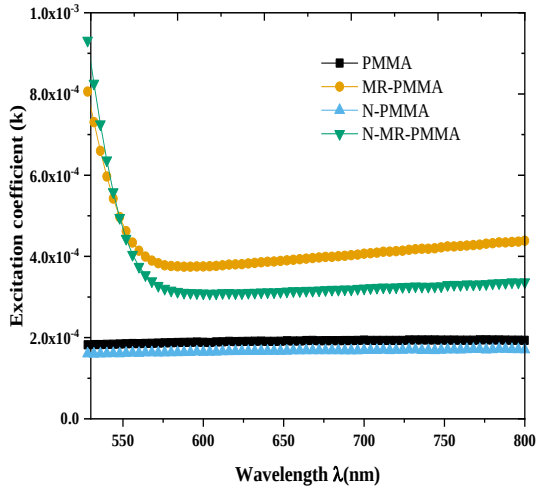

Figure 5. Variation of Extinction coefficient of the PMMA, N-PMMA, MR-PMMA and N-MR-PMMA composites.

3.4. Optical conductivity and skin depth studies

Using the absorption coefficient and refractive index data, the optical conductivity (σ_{opt}) for pure PMMA, N-PMMA, MR-PMMA, and N-MR-PMMA samples is estimated using the equation.

$$\sigma_{opt} = \frac{\alpha n c}{4\pi} \qquad (3)$$

Calculating the optical conductivity and reflectivity of materials enables us to determine their degree of reactivity to incident light. The behaviour of optical conductivity in

response to the variation in wavelength is depicted in Figure 6. Doping azo dye to PMMA and neutron irradiation on prepared composites result in an increase in optical conductivity [19]. This indicates that increasing the amount of azo dye ions and neutron radiation effect increases the contribution of electron transitions between the valence and conduction bands, resulting in a decrease in the energy gap. Figure 7 illustrates the change in skin depth(χ) with wavelength for prepared composites. The result clearly indicates that the skin depth increases with increasing wavelength but decreases with increasing doping concentration, indicating that the optical conductivity increases [20].

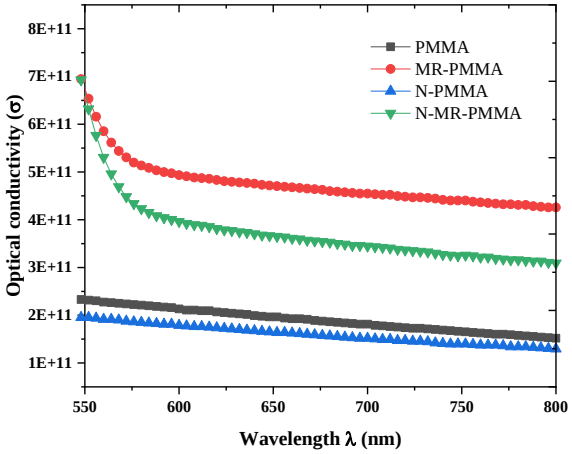

Figure 6. Variation of Optical conductivity of the PMMA, N-PMMA, MR-PMMA and N-MR-PMMA composites.

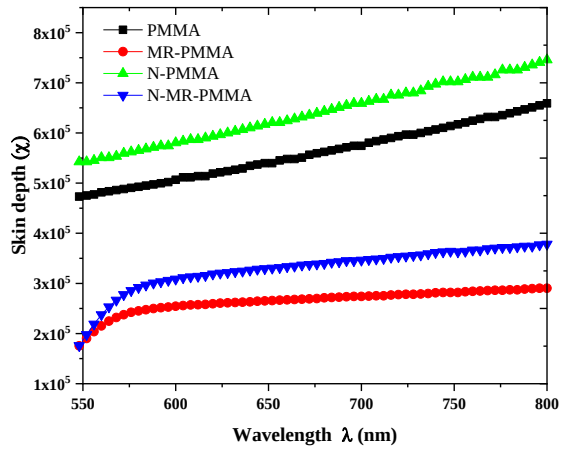

Figure 7. Variation of Skin depth of the PMMA, N-PMMA, MR-PMMA and N-MR-PMMA composites.

3.5. Optical dielectric analysis

Calculations of the real (ε_r) and imaginary (ε_i) components of the dielectric constant for a particular wavelength range are based on the values of η and k. The real and imaginary parts of the dielectric constant are obtained from the formulae $\varepsilon_r = \eta^2-k^2$ and $\varepsilon_i=2\eta k$. The real part of it is associated with the term that indicates how much it will slow down the speed of incident light in the material, while the imaginary part indicates how a dielectric absorbs energy from an electric field caused by dipole motion. The optical dielectric characteristics of composites are associated to electronic polarizability and dipole interactions of an electric field. The values of the real dielectric constant are depicted in Figure 8 demonstrate a significant increase in value when compared to the results for the virgin polymer. Observed values of the real part of the dielectric constant vary between 2 and 8 for the samples used in this study. The values of ε_r are between 4 and 15 for different concentrations of methyl red and blue are added to PMMA, according to studies of Z.T Khodair et. al [17,20]. The real dielectric constant values are higher than the imaginary dielectric constant values because to their reliance on the η and k values.

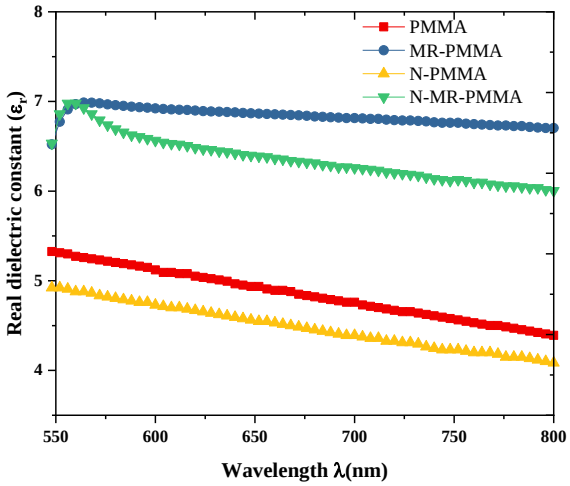

Figure 8. Variation of real (ε_r) part of dielectric constant vs wavelength of the PMMA, N-PMMA, MR-PMMA and N-MR-PMMA composites.

The values of ε_i for samples as presented in Figure 9 reveal that ε_i decreases initially with increasing wavelength, later it increases with increase in wavelength. The dielectric properties of polymer composites are altered by neutron irradiation. After irradiation, the dielectric permittivity values, i.e., both real and imaginary parts, decrease initially with wavelength, but increases with wavelength when compared to PMMA and MR-PMMA. This is due to inability to change of orientation direction of the dipolar molecules of polymer at the rate at which the applied field increases. Thus, it can be concluded that the neutron irradiation of the composites improves the ability of the polymer composite films to charge storage.

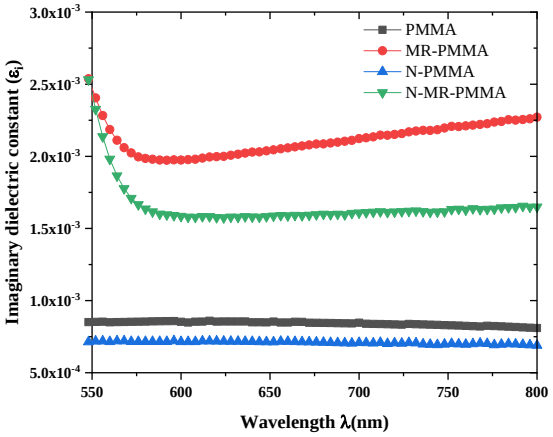

Figure 9. Variation of imaginary dielectric constant (ε_i) vs wavelength of the PMMA, N-PMMA, MR-PMMA and N-MR-PMMA composites.

4. Conclusion

The results of this investigation indicate the role of both the dopant and the fast neutrons on polymer structure forming cross linking and/or degradation. After irradiation with neutrons, the absorbance of PMMA and N-PMMA in the UV region (280 nm) decreases from 1.6 to 1.3 indicates the chain scission reaction, whereas in case of MR-PMMA and N-MR-PMMA the absorbance is increased from 1.6 to 1.92 (280 nm) indicates the cross-linking reaction. The composites exhibit high UV absorption at wavelengths 300, 336, 360nm and thus may be considered as a potential UV-shielding material when compared to pure PMMA and MR-PMMA films. After doping with methyl red (MR), the Urbach energy of PMMA was increased from 0.17 eV to 0.37 eV. Further, for N-PMMA and N-MR-PMMA the Urbach energy is found to be 0.18 eV, and 0.35 eV respectively. Based on these results one can state that after colliding with a high energy incoming particle, a lattice atom is displaced from its original lattice position in prepared PCs. Collisions between incident "heavy" particles such as neutrons and secondary particles cause cascade collisions. Radiation-induced PCs display change in physical and chemical characteristics.

Acknowledgments

Soumya S Bulla acknowledges the K.U. Dharwad for University Research Studentship (URS), and KSTePS for Research Fellowship (DST/KSTePS/PhD Fellowship/PHY-04:2018-19). The authors are thankful to USIC and SAIF, Karnatak University, Dharwad for providing experimental facilities. Chetan Chavan thanks the University Grants Commission (UGC), New Delhi, for JRF/SRF Fellowship (518772/Dec 2015). The authors are also thankful to KSHEC, Govt. of Karnataka for RUSA1.0 grant (KSHEC/254/KUD/15-16/544).

Compliance with Ethical Standards:

Conflict of interest: The authors declare that they have no conflict of interest.

References

[1] S. N. Bhavsar, PhD dissertation Maharaja Sayajirao University of Baroda (India), (2021).

[2] M. H. Anandalli, R. F. Bhajantri, S. R. Maidur, and P. S. Patil, Journal of Materials Research (Springer), 36, 2856–2871, (2021).

[3] M. Nandimath, R. F. Bhajantri, and J. Naik, Polymer Bulletin (Springer), 78, 4569–4592, (2021).

[4] I. M. Minisy, P. Bober, I. Šeděnková, and J. Stejskal, Polymer (Elsevier), 207, 122854, (2020).

[5] Y. Zheng, Q Ye, J Wang, Z Deng, J Mei, W Zhou, C Zhang, J Tian, Optics & Laser Technology (Elsevier), 75, 132–137, (2015).
[6] C. S. Paik and H. Morawetz, Macromolecules(ACS Publications), 5, 171–177, (1972).
[7] J. Lee, K. Park, T. Chang, and J. C. Jung, Macromolecules (ACS Publications), 25, 6977–6979, (1992).
[8] V Ravindrachary, R F Bhajantri, S D Praveena, B Poojary, D Dutta, P K Pujari, Polymer Degradation and Stability(Elsevier),95(6),1083-91, (2010).
[9] G. Raos and B. Zappone, Macromolecules (ACS Publications) 4(23),10617-44, (2021).
[10] Mirji, Rajeshwari, and Blaise Lobo. "24. Radiation shielding materials: A brief review on methods, scope and significance." In Proceedings of the National Conference on 'Advances in VLSI and Microelectronics, 2017.
[11] More, C.V., Alsayed, Z., Badawi, M.S. et al. Polymeric composite materials for radiation shielding: a review. Environ Chem Lett, 19, 2057–2090, (2021). https://doi.org/10.1007/s10311-021-01189-9
[12] S. S. Bulla, R. F. Bhajantri,Chavan C, Chalawadi S, M. H. Anandalli, Kalliguddi S,International Conference on Physics of Materials and Nanotechnology ICPN 2019, Mangalore, India, Sep. 19-21, 2244, p. 90004, (2020).
[13] H. Chandrappa, R. F. Bhajantri, and N. Prarthana, Optical Materials (Elsevier), 109, 110204, (2020).
[14] H. N. Najeeb, A. A. Balakit, G. A. Wahab, and A. K. Kodeary, Academic Research International (SAVAP International), 5, 48, (2014).
[15] S. Nambiar and J. T. W. Yeow, ACS applied materials & interfaces (ACS Publications), 4, 5717–5726, (2012).
[16] A. A. M. Farag and I. S. Yahia, Optics Communications (Elsevier), 283, 4310–4317, (2010).
[17] M. H. Abdul-Allah,Iraqi Journal of Physics(University of Baghdad), 12, 47–51, (2014).
[18] O. Taqatqa and H. Al Attar, Eur. Phys. The European Physical Journal - Applied Physics (Cambridge University Press), 37, 61–64, (2007).
[19] C. A. Emshary, Q. M. A. Hassan, H. Bakr, and H. A. Sultan, Physica B: Condensed Matter(Elsevier), 622, 413354, (2021).
[20] M. Bafna, A. K. Gupta, A. Agarwal, N. Sain, and V. Jain, Materialstoday: Proceedings(Elsevier), 38, 1209–1213, (2021).

Karnatak University Journal of Science 53 (2022) 29-36

Karnatak University Journal of Science

ISSN: 0075-5168

Impact of chronic administration of anabolic-androgenic steroid (17α-Methyl testosterone) on histoarchitecture of uterus and adrenal in mice, *Mus musculus*

Praveenkumar S. Kondaguli and Laxmi S. Inamdar (Doddamani)*

Molecular Endocrinology, Reproduction and Development Laboratory, Department of Zoology, Karnataka University, Dharwad 580 003, India

Corresponding author: ls_doddamani@yahoo.com; Tel: +91-836-2215230 (O); +91-836-2955168 (R)

ARTICLE INFO

Article history:
Received: 15 May 2022;
Revised: 18 June 2022;
Accepted: 28 July 2022;

Keywords:
Anabolic-Androgenic Steroid (AAS);
17α-Methyl testosterone;
Uterus; Adrenal;
Histomorphometry;
Mice;

ABSTRACT

The medicinal use of anabolic androgenic steroids (AAS) has been eclipsed in recent decades by illegal AAS usage by athletes and non-athletes. As a result, AAS can cause adverse health issues such as coronary heart disease, impairment in reproduction and endocrine disruption. The present investigation was undertaken to determine the efficacy of one of the AASs 17α-Methyl testosterone (17α-MT) on the endocrine physiology focusing on uterus and adrenal in Swiss albino mice, Mus musculus. In total 10 sexually mature healthy female mice (3-months-old) were assigned to two experimental groups and 17α-MT was administered via subcutaneous injection [0.75 mg/kg bwt in 0.5 ml of 1% alcohol, n=5; or 0.5 ml of 1% alcohol - vehicle control, n=5] for thirty days. The results revealed that treatment of 17α-MT led to significant cellular alterations in the uterus and adrenal. Histomorphometry of uterus exhibited profound alterations in histoarchitecture of the uterine endometrial compartments following 17α-MT treatment suggesting alterations in hypothalamic-pituitary-ovary-uterine axis. A significant increase in the myometrium region of the treated uterus when compared to control indicates the anabolic efficacy of this AAS compound. Histomorphology of the adrenal in treated mice revealed remarkable cellular variations in the zona fasciculata and zona reticularis regions of the adrenal cortex when compared to control may indicate functional impairment in the secretions of glucocorticoids and sex steroids. Based on the observed results it is inferred that 17α-MT has negative impact on endocrine and reproductive physiology.

1. Introduction

Anabolic-Androgenic Steroids (AAS) are a group of engineered subsidiaries of testosterone. They are intended to give upgraded anabolic strength with minimum androgenic impacts (1). These are used to treat chronic disorders that are caused by the patient's catabolic state, such as AIDS, COPD, hepatic or renal failure, cancer, burns and postsurgical recovery (2). Nevertheless, potential applications, these AAS compounds are being mishandled by numerous sporting and proficient competitors and teenagers to upgrade the athletic performance, build strength and perseverance (3,4). They have also been used as performance enhancers in competitive sports to boost muscle strength and growth. The majority of anabolic steroids are only available with a prescription and are closely regulated (5). Steroid supplements are used not just because many people believe they can be turned into testosterone or a comparable molecule in the body, but also because they are readily available as dietary supplements and may be acquired from a variety of commercial sources (6).

Because MT is the only androgen approved by the FDA for use in estrogen-androgen hormone replacement. Thereby, understanding how it works in the uterus becomes crucial (7). The primary function of the uterus is to support fertility, and therefore the endometrium is involved in receiving an embryo, facilitating implantation, and decidualization, facilitating embryo growth and development (8). Recently the role of stanozolol on endometrial receptivity has been published from our laboratory. Which implicates that, during the implantation window, ST reduces endometrial receptivity in mice, preventing embryo implantation.

Androgens, which are largely produced by the adrenal gland and the gonad, are vital both during pregnancy and after birth. Adrenal androgens regulate pregnancy homeostasis, influence foetal organ maturation, and may influence parturition timing (9). Hence, we are interested to know the effect of 17α-MT on the adrenal gland.

In this context, we wish to know the role of one of the AAS compounds 17α-MT on histoarchitecture of the uterus and adrenal gland in female mice, *Mus musculus* with the following objectives:

1. To examine the effect of 17α-MT on morphometry and histoarchitecture of uterus.
2. To understand the effect of 17α-MT on histomorphometry of adrenal.

1. MATERIALS AND METHODS

2.1 Hormone treatment

All protocols used in this experiment adhere to the CPCSEA guidelines for the Care and Use of Laboratory Animals approved by the Institutional Animal Care and Use. Committee No.639/GO/02/a/CPCSEA at Department of Zoology, Karnatak University, Dharwad.

In total 10 sexually mature female Swiss albino ‘strains’ (25 to 30 gms.) exhibiting regular estrous cycle were obtained from mice breeding centre maintained in the Department of Zoology, Karnatak University, Dharwad. All mice were housed in individual polypropylene cages, maintained a 12 h light:dark cycle at 27±1˚C with 40-50% rh, food (pelleted diet, Goldmohur, Lipton, India) and water supplied *ad libitum*. 17α-MT was obtained from Sigma Chemical Co., USA. The mice were randomly assigned to two experimental groups and 17α-MT dosed subcutaneously (0.75mg/kg bwt; n=5 and 1% alcohol-baseline control, n=5) for 30 consecutive days. On 31st day immediately after withdrawal of treatment, animals were sacrificed by phenobarbitone injection. The body weight was recorded on the first day of experiment and on the day of autopsy. The uteri and adrenals were dissected out, weighed to the nearest mg, fixed in Bouin’s fluid and processed for histology and histomorphometry.

2.2 Histoarchitecture and histo-morphometrical kinetics of uterus:

A total of twenty five readings from each animal (both control and treated group)

were taken into consideration for the following parameters:

a) Uterine diameter
b) The thickness of endometrium:
c) The thickness of myometrium
d) Number of endometrial glands per section were counted and averaged.

2.3 Measurement of adrenal gland diameter and width of zones of adrenal cortex:

The adrenals after the completion of embedding process were subjected to morphometric analysis. Histological sections (5µm) were obtained on Leica microtome and stained with Hematoxylin and Eosin. Diameter of the adrenal glands was measured using 10X objective under Olympus phase contrast microscope. Morphometric analysis was carried out from 10 randomly selected sections from each animal (five from each adrenal) of both control and treated groups. Mean width of three different zones of adrenal cortex (Zona Glomerulosa – ZG, Zona Fasciculata – ZF, Zona Reticularis – ZR) were also measured in both control and 17α-MT treated mice.

2.4 Statistical analysis:

Data were expressed as mean ± SE using SPSS version 16.0 (SPSS, Chicago, IL, USA). All variables were analysed by independent sample T test. All statistical tests were two sided tests with a 5% level of significance ($P<0.05$).

2. Results and Discussion

17α-MT is a testosterone-derived synthetic anabolic steroid. The weightlifters, bodybuilders, recreational athletes and teenagers have all abused it to increase muscle mass and decrease fat mass (10). The present investigation has been designed in order to know the effect of 17α-Methyltestosterone (17α-MT) in female mice, giving emphasis on the adrenal and the uterus. The results revealed profound alteration in adrenal and uterus structure upon 17α-MT administration. The misuse of AAS compounds in women accompanied by adverse effect on the reproductive system and sexual behaviour (11,12).

2.1 Effect of 17α-MT on body weight: It is found that a statistically significant increase in body weight in the treatment group (t_8= 2.746; $P < 0.05$) when compared to that of control was noted (Graph 1). It is established that muscle mass can be increased by testosterone treatment (13). In this study, 17α-MT induced body weight gain which may be primarily due to anabolic effect on muscle mass as well as due to the increased food consumption.

Graph 1. Effect of 17α-methyltestosterone on body weight of mice

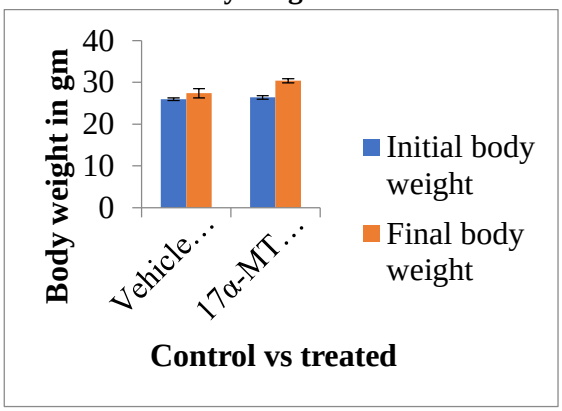

2.2 Effect of 17α-MT on organ weight: Weight of the uterine horn in control mice was 35.38 ± 3.05 mg and in 17α-MT treated mice it was 34.9 ± 2.5 mg there was no significant difference (t_8 = 0.107; $P > 0.05$) in the uterus weight between control and 17α-MT treated group. And also it was noted that, insignificant decrease (t_8 = 1.716; $P > 0.05$) in the weight of adrenal gland was observed in the 17α-MT treated mice. Weight of the adrenal gland in vehicle group was 8.99 ± 0.39 mg and that of treated group was 8.00 ± 0.41mg (Graph 2). It is well documented that the AAS promotes reduction in the weight of the reproductive organs (14-18). However, in this study the results showed no significant differences in the organ weights.

Graph 2. Effect of 17α-methyltestosterone on uterus & adrenal organ weight of mice

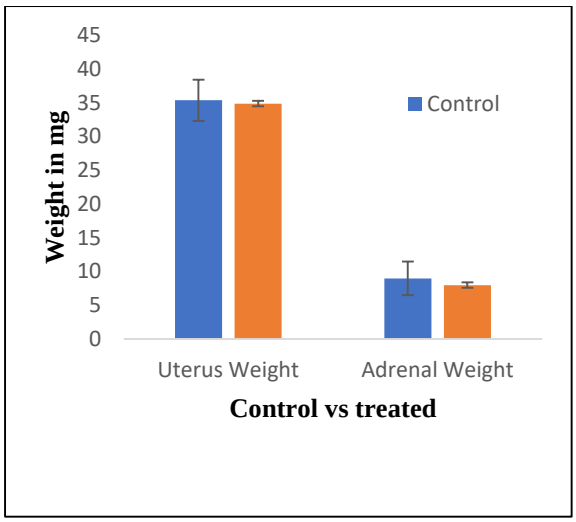

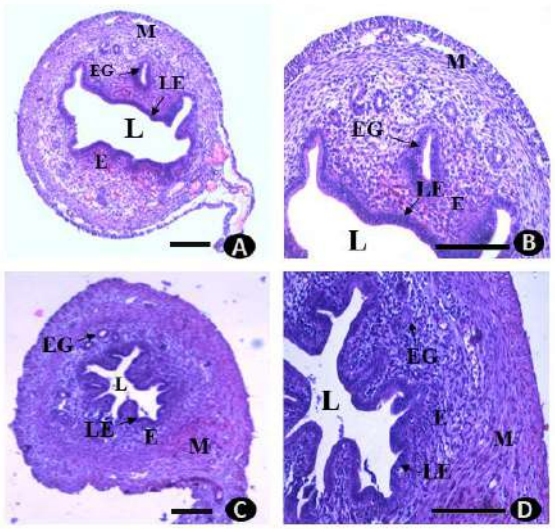

Figure 1: Effect of 17α-methyltestosterone on uterus histoarchitecture. **(A)** T. S. of uterus of control mouse showing normal endometrium (E), myometrium (M) and lumen. **(B)** Higher magnification of figure A showing luminal epithelium (LE), glandular epithelium (GE) . Endometrium (E) and Myometrium (M). **(C)** T. S. of uterus of 17α-methyltestosterone (17α-MT) treated mice showing myometrial hypertrophy (M) and narrow lumen (L) and Endometrium (E). **(D)** Higher magnification of figure C showing decrease in the height of luminal epithelium (LE), endometrial gland (EG), myometrial hypertrophy (M) and narrow lumen (L). Scale bar - A and B - 100µm; C and D - 40 µm.

17α-MT lead to alterations in uterine histomorphology:

Control mice showed normal histological cellular structural arrangement (Fig. 1A&B). However, in 17α-MT treated mice a decrease in the size of the lumen (Fig. 1C&D) and insignificant decrease in the size of the diameter of the uterus was observed (t_8 = 0.804; P>0.05) (Graph 3). Decrease in the height of luminal epithelium in treated mice was noticed when compared to control (Fig. 1D). An insignificant decline in thickness of endometrium (t_8 = 1.811; P > 0.05, Graph 4) and significant increase in thickness of myometrium (t_8 = 4.315; P <0.01, Graph 4);(Fig. 1D) was noticed in uterus of treated mice. Thickness of longitudinal muscles of myometrium was drastically increased upon treatment. Quantification of endometrial glands per uterine cross-section revealed decrease in the number of glands (t_8 = 3.133; P < 0.05) in treated mice compared to control (Graph 5);(Fig. 1D).

Graph 3. Effect of 17α-methyltestosterone on uterus diameter

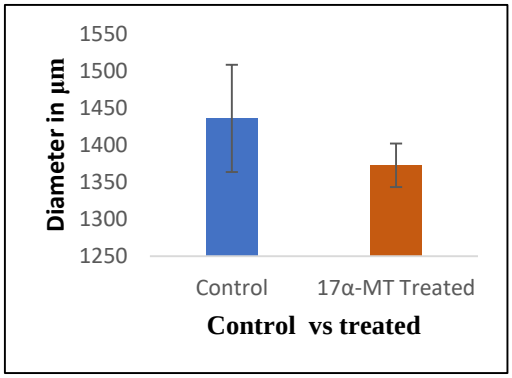

Graph 4. Effect of 17α-methyltestosterone on endometrial and myometrial thickness.

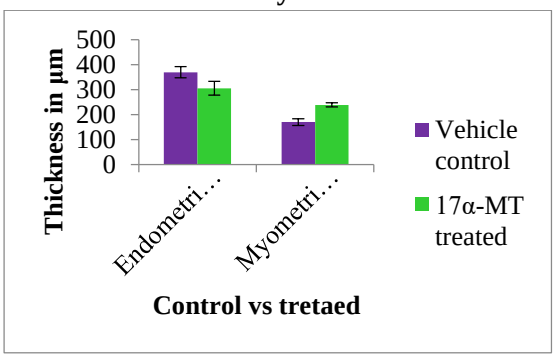

Graph 5. Effect of 17α-methyltestosterone on number of endometrial glands

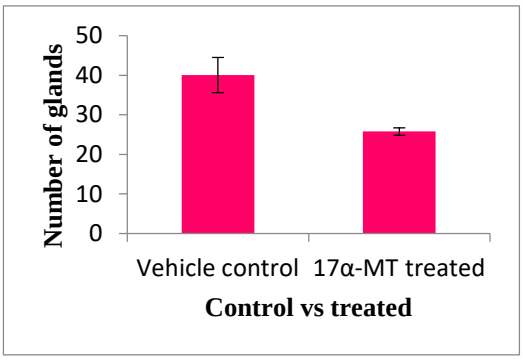

Overall, uterine morphometric analysis after withdrawal of treatment revealed pronounced alterations in the uterine morphology specifically by decreasing luminal epithelial cell height and endometrial proliferation into the lumen. It is possible that continuous treatment of 17α-MT for 1 month might have interfered with hypothalamic-pituitary-gonadal axis, thus altering ovarian signal to uterus leading to its disorganization. The AAS compounds alter the hypothalamic-pituitary-gonadal axis, which has been shown to occur in response to high levels of androgens (19-22). Androgens such as testosterone and 5α-DHT have both uterotrophic and anti-uterotrophic effects in rats and mice (23,24). The effect observed on the uterine myometrium was may be due to hypertrophic activity of 17α-MT and this might be mediated through both the androgen and estrogen receptors. The hypertrophy of both the layer of myometrium was may be due to increased anabolic potency of 17α-MT.

2.317α-MT lead to alterations in adrenal histomorphology: The histoarchitecture of adrenals from the control group showed well placed medulla and cortex with all three regions (zona glomerulosa, fasciculata and reticularis) distinctly visible (Fig. 2A&C**).** The histological data revealed characteristic alterations in adrenal cortex in treated group (Fig. 2B&D). Insignificant decrease (t_8 = 1.704; P > 0.05) in the diameter of adrenal gland was observed in the treated mice (Graph 6). The Diameter of the adrenal gland in vehicle group was 2156.1 ± 3.40µm and that of treated group was 1949.8 ± 121.007µm. An insignificant decrease in the thickness of zona glomerulosa (ZG) (t_8= 1.553; P > 0.05) as well as zona fasciculata (ZF) (t_8= 2.049; P > 0.05) was noticed in 17α-MT treated mice adrenal (Graph 7). However, the thickness of zona reticularis (ZR) decreased significantly in treated mice when compared to control (t_8 = 3.247 ; P < 0.05, Graph 7). Signs of macro vacuoles were present exclusively in Zona Fasciculata of the adrenal cortex in treated group, suggesting alteration in the glucocorticoids production process that occurs in this region. Clear signs of proliferation were seen in Zona Fasciculata in 17α-MT treated groups (Fig. 2D).

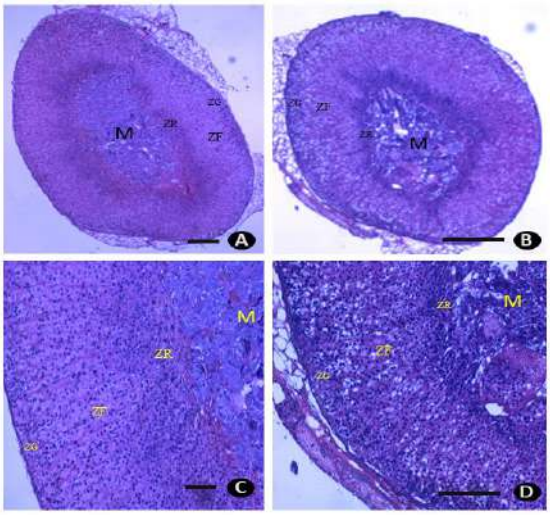

Figure 2: Effect of 17α-methyltestosterone on adrenal histoarchitecture **(A)** T. S. of adrenal of control mice showing normal medulla (M) and different zones of cortex. (**B)** T. S. of adrenal of 17α-methyltestosterone (17α-MT) treated mice showing medulla (M) and different zones of cortex. (**C)** T. S. of adrenal of control mice showing magnified view of figure A. **(D)** T. S. of adrenal of 17α-MT treated mice showing higher magnification of figure B showing significant decrease in the zona reticularis (ZR). Scale bar - A and B - 100µm; C and D - 40 µm.

Graph 6. Effect of 17α-methyltestosterone on adrenal diameter

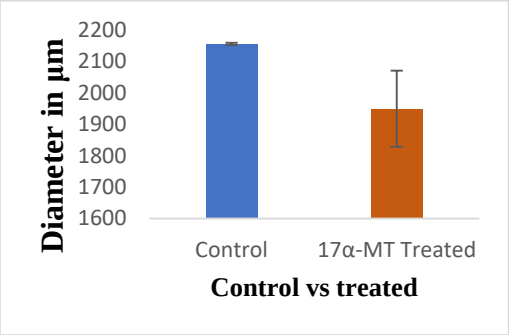

Graph 7. Effect of 17α-methyltestosterone on adrenal cortex thickness

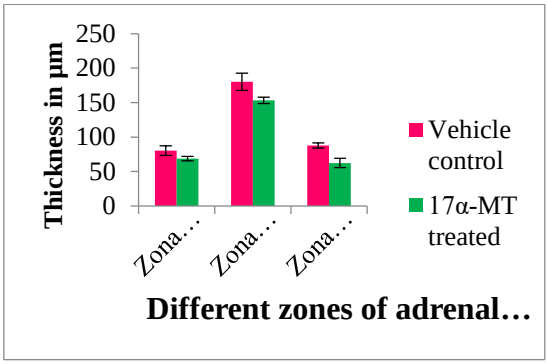

Exogenous steroids exert their effect on adrenal hormones by negative feedback on the hypothalamic-pituitary-gonadal axis (25). Significant decrease in the thickness of zona reticularis on treatment may elucidate that, the administration of 17α-MT might have interfered with hypothalamus-pituitary-adrenal axis thus disrupting the steroidogenesis and production of androgen in the zona reticularis and leading to the decrease in the zonal thickness. The cells of ZF layer showed vacuolated cytoplasm with enlarged cells and this result is in accordance with (26). Which states that, on treating male rats with nandrolone decanoate noticed most of the cells with loss of normal structure had obvious signs of necrosis expressed by vacuolated cytoplasm and their nuclei showed symptoms of pyknosis, karyorrhexis and karyolysis, in addition to the presence of fibrous regions between destructed ZG and ZF cells. On treatment with 17α-MT has resulted in insignificant decrease in the ZF layer thickness. This elucidate that the treatment with 17α-MT may impede the secretion of glucocorticoids that occurs in this region. In our study, treated mice ZG layer width decreased insignificantly. On the basis of *In vitro* data given by (27), it seems that, testosterone appeared to have a direct inhibitory effect at the level of the adrenal ZG cells on basal aldosterone secretion. And the conversion of pregnenolone 25-OH-cholesterol to pregnenolone and corticosterone to aldosterone was hindered by testosterone.

Conclusion:

Hence, based on the above results it is concluded that treatment of mice with 17α-MT lead to impairment in the uterine function and alterations in the secretion of glucocorticoids and sex steroids in the adrenal. It is inferred that 17α-MT has negative impact on endocrine and reproductive physiology.

Acknowledgement: All procedures used in this experiment adhere to CPCSEA guidelines for the care and use of laboratory animals approved by the Institutional Animal Ethical Committee No. 639/02 at Department of Zoology, Karnatak University, Dharwad. One of the authors (PSK) thank Karnatak University, Dharwad for granting URS fellowship.

References

1. J. C. Jorge-Rivera, K. L. McIntyre, and L. P. Henderson, Anabolic Steroids Induce Region and Subunit-Specific Rapid Modulation of GABAA Receptor-Mediated Currents in the Rat Forebrain. Journal of Neurophysiology, 83(6), 3299–3309 (2000).
2. K. Doust and A. Noorafshan. Stereological study of the effects of nandrolone decanoate on the rat prostate. Micron 37, 617-623 (2006).
3. S. E. Lukas, Current perspectives on anabolic-androgenic steroid abuse. Trends in Pharmacological Sciences, 14(2), 61–68 (1993).
4. J. D. Wilson (1988). Androgen abuse by athletes. Endocrine Rev. 9,181-199.
5. Anabolic Steroid Control Act of 1990, Title 21, Chapter 13 of the United States Code.
6. R. L. Sprando, s, T. F. Collin, T. N. Black, N. Olejnik, , E. Grundel, and, D. I. Ruggles. Effects of androstenedione on in utero development in rats. Food and Chemical Toxicology, 42(6), 917–924 (2004).

7. A. D. Papaconstantinou, T. H. Umbreit, P. L. Goering, and K. M. Brown, Effects of 17α-methyltestosterone on uterine morphology and heat shock protein expression are mediated through estrogen and androgen receptors. The Journal of Steroid Biochemistry and Molecular Biology, 82(4-5), 305–314 (2002).

8. C. R. Sharma, , N. H. Balasinor, and L. S. Inamdar (Doddamani), High, not low-dose of stanozolol (anabolic - androgenic steroid) impedes embryo implantation by attenuating endometrial receptivity in the mouse, Mus musculus. Steroids, 108752 (2021).

9. E. Knobil, & J. D. Neill, Encyclopedia of Reproduction. Volume 1, Academic Press. USA.(1998).

10. S. Bhasin, L. Woodhouse, R Casaburi, A. B. Singh, D. Bhasin, N. Berman, X. Chen, K. E. Yarasheski, L. Magliano, C. Dzekov, J. Dzekov, R. Bross, J. Phillips, I. Sinha-Hikim, R. Shen, T. W. Storer, Testosterone dose response relationship in healthy young men. American Journal of Physiology Endocrinology and Metabolism. 281: E1172-E1181 (2001).

11. W. B. Malarkey, R. H. Strauss, D. J. Leizman, M. Liggett, and L. M. Demers, Endocrine effects in female weight lifters who self-administer testosterone and anabolic steroids. American Journal of Obstetrics and Gynecology, 165(5), 1385–1390 (1991).

12. R. H. Strauss, C. E. Yesalis. Additional effects of anabolic steroids on women, in: C.E. Yesalis(Ed.), Anabolic Steroids in Sport and Exercise, Human Kinetics Publishers, Inc., Champaign, 1L, pp. 151-160, (1993).

13. N. Alrabadi, G. J. Al-Rabadi, R, Maraqa, H. Sarayrah, K. H. Alzoubi, M. Alqudah, and D. G. Al-u'datt, Androgen effect on body weight and behaviour of male and female rats: novel insight on the clinical value (2020). Andrologia.

14. I.C.C. Camargo, R. B .Souza, S.F.P Mesquita, L.G.A Chuffa and F. Frei, Ovarian histology and follicular score in female rats treated with nandrolone decanoate and submitted to physical effort. Acta Biologica Hungarica. 60, 253-261 (2009a).

15. I.C.C. Camargo, A.L.C. Gaspar, F. Frei, and S.F.P. Mesuita, Efeitos dos esteroides anabolicós androgênicos sobre o útero e parâmetros reprodutivos de ratas adultas. Revista Brasileira de Ginecologia e Obstetricia. 31, 453-460 (2009b).

16. I. C. C. Camargo, G. A. A. Leite, T. Pinto, and J. T. Ribeiro-Paes, Histopathological findings in the ovaries and uterus of albino female rats promoted by co-administration of synthetic steroids and nicotine. Experimental and Toxicologic Pathology, 66(4), 195–202 (2014).

17. M. T. Bento-Silva, Martins, M. do C. de C. e, Torres-Leal, F. L., Barros, T. L., Carvalho, I. L. do N. F. de, Carvalho Filho, H. A., & Almeida, F. R. de C. Effects of administering testosterone undecanoate in rats subjected to physical exercise: effects on the estrous cycle, motor behavior and morphology of the liver and kidney. Brazilian Journal of Pharmaceutical Sciences, 46(1), 79–89 (2010).

18. K. Doust and A. Noorafshan. Stereological estimation of ovarian oocyte volume, surface are and number; application on mice treated with nandrolone decanoate. Folia Histochemica. 50, 275-279(2012).

19. M. Alén, P. Rahkila, and J. Marniemi, Serum Lipids in Power Athletes Self-Administering Testosterone and Anabolic Steroids. International Journal of Sports Medicine, 06(03), 139–144 (1985).

20. F. H. Bronson, Effects of prolonged exposure to anabolic steroids on the behavior of male and female mice. Pharmacology Biochemistry and Behavior, 53(2), 329–334 (1996).

21. R. E. Harlan, M. M. Garcia, Neurobiology of androgen abuse. In: Watson, R. R., ed. Drugs of abuse and neurobiology. New York: CRC Press; 185–207 (1992).

22. L. W. Liu Kao, and J. Weisz, Direct Effect of Testosterone and Its 5α-Reduced Metabolites on Pituitary LH and FSH Release in Vitro: Change in Pituitary Responsiveness to Hypothalamic Extract. Endocrinology, 96(2), 253–260 (1975).

23. G. Giannopoulos, Binding of testosterone to uterine components of the immature rat. Journal of Biological Chemistry, 248(3), 1004-1010(1973).
24. P. V. Nantermet, P. Masarachia, M. A. Gentile, B. Pennypacker, J. Xu, D. Holder, D. Gerhold, D. Towler, A. Schmidt, D. B Kimmel, L. P Freedman, S. Harada, and W. J. Ray, Androgenic Induction of Growth and Differentiation in the Rodent Uterus Involves the Modulation of Estrogen-Regulated Genetic Pathways. Endocrinology, 146(2), 564–578 (2005).
25. Friedl KE: Effects of anabolic steroids on physical health. In Anabolic Steroids in Sport and Exercise. Edited by Yesalis CE. Champaign: Human Kinetics; 107–150 (1993).
26. H. R. Aboelwafa, Impact of the Anabolic Androgenic Steroid "Nandrolone Decanote" on the Histological and Ultrastructural Characteristics of Adrenal Cortex of Adult Male Rat. International Journal of Current Research and Academic Review. 5(6): 69-80 (2017).
27.M.-M. Kau, M.-J. Lo, S.-W. Wang, S.-C. Tsai, J.-J. Chen, Y.-C Chiao, J.-Y. Yeh, H. Lin, A. Y. Shum, V. S. Fang, L.-T. Ho, P. S. Wang, Inhibition of Aldosterone Production by Testosterone in Male Rats. Metabolism, Vol 48, No 9 (September), pp 1108-1114 (1999).

Karnatak University Journal of Science 53 (2022) 37-43

Karnatak University Journal of Science

ISSN: 0075-5168

Impact of Bordeaux mixture on Behavioural, Histological and Some Biochemical Parameters of Common Carp (*Cyprinus carpio* L)

Annapurneshwari H[1], Manoj Godbole[2*], Navya KM[1]

[1] Department of Zoology, IDSG Government College, Chikkamagaluru.

[2] PG Department of Biotechnology, Sri Dharmasthala Manjunatheshwara College (Autonomous), Ujire - 74240

Author for Correspondence: [2*] PG Department of Biotechnology, Sri Dharmasthala Manjunatheshwara College (Autonomous), Ujire - 574240

***Corresponding author:** *manojgodbole@gmail.com*

ARTICLE INFO

Article history:
Received: 04 Feb 2022;
Revised: 12 April 2022;
Accepted: 8 May 2022;

Keywords:
Common Carp;
Cyprinus carpio;
Bordeaux mixture;
Fungicide; Gill;

ABSTRACT

Copper based compounds are used to control pests worldwide but they can be toxic to fish and other non-target organisms. It is therefore essential to identify effective formulations with the lowest non-target toxicities. In this study the toxic effects of Bordeaux mixture on fingerlings of common carp (*Cyprinus carpio L.*) was studied. In the common carp fingerlings behavioural, histological alteration and biochemical variations were evaluated. The LC50 of Bordeaux on common carp was 0.04, 0.05, 0.06 and 0.07 mg/L. During toxicity study fish mortality increased significantly with increase in concentration and time of exposure. Behavioural responses of the fish exposed to Bordeaux mixture included uncontrolled swimming, erratic movements, loss of balance, swimming near the water surface with sudden jerk movements. The treated fingerlings showed histopathological alterations in the muscle and gill lamellae. Splitting of muscle fibre and muscle band degeneration was observed in muscle tissue. The major changes observed in gill were ruptured gill epithelium, lamellar fusion, epithelial lifting and vacuolization at the tip of lamellae. The fungicide decreased the concentration of glycogen and protein in muscle and gill tissue compared to control samples. Results suggest judicious use of fungicides should be practiced by farmers. Use of Bio pesticides and natural products should be encouraged to reduce the toxic effects of the fungicides.

Introduction

Water resources are utmost important and the sanctity of which should be preserved and maintained in order to make it safe not only for humans but also for the wild life. Pollution is a major global problem which requires ongoing evaluation and revision of water resource policies at all level. The application of pesticides has become an essential part of present day agricultural practices. The benefits of pesticides are numerous but at the same time they cause considerable damage to the ecosystem. Water pollution is caused by the improper use of pesticides. Pesticides not only alter the physicochemical properties of water but also adversely affect the aquatic organisms (Ghais et al., 2019). These pesticides at high concentration are known to reduce the survival, growth and reproduction of the fishes (Ghais et al., 2019). Pesticides wash into the fresh and marine water sources when applied to agriculture field. A fungicide is a specific type of pesticide that controls fungal disease by killing the fungus causing the diseases. The devastating effects of heavy metals – ingradient of pesticides – are mainly due to the dispersal performance and bio-magnification into aquatic food chains in addition to their toxicity and accumulative behaviour in the biological tissues (Matta et al., 1999; Islam and Tanaka, 2004; Yi et al., 2011).

Bordeaux mixture is a mixture of copper sulphate ($CuSO_4$) and slaked lime [$Ca(OH)_2$] used as fungicide. Bordeaux mixture is the undefined reaction product of copper sulphate with calcium dihydroxide (https://echa.europa.eu). It is used in vine yards, fruit farms and arecanut, rubber, coffee gardens to prevent fungal infections. The Bordeaux mixture can also be used as a precaution, before the onset of fungal attack (Pears Pauline, et al., 2005). Bordeaux mixture is an effective fungicide because of the cupric ions (Cu^{2+}). At low concentrations, copper is a minor nutrient for plants and animals, but at higher concentrations, ionic copper formulations are considered fairly toxic to fish and other non-target organisms (Mastin & Rodgers, 2000). Cupric ions react with enzymes in the fungal spores and prevent their germination. Bordeaux mixture has been found to be harmful to non target organisms like fish and livestock as it washes away into the water bodies and while grazing (Deepasree and Nair, 2016). Copper sulphate, the key ingradient of the Bordeaux mixture, is approved by the EPA as a general use chemical (algaecide, fungicide, insecticide, molluscicide and water treatment) (Straus, 2017). Economically, copper sulphate compounds are the superlative choice in the aquaculture sector compared to formalin and hydrogen peroxide which also pose threat to the environment and to human health. But at the same time, copper sulphate too could be extremely toxic to fishes under certain conditions of alkalinity/hardness (Straus, 2017). In Uttara Kannada, Dakshina Kannada and Chikkamagaluru districts to control phytophthara diseases, arecanut, coffee and rubber plantations use excess amount of Bordeaux mixture during monsoon season. As these regions receive heavy rain, the fungicide washes along with the rain into the water bodies and their effect on the local fishes is largely remain unknown.

Cyprinus carpio L. is one of the Indian major carp which could be seen across the country's fresh water. It occurs abundantly in the fresh water tanks, rivers and ponds in and around Chikkamagaluru. Common carp are acclimated to a variety of habitats and extremes of environment, eg high salinities and low oxygen concentrations (Froese & Pauly, 2013). Fishes are very sensitive to aquatic contamination and serious concerns remains due to their population. Fishes are widely used to evaluate the health of aquatic ecosystem, because pollutants build up in the food chain and are responsible for adverse effects and death in the aquatic system (Das and Mukharjee, 2003). The objective of this study was to determine the effect of Bordeaux mixture on the Common Carp (*Cyprinus*

carpio L.) fish fingerlings to study its behavioural, histological alteration and biochemical variation.

Materials and Methods:

The fingerlings of common carp (Weight:3±1g, length:7±1cm) were collected from Department of Fisheries, Chikkamagaluru. Prior to caging in the plastic tubs fingerlings were treated with potassium permanganate (2 mg/L). They were fed with powdered rice bran and ground nut oil cake (3:1). In the laboratory, fishes were acclimatized for fifteen days before the experiments. The static renewal method is used to determine the Lc_{50} value of Bordeaux mixture. After acclimatization of fish for two weeks, the fishes of almost equal size were taken in eight tubs having 5 litres of water with 10 fingerlings in each tub, four tubs were used for control and another 4 tubs were exposed with different concentrations of Bordeaux mixture (1:1 copper sulphate and quick lime) (0.04, 0.05, 0.06, 0.07 mg/L). The mortality was noted down for every 24 hours, 48 hours and 72 hours. The behavioural changes (Table 1) in the fishes were noted after the application of testing dose till the end of the experiment.

Estimation of protein:

The amount of protein in the samples of fishes was estimated by Lowry's method (Lowry's *et.al.*, 1951). The tissue was extracted by dissecting the fishes and was homogenized in distilled water, centrifuged at 3000 rpm for 10 minutes. To 1 ml of the supernatant taken in a test tube 4.5 ml of Reagent I was added (A. 2% Na2CO3 in 0.1 N NaOH B. 1% NaK Tartrate in H2O C. 0.5% CuSO4.5 H2O in H2O D. Reagent I: 48 ml of A, 1 ml of B, 1 ml C) and incubated for 10 minutes. After incubation, 0.5 ml of FC reagent diluted with water (1:1) was added and incubated for 30 minutes at room temperature. Optical density at 660 nm was measured in a spectrophotometer. Simultaneously, BSA standard curve too was plotted. Amount of protein in the sample was calculated by comparing with the standard curve of BSA

Estimation of glycogen:

The amount of glycogen in the tissue sample was estimated by Kemp's method (Kemp *et al.,* 1954). The tissue was extracted and 100 mg of the tissue was homogenized in 5 ml of 80% methanol. It was centrifuged at 5000 rpm for 10 minutes. To the residue, 5 ml of 5% Trichloroacetic acid (TCA) was added and centrifuged for 5 minutes. For 1 ml of the supernatant, 3 ml of concentrated sulphuric acid was added and heated in boiling water bath for 15 minutes and cooled at room temperature. OD was measured at 540 nm.

Estimation of glucose:

The Anthrone method was used to estimate the glucose in the sample (Roe*et.al*., 1955). The sample tissues were extracted by dissecting the fishes and homogenised (100 mg) using 5% TCA. The contents were centrifuged at 2000 RPM for 10 minutes. Supernatent was collected and distilled water is added make up to the volume 2 ml. To this, 4 ml of 0.2% anthrone reagent was added and incubated at room temperature for 10 minutes and intensity of colour was read at 620 nm.

Histological analysis:

For histological analysis fishes were sacrificed and gills and muscles were removed and fixed in Bouin's solutions (Robert, 2001), dehydrated through graded series of ethanol, cleared in xylene and embedded in paraffin. Thro microtoming, 2 micron sections were taken, stained and examined under microscope.

Results and Discussion:

In the present study the effect of Bordeaux mixture on the biochemical (protein, glycogen and glucose content) aspects in the tissues (gills and muscles), histological changes in the gills and muscles and behavioural changes of Common carp were studied. The present study reveals that there was no mortality in the control group; The Lc_{50} values of the pesticide were found that 0.07 mg/L concentration of fungicide was toxic to the fingerlings.

Behavioural studies: The behaviour condition of the fish in both control and treated groups were noted .The fishes showed marked

changes in their behaviour when exposed to different concentration of Bordeaux (Table.1). The behavioural changes includes, loss of balance, moving in spiral fashion with jerks, erratic swimming, loss of balance, restlessness and motion less.

Table1: The behavioural changes in common carp (*Cyprinus carpio*) treated with Bordeaux mixture.

Behaviour	Concentration in mg/L			
	0.04	**0.05**	**0.06**	**0.07**
Erratic swimming	-	-	+	+
Restlessness	-	+	+	+
Loss of balance	-	-	+	+
Enhanced surfacing	-	-	+	+
Motionlessness	-	+	+	+

(+) = Present, (-) = Absent

Biochemical changes in Tissues: The variation of protein content in fish control and treated is represented in (Table 2) and (Fig: 1). The amount of protein in controlled muscle and gill was 0.07 mg/g and 0.066 mg/g respectively whereas when treated with Bordeaux the amount of protein in muscle and gills was 0.02 mg/g and 0.043 mg/g respectively. The protein concentration is decreased in treated fish compared to the controlled tissues. The percentage of depletion is maximum in muscle and minimum in gills. The decrease in the protein content in the treated fish may be due to the protein consumed by the fish stored in the body under toxic stress.

Table 2: Protein concentration in the control and pesticide exposed fish tissues

	Parameters	**Control**	**Treated**
Protein (mg/g)	Muscle	0.072	0.026
	Gills	0.066	0.043

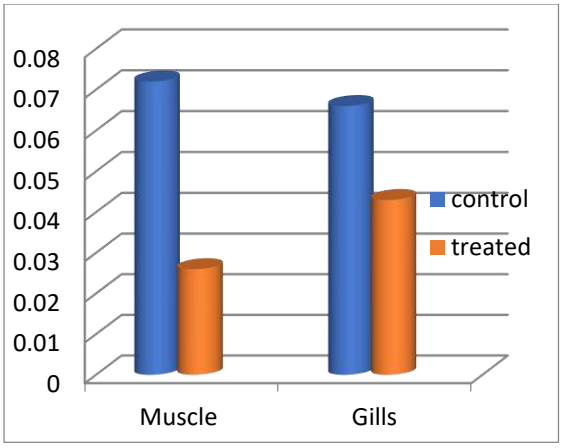

Fig: 1. Average of protein content **(**mg/g**)** in the Tissues of *Cyprinus carpio.*

Table 3: Glycogen concentration in the control and pesticide exposed fish tissues

	Parameters	**Control**	**Treated**
Glycogen (mg/g)	Muscle	0.04	0.026
	Gills	0.03	0.018

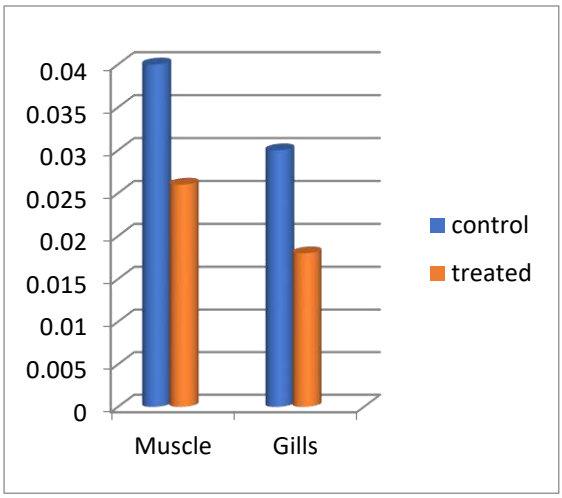

Fig:2. Average of glycogen content **(**mg/g**)** in the Tissues of *Cyprinus carpio*

The alteration occur in the treated fingerlings in the amount of glycogen showed in (Table.3) and (Fig 2). The amount of glycogen in the controlled muscles and gills was 0.040 mg/g and 0.030 mg/g respectively whereas when treated with Bordeaux the amount of glycogen in muscles and gill was 0.026 mg/g and 0.018 mg/g respectively. The glycogen concentration is decrease in treated

fish tissues compared to the controlled fish tissues. The percentage of the depletion was maximum in muscle and minimum in gills. A fall in the glycogen level indicates its rapid utilization to meet the enhanced energy demand in pesticide treated animal through glycolysis (Susan *et al.*, 2010).

The variation of amount of glucose in the controlled and treated fish muscles and gills was 1.148 mg/g and 1.235 mg/g respectively; whereas the amount of glucose in treated fish muscle and gills was 1.387 mg/g and 1.795 mg/g respectively. The glucose concentration is increased in treated fish tissues compared to the controlled fish. The percentage of the restoring of glucose is maximum in gills and minimum in muscles.

Table 4. Glucose concentration in the control and pesticide exposed tissues.

	Parameters	**Control**	**Treated**
Glucose (mg/g)	Muscle	1.148	1.387
	Gills	1.235	1.795

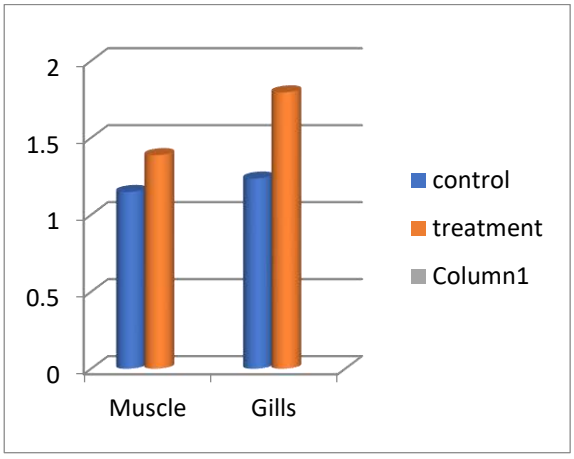

Fig: 3. Average of glucose content **(**mg/g**)** in the Tissues of *Cyprinus carpio*.

Histological Analysis: In gills The major histological changes observed were vacuolization at the tip of the lamellae, ruptured gill epithelium, epithelial lifting, lamellar fusion, epithelial necrosis. In muscles: After exposing to lethal doses shows that vacuoles in muscle tissues, degeneration in the muscle bundle, splitting muscle fibres and cellular degeneration in muscle tissue. It may be due to the high concentration of copper present in the Bordeaux mixture which causes the histological damage in the tissues.

Straus (2017) reported that when high doses of copper sulphate was added to high alkaline water a compound called tenorite (copper oxide) is formed which was severe in 7 fish varieties including cat fish, golden shiner, koi, larger mouth Bass, rainbow trout and walleye. Rainbow trout, koi and walleye were very sensitive compared to catfish which could tolerate 12.5X the recommended rate. Large-mouth bass tolerated up to 64X the recommended rate (Straus, 2017). Results showed a significant difference in the tolerable limit among the various fishes studied.

In another study, Mozambique Tilapia (*Tilapia mossambica*), a freshwater edible fish were exposed to different doses of copper nanoparticles (15mg/L, 10mg/L, 5mg/L, 2mg/L) and Dibutyltin (0.08mg/L, 0.04mg/L, 0.12mg/L) for 96 hours. The results indicated that the activity of oxidative stress enzymes GSH, AChE and glutathione -Stransferase were significantly decreased (Ghais et al., 2019). The results showed more serious negative impact in the tissues in case of copper nanoparticles compared to dibutyltin, which may affect fish growth and development, protein content and causes death (Ghais et al., 2019). They reported a decrease in protein content in the liver and brain at 10mg/L where as in the gills, copper oxide at 15mg/L lowered the protein concentration.

Copper based paints are being used all over the globe to prevent fouling of submerged vessels and boats. Copper-oxide based compounds including nanoparticles are serious water pollutants but their impact in fish performance remains poorly understood.

Sub-lethal copper toxicity can change gill permeability to copper (Taylor et al., 1998) and cause gill lesions, hypertrophy, hyperplasia, epithelial lifting and necrosis (Mallatt, 1985). Gill lesions from acute waterborne copper exposure can increase the distance of diffusion across the secondary lamellae, decreasing the amount of oxygen

transferred across the gill epithelium (Tuurala et al., 1984). Additionally, copper exposure can negatively impact sensory abilities and swimming performance. Coho salmon (*Oncorhynchus kisutch*), for example, exhibited a reduced olfactory response within 10 minutes of copper exposure (Baldwin et al., 2003), and critical swimming speed decreased by 48, 31, and 13% for rainbow trout, common carp (*Cyprinus carpio*), and gibel carp (*Carassius gibelio*), respectively, after exposure (De Boeck et al., 2006). Further investigation into the sublethal effects of these copper compounds and the extent to which factors like temperature and other herbicides mediate these effects, is therefore warranted.

To reduce the copper toxicity, instead of ionic copper formulations, chelated copper products were being released which is acclaimed to be less toxic (Wagner et al., 2017). In one of the studies, Wagner et al., (2017) failed to replicate their own laboratory investigation results in the field settings wherein they reported chelated copper can elevate fathead minnows and brook trout fish mortality in field settings at concentrations much lower than those observed in the laboratory. Authors reported that greater (2.3 times) mortality risk for caged fish within the first 72 h after treatment than the reference sites could be attributed to high water temperature (Wagner et al., 2017). These results suggest that in the open environment there are so many factors to be considered before the conclusion.

Conclusion:

The present study was carried out to examine the impact of Bordeaux mixture on the fresh water Common carp (*Cyprinus carpio*) fish fingerlings to study its behavioural, histological alteration and biochemical variation. The Bordeaux mixture exposures have produced the following changes in the treated fingerlings, the behavioural changes includes loss of balance and moving in spiral fashion with jerks. Histological alteration includes ruptured gill epithelium, epithelial lifting and lamellar fusion. Splitting muscle fibres and cellular degeneration in muscle tissue. Fungicide can induce considerable changes in the biochemical parameters in fish tissues. A decrease in the concentration of glycogen and protein was found to significant compare to control groups. It can be concluded that Bordeaux mixture is highly toxic to fish *Cyprinus carpio.* So the fungicide should be used with great caution and in a sustainable way to that it may not be hazards to aquatic environment.

References:

[1] Ahmad MK., Sharma DK., Ansari S and BA. Ansari (2011). Comparative Study of fertilizer and weedicide on fingerlings of Zebra fish *Daniorerio* (Cyprinidae). Res.J.Chem.Sci., 1:91-94.

[2] Das BK and SC Mukherjee, (2003). Toxicity of cypermethrin in *Labeorohita* Fingerlings. Biochemica Enzymatic and Haematological Conseqences,Comp.Bioche.Physiol.Toxicil.Pharmacol.134:109-121.

[3] Loganathan PR, Ganapathi N and Narendiran NJ (2014). Estimation of protein in the detergent induced toxicity fish, *Catla catla*. Journal of Global Bioscience. 3(1):314-320.

[4] Vijayalakshmi M, Sumathy R and Sharmila J (2013). Electrophoretic pattern and Histopathological study of Muscle Tissue Tilapia, O*reochromis mossambicus* exposed to Textile Dyes. International Journal of Science and Research.5:804-812.

[5] Straus Dave, 2017. Copper sulphate toxicity to various fish: Role of alkalinity/hardness. National aquaculture extension conference, Boise, Idaho.

[6] Ghais SA, Bhardwaj V and Kumbhar P, 2019. Impact of different concentration of copper nanoparticles and organometallic compounds on biomarkers of tilapia fish. Int. J. Adv. Res. 7(10), 1074-1080

[7] Islam M.D and Tanaka M., (2004). Impacts of pollution on coastal and marine ecosystems including coastal and marine fisheries and approach for management: a review and synthesis. Mar. Pollut. Bull. 48, 624–649.

[8] Matta J., Milad M., Manger R. and Tosteson T., (1999). Heavy metals, lipid

peroxidation, and ciguatera toxicity in the liver of the Caribbean barracuda (Sphyraena barracuda). Biol. Trace Elem. Res. 70, 69–79.
[9] Yi Y., Yang Z. and Zhang S., (2011). Ecological risk assessment of heavy metals in sediment and human health risk assessment of heavy metals in fishes in the middle and lower reaches of the Yangtze River basin. Environ. Pollut. 159, 2575–2585.
[10] Wagner JL, Townsend AK, Velzis AE and Paul EA, (2017). Temperature and toxicity of the copper herbicide (Nautique^{TM}) to freshwater fish in field and laboratory trials, Cogent Environmental Science, 3:1, 1339386, DOI:10.1080/23311843.2017.1339386
[11] Mastin BJ., and Rodgers JH. (2000). Toxicity and bioavailability of copper herbicides (clearigate, cutrine-plus, and copper sulfate) to freshwater animals. *Archives of Environmental Contamination and Toxicology, 39,* 445–451.
[12] Taylor LN., McGeer J., Wood C. and McDonald D. (1998). Modelling chronic thresholds for toxicity–physiological effects of chronic copper exposure to rainbow trout. *Fish Response to Toxic Environments,* 95
[13] Mallatt, J. (1985). Fish gill structural changes induced by toxicants and other irritants: A statistical review. *Canadian Journal of Fisheries and Aquatic Sciences, 42,* 630–648.
[14] Tuurala H., Part P., Nikinmaa M. and Soivio A. (1984). The basal channels of secondary lamellae in *Salmo gairdneri* gills—A non-respiratory shunt. *Comparative Biochemistry and Physiology, 79,* 35–39.
[15] Baldwin DH., Sandahl JF., Labenia JS. and Scholz NL, (2003). Sub-lethal effects of copper on coho salmon: Impacts on non overlapping receptor pathways in the peripheral olfactory nervous system. *Environmental Toxicology and Chemistry, 22,* 2266–2274.
[16] De Boeck, G., van der Ven, K., Hattink, J., and Blust, R. (2006). Swimming performance and energy metabolism of rainbow trout, common carp and gibel carp respond differently to sublethal copper exposure. *Aquatic Toxicology, 80,* 92–100. https://doi.org/10.1016/j.aquatox.2006.07.017
[17] Froese R. and D. Pauly. (2013). FishBase. World Wide Web electronic publication:http://www.fishbase.org/Country/CountrySpeciesSummary.php?c_code=356&id=1450, version (12/2013)

Karnatak University Journal of Science 53 (2022) 44-53

Karnatak University Journal of Science

ISSN: 0075-5168

Evaluation of ground and excited state dipole moments of laser dye DCM by solvatochromic shift measurements and computational study

Shrikrupa K. Chavan, Vikram Pujari, Shivaraj A. Patil and Sanjeev R. Inamdar*

Laser Spectroscopy Programme, Department of Physics, Karnatak University, Dharwad 580003, India

***Corresponding author:** him_lax3@yahoo.com; srinamdar@kud.ac.in*

ARTICLE INFO

Received: 21 March 2022;
Revised: 11 April 2022;
Accepted: 19 April 2022;
Keywords:

ABSTRACT

As part of our ongoing research on fluorescence spectroscopy of laser dyes, the solvatochromism of a medium sized polar laser dye ([2-[2-[4-(dimethylamino) phenyl] ethenyl]-6-methyl-4H-pyran-4-ylidene]-propanedinitrile (DCM) was investigated experimentally and computationally. The experimental investigation reveals a bathochromic shift both in the absorption and fluorescence spectra with increasing solvent polarity which is indicative of occurrence of $\pi \rightarrow \pi^*$ transition. The ground and singlet excited state dipole moments were determined employing several solvent correlation approaches such as Bilot-Kawski, Lippert-Mataga, Kawski-Chamma-Viallet and Bakhshiev methods. The computational studies were carried out to optimise the ground and excited state geometries of DCM using density functional theory (DFT) and time dependent density functional theory (TD-DFT), respectively, in gas phase employing Gaussian09 software. The empirically measured and calculated values of ground (μ_g) and excited (μ_e) state dipole moments of this dye are compared and the results are discussed to understand the photophysics of the DCM molecule. The values of μ_g and μ_e determined from Bilot-Kawski, Lippert-Mataga, Kawski-Chamma - Viallet and Bakhshiev methods agree well with those obtained from computational studies.

1. Introduction

The compound 2-[2-[4-(dimethylamino)phenyl] ethenyl]-6-methyl-4H-pyran-4-ylidene]-propanedinitrile or 4-(Dicyanomethylene)-2-methyl-6-(4-dimethylaminostyryl)-4*H*-pyran (DCM) is a merocyanine dye category commonly referred to as "red fluorescent dye" in literature.Eastman Kodak Company first reported the DCM dye, which was initially utilised as a dopant in the development of red laser materials[1-2].Later research revealed that DCM has excellent fluorescence quantum efficiency, a large Stokes shift and solvatochromic behaviour.DCM and DFSBO (7-dimethyl-amino-3-(p-formylstyral)-1,4-benzoxazin-2-one) show extremely comparable absorption spectra with peaks in the 450-500nm region that are strongly dependent on the solvent polarity [22]. The fluorescence and quantum yield (Q_0=0.71) measurement were made as already reported[23] on a 2.4×10^{-7} M solution, compared with alkaline fluorescein in ethanol, and the decay time at this concentration is 1.9ns. DCM is more efficient and has a wider tuning range than the other dyes. It has a broad tunning range in DMSO (Dimethyl Sulfoxide) and is the most effective dye reported for the 630-680nm region [24].The fluorescence maxima of DCM in methanol and Decanol are found to be at 612nm and 588nm (Stokes Shift is ≅150 nm),this shifts the fluorescence peak with increasing polarity of the solvent and fluorescence peaks shift toward the red end of the visible spectrum as a function of wavelength.Using Lippert-Mataga theory and several solvents, it was determined that the excited state dipole moment(μ_e)is 26.3D[3].

Dipole moments measurements of laser dyes plays an important role in research as it provides information about electron density, charge distribution around the probes, electronic and geometrical structure of a dye. In general, the electronic spectra of organic compounds and laser dyes are influenced by their surroundings.There are several significant aspects that affect the electrical spectrum. Among the key environmental elements, a special emphasis is placed on the impacts of solvents.It's common for organic solvents change in dielectric constant, polarizability, and polarity of the surrounding medium, So, the solvent has a big impact on the dipole moment of the ground and excited states.Analysis of the solvent's effects is important in understanding how the probe behaves in the excited state.Numerous researchers, including our group, have reported on the photophysical and chemical properties of several chromophores as a function of refractive index, solvent polarizability and polarity, concentration, viscosity, and pH, among other parameters.The excitation and emission spectra of a dye are often altered by solvents and provide information on the behaviour of the excited state in comparison to the ground state.Using the spectral shift data as a function of solvent polarity, the spectral transition ($\pi \rightarrow \pi^*$, $\pi^* \rightarrow$ n, etc) can be identified.As a function of solvent polarity, the $\pi^* \rightarrow$ n and $\pi \rightarrow \pi^*$bands exhibit blue and red shifts, respectively.

Number of studies exist on the solvatochromic shift technique for determining the dipole moments of various laser dyes[4-13]. The current study is concern about the effects of the solvent on the electronic absorption and emission spectra of DCM dye in a number of alcohol solvents.By various solvent correlation approaches using solvatochromic spectral shift methods were used to determine the experimental dipole moments and changes in dipole moments for the ground and excited states.In addition, DFT and TD-DFT formalisms were used to calculate the ground and excited state dipole moments.

2. Materials and methods:

2.1: Materials:

Exciton chemical company, USA supplied DCM, an orange-red fluorescent laser dye and it was used without any further purification.

2.2: Experimental methods:

Absorption spectra were recorded in the 200-800 nm wavelength range using a dual beam UV-VIS NIR spectrophotometer (JASCO, Model V-670). A spectrofluorometer was used to record the fluorescence spectra (JY Horiba, Model Fluoromax4). In this experiment we used a rectangular quartz cuvette with a one-centimeter-long path length. And Origin Pro 9.0 software was used to analyse the experimental data. For the computational studies we are using Gaussian09 package for geometry optimizations of ground state and excited state studies carried out by applying B3LYP/6-311G basis set level. DFT/TD-DFT methods are also used to calculate ground and excited state dipole moments of DCM polar dye.

3.Theoretical background for the evaluation of dipole moment:

The electrical distribution of a molecule can be determined by studying its ground and excited state dipole moments. Among the several ways of investigating excited state dipole moment, following solvatochromic shift methods are used for DCM polar laser dye.

3.1. Bilot and Kawski method:

Bilot and Kawski used quantum mechanics to figure out how dipole moments in the ground (μ_g) and singlet excited (μ_e) states were measured in different solvents with different polarities. They did this by measuring the absorbance (ν_a) and fluorescence (ν_f) band shifts in different solvents with different polarities [14,15]. According to this relation, the difference and sum of absorption and fluorescence maxima in (cm^{-1}) involved two solvatochromism expressions.

$$\bar{\nu}_a - \bar{\nu}_f = -m^2(f(\varepsilon,n) + 2g(n)) + const \quad (1)$$

$$\bar{\nu}_a - \bar{\nu}_f = m^1 f(\varepsilon,n) + const \quad (2)$$

Where, m^1 and m^2 are slopes taken from the relation (1) and (2), respectively. If the solvent polarity of the solute can be studied with refractive index (n), permittivity of distinct solvents (ε) then, $f(\varepsilon,n)$ and $g(n)$ can be characterized as

$$f(\varepsilon,n) = \frac{2n^2+1}{n^2+2}\left[\frac{\varepsilon-1}{\varepsilon-2} - \frac{n^2-1}{n^2+2}\right] \quad (3)$$

And

$$g(n) = \frac{3}{2}\frac{(n^4-1)}{(n^2+2^2)} \quad (4)$$

If the polarizability of the solute is isotropic with the $2\alpha/a^3$ [14-15] where $'\alpha'$ is an isotropic polarizability and 'a' the Onsager cavity radius of the solute. According to reaction field theory of Onsager

$$m_1 = \frac{2(\mu_e - \mu_g)^2}{hca^3} \quad (5)$$

and

$$m_2 = \frac{2(\mu_e^2 - \mu_g^2)}{hca^3} \quad (6)$$

Where 'c' denotes the speed of light in vacuum, and 'h' denotes Planck's constant. If the solute's symmetry does not change throughout the electronic transition, μ_g and μ_e are parallel and are given by [15-16].

$$\mu_g = \frac{m_2 - m_1}{2}\left[\frac{hca^3}{2m_1}\right]^{1/2} \quad (9)$$

$$\mu_e = \frac{m_1 + m_2}{2}\left[\frac{hca^3}{2m_1}\right]^{1/2} \quad (10)$$

$$\text{or } \mu_e = \frac{m_1 + m_2}{m_2 - m_1}\mu_g \; ; (m_2 > m_1) \quad (11)$$

Eq.(10)[16] can be used to figure out the angle between the dipole moments of the ground state and the excited state.

$$\cos\phi = \frac{1}{2(\mu_e - \mu_g)}[(\mu_g^2 + \mu_e^2) - \frac{m^1}{m^2}(\mu_e^2 - \mu_g^2)] \quad (10)$$

3.2. Lippert -Mataga, Bakhshiev and Kawski-Chamma-Viallet methods Solvatochromic techniques may also be used to determine the ground and singlet excited state dipole moments using the equations reported by Lippert-Mataga (Eq.11) [17,18], Bakhshiev (Eq.12) [19], and Kawski-Chamma-Viallet (Eq.13) [20,21].

$$\bar{\upsilon}_a - \bar{\upsilon}_f = m_{M-L} + cons\tan t \quad (11)$$

$$\bar{\upsilon}_a - \bar{\upsilon}_f = m_B f(\varepsilon, n) + cons\tan t \quad (12)$$

$$\frac{\bar{\upsilon}_a + \bar{\upsilon}_f}{2} = -m_{K-C-V} f_{K-V-C}(\varepsilon, n) + const \quad (13)$$

where, $\bar{\upsilon}_a$ and $\bar{\upsilon}_f$ are absorption and fluorescencemaxima wave number in (cm^{-1}) respectively, $m_{L\text{-}M}$, m_B, $m_{K\text{-}C\text{-}V}$ are slopes derived from linear graphs(Fig.1) and $f_{L-M}(\varepsilon, n), f_B(\varepsilon, n), f_{K-C-V}(\varepsilon, n)$ are solvent polarity function defined by Eqs. (14)-(16).

$$f_{L-M}(\varepsilon, n) = \frac{\varepsilon + 1}{2\varepsilon + 1} - \frac{n^2 - 1}{2n^2 + 1} \quad (14)$$

$$f_B(\varepsilon, n) = \frac{2n^2 + 1}{n^2 + 2}[\frac{\varepsilon - 1}{\varepsilon + 2} - \frac{n^2 - 1}{n^2 + 2}] \quad (15)$$

$$f_{K-C-V}(\varepsilon, n) = [\frac{2n^2 + 1}{2(n^2 + 2)}(\frac{\varepsilon - 1}{\varepsilon + 2} - \frac{n^2 - 1}{n^2 + 2}) + \frac{3(n^4 - 1)}{(2n^2 + 2)^2}] \quad (16)$$

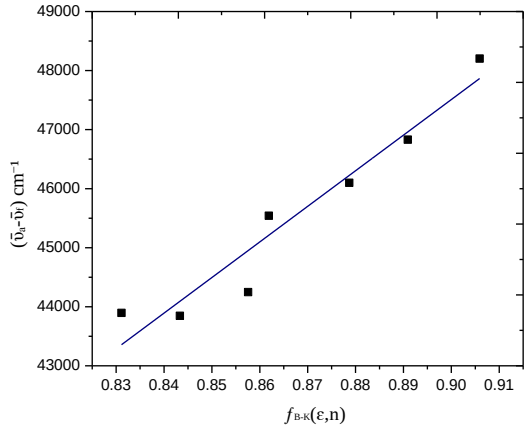

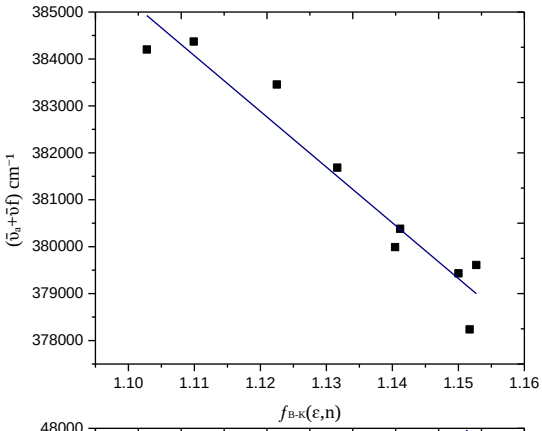

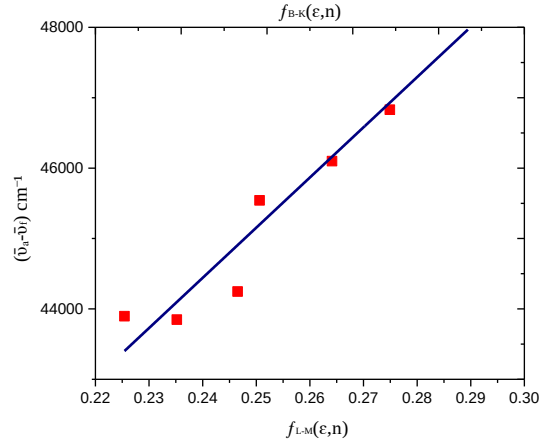

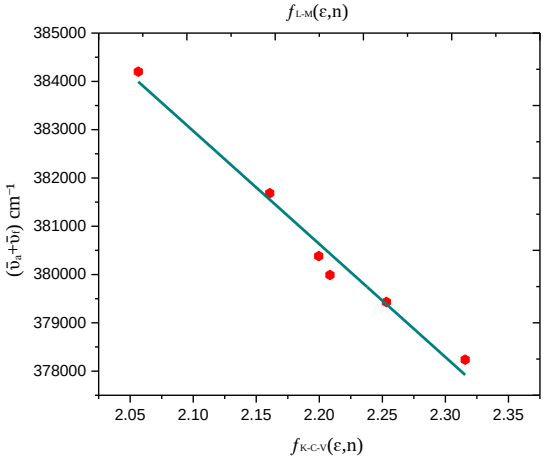

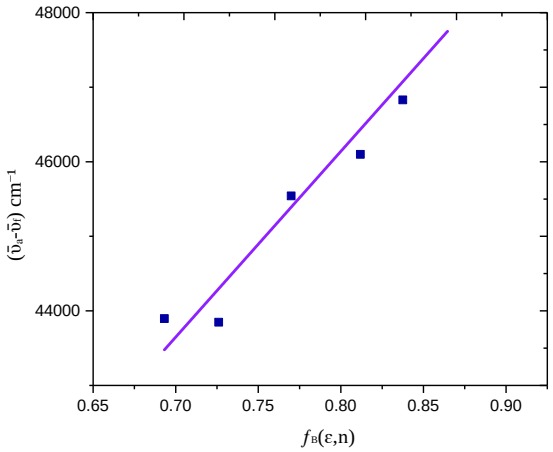

Fig1.(A) Graph of $\bar{\upsilon}_a-\bar{\upsilon}_f vsf_{L-M}(\varepsilon,n)$, $f_{L-M}(\varepsilon,n),\bar{\upsilon}_a-\bar{\upsilon}_f vsf(\varepsilon,n),\bar{\upsilon}_a+\bar{\upsilon}_f vs[f(\varepsilon,n)+2g(n)]$ and $\bar{\upsilon}_a+\bar{\upsilon}_f vs2f_{K-C-V}(\varepsilon,n)$ of DCM laser dye in alcohol series.

The graph $\bar{\upsilon}_a-\bar{\upsilon}_f vsf_{L-M}(\varepsilon,n)$ $f_{L-M}(\varepsilon,n),\bar{\upsilon}_a-\bar{\upsilon}_f vsf(\varepsilon,n)$ $\bar{\upsilon}_a+\bar{\upsilon}_f vs[f(\varepsilon,n)+2g(n)]$ and $\bar{\upsilon}_a+\bar{\upsilon}_f vs2f_{K-C-V}(\varepsilon,n)$ exhibits linear patterns with the respective slopes $m_{L\text{-}M}$, m_B, $m_{K\text{-}C\text{-}V}$ as given in the equations below.

$$m_{L-M}=\frac{2(\mu_e-\mu_g)^2}{hca^3} \quad (17)$$

$$m_B=\frac{2(\mu_e-\mu_g)^2}{hca^3} \quad (18)$$

$$m_{K-C-V}=\frac{2(\mu_e-\mu_g)^2}{hca^3} \quad (19)$$

3.3. Onsager cavity radius

The value of Onsager cavity radius "a" of DCM dye was determined by using Eq. (20) [22,23]

$$\alpha=[\frac{3M}{4\pi\rho N_A}]^{1/3} \quad (20)$$

Where, ρ is density of the solute molecule, M, molecular weight of the solute molecule and N_A is the Avogadro's number.

3.4. Computational details

Density functional theory (DFT) and time-dependent functional theory (TD-DFT) at the B3LYP/6-311G level in vacuum were used to optimise the ground and excited state geometries of the tagged fluorescent DCM molecule [23]. The shape of the probe's ground and excited states is optimised in vacuum.

4. Results and discussion:

The spectral characteristics of DCM laser dye were analysed in alcohol series solvents to estimate the solvent effect on electronic transition. Table 1 and Table 2 summarise the solvent properties of DCM dye in polar protic solvents such as thedielectric constant (ε), refractive index (n), polarity parameters $f(\epsilon,n)$ and $\varphi(\epsilon,n)$ from several solvent correlation approaches such as Bilot-Kawski, Lippert-Mataga, Kawski-Chamma -Viallet and Bakhshiev methods.

4.1: Solvent effects on absorption and fluorescence spectra:

The spectral position of dye in polar protic solvents has revealed interesting results. The fluorescence maxima of DCM in Methanol and Decanol are 612 nm and 588 nm, respectively (Stokes Shift ≅150 nm). As the polarity of the solvent increases, the fluorescence peak shifts toward the red end of the visible spectrum, and the fluorescence peaks shift toward the red end of the visible spectrum as a function of wavelength.With increasing solvent polarity, the experimental analysis indicates a bathochromic change in both the absorption and fluorescence spectra, indicating the occurrence of the $\pi \rightarrow \pi^*$ transition.The information of photophysical properties of laser dye in polar solvents of different polarities helps in understanding their applicability as fluorescent dye as shown in Fig 2. Table 1 summarises Experimentally determined values of absorption maxima(ν_a), emission maxima (ν_f), stokes shift (ν_a- ν_f) and (ν_a+ ν_f) values of DCM in alcohols solvent.

Table 1. Experimentally determined values of Dielectric constant (ε), refractive index (n), absorption maxima(ν_a), emission maxima (ν_f), stokes shift (ν_a- ν_f) and (ν_a+ ν_f).

Solvents	**λ_{abs} (nm)**	**λ_{emi} (nm)**	**Dielectric constant (ε)**	**refractive index (n)**	**ν_a cm^{-1}**	**ν_f cm^{-1}**	**ν_a- ν_f cm^{-1}**	**ν_a+ ν_f cm^{-1}**
Methanol	464	612	33.62	1.388	215517.24	163398.69	52118.5485	378915.934
Ethanol	469	606	25.07	1.3611	213219.61	165016.50	48203.1145	378236.117
Propanol	469	601	20.79	1.385	213219.61	166389.35	46830.2651	379608.967
Butanol	470	600	17.8	1.3993	212765.95	166666.66	46099.2907	379432.624
Pentanol	470	598	14.27	1.4101	212765.95	167224.08	45541.8771	379990.037
Hexanol	471	595	13.85	1.4178	212314.22	168067.22	44246.9981	380381.451
Heptanol	470	592	11.75	1.4249	212765.95	168918.91	43847.0385	381684.876
Octanol	468	589	10.3	1.4295	213675.21	169779.28	43895.9267	383454.500
Nonanol	466	589	8.83	1.4333	214592.27	169779.286	44812.98775	384371.5616
Decanol	467	588	8.1	1.4372	214132.76	170068.027	44064.7351	384200.7895

Table 2: Experimentally determined values ofpolarity parameters $f(\epsilon, n)$ and $\varphi\ (\epsilon, n)$ from several solvent correlation approaches such as Bilot-Kawski, Lippert-Mataga, Kawski-Chamma -Viallet and Bakhshiev methods.

$f_{B\text{-}K}\ (\epsilon, n)$	$\Phi_{B\text{-}K}\ (\epsilon, n)$	$f_{L\text{-}M}\ (\epsilon, n)$	$f_{B}\ (\epsilon, n)$	$f_{K\text{-}C\text{-}V}\ (\epsilon, n)$
0.909619724	1.17342983	0.287100315	0.895903761	2.340222
0.905908161	1.15169955	0.289465898	0.864650493	2.315675
0.890919607	1.15272609	0.274917031	0.837514631	2.282596
0.878682433	1.15002552	0.264137486	0.811810729	2.253223
0.861893347	1.14041483	0.250622063	0.769917281	2.208505
0.857562399	1.14118868	0.246521303	0.763047397	2.199594
0.843325456	1.13164880	0.235178364	0.726040889	2.160686
0.831121916	1.12248323	0.225428279	0.693155355	2.126559
0.816023555	1.10989136	0.213231047	0.650954622	2.083327
0.80634859	1.10278586	0.205126376	0.625121384	2.05643

4.1: Solvent effects on absorption and fluorescence spectra:

The spectral position of dye in polar protic solvents has revealed interesting results. The fluorescence maxima of DCM in Methanol and Decanol are 612 nm and 588 nm, respectively (Stokes Shift ≅150 nm). As the polarity of the solvent increases, the fluorescence peak shifts toward the red end of the visible spectrum, and the fluorescence peaks shift toward the red end of the visible spectrum as a function of wavelength.With increasing solvent polarity, the experimental analysis indicates a bathochromic change in both the absorption and fluorescence spectra, indicating the occurrence of the $\pi \rightarrow \pi^*$

transition.The information of photophysical properties of laser dye in polar solvents of different polarities helps in understanding their applicability as fluorescent dye as shown in Fig 2. Table 1 summarises Experimentally determined values of absorption maxima(ν_a), emission maxima (ν_f), stokes shift (ν_a- ν_f) and (ν_a+ ν_f) values of DCM in alcohols solvent.

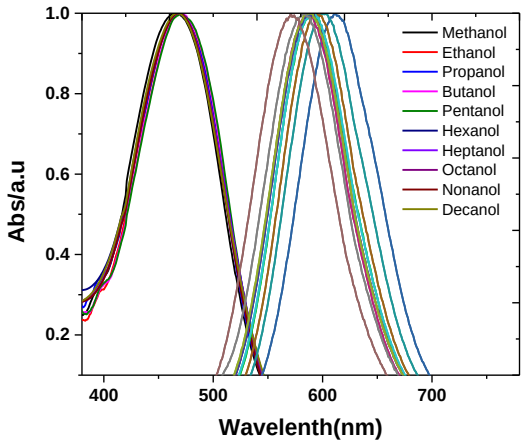

(a)

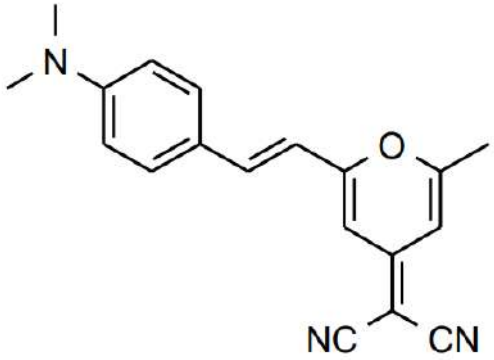

(b)

Fig.2(a)Absorption and Emission spectra of DCM in alcohol solvents (b). Molecular structure of DCM Laser Dye.

4.2: Solvatochromism of dye: Estimation of ground and singlet excited state dipole moments

In solvatochromism, the shifts are caused by the solute and the solvent. In general type of interactions, the refractive index and dielectric constant of solvents play a key role in the shift in spectral range. In specific type of interaction, shifts are due to hydrogen bonding, n-donor and excited state dipole moments.In order to calculate the dipole moment in the ground and excited states, Solvatochromism shift approaches based on spectral shift (Stokes shift) and solvent polarity is given by Bilot-Kawski [Eqs. (1) & (2)], Lippert-Mataga [(Eq.11)], Bakhshiev [Eq.(12)] and Kawski-Chamma-Viallet methods [Eq.(13)]. The graphs of andthe slopes, intercepts and correlation co-efficient determined from them are given in Table 3.

Table 3: Linear plot data for DCM Calculated from Varity of Solvatochromism Methods

Methods		**Slope**	**Intercept**	**R**
Bilot-Kawski	m^1	60277.37	-6740.54	0.918
	m^2	118712.56	515840.99	0.922
Lippert-Mataga	$m_{L\text{-}M}$	71290.79	27331.41	0.975
Bakhshiev	m_B	24918.69	26203.70	0.932
Kawski-Chamma-Viallet	$m_{K\text{-}C\text{-}V}$	23413.43	432340.89	0.975

Using Eqs. (7) and (8), the slopes m^1 and m^2 of the Bilot-Kawski correlation are utilised to compute the ground (μ_g) and singlet excited state (μ_e) dipole moments. Also, using the equations (17-19) we determined the solvent polarity function f_{L-M} ,$f_B$and f_{K-C-V}.Table 4 summarises the computed values of ground and excited state dipole moments, the difference in dipole moments ($\Delta\mu$), the dipole moments ratio (μ_e/ μ_g), the Onsager cavity radius (a), and the angle between dipole moment ($\emptyset$) vectors of DCM.

As shown in Table 4, the ground state dipole moments (μ_g) were calculated to be 14.0470D and the singlet excited state dipole moment (μ_e) to be 16.8359D using Gaussian 09 software. And Figure 3 depicts the optimised shape and the orientation of the ground and excited state dipole moments. In addition, we have observed a comparatively good agreement between the excited state dipole moments calculated by several solvent correlation approaches, such as Bilot-Kawski,

Lippert-Mataga, Bakhshiev, and Kawski-Chamma -Viallet. It is observed that μ_e (38.39D) obtained from the Bilot-Kawski approach is greater than values obtained from other methods. The ratio of the excited state to ground state dipole moment was calculated using the Bilot-Kawski technique and found to be 3.06. We also calculated the angle between the ground and excited state dipole moments.

Conclusion:

In this paper, we evaluated the ground and singlet excited state dipole moments of DCM dye using various correlation techniques and compared them with theoretical studies utilising DFT/TD-DFT calculations. The detailed solvatochromic effect on the absorption and fluorescence spectra of the molecule was studied. The experimental and computational results show that DCM dye has smaller dipole moments in the ground state than in the excited state, indicating that the excited state is more polar or stable. The experimental ground state and excited state dipole moments of DCM were compared to those obtained using several solvent correlation approaches, such as the Bilot-Kawski, Lippert-Mataga, Bakhshiev, and Kawski-Chamma-Viallet methods. We prefer the Bilot-Kawski approach because it allows us to calculate both the ground and excited state dipole moments of molecules and we can easily compare them with theoretical results. Other approaches only provide the value of the excited state dipole moment. The dipole moments calculated by these methods are very close to those calculated by the Gaussian09 software.

Table 4: Ground (μ_g) and Excited state dipole moment (μ_e) in Debye, angle between dipole moment ('φ' in Degree) and Onsager cavity radius ('a' in A^0) of DCM.

μ_g[a]	μ_e[a]	a[j] A^0	μ_g[c] B-K	μ_e[c] B-K	μ_e[d] L-M	μ_e[e] B	μ_e[f] K-C-V	(μ_g/μ_e)[g]	$\Delta\mu$[h]	Φ[1]
14.299	16.8359	111.980	12.534	38.39	14.04	8.320	8.065	3.06	2.536	22.14

[a]Calculated at DFT/B3LYP/6-311 G level using G09 software
[b]Calculated at TDDFT/B3LYP/6-311 G level using G09 software
[c] The Bilot-Kawski technique was used to obtain this result. (Eq .(1)&(2)).
[d] The Lippert- Matag technique was used to obtain this result. (Eq. (11)).
[e] The Bakhshiev technique was used to obtain this result. (Eq. (12)).
[f]The Kawski- Chamma Viallet technique was used to calculate this result. (Eq. (13)).
[h] difference in dipole moment.
[g]The ratio of excited state to ground state dipole moment. (Bilot-Kawski method)
[i] Angle between the ground and excited state dipole moments obtained using (Eq. (10)).
[j] The Onsager cavity radius was determined using Edward's atomic increment approach.

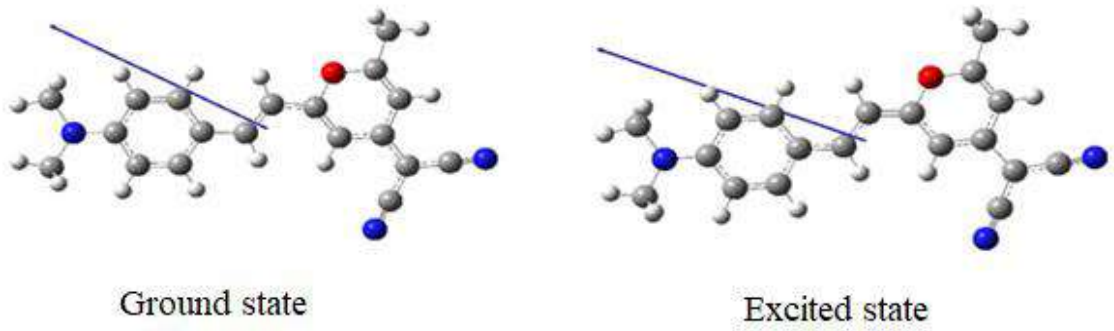

Fig.3:Optimized geometry with dipole moment vector of DCM

Acknowledgment:
One of the authors (SKC) is grateful to Karnatak University for providing financial assistance in the form of a University Research Scholarship. Authors thank Karnatak University's Scientific Instrumentation Centre for providing the UV-Vis Spectrophotometer.

References

1. R.K. Kanaparthi, "Photophysical Properties of 4-(Dicyanomethylene)-2-Methyl-6-(4-Dimethylaminostyryl)-4H-Pyran (DCM) and Optical Sensing Applications," in: S. Saha (Ed.), IntechOpen, Rijeka, 2021: p. Ch. 1. https://doi.org/10.5772/intechopen.93149.

2. B. Boldrini, E. Cavalli, A. Painelli, F.Terenziani, "Polar dyes in solution: A joint experimental and theoretical study of absorption and emission band shapes", J. Phys. Chem. A. 106 (2002) 6286–6294.

3. Liptay,W. "dipole moments and Polariziilities of molecules in Excited states", in E.C.Lim, Ed., Excited States, Vol.1,pp.129-229,Academic Press, New York,194.

4. G.H. Pujar, M.N. Wari, B. Steffi, H. Varsha, B. Kavita, C. Yohannan Panicker, C. Santhosh, A. Patil, S.R. Inamdar, "A combined experimental and computational investigation of solvatochromism of nonpolar laser dyes: Evaluation of ground and singlet excited-state dipole moments", J. Mol. Liq. 244 (2017) 453–463. https://doi.org/https://doi.org/10.1016/j.molliq.2017.08.078

5. Patil SK, Wari MN, Panicker CY, Inamdar SR. "Determination of ground and excited state dipole moments of dipolar laser dyes by solvatochromic shift method". Spectrochim. Acta A Mol BiomolSpectrosc2014;123:117–26. doi:10.1016/j.saa.2013.12.031.

6. Basavaraja J, Inamdar SR, Suresh Kumar HM. "Solvents effect on the absorption and fluorescence spectra of 7-diethylamino-3-thenoylcoumarin: Evaluation and correlation between solvatochromism and solvent polarity parameters". Spectrochim Acta A Mol Biomol Spectrosc 2014;137C:527–34. doi:10.1016/j.saa.2014.08.118.

7. Mannekutla JR, Mulimani BG, Inamdar SR. "Solvent effect on absorption and fluorescence spectra of coumarin laser dyes: Evaluation of ground and excited state dipole moments". Spectrochim Acta - Part A Mol Biomol Spectrosc 2008;69:419–26. doi: 10.1016/j.saa.2007.04.016.

8. Basavaraja J, Suresh Kumar HM, Inamdar SR, Wari MN. "Estimation of ground and excited state dipole moment of laser dyes C504T and C521T using solvatochromic shifts of absorption and fluorescence spectra". Spectrochim Acta Part A Mol Biomol Spectrosc 2016;154:177–84. doi:10.1016/j.saa.2015.10.020.

9. Bayrakçeken F, Yaman A, Hayvali M. "Photophysical and photochemical study of laser-dye coumarin-481 and its photoproduct in solution". Spectrochim Acta - Part A Mol Biomol Spectrosc 2005;61:983–7. doi:10.1016/j.saa.2004.05.046.

10. Thipperudrappa J, Biradar DS, Manohara SR, Hanagodimath SM, Inamadar SR, Manekutla RJ. "Solvent effects on the absorption and fluorescence spectra of some laser dyes: Estimation of ground and excited-state dipole moments". Spectrochim Acta - Part A Mol Biomol Spectrosc 2008;69:991–7. doi:10.1016/j.saa.2007.06.002.

11. Joshi S, Kumari S, Bhattacharjee R, Sakhuja R, Pant DD. "Estimation of ground and excited state dipole moments of synthesized coumarin derivative [N-(2-oxo-2H-chromen-4- yl)imino]triphenyl-phosphorane".J. Mol. Liq 2014;200:115–9. doi: 10.1016/j.molliq. 2014.09.054.

12. Kumar.S,Rao.VC, Rastogi RC. "Excited-state dipole moments of some hydroxycoumarin dyes using an efficient solvatochromic method based on the solvent polarity parameter", ETN. Spectrochim Acta - Part A Mol Biomol Spectrosc 2001;57:41–7. doi:10.1016/S1386- 1425(00)00330-9.

13. Ravi M, Soujanya T, Samanta a., Radhakrishnan TP. "Excited-state dipole moments of some Coumarin dyes from a solvatochromic method using the solvent polarity parameter". J. Chem. Soc. Faraday Trans 1995;91:2739. doi:10.1039/ft9959102739

14. L.Bilot, A. Kawski, Zur "Theorie des einflusses von lösungsmitteln auf dieelektronenspektrendermoleküle",Z.Naturforsch.,A:Phys.Sci.17a(1962)621–627.

15. A.Kawski, in:J.F.Raek(Ed),Progress In Photochemistry and Photophysics, Vol.5,CRC Press, Boca Raton,USA 1992,pp.1-47.

16. A.Kawski, "Ontheestimationofexcited-statedipolemomentsfromsolvatochromic shifts of absorption and fluorescence spectra",Z. Naturforsch., A: Phys. Sci. 57a (2002)255–262

17. V.E.Lippert, "Dipole Moment and elekroestructure von angeregrenmoiekuien",Z: naturforsch.,A:Phys.Sci.10a(1995)541-545.

18. N.Lataga,Y.Kaifu,M.Kolzumi,"Solventeffectsuponfluorescencespectraandthe dipolemomentsofexcitedmolecules",Bull.Chem.Soc.Jpn.29(1956)465–470.

19. N.G. Bakhshiev.opt.Spetrosk.16(1964) 821-832.

20. A. Kawaski, Acta Phys. Polon. 29 (1966)507–518.

21. A.Chamma,P.Viallet,C.R.Hebd.Seances Acad.Sci.270(1970)1901–1904.

22. Jean-Claude Mialacq and Martine Meyer, "Photophysical properties of the DCM and DFSBO styryl dyes consequence for their laser properties". Laser Chem Volume 10,276-296.

23. P.R.Hammond, Lawrence Livermore laboratory, P.O Box 808, Livermore, CA 9550 USA."Laser Dye DCM, its spectral properties, Synthesis and comparison with other dyes in the Red". Optic communication.

Karnatak University Journal of Science 53 (2022) 54-59

Karnatak University Journal of Science

ISSN: 0075-5168

On nδpδβ-open sets in nano topological spaces

J.B.Torangatti*

Department of Mathematics,Karnatak University's Karnatak Arts College,Dharawad-580001,India

***Corresponding author:** Email:jagadeeshbt2000@gmail.com*

ARTICLE INFO

Article history:
Received: 4 Feb 2022;
Revised: 19 May 2022;
Accepted: 3 July 2022;

Keywords:
nano δ-preopen;
nano δ-preclosed;
nano δβ-open;
nano δβ-open;
nδpδβ-open;
nδpδβ-closed.

ABSTRACT

The aim of this paper is to introduce and investigate a new class of sets called nδpδβ-open sets in nano topological spaces. Several properties and characterizations of nδpδβ-open sets are established.

1. Introduction

A"space" will always mean a topological space. Broadly speaking topology is the study of space and continuity. The concept of continuity plays a very major role in general topology and they are now the research topics of many topologists worldwide. In 2002 [4], Z. Pawlak discussed the applications of rough set theory with an example. Based on this the theory of nano topology [5] proposed by Lellis Thivagar and Richard is an extension of set theory for the study of intelligent systems characterized by insufficient and incomplete information.Further they defined nano-interior and nano-closure to study nano topological spaces. Recently, M. Hosny[1] introduced new notions namely, nano δ-open sets, nano δ-preopen sets, nano δ-semiopen sets, nano δα-open sets and nano δβ-open sets. In this paper, we introduce and study the notion of nano δ-preregular δβ-open sets.

2. Preliminaries

Definition 2.1 [4] The pair $(U,\Re)$ is called the approximation space where U be a non-empty finite set of objects, called the universe, and $\Re$ be an equivalence relation on U named as the indiscernible relation. Let $X \subseteq U$.

(i)The lower approximation of X with respect to $\Re$ is $L_{\Re}(X)= \bigcup_{y\in U} \{\Re(y):\Re(y) \subseteq X\}$

where $\Re(y)$ denotes the equivalence class determined by $y \in U$.

(ii) The upper approximation of X with respect to $\Re$ is $H_{\Re}(X)= \bigcup_{y\in U} \{ \Re(y):\Re(y) \cap X\neq \phi\}$.

(iii)The boundary region of X with respect to $\Re$ is $B_{\Re}(X) = H_{\Re}(X)/L_{\Re}(X)$.

Definition 2.2 [5] In $(U, \Re)$,let $X \subseteq U$. Then $\Im_{\Re}(X)=\aleph^T=\{U,\phi,L_{\Re}(X),H_{\Re}(X),B_{\Re}(X)\}$ forms a topology on U and it is called as the nano topology with respect to X. The pair $(U,\aleph^T)$ is called nano topological space. Elements of $\aleph^T$ are known as thenano open(briefly,n-open) sets and the relative complements of nano open sets are called nano closed(briefly,n-closed) sets.

Definition 2.3 [1, 5] Let $(U,\aleph^T)$ be a NTS and $M_1 \subseteq U$,then $M_1$is said to be:

(i)nano δβ-open if $M_1 \subseteq \aleph cl(\aleph int(\aleph cl_{\delta}(M_1))$,

(ii) nano regular open if $M_1= \aleph int(\aleph cl(M_1))$,

(iii)nano δ-open if $M_1 = \aleph int_{\delta}(M_1)$ where $\aleph int_{\delta}(M_1) = \cup\{B:B$ is a nano regular open and $B \subseteq M_1\}$,

(iv) nano δ-preopen if $M_1 \subseteq \aleph int(\aleph cl_{\delta}(M_1))$,

(v) nano δ-semiopen if $M_1 \subseteq \aleph cl(\aleph int_{\delta}(M_1))$,

(vi)nano δα-open if $M_1 \subseteq \aleph int(\aleph cl(\aleph int_{\delta}(M_1)))$,

(vii)nano e-open if $M_1 \subseteq \aleph cl(\aleph int_{\delta}(M_1)) \cup \aleph int(\aleph cl_{\delta}(M_1))$.

The complements of the above respective open sets are their respective closed sets. The class of nano δ-preopen(resp.,nano δ-semiopen,nano δβ-open,nano δ-open)sets of $(U,\aleph^T)$ is denoted by $\aleph\delta PO(U)$(resp., $\aleph\delta SO(U)$, $\aleph\delta\beta O(U)$ and $\aleph\delta O(U)$) and the class of nano δ-preclosed (resp., nano δ-semiclosed, nano δβ-closed, nano δ-closed) sets of $(U,\aleph^T)$ is denoted by $\aleph\delta PC(U)$ (resp., $\aleph\delta SC(U)$,$\aleph\delta\beta C(U)$ and $\aleph\delta C(U)$).

Definition 2.4 [1, 2, 4] If $(U,\aleph^T)$ is a NTS and $M \subseteq U$, then the nano δ-pre(resp., nano δ-, nano δβ-)interior of M is the union of all $\aleph\delta PO(U)$ (resp.,$\aleph\delta O(U)$ and $\aleph\delta\beta O(U)$) sets contained in M and denoted by $\aleph int_{\delta p}(M)$ (resp.,$\aleph int_{\delta}(M)$ and $\aleph int_{\delta\beta}(M)$) and the nano δ-pre(resp., nano δ-, nano δβ-) closure of M is the intersection of all $\aleph\delta PC(U)$ (resp.,$\aleph\delta C(U)$ and $\aleph\delta\beta C(U)$) sets containing M and denoted by $\aleph cl_{\delta p}(M)$(resp., $\aleph cl_{\delta}(M)$ and $\aleph cl_{\delta\beta}(M)$

3. More properties of nanoδβ-closed sets:

In this section,we give additional results on nano δβ-closed and nano δβ-open sets which would be useful in our later section.

Lemma 3.1 In a NTS $(U,\aleph^T)$,let $M \subseteq U$ be open, then $\aleph cl_{\delta}(M) = \aleph cl(M)$.

Proof: Clearly $\aleph cl(M)) \subseteq \aleph cl_{\delta}(M)$ for any $M \subseteq U$. On the otherhand, let $p \notin \aleph cl(M))$.Then there exists a nano open set H containing p such that $H \cap M = \phi$ which implies there exists a nano open set H containing p such that $\aleph int(\aleph cl(H) \cap M = \phi$. Then $p \notin \aleph cl_{\delta}(M)$.

Theorem 3.2 Let $(U,\aleph^T)$ be a NTS and let $M_1,M_2 \subseteq U$.Then:
(i) $M_1 \cap \aleph cl_\delta(M_2) \subseteq \aleph cl_\delta(M_1 \cap M_2)$ if M_1 is nano regular open.
(ii)$\aleph int_\delta(M_1 \cup M_2) \subseteq M_1 \cup \aleph int_\delta(M_2)$ if M_1 is nano regular closed.
Proof: Let $p \in M_1 \cap \aleph cl_\delta(M_2)$ Then $p \in M_1$ and $p \in \aleph cl_\delta(M_2)$.Let H_1be a nano regular open set containing p, then $H_1 \cap M_1$ is a nano regular open set containing p.
Now, $p \in \aleph cl_\delta(M_2)$
$\rightarrow (H_1 \cap M_1) \cap M_2 \neq \phi$
$\rightarrow H_1 \cap (M_1 \cap M_2) \neq \phi$
$\rightarrow p \in \aleph cl_\delta(M_1 \cap M_2)$.
Hence $M_1 \cap \aleph cl_\delta(M_2) \subseteq \aleph cl_\delta(M_1 \cap M_2)$.
(ii)Similar to (i)
Remark 3.3 In a NTS $(U,\aleph^T)$,let $M \subseteq U$. Then $\aleph cl(\aleph int_\delta(M))$ is nano regular open.
Theorem 3.4 Let M be a subset of a NTS $(U,\aleph^T)$, then
(i) $\aleph cl_{\delta\beta}(M) = M \cup \aleph int(\aleph cl(\aleph int_\delta(M)))$.
(ii) $\aleph int_{\delta\beta}(M) = M \cap \aleph cl(\aleph int(\aleph cl_\delta(M)))$.
Proof: Since$\aleph cl_{\delta\beta}(M)$ is nano δβ-closed, then
$\aleph int(\aleph cl(\aleph int_\delta(M)) \subseteq \aleph int(\aleph cl(\aleph int_\delta(\aleph cl_{\delta\beta}(M)))$
$\subseteq \aleph cl_{\delta\beta}(M)$.
On the other hand we have
$\aleph int(\aleph cl(\aleph int_\delta(M \cup \aleph int(\aleph cl(\aleph int_\delta(M)))$
$\subseteq \aleph int(\aleph cl(\aleph int_\delta(M \cup \aleph cl(\aleph int_\delta(M))))$
$\subseteq \aleph int(\aleph cl(\aleph int_\delta(M) \cup \aleph cl(\aleph int_\delta(M))$
$= \aleph int(\aleph cl(\aleph int_\delta(M) \cup \aleph cl(\aleph int_\delta(M))$
$= \aleph int(\aleph cl(\aleph int_\delta(M)$
$\subseteq M \cup Nint(Ncl(Nint_\delta(M))$.
Therefore, $M \cup \aleph int(\aleph cl(\aleph int_\delta(M)$ is a nano δβ-closed set containing M, it follows that $\aleph cl_{\delta\beta}(M) \subseteq M \cup \aleph int(\aleph cl(\aleph int_\delta(M)$.Then
$\aleph cl_{\delta\beta}(M) = M \cup \aleph int(\aleph cl(\aleph int_\delta(M)))$.
(ii) It follows from (i).
Theorem 3.5 [2] Let M be a subset in $(U,\aleph^T)$, then:
(i) $\aleph cl_{\delta p}(M) = M \cup \aleph cl(\aleph int_\delta(M))$.
(ii) $\aleph int_{\delta p}(M) = M \cap \aleph int(\aleph cl_\delta(M))$.
Theorem 3.6 Let M be a subset in $(U,\aleph^T)$, then:$\aleph int(\aleph cl(\aleph int_\delta(M)) = \aleph cl_{\delta\beta}(\aleph int_\delta(M)) = \aleph int_\delta(\aleph cl_{\delta\beta}(M))$.
Theorem 3.7 Let M be a subset in $(U,\aleph^T)$,then:
(i) $\aleph int_{\delta p}(\aleph cl_{\delta\beta}(M)) = \aleph cl_{\delta\beta}(M) \cap \aleph int(\aleph cl_\delta(M))$.
(ii) $\aleph int_{\delta p}(\aleph cl_{\delta\beta}(M)) = \aleph int_{\delta p}(M) \cup \aleph int(\aleph cl(\aleph int_\delta(M))$.
(iii) $\aleph int_{\delta p}(\aleph cl_{\delta\beta}(M)) = \aleph int_{\delta p}(M) \cup \aleph cl_{\delta\beta}(\aleph int_\delta(M))$
(iv) $\aleph int_{\delta p}(\aleph cl_{\delta\beta}(M)) = \aleph int_{\delta p}(M) \cup \aleph int_\delta(\aleph cl_{\delta\beta}(M))$.
(v) $\aleph int_{\delta p}(\aleph cl_{\delta\beta}(M)) = (M \cap \aleph int(\aleph cl_\delta(M)) \cup \aleph int(\aleph cl(\aleph int_\delta(M))$.

4 nanoδ-preregularδβ-open:

Definition 4.1 Let $(U,\aleph^T)$ be a NTS.Then a set $H \subseteq U$ is said to be:
(1) nano δ-preregular δβ-open(briefly,nδpδβ-open) if $H = \aleph int_{\delta p}(\aleph cl_{\delta\beta}(H))$,
(2) nano δ-preregular δβ-closed(briefly,nδpδβ-closed) if $H = \aleph cl_{\delta p}(\aleph int_{\delta\beta}(H))$.
The class of nδpδβ-open (resp.,nδpδβ-closed) sets of $(U,\aleph^T)$ will be denoted by $\aleph\delta P\delta\beta O(U)$ (resp.,$\aleph\delta P\delta\beta C(U)$).
Theorem 4.2 Let K and L be any subsets in $(U,\aleph^T)$. If $K \subseteq L$,then
$\aleph int_{\delta p}(\aleph cl_{\delta\beta}(K) \subseteq \aleph int_{\delta p}(\aleph cl_{\delta\beta}(L)$..
Proof: Obvious.
Theorem 4.3 In a NTS $(U,\aleph^T)$,let $K,L \subseteq U$. Then:
(i) If $K \in N\delta PO(U)$, then $K \subseteq \aleph int_{\delta p}(\aleph cl_{\delta\beta}(K)$.
(ii) If $K \in N\delta\beta C(U)$, then $\aleph cl_{\delta\beta}\aleph int_{\delta p}(K)) \subseteq K$.
Proof: (i) Let $M \in \delta PO(U)$, then
$M \subseteq \aleph int_{\delta p}(\aleph cl_{\delta\beta}(M)$ as $M \subseteq \aleph cl_{\delta\beta}(M)$.
(ii) Let $M \in \delta\beta C(U)$. Since $\aleph int_{\delta p}(M) \subseteq M$, then $\aleph cl_{\delta\beta}(\aleph int_{\delta p}(M)) \subseteq M$.
Theorem 4.4 In a NTS $(U,\aleph^T)$, let $K \subseteq U$. Then:(i) $\aleph int_{\delta p}(\aleph cl_{\delta\beta}(K))$ is nδpδβ-open.
(ii) If $K \in N\delta\beta C(U)$, then $\aleph int_{\delta p}(K)$ is nδpδβ-open.
Proof:(i) We have $\aleph int_{\delta p}(\aleph cl_{\delta\beta}(\aleph int_{\delta p}(\aleph cl_{\delta\beta}(K))$
$\subseteq \aleph int_{\delta p}(\aleph cl_{\delta\beta}(\aleph cl_{\delta\beta}(K))$
$= \aleph int_{\delta p}(\aleph cl_{\delta\beta}(K))$ and
$\aleph int_{\delta p}(\aleph cl_{\delta\beta}(\aleph int_{\delta p}(\aleph cl_{\delta\beta}(K)))$
$\supseteq \aleph int_{\delta p}(\aleph int_{\delta p}(\aleph cl_{\delta\beta}(K))$
$= \aleph int_{\delta p}(\aleph cl_{\delta\beta}(K))$.
Hence,
$\aleph int_{\delta p}(\aleph cl_{\delta\beta}(\aleph int_{\delta p}(\aleph cl_{\delta\beta}(K))) = \aleph int_{\delta p}(\aleph cl_{\delta\beta}(K))$.
(ii) Suppose that $K \in \delta\beta C(U)$. By (i), we have
$\aleph int_{\delta p}(\aleph cl_{\delta\beta}(\aleph int_{\delta p}(K)) \subseteq \aleph int_{\delta p}(\aleph cl_{\delta\beta}(K)$
$= \aleph int_{\delta p}(K)$.
On the other hand, we have
$\aleph int_{\delta p}(K) \subseteq \aleph cl_{\delta\beta}(\aleph int_{\delta p}(K)$ so that

$\aleph int_{\delta p}(K) \subseteq \aleph int_{\delta p}(\aleph cl_{\delta\beta}(\aleph int_{\delta p}(K))$.Therefore $\aleph int_{\delta p}(\aleph cl_{\delta\beta}(\aleph int_{\delta p}(K)) = \aleph int_{\delta p}(K)$.

This shows that $\aleph int_{\delta p}(K)$ is nδpδβ-open.

Theorem 4.5 In a NTS $(U,\aleph^T)$,every nδpδβ-open set is,(i) nδp-open, (ii) ne-open,

(iii) nδβ-open and (iv) nδβ-closed.

Proof: (i)By Theorem 3.7,

$\aleph int_{\delta p}(\aleph cl_{\delta\beta}(M)) = \aleph cl_{\delta\beta}(M) \cap \aleph int(\aleph cl_{\delta}(M)$

$\subseteq \aleph int(\aleph cl_{\delta}(M)$.

Then $M \subseteq \aleph int(\aleph cl_{\delta}(M)$,M is nδp-open.

(ii) and (iii): Obvious

(iv) Let M be nδpδβ-open. By Theorem 3.7(ii), $M = \aleph int_{\delta p}(M) \cup \aleph int(\aleph cl(\aleph int_{\delta}(M)))$.

Therefore, $\aleph int(\aleph cl(\aleph int_{\delta}(M))) \subseteq M$. Thus M is nδβ-closed.

Remark 4.6 By the following example,we show that every nδp-open(resp,nδβ-closed) set need not be a nδpδβ-open set.

Example 4.7 Let U = {p,q,r,s} with U/R= {{p},{r},{q,s}} and let X = {p,q}, $\aleph^T$ = {U, ϕ, {p},{p,q,s},{q,s}}. Then {p,q,r} is nano δ-preopen but it is not nδpδβ-open and {s} is nano δβ-closed but it is not nδpδβ-open.

Corollary 4.8 For a NTS $(U,\aleph^T)$, we have

$\aleph\delta PO(U) \cap \aleph\delta PC(U) \subseteq \aleph\delta P\delta\beta O(U)$

$\subseteq \aleph\delta\beta O(U) \cap \aleph\delta\beta C(U)$.

Proof: Obvious.

The converse inclusions in the above Corollary need not be true as seen from the following example:

Example 4.9 Let $(U,\aleph^T)$ as in Example 4.7, then {q} is nδpδβ-open but it is not both nano δ-preopen and nano δ-preclosed. Moreover, {p,s} is both nano δβ-open and nano δβ-closed but not a nδpδβ-open set.

Definition 4.10 [6] A subset M of a NTS (U,N^T) is called nano η-set if

$Nint(Ncl_{\delta}(M)) \subseteq Ncl(Nint_{\delta}(M))$.

Theorem 4.11 [6] (i) Every nδs-open set is nano η-set.

(ii)Every nδs-closed set is nano η-set.

Remark 4.12 The notions of nδpδβ-open sets and nδ-open sets (hence nα-open sets, nδs-open sets, nano η-sets) are independent of each other.

Example 4.13 Consider $(U,\aleph^T)$ as in Example 4.7.The set {p} is nδpδβ-open but it is not nano η -set. Moreover, {p,q,r} is nano δ-open but not nδpδβ-open.

Theorem 4.10 A subset K in $(U,\aleph^T)$ is nδpδβ-open if and only if K is nδβ-closed and nδp-open.

Proof: Let K be nδpδβ-open, then by Theorem 4.5[(i)and (iv)] ,K is nδβ-closed and nδp-open. Converse is obvious.

Remark 4.11 The class of nδpδβ-open sets is not closed under finite union as well as finite intersection. It will be shown in the following example.

Example 4.12 Consider $(U,\aleph^T)$ as in Example 4.7. Let A = {p,r} and B= {q,r},then A and B are nδpδβ-open sets but

$A \cup B = \{p,q,r\} \notin N\delta P\delta\beta O(U)$.

Moreover,C = {p,q,s} and D = {q,r,s} are nδpδβ-open sets but

$C \cap D = \{q,s\} \notin N\delta P\delta\beta O(U)$.

Theorem 4.13 For a subset M in $(U,\aleph^T)$,the following are equivalent:

(a) M is nδpδβ-open.

(i) $M = \aleph cl_{\delta\beta}(M) \cap \aleph int(\aleph cl_{\delta}(M))$.

(ii) $M = \aleph int_{\delta p}(M) \cup \aleph int(\aleph cl(\aleph int_{\delta}(M))$.

(iii)$M = \aleph int_{\delta p}(M) \cup \aleph cl_{\delta\beta}(\aleph int_{\delta}(M))$

(iv) $M = \aleph int_{\delta p}(M) \cup \aleph int\delta(\aleph cl_{\delta\beta}(M))$.

(v)$M = (M \cap \aleph int(\aleph cl_{\delta}(M)) \cup \aleph int(cl(\aleph int_{\delta\beta}(M))$

Proof: It follows from Theorem 3.7

Definition 4.14 A NTS $(U,\aleph^T)$ is called a nano δ-door space if every subset of U is nano δ-open or nano δ-closed.

Theorem 4.15 If $(U,\aleph^T)$ is a nano δ-door space, then every nano δ-preopen subset in $(U,\aleph^T)$ is nano δ-open.

Lemma 4.16 If $(U,\aleph^T)$ is nano δ-door space, then any finite intersection of nδp-open sets is nδp-open.

Proof: Obvious

Theorem 4.17 If $(U,\aleph^T)$ is nano δ-door space, then any finite intersection of nδpδβ-open sets is nδpδβ-open.

Proof: Let $\{D_i : i=1,2,...,n\}$ be a finite family of nδpδβ-open sets. Since the space $(U,\aleph^T)$ is nano δ-door, then by Lemma 4.16,we have

$\bigcap_{i=1}^{n} D_i \in \delta PO(U)$. By Theorem 4.3(i),

$\bigcap_{i=1}^{n} D_i \subseteq \aleph int_{\delta p}(\aleph cl_{\delta\beta}(\bigcap_{i=1}^{n} D_i)$.

For each i, we have $\bigcap_{i=1}^{n} D_i \subseteq Di$ and thus

$\aleph int_{\delta p}(\aleph cl_{\delta\beta}(\bigcap_{i=1}^{n} D_i) \subseteq \aleph int_{\delta p}(\aleph cl_{\delta\beta}(Di) = Di.$

Therefore, $\aleph int_{\delta p}(\aleph cl_{\delta\beta}(\bigcap_{i=1}^{n} D_i) = \bigcap_{i=1}^{n} D_i$

Lemma 4.18 [6] If a subset M of a NTS $(U,\aleph^T)$ is nr-open ,then
$M = \aleph int(\aleph cl(M) = \aleph int(\aleph cl_\delta(M))$.

Theorem 4.19 Every nr-open set is nδpδβ-open.

Proof: Let M be nr-open. Then
$M = \aleph int(\aleph cl(M)) = \aleph int(\aleph cl\delta(M))$.
By Theorem 3.7,
$\aleph int_{\delta p}(\aleph cl_{\delta\beta}(M)) = \aleph cl_{\delta\beta}(M) \cap \aleph int(\aleph cl_\delta(M))$
$= \aleph cl_{\delta\beta}(M) \cap M$
$= M.$
This shows that M is nδpδβ-open.

Definition 4.20 A subset M in $(U,\aleph^T)$ is called,

(1) nanob*-open if
$M = \aleph cl(\aleph int_\delta(M)) \cup \aleph int(\aleph cl_\delta(M))$.

(2) nanob*-closed if
$M = \aleph cl(\aleph int_\delta(M)) \cap \aleph int(\aleph cl_\delta(M))$.

Theorem 4.21A subset M in $(U,\aleph^T)$ is nr-open if and only if it is nano b*-closed.

Proof: Let M be nr-open. Then by Lemma 4.18, $M = \aleph int(\aleph cl(M) = \aleph int(\aleph cl_\delta(M))$.
Since every nr-open set is nδ-open, we have
$\aleph cl(\aleph int_\delta(M)) \cap \aleph int(\aleph cl_\delta(M)) = \aleph cl(M) \cap M$
$= M.$
Hence, M is nano b*-closed.
Conversely, let M be nanob*-closed.Then
$\aleph int(\aleph cl(\aleph int_\delta(M)) \subseteq \aleph int(\aleph cl_\delta(\aleph int_\delta(M))$
$\subseteq \aleph cl(\aleph int_\delta(M)) \cap \aleph int(\aleph cl_\delta(M))$
$= M.$
Also, we have
$M \subseteq \aleph int(\aleph cl_\delta(M))$
$\subseteq \aleph int(\aleph cl_\delta(\aleph cl(\aleph int_\delta(M)))$
$= \aleph int(\aleph cl(\aleph cl(\aleph int_\delta(M)))$
$= \aleph int(\aleph cl(\aleph int_\delta(M)))$.
Therefore, $M = \aleph int(\aleph cl(\aleph int_\delta(M))$.
Now,
$\aleph int(\aleph cl(M)) = \aleph int(\aleph cl(\aleph int(\aleph cl(\aleph int_\delta(M)))$
$= \aleph int(\aleph cl(\aleph int_\delta(M))$
$= M.$
Hence, M is nr-open.

Theorem 4.22 In a NTS $(U,\aleph^T)$,every nano b*-closed set is,
(i) nδ-open,(ii) nδs-open,(iii) nδpδβ-open.

Proof: (i) and (ii) are obvious
(iii)Let M be nano b∗-closed, then
$M = \aleph int(\aleph cl(\aleph int_\delta(M))$.
By Theorem 3.7(ii),
$\aleph int_{\delta p}(\aleph cl_{\delta\beta}(M))$
$= \aleph int_{\delta p}(M) \cup \aleph int(\aleph cl(\aleph int_\delta(M))$
$= \aleph int_{\delta p}(M) \cup M$
$= M.$
Therefore, M is nδpδβ-open

Remark 4.23 The above discussions can be summarized in the following diagram:

DIAGRAM

nr-open → nδ-open → nδα-open → nδs-open → nanoη-set
↕ ↓ ↓
nb*-closed → nδpδβ-open → nδp-open → ne-open → nδβ-open

Theorem 4.24 For a subset M in $(U,\aleph^T)$, the following are equivalent:
(i) M is nr-open;
(ii) M is nδpδβ-open and nδ-open;.
(iii) M is nδpδβ-open and nδα-open;
(iv) M is nδpδβ-open and nδs-open;
(v) M is nδpδβ-open and nano η-set;
(vi) M is nδpδβ-open and nδs-closed;
(vii) M is nanoδβ-closed and nδα-open;
(viii) M is nanob*-closed.

Acknowledgment

The author is grateful to Karnatak University Dharwad for the financial support to this research work under University Research Seed Grant Policy (grant no.: KU/PMEB/2021-22/182/723 Dated:12-11-2021).

References

[1]M.Hosny, Nano δβ-open sets and nano δβ-continuity, Journal of the Egyptian Mathematical Society, 26(2), 365-375, 2018).

[2] A.Padma, M.Saraswathi, A.Vadivel and G. Saravanakumar, New notions of nano M-open sets, Malaya Journal of Matematik,1, 656-660, (2019).

[3]S.Parimala,J.Sathiyaraj and V.Chandrasekar Nano δ-open sets and their notions, Malaya Journal of Matematik, 1, 664-672, (2019),.

[4] Z.Pawlak, Rough sets, International Journal of Computer and Information Science, 11(5), 341–356, (1982).

[5] M.L.Thivagar and C.Riclord, On nano forms of weakly open sets, International Journal of Mathematics and Statistics Invention, 1(1), 31-37, (2013).

[6]J.B.Toranagatti, On rnδp-open sets, Advances in Mathematics: Scientific Journal , 10(2), 1013–1023, (2021).

Karnatak University Journal of Science 53 (2022) 60-68

Karnatak University Journal of Science

ISSN: 0075-5168

Solvatochromic Study of Organic Dyes: an Approach using Semiempirical (ZINDO-IEFPCM) Method

Manjunath N. Wari[1]*, Vikram Pujari[1], Shrikrupa K. Chavan[1] and James. R. Mannekutla[2]

[1]*Laser Spectroscopy Programme, Department of Physics, Karnatak University, Dharwad 580003, India*

[2]*A.B.B. Corporate Research, Forskargrand 7, 72178, Vasteras, Sweden.*

***Corresponding author:** sm5wari@gmail.com*

ARTICLE INFO

Article history:
Received: 11 April 2022;
Revised: 27 May 2022;
Accepted: 3 July 2022

Keywords:
solvatochromism;
polarity switch;
ZINDO/PCM;
polarity scale $E_T(30)$

ABSTRACT

The present investigation accounts for computationally determining the solvatochromic behavior of Coumarin dyes (C478, C519, C523, C307 and C522B) in series of alcohols. Experimentally observed positive and negative solvatochromism are accounted and their behavior is well explained by computational results. The semi empirical $E_T(30)$ scale has been adopted to define the polarity dependent solvent-solute interaction. The ZINDO/PCM method follows the observed experimental trends for all the Coumarin dyes. Small discrepancies with experimental values are discussed in detail. Computational results suggest that ZINDO/PCM values lie in closer proximity to the experimental values depending on the polarity of Coumarin molecules. Switching between positive and negative solvatochromism in polarity scale referred as polarity switch is discussed. Further the study is extended to test the ZINDO/PCM applicability in case of 1-naphthol (N1) and 2-naphthol (N2) in different solvents and a reasonably good agreement has been found with experimental results.

1 Introduction

The information about electronic distribution of molecules in the ground and excited states can be obtained by the studies of solvatochromic effect on the absorption and fluorescence spectra of laser dyes. The predominant role of solute-solvent interaction on positive and negative solvatochromism, referred to as bathochromic and hypsochromic shift respectively, generally depends on their relative polarity, linear response to their electrostatic interaction, non-electrostatic interaction and hydrogen bonding strength, etc. The solute molecule finds itself in a cavity inside the solvent, resulting in a net stabilization of their ground state. Concept of modelling the cavity is different from spherical Onsager cavity to molecularly shaped cavities by various versions of polarizable continuum model (PCM) [1]. These approaches differ mainly because the continuum models are required to introduce specific boundary between the solute and continuum solvent which defines the molecular cavity. The definition about shape and dimension of cavity varies with various continuum models and the advanced continuum methods model cavity depending on the real geometry. If the dipole moment of solute increases through electronic transition, the excited state is formed inside the solvent cavity which is surrounded partly by oriented solvent dipoles. The net stabilization of the excited state as compared to the ground state with increasing solvent polarity results in bathochromic shift. Here the excited state is more dipolar than ground state ($\mu_g < \mu_e$). If there is a decrease in dipole moment of solute during the electronic transition, the excited state is formed in a strained solvent cavity of oriented dipoles not correctly disposed for its efficient stabilization. The energy of the ground state lowered more than that of the excited state with increasing solvent polarity results in a hypsochromic shift and in this case ground state is more dipolar than excited state ($\mu_g > \mu_e$). According to the valence-band theory, the extent and direction of sovatochromism depends on whether the zwitterionic mesomeric structure is more important in the ground state or in the excited state [2]. The solvent effect on absorption spectra is understood computationally by assuming the electronic states of the isolated and solvated molecule and treating this effect only as a physical perturbation of the relevant molecular states.

Solvation capability defining the solvating power of dissolved apolar or dipolar, charged or neutral, species is commonly related to the solvent polarity function. The solvation power accounts overall possible actions of specific and non-specific, intermolecular interactions between solute and solvent molecules. The typical question of accuracy in defining the solvent polarity on single solvent properties such as relative permittivity, dipole moment or refractive index remains in debate. The qualitative concept of grasping solvent polarity seems to be easy, but it is difficult to define precisely and even more difficult to express quantitatively. Besides, many attempts to express it quantitatively by single macroscopic solvent properties are found to be inadequate. The empirical parameter has been introduced to provide a scale for polarity of solvents on highly selected solvent-sensitive reference process. Some particular approach of them like equilibrium, reaction rate and spectral absorption are assumed as suitable for large class of other solvent dependent process. Among many such ideas the most popular polarity scale $E_T(30)$ proposed by Dimorth and Reichardt [2] is most commonly used. Here the solvent polarity scale was built on the basis of transition energy for the longest wavelength solvatochromic absorption band of the pyridinium N-phenolate betaine dye. The present study aims to understand the solvatochromism of Coumarin dyes on this polarity scale by comparing experimental results with computed values. The Zerner's Intermediate Neglect of Differential Overlap (ZINDO) is a semiempirical method used to compute absorption maxima of molecules. The

Polarizable Continuum Model (PCM) [3,4] using the integral equation formalism variant (IEFPCM) [5,6], which describes the solvent as structureless, continuum medium defined by dielectric constant to account the bulk solvent effect is previously coupled with *ab initio* and ZINDO methods. ZINDO approach was successfully adopted with PCM for the first time by Caricato et al. [7] for qualitative explanation of absorption maxima proved as less computational cost, than simulating absorption of molecule in different solvents with time dependent Hartree-Fock (TDHF) and time dependent density functional theory (TDDFT) methods. Three coumarin molecules (Coumarin 102, Coumarin 522, Coumarin 153) were selected by authors to test the validation of ZINDO/PCM over the *ab initio* calculations. This study reported close agreement between experimental and computed (ZINDO/PCM) transition energies. The underway of constant effort in best reproducing observed transition energy by computationally was also made previously [8], as a good theoretical representation may help us in understating the solute and solvent interactions in better. Some studies also have suggested placing few solvent molecules nearby the solute to account the specific interactions under combined continuum/discrete approaches [9-14]. Caricato et al. [12] calculated the absorption energy of Betaine 30 molecule in vacuum and water medium with one explicit water molecule nearby and no such good agreement has been found with experimental results. The continuum models neglect of microscopic nature of the solvent and describe the bulk solvent effect by considering the solvent as structureless medium. Further with these characters the validity of PCM is tested as how best the experimental results can be predicted by considering the Betaine 30 molecule in apolar, aprotic polar and protic polar solvents [12]. In another study by Caricato et al.,[15] ZINDO/PCM method has been applied to predict the radiative and nonradiative decay rates of molecule close to metal nanoparticles. Coumarin dyes were selected for present study because they undergo very little nuclear reorganization and are solvatochromic owing to the change in electronic distribution resulting in an increase of dipole moments from the ground to excited state [16, 17]. The large change in dipole moments of a molecule in the ground state and excited state is observed due to the fact that Coumarins are influenced by their immediate environment as energy in the lowest singlet excited state relative to the ground state is quite sensitive regardless of various substituent effects [18, 19]. Here in this chapter we discuss applications of the ZINDO/PCM approach to a series of Coumarin molecules to estimate the transition energies from the ground state to the first singlet excited state. The comparison is also made between the transition energy obtained by experimentally and semiempirically for all the molecules in series of alcohols. With a view to investigate how ZINDO/PCM can predict the excitation molecules other than Coumarins we have chosen 1-naphthol (N1) and 2-naphthol (N2) in different solvents and the results obtained are discussed in detail.

2 Theory of ZINDO/PCM

The previous theoretical simulation work has been done on absorption of molecule in different solvents with time dependent Hartree-Fock (TDHF) and time dependent density functional theory (TDDFT) methods. Besides these, fast computational ZINDO approach is adopted successfully with quantum mechanical treatment of solvents (PCM versions) for qualitative explanation of absorption maxima. Here the electronic spectra are interpreted by the Tamm-Dancoff approximation (TDA), with reference state as defined by Hartree-Fock. The detailed discussion and development of ZINDO and ZINDO/PCM theories are represented in refs. 7 and 12. We present in short the ZINDO/PCM theory with the idea to provide basic bench for further discussion. Actually, the PCM method represents solvent as a homogeneous continuum medium polarizable

by the solute placed in a molecularly shaped cavity built in the bulk of the dielectric. It is now convenient to speak of solute-solvent interaction in terms of the solvent reaction potential $\hat{V}_{\text{int}}$. This potential term introduced as a perturbation to Hamiltonian of the isolated molecule, $H^0 : H_{eff}\psi = [H^0 + V_{\text{int}}]\psi = E\psi$. The definition of potential is different as it depends on the method employed to set the electrostatic problem, which has to be solved within the framework of the QM equation $H_{eff}|\psi\rangle = E|\psi\rangle$. Generally, V_{int} is assumed as a summation of dispersion, repulsion and electrostatic forces between solute and solvent molecules. The IEFPCM assumes the solvent effect by the apparent surface charges on the cavity. These charges can be computed by matrix elements formed by linear equations which are related to dielectric constants and to the geometry of the boundaries.

3 Computational Details

The geometries of these molecules were first optimized in vacuum with semi-emphirical AM1 method and solvent effect is introduced by combining AM1/PCM, the molecules optimized in ground state in all alcohols. Subsequent geometries were assumed as initial guess for excited state calculation according to ZINDO/PCM in respective solvents using Gaussian 09 software package [20].

4 Results and Discussion

The solvent shifts can be accounted in terms of the overall effect of the interaction forces (which are mainly of van der Waals type) on the electron system of the molecule. A change of solvent is accompanied by a change in polarity, dielectric constant and change in polarizability of the surrounding medium, thus number of solvents have been selected to study the solvatochromism. The experimentally observed absorption maxima $\lambda_{\max}(nm)$ is transformed into intermolecular charge transfer transition energy in eV by using equation, $E_T(dye) = 28591.5/\lambda_{\max}(nm)$. The experimental absorption maxima data (methanol-decanol) of C478, C519, C523, C307 and C522B have been taken from refs. 16 & 17. The fundamental aspect for comparing and evaluating both the theoretical and experimental results is to provide the physical insight on solute-solvent interaction. Consider Fig. 5.1 wherein $E_T(dye)$ is plotted vs $E_T(30)$ polarity functions for C478. This plot shows qualitative agreement between the transition energy predicted by ZINDO/PCM for $S_0 \rightarrow S_1$, is in good agreement with the experimental values making it reliable calculation for excited state energies. The experimentally observed positive and negative solvatochromism trend is exactly followed by theoretically predicted values (Table 1). Oscillating behaviour from positive to negative solvatochromism in polarity scale at particular stage, usually referred to as polarity switch, is observed. In case of C519 (Fig. 5.1), the computed values are very close to the experiment in most of the solvents. Comparing the results of C478 and C519 it clears the idea that excited energies of highly polar molecules are well characterized by ZINDO/PCM calculations. The resonance contributors which define the electron mobility in the aromatic ring are more in C519 than C478, makes it more polar in nature [17]. Small discrepancies exist in some of the solvents is attributed to discarding the hydrogen bonding at specific sites of solute because solvent structure is missing in PCM formulation. Fig. 5.1 shows plots for C523 and C307, where behaviour of experimental results is followed by theoretical values. More polar nature of C523 than C307 enables ZINDO/PCM calculation to be in close proximity to the experimental results. The C522B (Fig. 5.1) shows interesting behaviour where the experimental results show only positive solvatochromism but ZINDO/PCM calculation predicts a negative solvatochromism also. Further detailed study necessitates explaining this result by considering the non electrostatic behaviour of solvents. The theoretical calculation has two

advantages: first, it provides effect of solvatochromism on solvated molecules and its behaviour on a polarity scale with less computational cost. The computational calculation thus estimates the properties of molecule in the solvent environment. Another advantage is that it helps to evaluate the energy distribution of molecule in ground and excited state in particular solvents. These results can be combined to see the change of energy in both states in subsequent solvents. Here looking more closely at the problem when there is change in solvent from pentanol to hexanol the positive solvatochromism switches to negative. Dipole moment which is form of energy is calculated for ground and excited state in all the individual solvents. The difference in dipole moments from ground to excited state remains almost unaltered (Fig. 5.2). The observation of subsequent difference in ground state and also the case of excited state dipole moments in solvents studied suffers abrupt change in value as crossing from pentanol to hexanol. This is the particular solvent where the negative solvatochromism starts and this change in polarity scale is referred as polarity switch [21].

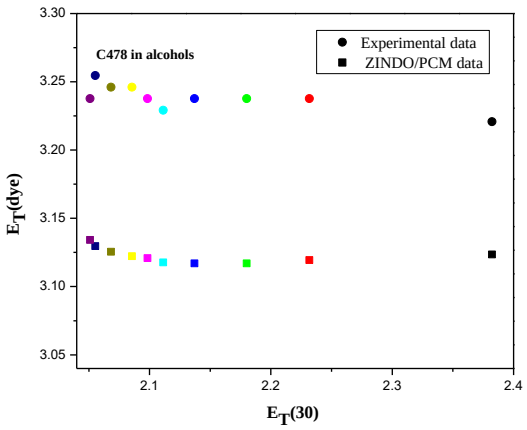

(a)

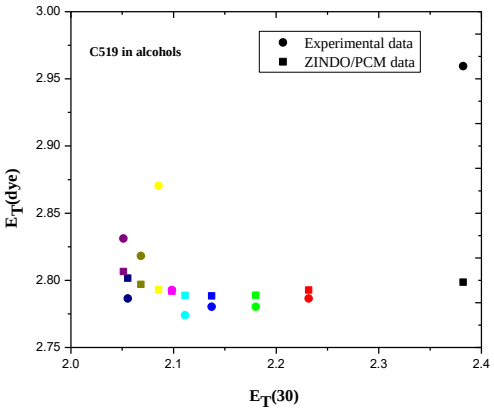

(b)

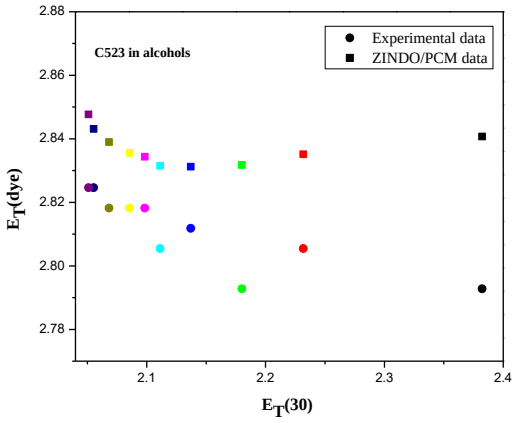

(c)

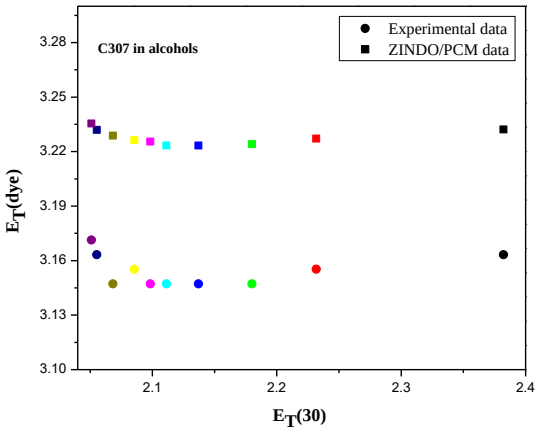

(d)

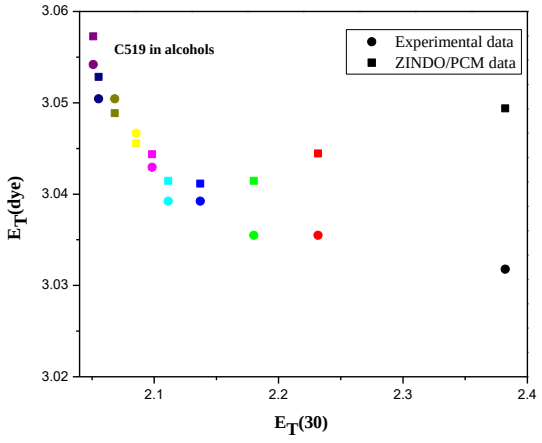

(e)

Fig. 5.1 Comparison of experimental transition energies of (a) C478 and (b) C519 (c) C523 (b) C307 and (e) C522B, with calculated ZINDO-PCM on $E_T(30)$ scale in alcohols (methanol-decanol).

The question also arises as to where the ZINDO/PCM theory can be extended to study any kind of molecules apart from well known Coumarins. This study also continues to investigate solvatochromism of 1-naphthol (N1) and 2-naphthol (N2) by ZINDO/PCM method. The experimental absorption energies of N1 and N2 in various non polar, polar aprotic and polar protic solvents were taken from the ref. 22. The comparative plot against transition energies calculated by ZINDO/PCM are shown in Fig. 5.3 and listed in Table 2. Here the ZINDO/PCM results, despite some discrepancy, followed the experimental trend in transition energies on polarity scale. In case of N1 the computed values tend to attain towards experimental results more rigorously than N2 for all solvents and particularly in nonpolar solvents. Both N1 and N2 have same formula $C_{10}H_7OH$ but differ in the location of the hydroxyl group on naphthalene ring. This is quite interesting as a change in the transition energy is observed experimentally with change in location of hydroxyl group and ZINDO/PCM calculations found in lacking to attain the same. Plausible reasons may be due to the measured experimental values of $E_T(30)$ are not strictly related to the polarity of the solvent or may be attributed to the peculiarities of the solute-solvent interactions that PCM cannot reproduce [15].

Table 1:- Comparison of experimental and computed electronic transition energies (in eV).

Solvent	C478		C519		C523		C307		C522B	
	E_{Exp} (eV)	E_{Theo} (eV)	E_{Exp} (eV)	E_{Theo}(eV)	E_{Exp} (eV)	E_{Theo}(eV)	E_{Exp} (eV)	E_{Theo} (eV)	E_{Exp} (eV)	E_{Theo} (eV)
Methanol	3.220779	3.123504	2.959427	2.798655	2.792793	2.840714	3.163265	3.232197	3.031785	3.049380
Ethanol	3.237598	3.119340	2.786517	2.792730	2.805430	2.835128	3.155216	3.227150	3.035496	3.044439
Propanol	3.237598	3.116988	2.780269	2.788961	2.792793	2.831761	3.147208	3.224045	3.035496	3.041452
Butanol	3.237598	3.116988	2.780269	2.788334	2.811791	2.831244	3.147208	3.223375	3.039216	3.041154
Pentanol	3.229167	3.117615	2.774049	2.788710	2.805430	2.831503	3.147208	3.223375	3.039216	3.041452
Hexanol	3.237598	3.120832	2.792793	2.791975	2.818182	2.834350	3.147208	3.225555	3.042945	3.044364
Heptanol	3.246073	3.122167	2.870370	2.793296	2.818182	2.835517	3.155216	3.226310	3.046683	3.045561
Octanol	3.246073	3.125551	2.818182	2.797014	2.818182	2.838958	3.147208	3.228830	3.050431	3.048855
Nonanol	3.254593	3.129653	2.786517	2.801563	2.824601	2.843124	3.163265	3.231944	3.050431	3.052834
Decanol	3.237598	3.134083	2.831050	2.806573	2.824601	2.847694	3.171355	3.235402	3.054187	3.057275

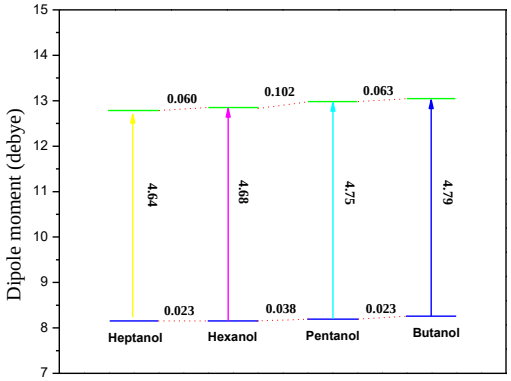

Fig. 5.2 Schematic diagram for the polarity switch in case of C522B.

The question also arises as to where the ZINDO/PCM theory can be extended to study any kind of molecules apart from well known Coumarins. This study also continues to investigate solvatochromism of 1-naphthol (N1) and 2-naphthol (N2) by ZINDO/PCM method. The experimental absorption energies of N1 and N2 in various non polar, polar aprotic and polar protic solvents were taken from the ref. 22. The comparative plot against transition energies calculated by ZINDO/PCM are shown in Fig. 5.3 and listed in Table 2. Here the ZINDO/PCM results, despite some discrepancy, followed the experimental trend in transition energies on polarity scale. In case of N1 the computed values tend to attain towards experimental results more rigorously than N2 for all solvents and particularly in nonpolar solvents. Both N1 and N2 have same formula $C_{10}H_7OH$ but differ in the location of the hydroxyl group on naphthalene ring.

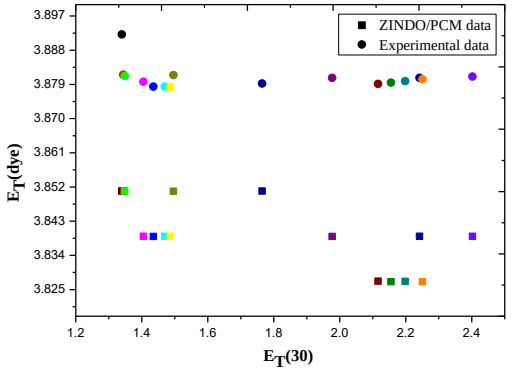

(a)

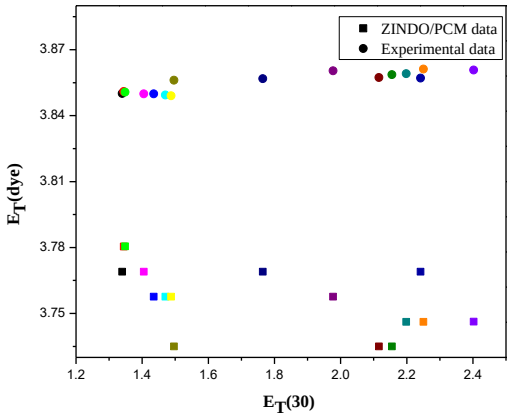

(b)

Fig. 5.3 Comparison of experimental transition energies of (a) 1-naphthol (N1) and (b) 2-naphthol (N2) with calculated ZINDO-PCM on $E_T(30)$ scale.

Plausible reasons may be due to the measured experimental values of $E_T(30)$ are not strictly related to the polarity of the solvent or may be attributed to the peculiarities of the solute-solvent interactions that PCM cannot reproduce [15].

Solvent	1-naphthol (N1)		2-naphthol (N2)	
	E_{Exp} (eV)	E_{Theory} (eV)	E_{Exp} (eV)	E_{Theory} (eV)
Cyclohexane	3.850944	3.892150	3.768980	3.850095
n-hexane	3.850944	3.881550	3.780388	3.850932
Heptane	3.850944	3.881186	3.780512	3.850693
Xylene	3.838978	3.878394	3.757572	3.849856
Toluene	3.839040	3.878394	3.757572	3.849378
Carbon tetra chloride	3.839040	3.879728	3.768980	3.849856

Benzene	3.839040	3.878272	3.757572	3.849019
Diethyl ether	3.850882	3.881429	3.734942	3.856081
Dichloromethane	3.850944	3.879243	3.768980	3.856801
Acetonitrile	3.838978	3.880700	3.757572	3.860403
Heptanol	3.827198	3.879122	3.735004	3.857281
n-Butanol	3.827074	3.879486	3.734942	3.858601
Propanol	3.827136	3.879850	3.746164	3.859081
Acetic acid	3.839040	3.880700	3.768980	3.857041
Ethanol	3.827074	3.880335	3.746164	3.861124
Methanol	3.839040	3.881064	3.746226	3.860763

Table 2:- Comparison of experimental and computed electronic transition energies (in eV).

5 Conclusion

The excitation energies were investigated computationally to explain the solvatochromic behavior of Coumarin dyes (C478, C519, C523, C307 and C522B) in series of alcohols. The semi empirical $E_T(30)$ polarity scale has been adopted to compare the experimental values with computational results. Experimentally observed positive and negative solvatochromism are accounted and their behavior is well explained by computational study. Oscillating behaviour from positive to negative solvatochromism in polarity scale at particular stage is observed. Here looking at the problem more closely, when there is change in solvent from pentanol to hexanol the positive solvatochromism switches to negative. Dipole moment is calculated for ground and excited states in all the individual solvents. The difference in dipole moments from ground to excited state remains almost unaffected in all the solvents. The observation of subsequent difference in ground state and also the case of excited state dipole moments in solvents studied suffers rapid change in value when crossing from pentanol to hexanol. This is the particular solvent where the negative solvatochromism starts and this change in polarity scale is referred as polarity switch. The ZINDO/PCM method follows the observed experimental trends for all the Coumarin dyes. Computational results suggest that ZINDO/PCM values lie in closer proximity to the experimental results depending on the polarity of Coumarin molecules. Comparing the results of C478 and C519 it is clear that excited state energies of highly polar molecules are well approximated by ZINDO/PCM calculations. The resonance contributors are more in C519 than C478, making it more polar in nature. Discrepancies exist in some of the solvents and are attributed to discarding the hydrogen bonding at specific sites of molecule because missing solvent structure in PCM formulation. Further study was intended to test the ZINDO/PCM applicability in case of 1-naphthol (N1) and 2-naphthol (N2) in various solvents and good agreement has been found with experimental results. In summary the solvatochromism of Coumarin dyes are compared with ZINDO/PCM results. The ZINDO/PCM calculation explains the observed positive and negative solvatochromism. Depending on polarity of molecule the ZINDO/PCM values are nearer to measured ones as it can be seen in cases of C519 and C523compared to C478. The study also provides strong evidence about the accuracy and shortfalls of ZINDO/PCM method by considering five different Coumarin molecules with variation in their polarity.

6 ACKNOWLEDGMENTS

The authors acknowledge Prof. Dr. Sanjeev R. Inamdar, FRSC (UK), FKSTA, for his constant support in accomplishing this work.

References

1. T. Jacopo, M. Benedetta and C. Roberto, *Chem. Rev*., 105 (8), 2999–3094 (2005).

2. C. Reichardt, Solvents and Solvent Effects in Organic Chemistry, third ed., Wiley-VCH Verlag GmbH and Co., Weinheim (2004).
3. T. Jacopo and P. Maurizio, *Chem. Rev*., *94* (7), 2027–2094 (1994).
4. S. Miertus, E. Scrocco and J. Tomasi, *Chem. Phys*., 55 (1), 117-129 (1981).
5. E. Cances, M. Benedetta and J. Tomasi, *J. Chem. Phys*., 107, 3032-3041 (1997).
6. M. Benedetta, E. Cances and J. Tomasi, *J. Phys. Chem. B.*, 101 (49), 10506–10517 (1997).
7. M. Caricato, M. Benedetta and T. Jacopo, *J. Phys. Chem. A*., 108, 6248-6256 (2004).
8. D. Loco, E. Polack, S. Caprasecca, L. Lagardere, F. Lipparini, J. P. Piquemal and M. Benedetta, *J. Chem. Theory Comput*., 12, 3654−3661 (2016).
9. W. Zhao, L. Pan, W. Bian, and J. Wang, *Chem. Phys. Chem*., 9, 1593–16020 (2008).
10. W. Zhao, Y. Ding and Q. Xia, *J. Comput. Chem.*, 32, 545–553 (2011).
11. W. Zhao, B. Li, S. Xu and Q. Zhao, *J. Theor. Comput. Chem*., 14(4), 1550030(13) (2015).
12. M. Caricato, M. Benedetta and T. Jacopo, *Mol. Phys*., 104 (5-7), 0875-887 (2006).
13.X. Liu, J. M. Cole, P. C. Y. Chow, L. Zhang, Y. Tan and T. Zhao, *J. Phys. Chem. C*, 118, 13042−13051 (2014).
*14.*X. Liu, J. M. Cole and Z. Xu, *J. Phys. Chem. C*, 121, 13274−13279 (2017).
15. M. Caricato, O. Andreussi and S. Corni, *J. Phys. Chem. B 110*, 16652-16659 (2006).
*16.*J. R. Mannekutla, B. G. Mulimani and S. R. Inamdar. *Spectrochim. Acta, Part A*., 69, 419-426 (2008).
17.S. K. Patil, M. N. Wari, C. Y. Panicker and S. R. Inamdar, *Spectrochim. Acta, Part A*., 123, 117-12 (2014).
18. X. Liu, J. M. Cole and K. S. Low, *J. Phys. Chem. C*, 117, 14731−14741 (2013).
19. X. Liu, Z. Xu and J. M. Cole, *J. Phys. Chem. C*, 117, 16584−16595 (2013).
20.Gaussian 09, Revision A.02, M. J. Frisch, G. W. Trucks, H. B. Schlegel, G. E. Scuseria, M. A. Robb, J. R. Cheeseman, G. Scalmani, V. Barone, G. A. Petersson, H. Nakatsuji, X. Li, M. Caricato, A. Marenich, J. Bloino, B. G. Janesko, R. Gomperts, B. Mennucci, H. P. Hratchian, J. V. Ortiz, A. F. Izmaylov, J. L. Sonnenberg, D. Williams-Young, F. Ding, F. Lipparini, F. Egidi, J. Goings, B. Peng, A. Petrone, T. Henderson, D. Ranasinghe, V. G. Zakrzewski, J. Gao, N. Rega, G. Zheng, W. Liang, M. Hada, M. Ehara, K. Toyota, R. Fukuda, J. Hasegawa, M. Ishida, T. Nakajima, Y. Honda, O. Kitao, H. Nakai, T. Vreven, K. Throssell, J. A. Montgomery, Jr., J. E. Peralta, F. Ogliaro, M. Bearpark, J. J. Heyd, E. Brothers, K. N. Kudin, V. N. Staroverov, T. Keith, R. Kobayashi, J. Normand, K. Raghavachari, A. Rendell, J. C. Burant, S. S. Iyengar, J. Tomasi, M. Cossi, J. M. Millam, M. Klene, C. Adamo, R. Cammi, J. W. Ochterski, R. L. Martin, K. Morokuma, O. Farkas, J. B. Foresman, and D. J. Fox, Gaussian, Inc., Wallingford CT (2016).
21.P. Mallika, P. Sabita, and K. M. Bijay, *J. Mol. Liq*., 177, 335–342 (2013).
22.R. Gahlaut, N. Tewari, J.P. Bridhkoti, N.K. Joshi, H.C. Joshi and S. Pant, *J. Mol. Liq*., 163, 141–146 (2011).

Karnatak University Journal of Science 53 (2022) 69-78

Karnatak University Journal of Science

ISSN: 0075-5168

Assessment of Fipronil Acute Toxicity on *Duttaphrynus Melanostictus* Tadpoles: Influences on Swimming Pattern and body Morphology

Kartheek RM and David M*

Environmental Toxicology and Molecular Biology Laboratory, Department of PG Studies and Research in Zoology, Karnatak University, Dharwad- 580003.

***Corresponding author:** *mdavid.kud@gmail.com*

ARTICLE INFO

Article history:
Received: 13 March 2022;
Revised: 20 May 2022;
Accepted: 30 May 2022

Keywords:
Anurans; Fipronil; Lordosis; Phenylpyrazole; Toxicity;

ABSTRACT

Amphibians occupy a critical point in the food web for having secured evolutionary gift of their survivalability in both aquatic and terrestrial ecosystems. However, their global decline is estimated to be far greater as compared to any other taxonomic groups in existence. The present investigation reports the primary data on acute toxicity of Fipronil (FPN) on larvae of Asian black spined toad *Duttaphrynus melanostictus* and its implications on the alterations in behavioural and morphological features following sublethal exposures. The 96 hours acute toxicity was determined to be 97.5 µg/L. Further, 5 day exposure to sub-lethal concentrations of 16.25 (E1) and 32.5 µg/L (E2) indicated alterations in swimming patterns including irregular, erratic, darting and dwindling types of swimming pattern accompanied by loss of equilibrium. Morphologically, the tadpoles were found with notochord curvature signifying khyphosis, lordosis and fin blistering conditions, resulting in the reduced activity patterns under dose dependent trend. The work highlights the need to focus on impact of environmental contaminants including new generation insecticides and their influences on possible extermination of amphibian populations. The work also provides an insight on the range of susceptiblility of *D. melanostitcus* to the selected sublethal concentrations of FPN.

1. Introduction

Concerns on amphibians have been raised over the past few decades, as they continue to remain one of the most threatened class across the globe (Babini et al., 2018; Bolochioa et al., 2020). Recent years have witnessed the decline in amphibian population which is thought to be greater than 40% of the total existing numbers (Hayes et al., 2010; Hoffmann et al., 2021). With pesticides being one of the few imperative reasons for the biodiversity crisis and their reckless state of over utilization has turned paradigmatic for elucidating their harmful influences on anurans (Adams et al., 2021). Extreme concern has been shown by ecologists and conservationists towards the amphibians, particularly on anurans due to their susceptibility and sensitivity to environmental pollutants (González-del-Pliego, 2019). As reported by International Union for the Conservation of Nature (IUCN), there have been reports of over 1,900 species in general, and 787 in specific, rare and endangered amphibian species continue to remain threatened due to the act of deforestation and habitat loss with pesticides also contributing to the said cause yet insignificantly (Frost et al., 2006; Stuart et al., 2008). Recent decades have witnessed significant decline among the four amphibian families *Rheobatrachidae*, *Leptodactylidae*, *Bufonidae*, and *Ambystomatidae* which is identified to be far more than the average among all amphibians (Stuart et al., 2004).

With ample of evidences being acknowledged against use and persistence of conventional pesticides like organophosphates, organochlorines and pyrethroids for their crucial role in contributing the decline of amphibians (Mann and Bidwell, 2001; David et al., 2012) the condition has turned inevitable to assess the safe and toxic concentrations of new class insecticides, which lack literature (Leeb et al., 2020; Agostini et al., 2020). The world faces the enigma to restore the lost population by controlling the utilization and disposal of pesticides that are essentially unambiguous in nature (Brühl et al., 2013). Resistance, however, is a serious matter of concern under entomological studies, for the pests having gained the opposing ability against the chemicals additionally (Matsuda et al., 2020).

Fipronil (5-amino-1- [2,6-dichloro-4-(trifluoromethyl)phenyl]-4-[(trifluoromethyl) sulfinyl]-1H-pyrazole-3-carbonitrile) is a new class phenylpyrazole insecticide (Tingle et al., 2003) which finds its application the pests of commercial crops including cotton and sugarcane in south Asia including India (Stark and Vargas, 2005). Concurrently occurrence of *D. melanostictus* is evident in parts of south Asia which mainly include countries like India and its territories like Andaman and Nicobar (Lever, 2003; van Dijk et al., 2004). The application of FPN is carried out against the pests of crops including sugarcane and paddy which have high potential to inhabit the different anuran species (Mandal and Singh, 2014; Teng et al., 2016). FPN has been proven to be highly effective, at low field application rates, against insect pests that are resistant to pyrethroids, organophosphates, and carbamate insecticides (Bobe et al., 1997). Considering the above, the present work was aimed to elucidate the possibilities of FPN toxicity against the larvae of Asian black spined toad *D. melanostictus* by emphasising on the endpoints of toxicity and additionally highlighting implications on behavioural and morphological stability.

2. Materials and Methods

2.1. Toxicant selected and test solutions

Commercial grade FPN of 5% SC was selected as the toxicant for the present study and was procured from the local market Dharwad, (Karnataka, India). A stock solution of the concentration 100.0 µg/ml was prepared by dissolving 1000 µg of FPN in 10 ml of double distilled water. The required test concentrations were freshly prepared by

diluting the stock solution just before the initiation of acute toxicity studies.

2.2. Procurement and maintenance of tadpoles

Two hundred and fifty tadpoles of *D. melanostictus* (Gosner Stage 21) were collected from uncontaminated ponds located in Karnatak University campus, Dharwad city (Karnataka, India) and were transported to the laboratory with care. The tadpoles were allowed to acclimatize to laboratory conditions and exposed in batches as explained in the earlier studies (David and Kartheek, 2015). The larvae were kept in the laboratory under ideal temperature pH and dissolved oxygen levels were monitored daily (Table 1) until they reached stages 29–33 (0.090 ± 0.015 g) just before the development of legs (Gosner, 1960). Tadpoles were fed with plant origin feed and boiled spinach with ad libitum. The water in aquaria was renewed once in every two days for removing of excess of food and faeces.

Table 1 Showing values for quality assessment of water used for the present investigation

Parameter	Values obtained
Temperature	25 ±2 _C
pH	7.3 ±0.2
Dissolved oxygen	7.7 ±0.8 mg/L
Total hardness	7.7 ±0.8 mg/L
Salinity	30.4 ±3.1 mg as CaCO3/L
Specific gravity	Nil
Conductivity	1.003
Conductivity	<14 lS/cm
Calcium	17.31±0.92 mg/L
Phosphate	0.34 ±0.004 lg/L
Magnesium	0.78 ±0.3 mg/L

2.3. Acute toxicity test

Acute toxicity of FPN is analysed by static renewal assay test after range finding of upper and lower limits of acute toxicity value on *D. melanostictus* in order to minimize the tadpole killing. Ten tadpoles (Gosner stage 27) were released into each aquarium (10 L) and were exposed to varying concentrations. Range finding test was carried out for reducing the number of experimental animal. Once obtained, tadpoles (10 each) were transferred to the aquaria consisting of concentrations ranging from 90.0 to 105.0 µg/l for 96 h of commercial grade FPN in different groups. Six replicates were maintained for each concentration. Among these, one set however, served as a control group consisting of tadpoles, which were being placed in dechlorinated tap water without any traces of FPN (n = 10). Observations were made at every 24 h intervals during the 96 h of exposure period. After every 24 h, the number of dead animals was recorded and the same were removed from the aquaria. Mortality data from the replicate samples from each FPN concentration were pooled prior to calculating the LC_{50} value and the 95% confidence limits (Table 2).

2.4. Exposure to sublethal concentrations

Tadpoles were exposed to two different sublethal concentrations of 16.25 and 32.5 µg/L. Each exposure batch consisted of 10 healthy *D. melanostictus* tadpoles of stage 27 which were randomly selected and transferred to glass aquaria containing 1000 ml water with its respective concentration of FPN solution. The tadpoles remained there for 96 h. For each concentration, including the control, 3 replicates were maintained and the mean values of these were taken into account for the present study. Further, the behavioural changes and the body morphology changes were observed on exposed tadpoles to different sublethal concentrations of FPN for five days.

2.5. Behavioural and Morphological abnormalities

Tadpole behavioural and morphological changes was monitored by video recording. The behavioural responses were studied according to the methods as described by Blaustein et al., (2005) and morphological changes as recorded according to David and Kartheek, (2015). The behavioural responses were investigated by making obligatory disturbances through tapping with a glass rod to evaluate the fright responses shown by

Table 2: Showing mortality of *Duttaphrynus melanostictus* tadpoles exposed to different concentrations of fipronil at 96 h.

Sl. No.	Concentration (µg/L)	Log concentration of Fipronil	No of Tadpoles Exposed	No of tadpoles alive	No of tadpoles dead	Percent mortality	Empirical Probit Mortality
1	90.0	1.954	10	10	00	00	0.0
2	91.5	1.961	10	09	01	10	3.72
3	93.0	1.968	10	08	02	20	4.10
4	94.5	1.975	10	08	02	20	4.48
5	96.0	1.982	10	06	04	40	4.75
6	97.5	1.989	10	05	05	50	5.00
7	99.0	1.995	10	04	06	60	5.25
8	100.5	2.002	10	03	07	70	5.52
9	102.0	2.008	10	02	08	80	5.84
10	103.5	2.014	10	01	09	90	6.28
11	105.0	2.021	10	00	10	100	7.33

tadpoles against the stimulus. The overall behavioural response was assessed in-situ by observing the swimming pattern of tadpoles (Table 4).

Table 3: Acute toxicity and 95% confidence limits of Fipronil on *Duttaphrynus melanostictus* tadpoles

Toxicant	96h LC_{50} (µg/L)	Probit	95% Confidence limits	
			Upper limit	Lower limit
Fipronil	97.5	5.00	105.0	97.5

2.6 Statistical analysis

The antioxidant activities are reported as the mean ± standard error of the mean (SEM) obtained from triplicates. The data were subjected to one-way analysis of variance and further subjected to Tukey's test for post hoc analysis by defining the significance level at $p<0.05$.

2.7 Ethics statement

The present study was carried out at Department of PG Studies and Research in Zoology, Karnatak University, Dharwad (Karnataka, India) as per ethics committee regulations. The test animals used were maintained and subjected to experimentation process as well as disposed upon completion of experiment, as per the guidelines issued by CPCSEA (Committee for the Purpose of Control and Supervision on Experiments on Animals).

3. Results and Discussion

Determination of LC_{50} remains the preliminary requirement to investigate the organism's capacity to resist and survive in the medium with the presence of toxicant(s). Higher LC_{50} values designate lesser toxicity as the increased amount of concentrations are necessary to induce 50% mortality in the exposed organisms (Eisler and Gardner, 1973). Besides this, pesticides have been reported for their ability to ultimately increase the propensity to parasitic infection through declining activity patterns among the tadpoles (Bridges and Semlitsch, 2000) as these tadpoles have the ability to evade free-swimming parasites by directing themselves away of through changing their swimming patterns (Thiemann and Wassersug, 2000, Koprivnikar et al., 2006).

Acute toxicity of 96h LC_{50} value of FPN is was evaluated and found to be 97.5 µg/L on *D. melanostictus* represented in Table 2 & 3; Figure 1, 2 and 3. It is to be noted that the LC_{50} value of 97.5 µg/l for commercial formulation of FPN is identified for the first time against the test species to the best of our knowledge, hence making the present work imperative. The present median lethal value is in the range of previously published reports on other species 96h LC_{50} of technical grade FPN on red swamp (*Procambarus clarkii*) and

white river (*Procambarus zonangulus*) crayfish were 14.3

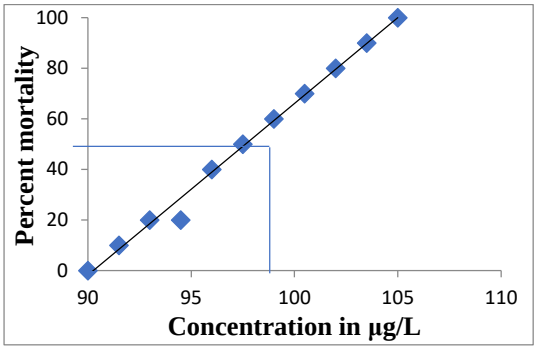

Figure 1: Showing concentration versus mortality for *Duttaphrynus melanostictus* tadpoles exposed to different concentrations of fipronil

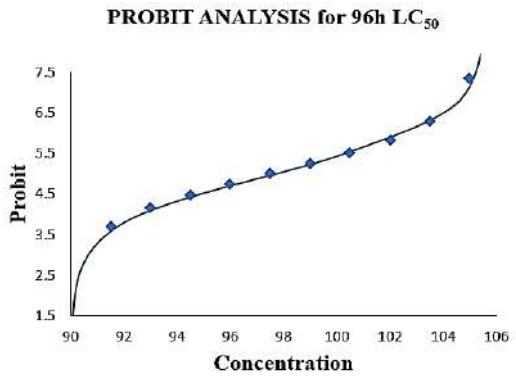

Figure 2: Showing mortality of *Duttaphrynus melanostictus* exposed to different concentrations of commercial grade fipronil

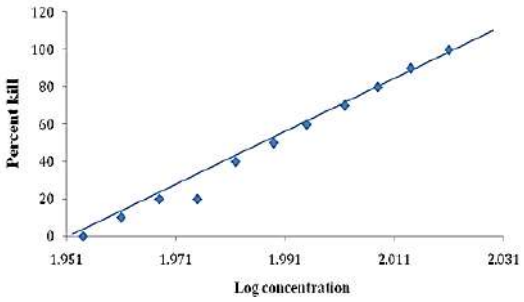

Figure 3: Showing mortality of *Duttaphrynus melanostictus* exposed to different concentrations of commercial grade fipronil

and 19.5 µg/L, respectively (Schlenk et al., 2001). Wu et al., (2014), reported that 24 h LC_{50} value of FPN on zebrafish was 220.4 µg/L (95% CI: 173.7–272.4 µg/L) denoting that zebrafish is more resistant to FPN compared to *D. melanostictus*. The existing other pesticide reports, show that 96h LC_{50} of dichlorvous 51.64 mg/L (Geng et al., 2005), and Malathion was found to be 7.5 mg/L on *D. melanostictus* (David and Kartheek, 2015), indicating higher degree of FPN toxicity against tadpoles of *D. melanostictus*. However, report by David et al., (2012) on cypermethrin toxicity indicated 96h LC_{50} of 3.34µg/L against *D. melanostictus* tadpoles far more toxic than the FPN formulation. The acute toxicity treatments showed strong negative effects on ability of survival to increased pesticide concentration. Mortality at highest concentrations suggesting that death have been influenced by pesticide concentrations and could also be attributed to threat to the amphibian larval stage. However, at lower concentrations of same, different anomalies have been found to be reported by various authors. It has also been reported that pesticidal exposure during the investigations on short-term effects on anurans indicated morphological and developmental deformities such as lateral flexure of the tail or deformities of eye and limb (Harries et al., 2000, Brunelli et al., 2009).

In the present investigation as well, it was evident that even though all the tadpoles survived in sublethal concentrations (16.25.0 and 32.5 µg/L) of FPN, indicating that the given FPN concentrations were not lethal to *D. melanostictus* at 5 days of exposure time. With normal behavioural responses being evidenced in the control group. However, the behavioural changes in tadpoles exposed to sublethal concentrations were found to demonstrate number of anomalies including changes in swimming pattern indicating irregularities, staggered behaviour, Whirling cork movement and loss of fright response represented in Table 4 and Figure 4. The morphological changes concerning the tail region mainly, suggested outcomes like, kyphosis, lordosis, fin blistering and notochord curvature and were found to be severe in E2 (a to c) group than E1 (a to c) in FPN intoxicated tadpoles and has been shown in Table 5 and Figure 5.

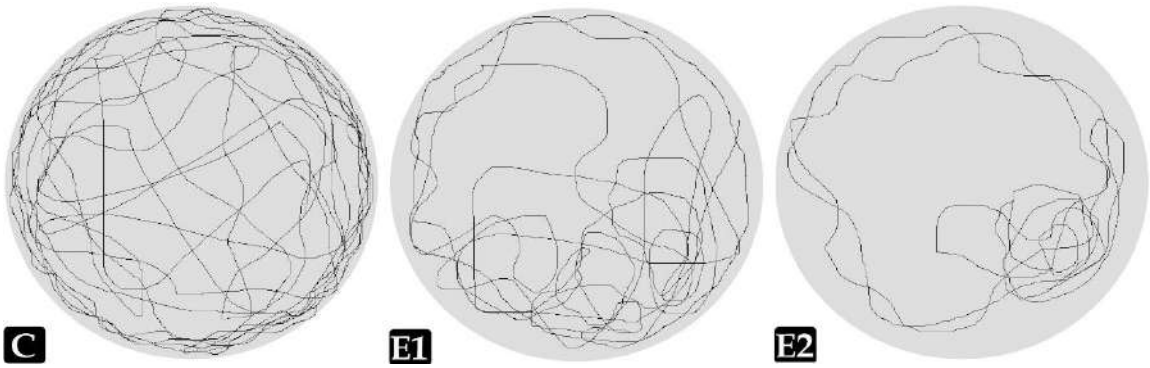

Figure 4: Showing changes in swimming pattern of *Duttaphrynus melanostictus* exposed to different concentrations of commercial grade fipronil.

Table 4: Behavioural changes in tadpoles of *Duttaphrynus melanostictus* in control and fipronil treated groups

Groups	Concentration (µg/L)	Behavioural changes recorded			
		Impaired swimming behaviour	Staggered behaviour	Whirling cork like movement	Loss of fright response
C	0.0	-	-	-	-
E1	16.25	+	-	+	+
E2	32.5	+ +	+	+ +	+ +

Tadpoles exhibiting various behavioural anomalies, indicate (-) Nil, (+) as Low, and (+ +) as Medium levels of impaired behaviour due to intoxication of fipronil at 5 days.

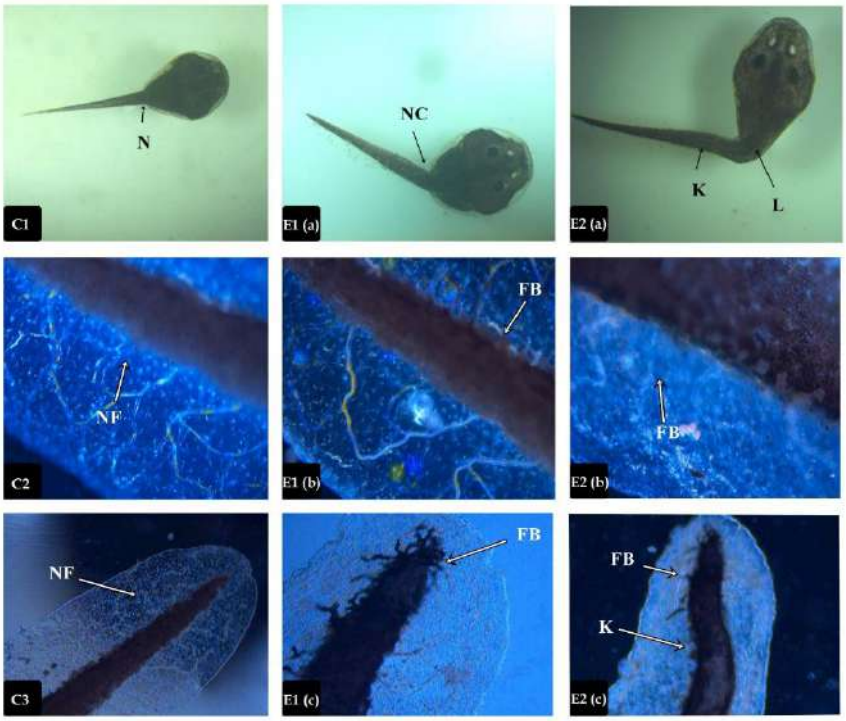

Figure 5: Morphological deformities in *Duttaphrynus melanostictus* exposed to different concentrations of commercial grade fipronil. E1 (a) Tadpole under control group showing normal morphology of notochord (N). C2 & C3 showing appearance of normal fin (NF) morphology. E1 Tadpole exposed to 16.25 µg/L of fipronil showing E1 (a) notochord curvature (NC); E1 (b) & (c) with fin blistering. E2 (a) Tadpole exposed to 32.5 µg/L of fipronil showing E2 (a) with Kyphosis (K) and Lordosis (L), E2 (b) & (c) Fin blistering (FB) and khyphosis (K).

Table 5: Morphological changes in tadpoles of *Duttaphrynus melanostictus* in control and fipronil exposed groups

Groups	Concentration (µg/L)	Morphological abnormality			
		Normal Notochord	Lordosis	Kyphosis	Fin blistering
C	0.0	+ + +	-	-	-
E1	16.25	-	+	-	+
E2	32.5	-	+ + +	+	+ + +

Tadpoles exhibiting various morphological features, indicate (-) Nil, (+) as Low, (+ +) as Medium and (+ + +) as high levels in tadpoles under control and exposed to fipronil for a duration of 5 days.

Behavioral and morphological characteristics have been since long time considered a sensitive indicators of toxicant response. Severe morphological and behavioural deformities in the E2 group show that higher concentration was able to induce increased amounts of deleterious health effects on tadpoles when compared to low concentration exposed E1 group. Typical signs observed in a present study can be viewed as the expression of neurotoxicity (Greulich, 2002). Alterations of the movement behavior after pesticide exposure are well known and documented for aquatic species including amphibians. An abnormal swimming behavior and a decreased activity of larvae can often be observed (Shuman-Goodier and Propper, 2016; Sievers et al., 2019), whereby such alterations are usually induced due to the neurotoxicity of the pesticide (Ockleford et al., 2018). Since, FPN has been reported to cause impairments in central nervous system of the mammals as per the reports of Raquel and Antonio, (2011), the deleterious effects on tadpoles of *D. melanostictus* as well was expected to be likely obvious and thus has been confirmed through the outcome of present investigation. The current study also draws support from findings of Stehr et al., (2006) who suggested the influence of FPN in degeneration of notochord, reduced length of the rostral-caudal body axis, and ineffective tail flips and uncoordinated muscle contractions along the body axis in zebrafish embryos following exposure to 0.7µM (333 µg/l) FPN. Additionally, the activity patterns remain a critical routine of tadpoles and compromises in the same have been known to result in underdevelopment and death among the different species.

The altered axis and bent tail orientations of these tadpoles exposed to different environmental contaminants have been previously reported to disrupt its capability to reach food sources and also minimise the possibilities to evade the predators thus, increasing the risks of predation (Punzo, 1992). Since higher pesticide concentrations are likely to occur immediately after their application; moreover, the remains of the applied pesticide have been reported to persist in the waterbodies for at least few weeks following a single large event of application (Eichelberger and Lichtenberg, 1971). Similar results have also been documented in *D. malanosticus* tadpoles exposed to cypermethrin and malathion in previous studies (David et al., 2012; David and kartheek, 2015). In yet another study reported by Pavan et al., (2021), a herbicide mixture of glyphosate and 2,4-D was found to affect the tadpoles of *Boana faber and Leptodactylus latrans* in terms of growth and swimming activity. However, the intensity of toxicity of FPN could be concluded as far more toxic than that of glyphosate and 2,4-D combined as FPN induced significant changes at 5 days of duration against the latter which induced

changes at 7 days. The toxicity however, can be attributed to the wide range of species of tadpoles which have their differences in terms of their susceptibility and resistance against the different toxicants.

4. Conclusion

From the present study it can be concluded that the commercial grade FPN has an median lethal concentration value of 97.5 µg/L for *D. melanostictus* tadpoles and its sublethal exposure at doses of 15.0 µg/L and 30.0 µg/L was found to induce behavioural and morphological anomalies. Hence it is highly recommended that the use of FPN be restricted considereing the declining trend of amphibian population. The present work however, has its own limitation and is viewed as a nutshell considering the limited gross analysis and thus, further investigations under molecular aspects are crucial to ascertain the mechanism of toxicity of FPN against larvae of *D. melanostictus*.

5. Acknowledgements

Financial support and sponsorship: The authors are thankful to University Grants Commission and Department of Science and Technology for providing financial assistance through UGC Major Research Project scheme (F. No. 41-103/2012 (SR); UGC SAP scheme [No. F.4-18/2015/DSA-I (SAP-II)] and DST Purse Phase-II program.

References

[1] Adams E, Leeb C, Brühl CA, Pesticide exposure affects reproductive capacity of common toads (Bufo bufo) in a viticultural landscape. Ecotoxicology, 30, 213–223, (2021).

[2] Agostini MG, Roesler I, Bonetto C, Ronco AE, Bilenca D, Pesticides in the real world: The consequences of GMO-based intensive agriculture on native amphibians. Biological Conservation, 241, 108355, (2020). https://doi.org/10.1016/j.biocon.2019.108355

[3] Blaustein AR, Romansic JM, Scheessele EA, Ambient levels of ultraviolet-B radiation cause mortality in juvenile western toads, *Bufo boreas*. Am Midi Nat 154, 375–382, (2005).

[4] Bolochioa BE, Lescanob JN, Cordier JM, Loyola R, Nori J, A functional perspective for global amphibian conservation. Biological Conservation, 245, 108572, (2020).

[5] Bobe A, Coste CM, Cooper JF, Factors influencing the adsorption of fipronil on soils. J Agr Food Chem 45, 4861-4865, (1997).

[6] Bridges CM, Semlitsch RD, Variation in pesticide tolerance of tadpoles among and within species of Ranidae and patterns of amphibian decline. Conserv Biol 14, 1490–1499, (2000).

[7] Brühl C, Schmidt T, Pieper S. et al., Terrestrial pesticide exposure of amphibians: An underestimated cause of global decline?. Sci Rep 3, 1135, (2013). https://doi.org/10.1038/srep01135

[8] Brunelli E, Bernabò I, Berg C, Lundstedt-Enkel K, Bonacci A, Tripepi S, Environmentally relevant concentrations of endosulfan impair development, metamorphosis and behaviour in Bufo bufo tadpoles. Aquatic Toxicology 91, 135–142, (2009). https://doi.org/10.1016/j.aquatox. 2008.09.006

[9] Buege A, Aust S, Microsomal lipid peroxidation. Methods Enzymol 52, 302.

[10] David M, Kartheek RM (2015) Malathion acute toxicity in tadpoles of *Duttaphrynus melanostictus*, morphological and behavioural study. The J Bas Appl Zoo 72, 1–7, (1978).

[11] David M, Shambanagouda RM, Patil VK, Ramesh H, Behavioral, morphological deformities and biomarkers of oxidative damage as indicators of sublethal cypermethrin intoxication on the tadpoles of *D. melanostictus* (Schneider, 1799). Pestic Biochem Physiol 103, 127–134, (2012).

[12] Eichelberger JW, Lichtenberg JJ, Persistence of pesticides in river water. Environ Sci Tech 5, 541-544, (1971).

[13] Eisler R, Gardner GR, Acute toxicity to an estuarine teleost of mixture of cadmium, copper and zinc salts. J Fish Biol 5, 131-142, (1973.).

[14] Frost DR, Grant T, Faivovich J, Bain RH, Haas A, Haddad CFB, De Sá RO, Channing A, Wilkinson M, Donnellan SC, Raxworthy CJ, Campbell JA, Blotto BL, Moler P, Drewes RC, Nussbaum RA, Lynch JD, Green DM, Wheeler WC, The Amphibian Tree of Life. Bulletin of the American Museum of Natural History, 297, 359, (2006).

[15] Geng BR, Yao D, Xue QQ, Acute toxicity of the pesticide dichlorvos and the herbicide

butachlor to tadpoles of four anuran species. Bull. Environ. Contam. Toxicol. 75, 343–349, (2005).
[16] Gonza´lez-del-Pliego P, Freckleton RP, Edwards DP, Koo MS, Scheffers BR, Pyron AR, Walter Jetz, Phylogenetic and Trait-Based Prediction of Extinction Risk for Data-Deficient Amphibians. Current Biology 29, 1557–1563, (2019).
[17] Gosner KL, A simplified table for staging anuran embryos and larvae with notes on identifcation. Herpetologica 16, 183-190, (1960).
[18] Greulich K, Hoque E, Pflugmacher S, Uptake, metabolism, and effects on detoxication enzymes of isoproturon in spawn and tadpoles of amphibians, Ecotoxicol. Environ. Saf. 52, 256–266, (2002).
[19] Hayes TB, Falso P, Gallipeau S, Stice M, The cause of global amphibian declines: a developmental endocrinologist's perspective. J Exp Biol 213, 921-933, (2010). doi:10.1242/jeb.040865.
[20] Harries J, Runnalls T, Hill E, Harris C, Maddix S, Sumpter J, Tyler C, Development of a reproductive performance test for endocrine disrupting chemicals using pair-breeding fathead minnows (Pimephales promelas). Environ Sci Technol 34, 3003–3011, (2000).
[21] IUCN (2020) The IUCN red list of threatened species. Version 2020-1. https://www.iucnredlist.org. Accessed 2 June 2020.
[22] Koprivnikar J, Forbes MR, Baker RL, On the efficacy of anti-parasite behaviour: a case study of tadpole susceptibility to cercariae of Echinostoma trivolvis. Canadian Journal of Zoology 84, 1623–1629, (2006).
[23] Leeb C, Kolbenschlag S, Laubscher A, Adams E, Brühl CA, Theissinger K, Avoidance behavior of juvenile common toads (*Bufo bufo*) in response to surface contamination by different pesticides. PLoS ONE 15, e0242720, (2020). https://doi.org/10.1371/journal.pone.0242720
[24] Lever C, Naturalized Reptiles and Amphibians of the World. New York: Oxford University Press (2003).
[25] Mandal K, Singh B, Persistence and metabolism of fipronil in sugarcane leaves and juice. Bull Environ Contam Toxicol 92, 220–224, (2014).
[26] Mann RM, Bidwell JR, The acute toxicity of agricultural surfactants to the tadpoles of four Australian and two exotic frogs. Environ. Pollut 114, 195–205, (2001).
[27] Matsuda K, Ihara M, Sattelle DB, Neonicotinoid Insecticides: Molecular Targets, Resistance, and Toxicity. Annual Review of Pharmacology and Toxicology 60, 241- 255, (2020). https:// doi.org/10.1146/annurev-pharmtox-010818-021747.
[28] Ockleford C, Adriaanse P, Berny P, Brock T, Duquesne S, Grilli S, et al., Scientific Opinion on the state of the science on pesticide risk assessment for amphibians and reptiles. EFSA J, 16, 32625798, (2018).
[29] Pavan FA, Samojeden CG, Rutkoski CF, Folador A, FRE SP, Muller C, Hartmann PA, Hartmann MT, Morphological, behavioral and genotoxic effects of glyphosate and 2,4-D mixture in tadpoles of two native species of South American amphibians. Environmental Toxicology and Pharmacology, 85, 1-11, (2021).
https://doi.org/10.1016/j.etap.2021.103637
[30] Punzo F, Socially facilitated behavior in tadpoles of *Rana catesbeiana* and R*ana heckscheri* (Anura: Ranidae), J Herpetol 26, 219–222, (1992).
[31] Schlenk D, Huggett DB, Allgood J, Bennett E, Rimoldi J, Beeler AB, Block D, Holder AW, Hovinga R, Bedient P, Toxicity of fipronil and its degradation products to *procambarus sp.* field and laboratory Studies. Arch Environ Contam Toxicol, 41, 325–332, (2001).
[32] Shuman-Goodier ME, Propper CR, A meta-analysis synthesizing the effects of pesticides on swim speed and activity of aquatic vertebrates. Sci Total Environ., 565, 758–766, (2016). pmid:27261557.
[33] Sievers M, Hale R, Parris KM, Melvin SD, Lanctôt CM, Swearer SE, Contaminant-induced behavioural changes in amphibians: A meta-analysis. Sci Total Environ., 693, 133570, (2019). pmid:31369889
[34] Stark JD, Vargas R, Toxicity and hazard assessment of fipronil to Daphnia pulex. Ecotoxicol Environ Saf, 62, 11-16, (2005).
[35] Stehr CM, Linbo TL, Incardona JP, Scholz NL, The Developmental neurotoxicity of fipronil: notochord degeneration and locomotor defects in zebrafish embryos and larvae. Toxicol Sci, 92, 270-278, (2006).
[36] Stuart S, Hoffmann M, Chanson J, Cox N, Berridge R, Ramani P, Young B, Threatened amphibians of the world. Lynx Edicions, Barcelona, Spain, IUCN, Gland, Switzerland

and Conservation International, Arlington, Virginia, USA. 758, (2008).
[37] Stuart SN, Chanson JS, Cox NA, Young BE, Rodrigues AS, Fischman DL, Waller RW, Status and Trends of Amphibian Declines and Extinctions Worldwide. Science reports, 306, 1783-1786, (2004).
[38] Teng Q, Hu XF, Luo F. et al., Influences of introducing frogs in the paddy fields on soil properties and rice growth. J Soils Sediments 16, 51–61, (2016). https://doi.org/10.1007/s11368-015-1183-6
[39] Thiemann GW, Wassersug RJ, Patterns and consequences of behavioural responses to predators and parasites in Rana tadpoles. Biol J Linn Soc, 71, 513–528, (2000). doi: 10.1006/bijl.2000.0459.
[40] Tingle CC, Rother JA, Dewhust CF, Lauer S, King WJ, Fipronil: environmental fate, ecotoxicology, and human health concerns. Rev Environ Contam Toxicol, 176, 1-66, (2003).
[41] Van Dijk PP, Iskandar D, Neng Lau MW, Huiqing G, Baorong G, Kuangyang, Wenhao C, Zhigang Y, Chan B, Dutta S, Inger R, Manamendra-Arachchi K, Sharif Khan M (2004) *Duttaphrynus melanostictus*. The IUCN Red List of Threatened Species 2004.
[42] Wu H, Gao C, Guo Y, Zhang Y, Zhang J, Ma E, Acute toxicity and sublethal effects of fipronil on detoxification enzymes in juvenile zebrafish (*Danio rerio*). Pestic Biochem Phys 115, 9–14, (2014).

Karnatak University Journal of Science 53 (2022) 79-98

Karnatak University Journal of Science

ISSN: 0075-5168

A computational study combined with experiments to investigate the molecular interactions of a novel organic dye: Exploring the values of ground and excited state dipole moments

T S Tilakraj[1], Mallikarjun K Patil[1], Mahesh S Najare[2], I M Khazi[2], S. R. Inamdar[1]*

[1]*Laser Spectroscopy Programme, UGC-CPEPA Dept. of Physics, Karnataka University, Dharwad 580003, India*

[2]*Department of Studies in Chemistry, Karnataka University, Dharwad 580003, India*

***Corresponding author**: him_lax3@yahoo.com*

ARTICLE INFO

Article history:
Received: 4 Feb 2022;
Revised: 3 July 2022;
Accepted: 7 July 2022;

Keywords:
DFT; TD-DFT;
Solvatochromism;
Dipole Moment;
IR spectrum;

ABSTRACT

In this work we use experimental and computational tools to explore dipole moments in ground and excited states of a home synthesized novel pyrene substituted 1,3,4- oxadiazole derivative, which finds potential applications in OLEDs. We have obtained the spectral response of the moleculesuch as UV-Vis absorption spectra and fluorescence emission spectra in various solvents. Here we discuss the solvent effects on the dye observed in alcohols, polar aprotic and slightly polar/nonpolar solvents. Considering the solvatochromic shifts in the fluorescence spectrum obtained in different classes of solvents, we have calculated the ground state and excited state dipole moments of this novel dye. The empirical solvatochromic models like Bilot-Kawski, Lippert-Mataga, Kawski-Chamma-Viallet, Bakhshiev and Reichardt methods are assessed for the same. The plots are used to get the deterministic values of dipole moments. As another dimension we compute to optimize the molecule in Density Functional Theory (DFT) and Time Dependant Density Functional Theory (TD-DFT) methods for ground and excited states, respectively, using Gaussian16 molecular modelling package. We have evaluated the electronic transition energies from ground to the first excited state of dye employing TD-DFT. This TD-DFT has been combined with integral equation formalism of polarisable continuum model (IEF-PCM) to calculate various solute-solvent interaction potential which is comparatively studied with experimental values. We have also compared the vibrational energies using InfraRed spectra obtained both experimentally and computationally. The work is further extended to compare the charges on each atom and natural population analysis. Natural bond orbital analysis was also carried out to understand the intramolecular charge transfer and stability.

1. Introduction

Fluorescence is a phenomenon which has kept both the researchers and common man curious and fascinating since ages. Now, even after all these findings and accurate understanding on the physics behind it, few thousands of new research articles get published based on fluorescence and its applications annually. Fluorescent organic molecules are such class of chemicals which are always leading this path till recent times. Organic Light Emitting Diodes (OLED) are one among the highly explored class of materials for lighting and other applications which are based on an organic dye with good fluorescence properties. OLEDs are being projected as the lighting of future because of its high efficiency, comparatively low power consumption, efficient and good thermal/optical stable devices [1,2]. Additionally, they have compatibility with large area with thin and flexible substrates and wavelength can be tuned by structural modifications in core molecules.

1,3,4- oxadiazoles are one such important type of molecules which have multiple usages. We have synthesized a pyrene substituted 1,3,4- oxadiazole derivative which is a potential candidate in OLED applications. The initial synthesis and characterization studies were carried out in previous article of our group [3]. The present work mainly deals with the continuation of the study on this molecule in order to understand the physics and chemistry of solute solvent interactions and the structural variations in ground as well as excited states.

In any fluorescent molecule, determination of dipole moments plays a vital role in understanding many of its properties like, charge distribution, electron density, geometrical and electronic structure when dissolved and so on. Along with that, the calculated values of dipole moments may help us in future to design new similar molecules with nonlinear optical properties [4]. It is quite common to know that for any solute, the surrounding molecules affect the optical properties. Therefore, the solvent effects on a molecule becomes an important part of the study. The distributions of electrons of the molecule in ground and excited states define the overall dipole moments in particular state. Different solvents are distinctive with different values of dielectric constant (K), refractive index (n), and even polarizability. Thus, the ground and excited state dipole moments are affected by changing solvents. Therefore, the study on solvent effect reveals important information on the behaviour of the molecule in excited state. To achieve this, we use one of the most relied and simplest way of understanding solvent effects, Solvatochromism [5,6]. This method is an experimental proof for the changes in the energies during transition due to change in solvents. Our group and many other researchers have reported theoretical and experimental explorations of these effects on the solute in various solvent environments as a function of solvent polarity, dielectric constant, viscosity, polarizability, refractive index and also pH [7-11].

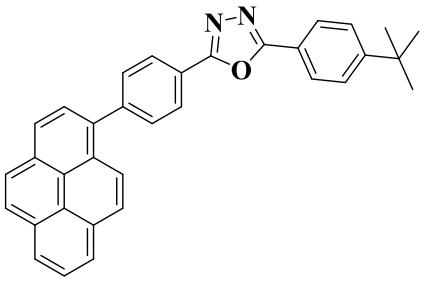

Figure 1. Molecular structure of the fluorophore under study (TBPO)

Since the solvent polarity parameter is complex to measure and understand quantitatively, even though it seems simpler when considered qualitatively, many theories have come up which are based on the individual macroscopic solvent parameters that include refractive index (n), dipole moment and relative permittivity (ε). In many cases some of these theories become inefficient and go out of line. However, Riechardt [12] has proposed an empirically deduced solvent

polarity parameter $E_T(30)$, based on the transition of pyridinium N-phenolate betaine dye. This is now widely accepted to be the best available theory for solvatochromism studies as it proves good with most of the solvents and dye [12]. Therefore, this method is more suitable to get precise values of excited state dipole moments over many similar methods. Also, the single solvent parameter is highly linear with various spectroscopic values obtained which indeed helps in easy calculations and accurate results. The theory of Riechardt demands that we must have value of ground state dipole moment before hand. So, we have used Bilot-Kawski method to obtain the ground state dipole moment value and use it for further calculations [13,14]. Along with this, we have also calculated few of the other solvatochromic methods like Lippert-Mataga [15,16], Bakhshiev [17], and Kawski-Chamma-Viallet [18,19] theories to calculate the first excited state dipole moments from the experimental spectroscopic data obtained. All these different theories yield slightly different outcome since they are based on different orders of parameters. The concise theory of all these are discussed further in the article.

This work aims at exploring the ground and excited state dipole moments of this home synthesized OLED candidate, both spectroscopically and computationally. For our computational job, we have extensively worked in Gaussian16 package [20], which is one of the most used software in the field of molecular modelling and quantum computational chemistry. Density Functional Theory (DFT) is one of the most appreciated and relied theory across research community which suits the real-world problem to a maximum extent. It is a powerful quantum mechanical tool to explore almost any kind of material and simulate most of the properties very similar to their experimental counterpart. The ground and excited state dipole moments of the dye is calculated with the best available level of theory paired with good basis sets. Further we have also solvated the molecule computationally in order to compare the outcomes of calculations found experimentally. The computational explorations have been extended to characterize the molecule by finding the mulliken charges in ground and excited states which gives us the knowledge on Natural Population analysis of the charges. Vibrational energies of the bonds are put under study both experimentally and computationally to compare the practicality of the theory by infrared spectra.

2. Materials and Methods

2.1 Materials

In this work we have used 2-(4-tert-butyl) phenyl-5-4- (pyren-1-yl) phenyl -1,3,4-oxadiazole (TBPO) which is a home synthesized fluorescent molecule [3]. The solvents used for experiments were of spectroscopic grade (HPLC) procured from Sigma-Aldrich.

2.2 Experimental Details

The experimental necessities were fulfilled by using UV-Vis-NIR Absorption Spectrophotometer (JASCO, Model-V670) and Spectrofluorometer (JY HORIBA, Model Fluoromax-4). Absorption spectrums were obtained in the range 200-600 nm, in quartz cuvette of path length 10mm. The concentrations of the compound in all the solvents were as low as to keep the maximum absorbance value below 0.1. The emission spectrum was recorded with the same concentrations for the same path length, with both excitation and emission slits being 1 nm. The integration time was 0.1 s with 1 nm spectral resolution. The IR spectrum was obtained using Nicolet NIR-IR spectrophotometer by KBr pellet method. The analysis of spectra and calculations were performed using various software available.

2.3 Computational Details

Molecular modelling for the molecule was performed to optimize the geometry using Gaussian16 package [20]. Solvent effects were simulated using the basis set DFT and TD-DFT at B3LYP/ 6-311G (d, p) for both ground and excited states. The molecular structure, vibrational frequencies along with Mulliken

charge distributions were simulated employing B3LYP/6-311G+ (d, p).

3. Theoretical Background

3.1 Methods for estimation of dipole moments

The ground (μ_g) and excited (μ_e) state dipole moments play key role in understanding the charge distribution of a molecule. In order to compile a theoretical calculation, we follow various theoretical and empirical relations like Bilot-Kawski, Lippert-Mataga, Bakhshiev, Kawski-Chamma-Viallet and Riechardt methods. We here consider the final formulae given by these theories and calculate dipole moments using solvent parameters like refractive index (n), bulk dielectric constant (ε) and solvatochromic shifts.

3.1.1 Bilot-Kawski method for ground and excited states

The quantum mechanical model to obtain the experimental value of both ground and excited state dipole moments of a molecule were given by Bilot and Kawski [13]. This includes two equations:

$$\overline{\nu_a} - \overline{\nu_f} = m_1 F(n,\varepsilon) + \text{constant} \quad (1)$$

$$\overline{\nu_a} + \overline{\nu_f} = -m_2[F(n,\varepsilon) + 2\,g(n)] + constant \quad (2)$$

where, $F(n,\varepsilon) = \frac{2n^2+1}{n^2+2}\left[\frac{\varepsilon-1}{\varepsilon+2} - \frac{n^2-1}{n^2+2}\right]$ (3)

and $g(n) = \frac{3}{2}\left[\frac{n^4-1}{(n^2+2)^2}\right]$ (4)

are solvent polarity functions with n (refractive index) and ε (dielectric constant) of each solvent, m_1 and m_2 being the slopes of the graphs plotted using equations (1) and (2). $\overline{\nu_a}$ and $\overline{\nu_f}$ are the wavenumbers (in cm^{-1}) at maxima of absorption and emission spectra respectively. Further,

$$m_1 = \frac{2(\mu_e-\mu_g)^2}{hca^3} \quad (5)$$

$$m_2 = \frac{2(\mu_e{}^2-\mu_g{}^2)}{hca^3} \quad (6)$$

where, h is the Planck's constant, c is the velocity of light and a is the Onsager's radius of the molecule. Suppose the molecular geometric symmetry remains same in both ground and excited state, then the corresponding dipole moments are said to be parallel [14]. Modifying equations (5) and (6) we get,

$$\mu_g = \frac{m_2-m_1}{2}\left(\frac{hca^3}{2m_1}\right)^{1/2} \quad (7)$$

$$\mu_e = \frac{m_2+m_1}{2}\left(\frac{hca^3}{2m_1}\right)^{1/2} \quad (8)$$

also, $\mu_e = \mu_g \frac{m_2+m_1}{m_2-m_1}$ for $m_2 > m_1$ (9)

When ground and excited state dipole moments are not parallel to each other, the angle between them (φ) is [22] :

$$cos\,\phi = \frac{1}{2\mu_g\mu_e}\left[(\mu_g^2+\mu_e^2) - \frac{m_1}{m_2}(\mu_g^2-\mu_e^2)\right] \quad (10)$$

3.1.2 Expressions for estimating excited state dipole moments

Here we consider three separate equations to determine the experimental values of the dipole moments of the molecule in first excited state. We use methods put forward by Lippert-Mataga (Eq. (11))[15,16], Bakhshiev (Eq. (12)) [17], Kawski-Chamma-Viallet (Eq. (13)) [18,19] for our calculations.

$$\overline{\nu_a} - \overline{\nu_f} = m_{LM}F_{LM}(\varepsilon,n) + \text{constant} \quad (11)$$

$$\overline{\nu_a} - \overline{\nu_f} = m_{Bk}F_B(\varepsilon,n) + \text{constant} \quad (12)$$

$$\frac{\overline{\nu_a}+\overline{\nu_f}}{2} = -m_{KCV}F_{KCV}(\varepsilon,n) + \text{constant} \quad (13)$$

where, $\overline{\nu_a}$ and $\overline{\nu_f}$ are the absorption and emission wavenumbers (in cm^{-1}) at maxima of spectra respectively. The m_{LM}, m_B, m_{KCV}, are the slopes obtained by the linear fit to the graph (Figure 3) plotted using Eq. (11), (12) and (13). The solvent polarity functions F_{LM}, F_B, F_{KCV}, are given by Eq. (14), (15), (16).

$$F_{LM}(\varepsilon,n) = \frac{\varepsilon-1}{2\varepsilon+1} - \frac{n^2-1}{2n^2+1} \quad (14)$$

$$F_B(\varepsilon,n) = \frac{2n^2+1}{n^2+2}\left[\frac{\varepsilon-1}{\varepsilon+2} - \frac{n^2-1}{n^2+2}\right] \quad (15)$$

$$F_{KCV}(\varepsilon,n) = \left[\frac{2n^2+1}{2(n^2+2)}\left(\frac{\varepsilon-1}{\varepsilon+2} - \frac{n^2-1}{n^2+2}\right) + \frac{3(n^4-1)}{2(n^2+2)^2}\right] \quad (16)$$

The slopes m_{LM}, m_B, m_{KCV}, obtained are expressed in equations (17), (18), (19) corresponding to the dipole moments.

$$m_{LM} = \frac{2(\mu_e-\mu_g)^2}{hca^3} \quad (17)$$

$$m_B = \frac{2(\mu_e-\mu_g)^2}{hca^3} \quad (18)$$

$$m_{KCV} = \frac{2(\mu_e-\mu_g)^2}{hca^3} \quad (19)$$

3.1.3 Empirical method of Riechardt

Unlike in previous methods, here we estimate the dipole moment of the probe in excited state

using empirical polarity scale proposed by Riechardt [5]. This method involves in correlating the spectral shifts with the empirical microscopic solvent polarity parameter [E_T^N]rather than the expressions involving bulk properties of solvents like dielectric constant (ε) and refractive index (n). The expression given by Riechardt is,

$$\overline{\nu_a} - \overline{\nu_f} = m_R E_T^N + \text{constant} \quad (20)$$

where $E_T^N$is the normalized solvent polarity [23] which is a solvatochromic parameter with reference to the absorption wave number of a standard Betaine dye in the corresponding solvent.

$$E_T^N = \frac{E_T(30)solvent - E_T(30)TMS}{E_T(30)water - E_T(30)TMS}$$

$$E_T^N = \frac{E_T(30)solvent - 30.7}{32.4} \quad (21)$$

where TMS is tetramethyl silane which is a well-known non-polar solvent and $E_T(30)$ is empirical solvent polarity parameter with

$$m_R = 11307.6\left[\left(\frac{\Delta\mu}{\Delta\mu_B}\right)^2\left(\frac{a_B}{a}\right)^3\right] \quad (22)$$

where Δμ and $\Delta\mu_B$ (=9D) are the differences is the dipole moments of ground and excited states of the solute molecule and the Betaine dye respectively. a and a_B(=6.2A) are the Onsager's cavity radii of the probe and the Betaine molecule respectively. Using the above values in equation (22) after finding the slope m_R in eq. (20), the final expression is,

$$\Delta\mu = \mu_e - \mu_g = \left[\frac{m_R \times 81}{\left(\frac{6.2}{a}\right)^3 11307.6}\right]^{1/2} \quad (23)$$

3.2 Onsager's equation for cavity radius

To compute all the dipole moment values it becomes necessary to find the cavity radius of the molecule. We follow the famous Onsager's cavity radius formula for the same [24,25].

$$a = \left[\frac{3M}{4\pi\rho N_A}\right]^{1/3} \quad (24)$$

where ρ is the density of the solute molecule, M being the molecular weight and N_A is the Avogadro's number.

3.3 Computational details

We have extensively used molecular modelling to explore the quantum chemistry taking place in and around the molecule. Gaussian 16 molecular modelling package was the tool for our work. We have optimized the geometrical structure of the molecule and then studied the solvatochromism effects on its stability and structure. We did ground state optimization in gaseous phase along with frequency calculations using Density Functionality Theory (DFT), with B3LYP – 6-311G + (d, p) basis sets [20]. Also carried out excited state optimization using TD-DFT. Later we switched over to a step lower due to the computational limits and explored the solvatochromism of the molecule in 6-311G (d, p). Both DFT and TD DFT methods were confronted in 14 different solvents so as to geometrically optimize and find the behaviour of the dipole moments of TBPO in ground and excited state. We extracted the Infrared spectroscopic data and also mulliken charges to study and compare them with experimental results.

4. Results and discussions

To gain an insight into the electronic properties of the dye in ground and excited state we have studied the solvatochromism and their effects on dipole moments in three classes of solvents, which are: Polar protic or

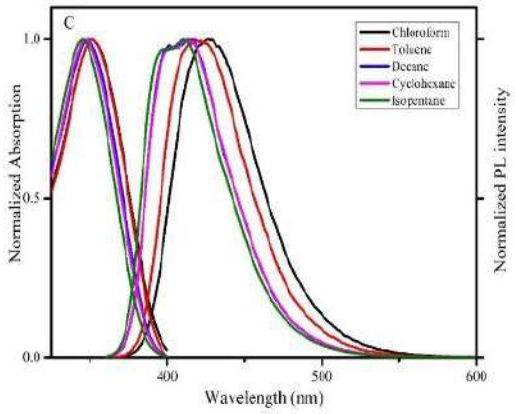

Alcohols, Polar aprotic and weakly polar or non-polar solvents. Both the experimental and computational results are described below:

4.1 Solvent effects on absorption and emission spectra of the dye

The molecule appears to be a competitive candidate for real-time OLED applications. In order to explore the solvent effects on the property of molecule we undertook this experiment of solvatochromism on our

molecule. The normalized absorption and fluorescence spectra are shown in Figure 2 being solvated in alcohols, polar and non-polar solvents. The spectroscopic information regarding maxima peaks in different solvents has been enlisted in Table S1 (ESI). All the calculated solvent polarity parameters which are to be used in plotting graphs of different methods are given out in Table 1. The necessary values of E_T^N are directly taken from reference [12].

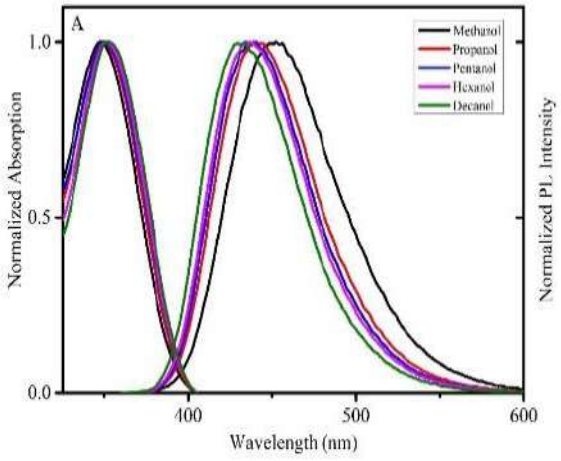

Figure 2. Normalized absorption and emission spectra of TBPO in (A) Alcohols, (B) Polar solvents (C) Non-polar Solvents.

The information in Table S1 (ESI) shows the behaviour of the dye in different solvent conditions. We have clearly seen the shifts observed in each class of solvents are discriminatory. In each group of solvents, we have noted an absolute hipsochromic shift with respect to decrease in the polarity (or dielectric

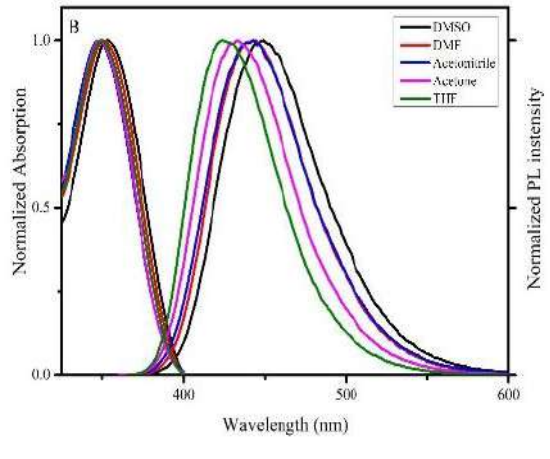

constant ϵ) of solvents. We have also observed very similar results in our previous work carried out on a well-known commercially available dye [26]. We should also consider the fact that even the Stokes' shift is following almost linear trend with polarity of the solvents. However, this effect ceases when it comes to nonpolar solvents. Another noteworthy point here is that the absorption maxima in all the solvents lie between 346 nm and 353 nm (7 nm difference), whereas, the emission maxima varies from 411 nm to 452 nm (41 nm difference). Which symbolizes the energy of the excited state is more affected than that of the ground. It means that this dye, in its excited state is more stabilized than that of the ground state. We can also regard here that the dipole moment of the excited state will be more than that of the ground state. The Stokes shift value varies from a minimum of 4522.5 cm^{-1} in cyclohexane to a maximum of 6694 cm^{-1} in methanol. These fluctuations reveal that there is substantial interaction of dye with the solvents, which alter its electronic structure and geometry at least up to a small extent. This may also be accounted to hydrogen bond acceptor/donor strength and polarity of the solvent.

4.2 Estimation of ground and excited state dipole moments using solvatochromism.

The solvatochromic shifts usually arise due to two different kinds of solute solvent interactions. In general type, an important role is played by the dielectric constant and the refractive index. Where as in specific type of interaction it is the hydrogen bonding, n-donor and π-donor of the solvents come into play. As discussed earlier in the theory, we have methods for correlating the spectral shifts and the solvent parameters using the models given by Bilot-Kawski, Lippert-Mataga, Bakhshiev, Kawski-Chamma-Viallet and Riechardt [Equations (1) to (20)]. The graphs for each methods were plot with $\overline{\nu_a} - \overline{\nu_f}$ vs.$F_1(\varepsilon, n)$, $\overline{\nu_a} - \overline{\nu_f}$vs.$F_1(\varepsilon, n) + 2g(n)$, $\overline{\nu_a} - \overline{\nu_f}$vs.$F_{LM}(\varepsilon, n)$, $F_B(\varepsilon, n)$, E_t^N and $\frac{\overline{\nu_a}+\overline{\nu_f}}{2}$vs.$F_{KCV}(\varepsilon, n)$for polar protic, polar

aprotic (alcohols) and non-polar solvents separately so as to get the maximum fit. Then the points were linearly fitted and the slopes, intercepts and correlation coefficients are extracted which are shown in Table 1. The plots for non-polar solvents are shown in Figure3and further are given in ESI (Figure S1 & S2). At some places we may note that the linearity is breached, for which short range specific interactions can be made responsible. We have fitted the data such that the correlation coefficient is always having a good value (0.811 to 0.999) also considering maximum solvents to come under the vicinity of the fitted line. We can also note here that the discrepancies are seen more in polar solvents than the non-polar solvents which proves the specific interaction like hydrogen bonds are stronger in polar solvents.

Table 1. Data of linear plots plotted for TBPO in various class of solvents.

Solvent set	Method		Slope	Intercept	Correlation coefficient (R^2)	No. of data point
Alcohols:	Bilot-Kawski	m_1	4344.30	2815.16	0.87598	4:5
		m_2	11882.07	66418.88	0.99573	3:5
	Lippert-Mataga	m_{L-M}	13542.09	2396.04	0.88845	5:5
	Bakhshiev	m_B	4510.33	2632.99	0.81607	5:5
	Kawski-Chamma-Viallet	m_{KCV}	2869.36	27534.61	0.85170	3:5
	Reichardt	m	172.4	-2811.58	0.91000	5:5
Polar Aprotic	Bilot-Kawski	m_1	3653.54	2976.12	0.99304	4:5
		m_2	5098.03	58193.44	0.96996	4:5
	Lippert-Mataga	m_{L-M}	12826.95	2420.12	0.81127	4:5
	Bakhshiev	m_B	3587.34	2967.18	0.88763	5:5
	Kawski-Chamma-Viallet	m_{KCV}	4037.75	28353.5	0.94319	5:5
	Reichardt	m	144.60	-427.97	0.94719	5:5
Non-Polar /Slightly Polar:	Bilot-Kawski	m_1	1475.54	4523.53	0.99978	4:5
		m_2	2625.83	54462.8	0.99493	4:5
	Lippert-Mataga	m_{L-M}	3616.98	4533.55	0.99047	5:5
	Bakhshiev	m_B	1442.73	4535.07	0.99090	5:5
	Kawski-Chamma-Viallet	m_{KCV}	2684.01	27229.44	0.95362	5:5
	Reichardt	m	62.71	2571.19	0.86015	5:5

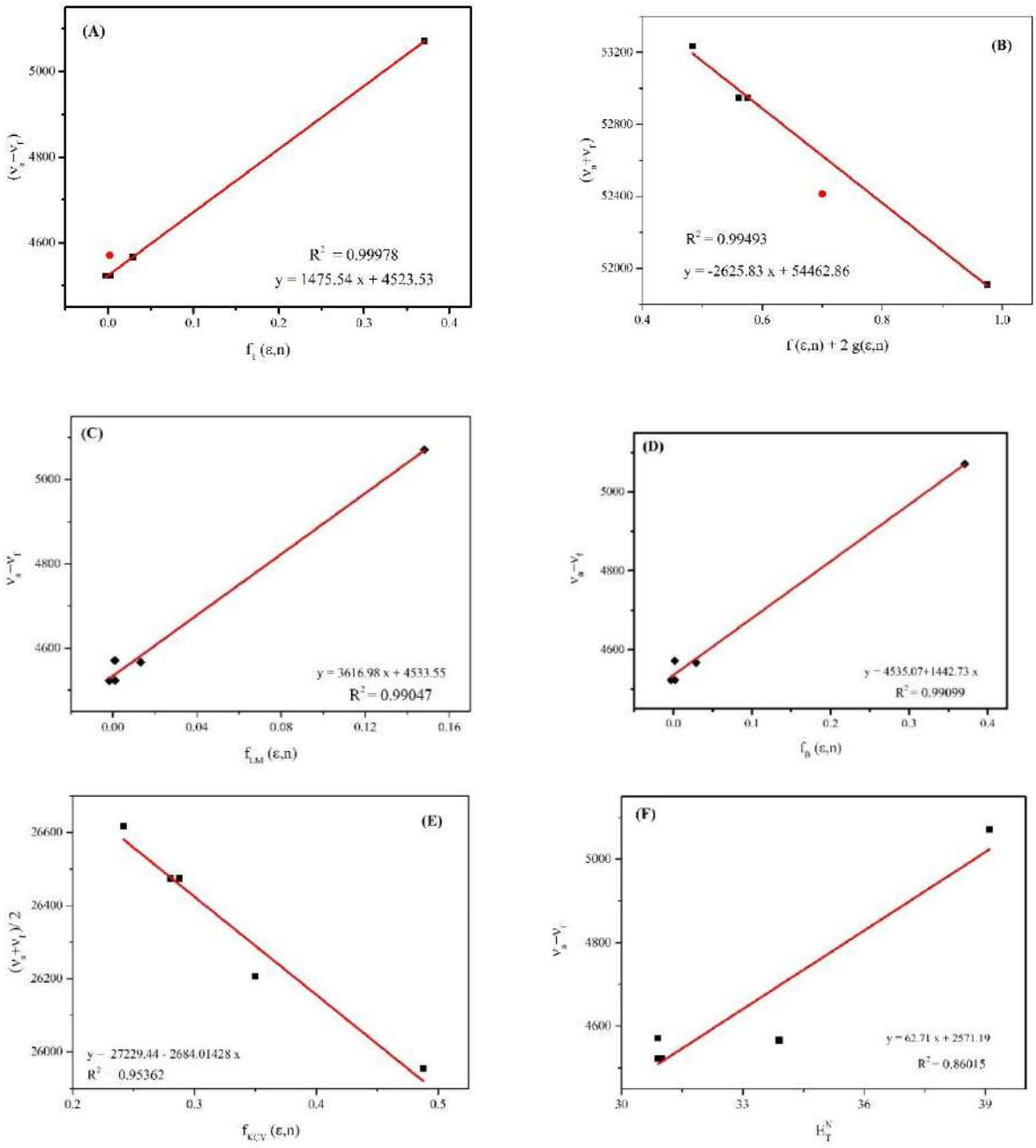

Figure 3. Linear correlation plots of various methods for nonpolar solvents; (A,B) Bilot-Kawski, (C) Lippert-Mataga, (D) Bakhshiev, (E)Kawski-Chamma-Viallet and (F) Riechardt.

The slopes m_1 and m_2 are obtained from Bilot-Kawski plots, to get the ground and excited state dipole moments using the equations (7) & (8). Further, the values of singlet excited state dipole moments of the molecule are calculated employing slopes found according to the theories put forward by Lippert- Mataga, Bakhshiev and Kawski-Chamma-Viallet which are m_{LM}, m_B and m_{KCV} respectively. These slopes are used in equations (17), (18) and (19) along with the ground state dipole moment calculated in Bilot-Kawski method to get the first excited state dipole moment value. The empirical microscopic solvent polarity (E_T^N) method by Riechardt also gives the excited state dipole moment value as per the theory. All the calculated data including the dipole moment values, the difference between dipole moments ($\Delta\mu$), dipole moment ratio (μ_e/μ_g), Onsager cavity radius and angle between the dipole moments have been tabulated in Table 2.

Table 2. The values of ground and excited state dipole moments calculated by various solvatochromism methods.

Solvents	A^a	μ_g^b	μ_e^b	$\mu_{e(LM)}^c$	$\mu_{e(B)}^d$	$\mu_{e(KCV))}^e$	$\mu_e^f(R)$	$_{\Delta}\mu_e^g$	$\frac{\mu_e{}^f}{\mu_g}$	ϕ^i
Alcohols	4.68	5.77	12.42	17.51	12.5	7.90	6.50	6.65	1.12	2.09
Polar aprotic	4.68	1.20	7.30	12.63	7.25	6.52	1.87	6.10	1.55	25.3
Non-polar	4.68	1.51	5.38	7.58	5.34	5.44	1.95	3.87	1.29	1.63

[a]Onsager radius calculated using Edward's atomic increment method.
[b] Ground and excited state dipole moments obtained using Bilot–Kawski method (eqn (1) and (2)).
[c] Excited state dipole moment calculated using Lippert Mataga method (eqn. (11)).
[d] Excited state dipole moment obtained using Bakhshiev method (eqn. (12)).
[e] Excited state dipole moment calculated using Kawski–Chamma–Viallet method (eqn. (13)).
[f] Excited state dipole moment calculated using Reichardt method (eqn. (20)).
[g] Difference between ground and excited state dipole moments is calculated for Bilot-Kawski method.
[h] Angle between the ground and excited state dipole moments obtained using eqn. (10).

Now, coming to the computational work using Gaussian16 software, the ground state dipole moment of the dye is 3.9433D and that of excited state is 4.0347D in gas phase. The solvatochromism effects on dipole moment and their values are enlisted in TableS2 (ESI)according to the class of solvents. In all the solvents and gas phase we must note that the excited state dipole moment is always higher than the ground state dipole moment. It clearly suggests that the molecule is highly stable in its first excited state. This may be accounted to the irregularity in charge distribution when excited which can be again attributed to the change in geometry. Basically, the existence of a strong dipole in a molecule enables it to interact with neighbouring entities. Direction of ground and excited state dipole moments along with optimized geometry has been shown in Figure 4.

We should also stress here that the dipole moment values of the dye in three different class of solvents has led us to understand the nature of interaction. We can clearly note that the values for each class of solvents varies considerably, which signifies this method of separating solvents will give a better result as compared to taking them all at once. We have also observed comparable agreement between different excited state dipole moment values calculated using various theoretical considerations. In our case the excited state dipole moment obtained from Lippert-Mataga method is highest in all the three cases as compared to all other methods (Table1). The reason behind this can be attributed to the fact that Lippert-Mataga co-efficient $F_{LM}(\varepsilon, n)$as in eq.(11), deals with simpler polynomials (second order), whereas other methods use higher order expressions of $(\varepsilon, n)$to go more deeper into the practicality. The ratios between excited and ground state dipole moment values have been calculated for Riechardt method and the values for polar, non-polar and alcoholic solvents are 1.55, 1.29 and 1.12, respectively, which are fairly comparable with the ratio we got from TD-DFT and DFT calculations which is 1.02 (Table 2). Another noteworthy point here to consider is that the difference between excited state and ground state dipole moments in highly polar solvents are nearly 6 D, whereas, that for the weakly polar solvent is low as 3 D, which shows that the TBPO is highly polarizable.

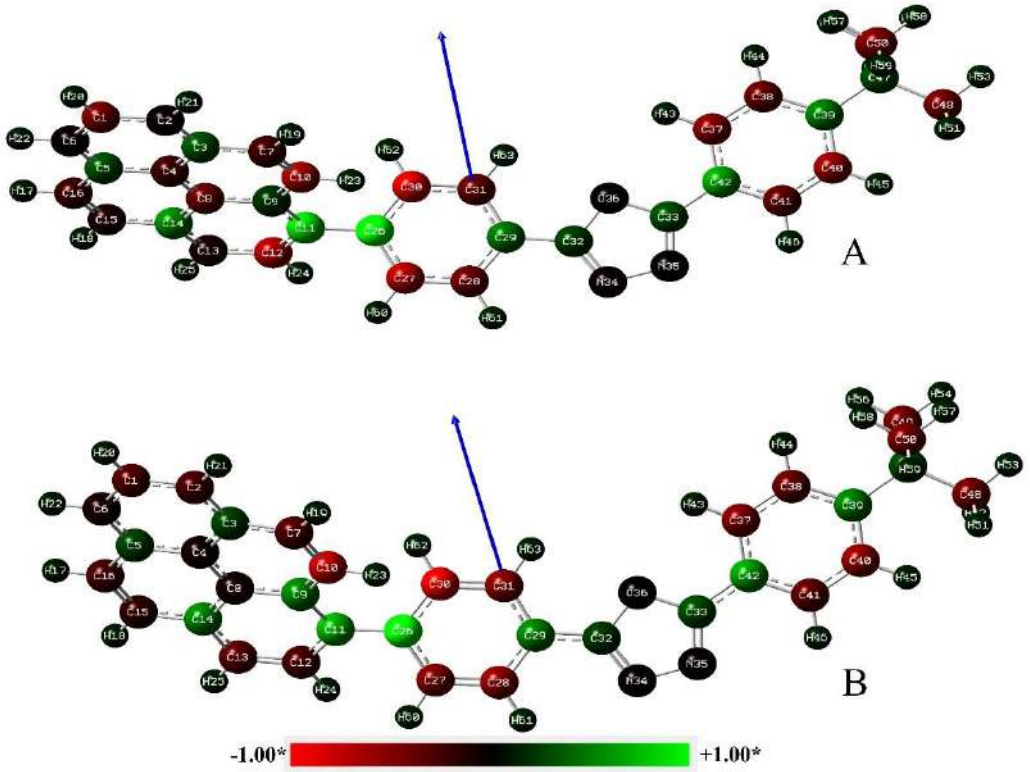

Figure 4. The optimized molecular structure of TBPO with charge gradient and dipole orientation; (A) Ground state, (B) First excited state. (*Normalized colour range for charge distribution).

4.3 *Computational studies using molecular modelling*

Apart from the experimental findings, we have also used the quantum mechanical formulations through Gaussian16 molecular modelling software, in order to obtain a more visual and statistical understanding of the molecular structure and electronic properties. For ground state calculations we have used DFT and Excited state calculations being carried out using TD-DFT at level B3LYP/6-311 G (d, p) for both. The optimized ground and excited state molecular geometry is shown in Figure 4, where the arrow mark signifies the direction of dipole moment.

We have employed the Integral Equation Formalism for the Polarisable Continuum Model (IEF-PCM) to observe the effects of various solvents on the geometry and electronic spectra of the molecule. We have obtained the theoretically computed values for the excitation energies, oscillator strengths and even the absorption spectra of the molecule in Polar, Nonpolar and Alcoholic solvents (except Isopentene) and also in gas phase using TD-DFT in B3LYP/ 6-311G (d, p) level. We have known that this theory is more reliable for computing excited state electronic properties of a molecule by articles on applications of TD-DFT [27-29]. The comparison between absorption energies estimated through software can be compared with the experimental results. Even though we see a significant difference; the trend is very similar. The above said data can be seen in Table S2 (ESI).

Charge on each atom are really an important parameter which determine the stability, molecular orbitals, polarizability and other electronic characters of the molecule [30]. We have obtained the mulliken charge distribution on each of the atoms using DFT/B3LYP 6-311G (d, p) in vacuum in order to gain understanding on the natural population (NPA) of charges throughout the molecule. We can see the ground state and

excited state mulliken charges listed in the Table S3. The graphical representation of the natural population analysis is given through a bar graph shown in Figure 5. In ground state few atoms which are highly electronegative considered to be donors to the molecular structure viz. C26, C11, C42 and so on. Also, almost half of the carbon atoms are positively charged so as to give it a stable structure. A notable feature here is that highly negative atom Oxygen after forming the molecule loses its charge and gets almost neutral and thus contributing not much of charges to the molecule. When the same molecule is excited, we see an increment in values of certain atomic charges. Even nitrogen (N34, N35) atoms do not carry a considerable charge on them in this scenario. The positively charged atoms gain more positive charge and negatively charged atoms get negatively charged due to the absorption of radiation and thus increasing the dipole value, also the stability. The region where atoms like C11, C26, C27 and C30 are present must be the cite with highest polarization and thus the point of formation of the dipole

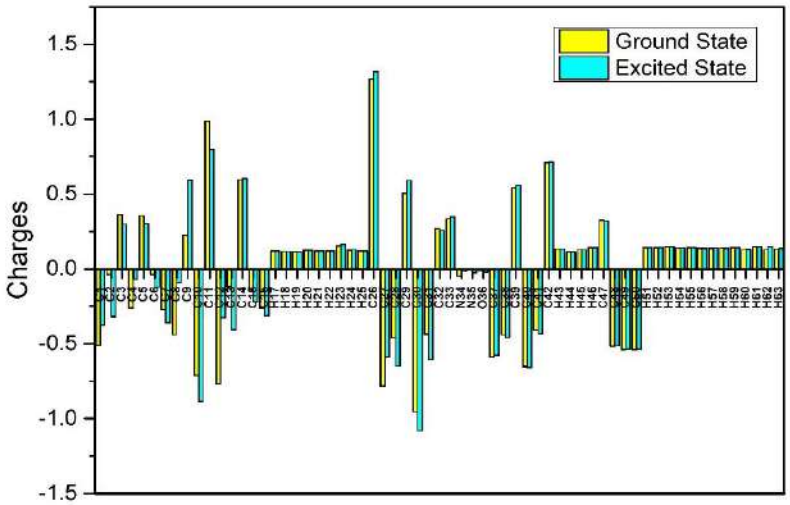

.

Figure 5. Bar graph for comparison of charges on atoms of TBPO in ground and excited state.

4.4 Comparison of IR spectra.

We here have also tried to include the study on the faithfulness of the computational method to simulate the IR absorption spectrum by comparing it with the experimental spectrum obtained by an FTIR spectrometer. For computation we have utilised DFT/ B3YLP 6-311G + (d, p) level of theory. We have compared the analysed data in the Table 3 for an easy understanding. The comparison of both DFT simulated data and the experimental spectra are given in Figure 6. The peaks we observe at higher wavenumbers are attributed to the C-H stretching, where the values of DFT and experiment vary with a small amount. However, when the peaks approach towards the lower wavenumbers, the gap between them decreases and comes to a very good agreement. This behaviour of experimental result which lags a bit at higher wavenumbers may have arrived due to various instrumental and optical errors. This method can be used to re-verify the synthesized molecule and the targeted molecules match a lot beyond all the experimental problems. We can also note that very important bonds and their vibrations like C-N stretching and C-O stretching without any bending show the molecule is structurally stable which indeed makes it a good emitter.

Table 3. Comparison of IR peaks of simulated and experimental data for TBPO with assignment of their groups.

Transmittance peaks (cm^{-1})		Character	Corresponding Vibrations
DFT	Experimental		
3180	3040		
3092	2950	Strong	C-H stretching
3028	2870		
1652	1610	Strong	C=C Stretching
1524	1490	Medium	C-H Bending
1436	1410		
1284	1270	Strong	C-O Stretching
1076	1070	Medium	C-N Stretching
1036	1020	Medium	C-O Stretching
860	841	Strong	C=C bending
732	721	Strong	C-H Bending

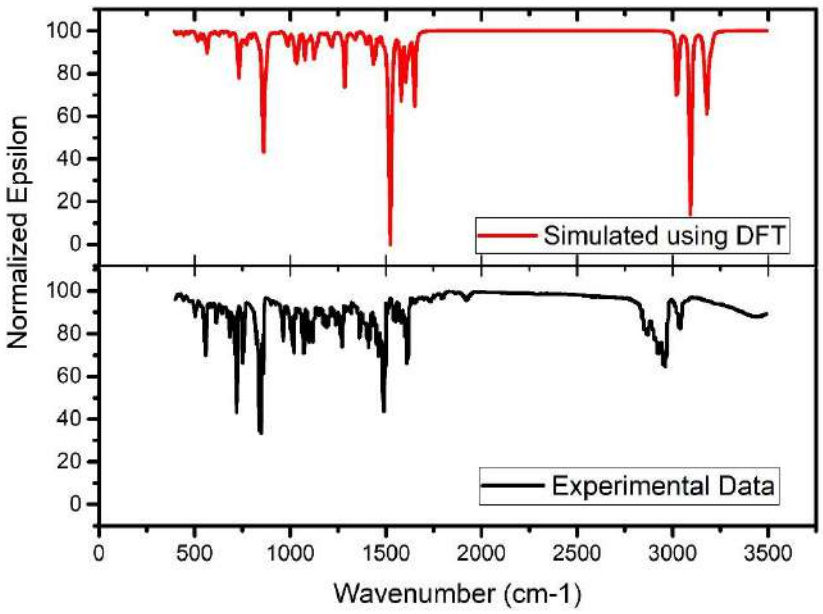

Figure 6. Spectra of infrared information obtained both by simulation and experiment.

5. Conclusion

Here, in this work we have continued to study few physical and chemical properties of a synthesized molecule along with few theoretical explorations on it. We have estimated the ground and excited state dipole moments experimentally using solvatochromic methods and also computationally. The effect of solvatochromism on the UV-Visible absorption and fluorescence spectra was studied with an aim to understand the behavior of the molecule in various environments. To estimate the ground and excited state dipole moments, we have used different solvatochromic methods like Bilot-Kawski,

Lippert Mataga, Bakhshiev, Kawski-Chamma-Viallet and Reichardt's solvent polarity parameter method. For computational studies we have used Gaussian16 package to compute the theoretical parameters of the molecule through DFT and TD-DFT methods. In all the above methods we have come to a good agreement with the fact that for this molecule, the excited state dipole moment is higher than the ground state one,which signifies the stability of the molecule in first excited state is higher than that of the ground state due to the absorption of energy leading to higher polarization. The study on NPA and mulliken charges reveal that the stability of the molecule is due to polarization in pyreneregion. The vibrational study was carried out to compare physical form of the sample with the theoretical counterpart, in which we see a good agreement between both.

Acknowledgement

The authors gratefully thank University Grants Commission (UGC) for financial support under CPEPA. TST would like to thank UGC for NET-JRF fellowship. The authors thank the University Scientific Instrumentation Centre, Karnatak University, Dharwad for providing instrumentation and UPE-FAR-1 Molecular Modeling Lab for computational facility.

ESI: Electronic supplementary information is available with this manuscript.

References

[1] A-monrat Thangthong, Narid Prachumrak, Supawadee Namuangruk, Siriporn Jungsuttiwong, Tinnagon Keawin, Taweesak Sudyoadsuk, Vinich Promarak, Eur. J. Org. Chem., 5263-5274 (2012).

[2] Aneta Slodek, Michal Filapek, Ewa Schab-Balcerzak, Marzena Grucela, Sonia Kotowicz, Henryk Janeczek, Karolina Smolarek, Sebastian Mackowski, Jan Grzegorz Malecki, Agnieszka Jedrzejowska, Grazyna Szafraniec- Gorol, Anna Chrobok, BeataMarcol, Stanislaw Krom, Eur. J. Org. Chem, 4020-4031 (2016).

[3] Mahesh S. Najare, Mallikarjun K. Patil, AfraQuasar A. Nadaf, ShivarajMantur, Sanjeev R. Inamdar, Imtiyaz Ahmed M. Khazi, Optical Materials, 256–265 (2019).

[4] N.H. Ayachit, G.N. Rani, Excited state electric dipole moments of two laser dyes from solvatochromic shift measurements, Phys. Chem. Liq, 615–621 (2007).

[5] Reichardt, C. Solvatochromic dyes as solvent polarity indicators, Chem. Rev, 2319-2358 (1994).

[6] Suppan, P. Solvatochromic shifts: the influence of the medium on the energy of electronic states, J. Photochem. Photobiol. A Chem., 50, 293–330 (1990).

[7] J. Basavaraja, H.M. Suresh Kumar, S.R. Inamdar, M.N. Wari. Estimation of ground and excited state dipole moment of laser dyes C504T and C521T using solvatochromic shifts of absorption and fluorescence spectra, Spectrochim. Acta A Mol. Biomol. Spectr., 154, 177-184 (2016).

[8] J.R. Mannekutla, B.G. Mulimani, S.R. Inamdar, Solvent effect on absorption and fluorescence spectra of coumarin laser dyes: evaluation of ground and excited state dipole moments, Spectrochim. Acta A Mol. Biomol. Spectrosc, 69, 419–426 (2008).

[9] R. Kumari, A. Varghese, L. George, Synthesis, crystal structure and photophysical properties of (E)-4-(4-(2-hydroxybenzylideneamino) benzyl) oxazolidin-2-one, J. Lumin., 179, 518-526 (2016).

[10] İ. Sıdır, Y.G. Sıdır, Investigation on the interactions of E-4-methoxycinnamic

acid with solvent: solvatochromism, electric dipole moment and pH effect., J. Mol. Liq., 249, 1161-1171 (2018).

[11] S. K. Patil, M.N. Wari, C. Yohannan Panicker, S.R. Inamdar., Determination of ground and excited state dipole moments of dipolar laser dyes by solvatochromic shift method. SpectrochimicaActa Part A: Molecular and Biomolecular Spectroscopy, 123, 117–126 (2014).

[12] Reichardt, C. Solvents and Solvent Effects in Organic Chemistry, Third ed. WeinheimGermany:WileyVCH, (2005).

[13] L. Bilot, A. Kawski, Z. Naturforsch., A: Phys. Sci., 17a, 621-627 (1962).

[14] A. Kawski, in: J.F. Rabek (Ed.). Progress in Photochemistry and Photophysics. Boca Raton, USA: CRC Press, 1–47 (1992).

[15] Lippert, V.E. Dipole moment und elektronenstruktur von angeregtenmolekülen, Z. Naturforsch., A: Phys. Sci., 10a, 541–545 (1955).

[16] N. Mataga, Y. Kaifu, M. Kolzumi, Solvent effects upon fluorescence spectra and the dipole moments of excited molecules, Bull. Chem. Soc. Jpn. , 29, 465–470 (1956).

[17] Bakhshiev, N.G., Opt. Spektrosk, pp. 16, 821–832 (1964).

[18] A. Kawaski., Acta Phys. Polon., 29, 507–518 (1966).

[19] A. Chamma, P. Viallet., C.R. Hebd. Seances Acad. Sci., 270, 1901–1904 (1970).

[20] M. J. Frisch, G. W. Trucks, H. B. Schlegel, G. E. Scuseria, M. A. Robb, et. Al., Gaussian 16, Revision A.03, Gaussian, Inc., Wallingford CT, (2016).

[21] G.H. Pujar, M.N. Wari, B. Steffi, H. Varsha, B. Kavita, C.Y. Panicker, C. Santhosh, A. Patil, S.R. Inamdar A combined experimental and computational investigation of solvatochromism of nonpolar laser dyes: evaluation of ground and singlet excited state dipole moments, J. Mol. Liq., 244, 453–463 (2017).

[22] Kawski, A. On the estimation of excited-state dipole moments from solvatochromic shifts of absorption and fluorescence spectra., Z. Naturforsch., A: Phys. Sci, 57a, 255–262 (2002).

[23] M. Ravi, T. Soujanya, A. Samanta, T.P. Radhakrishnan, Excited-state dipole moments of some coumarin dyes from a solvatochromic method using the solvent polarity parameter, J. Chem. Soc. Faraday Trans., 91, 2739–2742 (1995).

[24] P. Suppan. Excited-state dipole moments from absorption/fluorescence solvate chromic ratios., Chem. Phys. Lett., 94, 272–275 (1983).

[25] John T. Edward. Molecular volumes and the stokes-einstein equation., J. Chem. Educ., 47, 261–270 (1970).

[26] Mallikarjun K. Patil, M.G. Kotresh, Sanjeev R. Inamdar. A combined solvatochromic shift and TDDFT study probing solute-solvent interactions of blue fluorescent Alexa Fluor 350 dye: Evaluation of ground and excited state dipole moments., SpectrochimicaActa Part A: Molecular and Biomolecular Spectroscopy, 215, 142-152 (2019).

[27] Krawczyk, Przemysław. Time-dependent density functional theory calculations of the solvatochromism of some azo sulphonamide fluorochromes., J. Mol. Model., 21, 118 (2015).

[28] Abdulilah Dawoud Bani-Yaseen, Mona Al-Balawi, The solvatochromic, spectral, and geometrical properties of nifenazone: a DFT/TD-DFT and experimental study., Phys. Chem. Chem. Phys., 16, 15519 (2014).

[29] Wenwei Zhao, Yihong Ding, Qiying Xia, Time-dependent density functional theory study on the absorption spectrum of coumarin 102 and its hydrogen-bonded complexes. J. Comput. Chem., 32, 545–553 (2011).

[30] S. A. Khan, A.M. Asiri, S.H. Al-Thaqafy, H.M. Faidallah, S.A. El-Daly, Synthesis, characterization and spectroscopic behavior of novel 2-oxo-1, 4-disubstituted-1, 2, 5, 6- tetrahydrobenzo [h] quinoline-3-carbonitrile dyes, Spectrochim. Acta A Mol. Biomol., 133, 141–148 (2014).

[31] Eric D. Glendening, Clark R. Landis and Frank Weinhold. Natural bond orbital methods., WIREs Comput. Mol. Sci., 2, 1-42 (2012).

[32] F. Weinhold, C.R. Landis, Natural bond orbitals and extensions of localized bonding concepts., Chem. Educ. Res. Pract. Eur., 2, 91–104 (2001).

[33] M. Szafran, A. Komasa, E. Bartoszak-Adamska, Crystal and molecular structure of 4- carboxypiperidinium chloride (4-piperidinecarboxylic acid hydrochloride), J. Mol. Struct., 827, 101–107 (2007).

[34] R. J. Xavier, E. Gobinath, Experimental and theoretical spectroscopic studies, HOMO– LUMO, NBO and NLMO analysis of 3, 5-dibromo-2, 6-dimethoxy pyridine, Spectrochim. Acta A Mol. Biomol. Spectrosc., 97, 215–222 (2012).

[35] A.E. Reed, L.A. Curtiss, F. Weinhold,. Intermolecular interactions from a natural bond orbital, donor-acceptor viewpoint, Chem. Rev., 88, 899–926 (1988).

A computational study combined with experiments to investigate the molecular interactions of a novel organic dye: Exploring the values of ground and excited state dipole moments

Supplementary information:

Contents

Supplementary information:

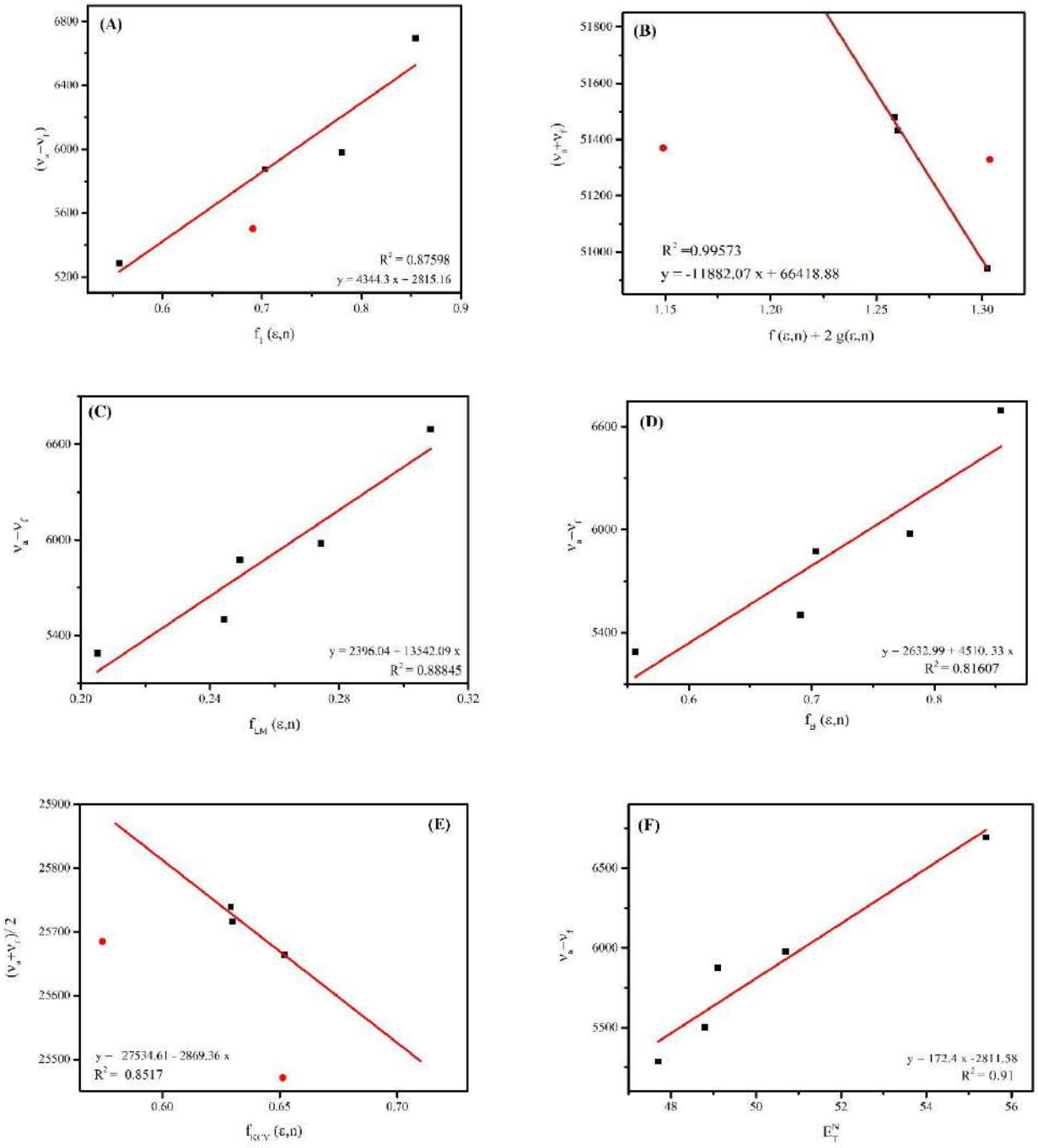

Figure S1. Linear correlation plots of various methods for Alcoholic solvents; (A, B) Bilot-Kawski, (C) Lippert-Mataga, (D) Bakhshiev, (E) Kawski-Chamma-Viallet and (F) Riechardt.

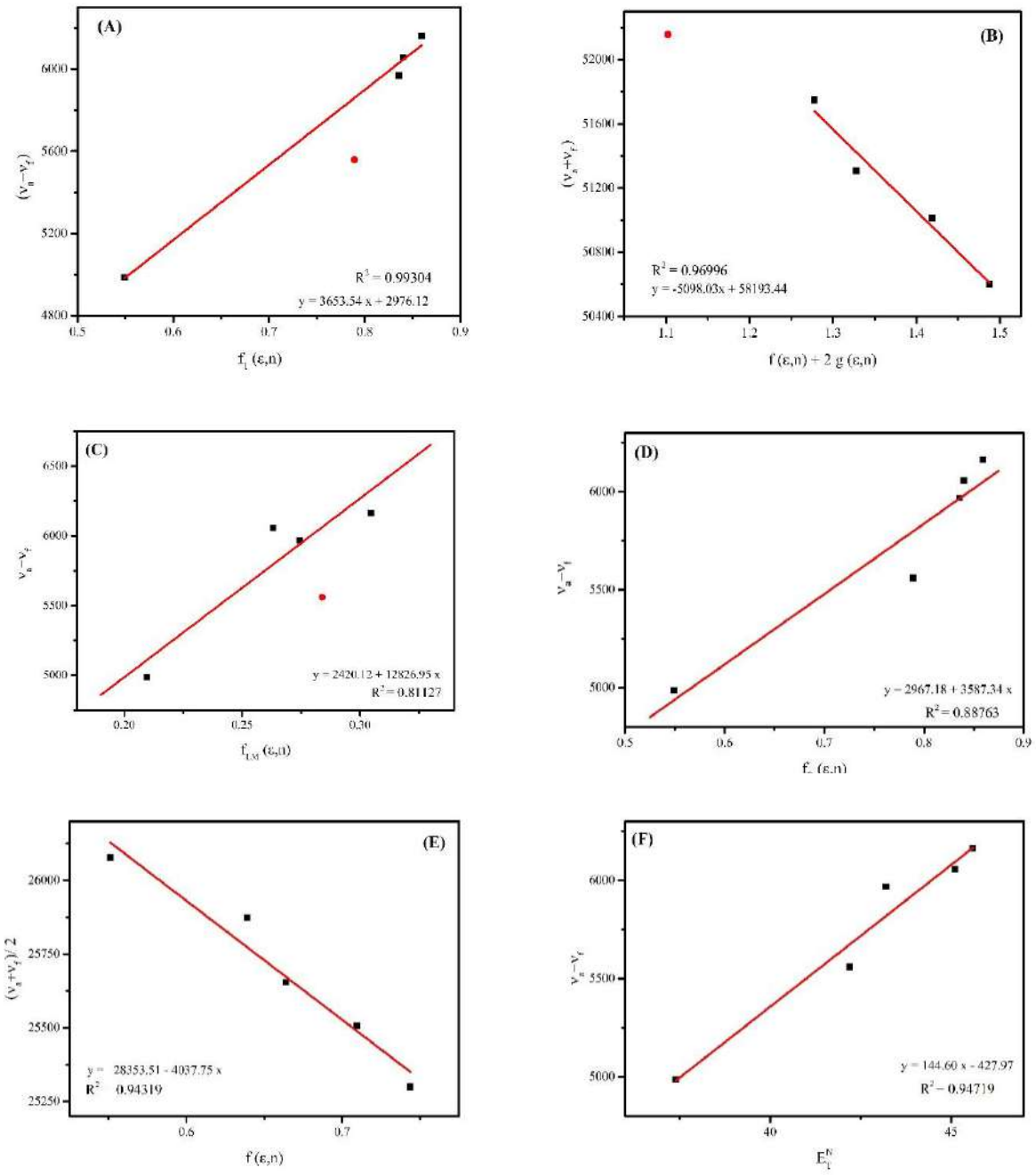

Figure S2. Linear correlation plots of various methods for Polar Aprotic solvents; (A, B) Bilot-Kawski, (C) Lippert-Mataga, (D) Bakhshiev, (E) Kawski-Chamma-Viallet and (F) Riechardt.

TableS1. Absorption and emission maxima in nm; listing of stokes shift in cm^{-1}.

Type of solvent	Solvents	λ_{abs} (nm)	λ_{emi} (nm)	$\bar{\nu}_a$ (cm^{-1})	$\bar{\nu}_f$ (cm^{-1})	$\bar{\nu}_a - \bar{\nu}_f$ (cm^{-1})	$\bar{\nu}_a + \bar{\nu}_f$ (cm^{-1})	$\frac{\bar{\nu}_a + \bar{\nu}_f}{2}$ (cm^{-1})
Alcohols:	Methanol	347	452	28818.4	22123.9	6694.5	50942.3	25471.2
	Propanol	349	441	28653.3	22675.7	5977.5	51329.1	25664.5
	Pentanol	349	439	28653.3	22779.0	5874.2	51432.3	25716.1
	Hexanol	351	435	28490.0	22988.5	5501.5	51478.5	25739.2
	Decanol	353	434	28328.6	23041.5	5287.1	51370.1	25685.1
Polar aprotic:	DMSO	353	449	28328.6	22271.7	6056.8	50600.3	25300.1
	DMF	351	444	28490.0	22522.5	5967.5	51012.5	25506.2
	Acetonitrile	348	443	28735.6	22573.4	6162.2	51308.9	25654.4
	Acetone	349	433	28653.3	23094.7	5558.6	51748.0	25874.0
	THF	350	424	28571.4	23584.9	4986.5	52156.3	26078.2
Weakly polar:	Chloroform	351	427	28490.0	23419.2	5070.8	51909.2	25954.6
	Toluene	351	418	28490.0	23923.4	4566.5	52413.4	26206.7
	Decane	348	413	28735.6	24213.1	4522.5	52948.7	26474.4
	Cyclohexane	348	413	28735.6	24213.1	4522.5	52948.7	26474.4
	Isopentane	346	411	28901.7	24330.9	4570.8	53232.6	26616.3

Table S2. The dipole moment values of TBPO found computationally using Density Functional Theory

Solvents	$E_T(30)$	E_{exp}	$E_{Theory}(eV)$	μ_g^a	μ_e^b	$\Delta\mu$	$\frac{\mu_e}{\mu_g}$	Oscillator strength
Gas			2.73491	3.8258	3.9173	0.0915	1.0239	1.1096
Methenol	55.4	3.573	2.4171	5.4322	5.7975	0.3653	1.0672	1.5217
Propanol	50.7	3.553	2.4266	5.3729	5.7275	0.3546	1.0660	1.5111
Pentanol	49.1	3.553	2.4313	5.3183	5.6624	0.3440	1.0646	1.5010
Hexanol	48.8	3.532	2.4409	5.2762	5.6124	0.3361	1.0637	1.4931
Decanol	47.7	3.512	2.4652	5.1263	5.4348	0.3084	1.0601	1.4638
DMSO	45.1	3.512	2.4077	5.4638	5.8352	0.3713	1.0679	1.5273
DMF	43.2	3.532	2.4124	5.4450	5.8132	0.3682	1.0676	1.5240
Acetonitrile	45.6	3.563	2.4124	5.4411	5.8086	0.3674	1.0675	1.5235
Acetone	42.2	3.553	2.4266	5.2905	5.7268	0.4362	1.0824	1.5109
THF	37.4	3.542	2.4652	5.1218	5.4287	0.3068	1.0599	1.4627
Chloroform	39.1	3.532	2.5000	4.9299	5.2018	0.2718	1.0551	1.4231
Toluene	37.1	3.532	2.5779	4.5228	4.7239	0.2010	1.0444	1.3280
Decane	31	3.563	2.6050	4.3930	4.5725	0.1795	1.0408	1.2939
Cyclohexane	30.9	3.563	2.6050	4.4049	4.5862	0.1813	1.0411	1.2972
Isopentane	30.9	3.583	-	-	-	-	-	-

[a] Obtained using DFT/B3LYP/6-311G (d,p)/ IEF-PCM

[b] Obtained employing TD-DFT/B3LYP/6-311G (d,p)/ IEF-PCM

Table S3. Mulliken charge distribution for ground and excited states of TBPO.

Atom	Charge		Atom	Charge	
	Mulliken	NPA		Mulliken	NPA
C1	-0.51096	-0.37514	C33	0.33399	0.34923
C2	-0.03677	-0.31981	N34	-0.04815	-0.01853
C3	0.36343	0.29723	N35	-0.00651	-0.02524
C4	-0.26234	-0.07154	O36	-0.01256	-0.01897
C5	0.35620	0.30074	C37	-0.58888	-0.57592
C6	-0.03674	-0.12224	C38	-0.43781	-0.45697
C7	-0.27399	-0.36066	C39	0.53914	0.55602
C8	-0.43954	-0.09134	C40	-0.65140	-0.65645
C9	0.22493	0.59253	C41	-0.41050	-0.43251
C10	-0.71305	-0.88704	C42	0.71083	0.71379
C11	0.98574	0.79875	H43	0.13516	0.13522
C12	-0.76912	-0.32683	H44	0.11332	0.11319
C13	-0.11897	-0.40832	H45	0.12918	0.12901
C14	0.59561	0.60359	H46	0.14490	0.14481
C15	-0.13191	-0.22218	C47	0.32411	0.32171
C16	-0.26276	-0.31565	C48	-0.51727	-0.5147
H17	0.11859	0.12007	C49	-0.53986	-0.53767
H18	0.11705	0.11820	C50	-0.53916	-0.53834
H19	0.11542	0.11558	H51	0.14390	0.14376
H20	0.12647	0.12600	H52	0.14382	0.14386
H21	0.11881	0.11989	H53	0.14974	0.14963
H22	0.11913	0.12010	H54	0.14049	0.14032
H23	0.15323	0.16229	H55	0.14477	0.14475
H24	0.12661	0.12973	H56	0.13795	0.13768
H25	0.11994	0.11988	H57	0.13761	0.14031
C26	1.26693	1.31904	H58	0.14052	0.13770
C27	-0.78231	-0.58944	H59	0.14476	0.14465
C28	-0.46114	-0.64980	H60	0.12887	0.13091
C29	0.50709	0.59167	H61	0.14971	0.14930
C30	-0.95337	-1.08099	H62	0.12955	0.14975
C31	-0.43638	-0.60840	H63	0.13522	0.13622
C32	0.26853	0.25745			

Karnatak University Journal of Science 53 (2022) 99-104

Karnatak University Journal of Science

ISSN: 0075-5168

Size Controlled Thiol Capped Silver Nanoparticles

V. S. Patil[1], B. Saraswathi[1], S. V. Halse[1*], Vikram Pujari[2], and M. N. Kalasad[1]*

[1]Department of Studies in Physics, Davangere University, Davangere - 577007, India.

[2]Laser Spectroscopy Programme, Department of Studies in Physics, Karnatak University, Dharwad - 580 003, India.

***Corresponding author:** mnkalasad@gmail.com, drsvhalse@rediffmail.com*

ARTICLE INFO

Article history:
Received: 13 April 2022;
Revised: 28 April 2022;
Accepted: 28 June 2022;

Keywords:
Stability;
Nanoparticles;
XRD; optical;
Ag nanoparticles;
Thioglycolic Acid;

ABSTRACT

Silver (Ag) nanoparticles have wide range of applications due to their unique physical, chemical and biological properties dependent on their shape, size, crystallinity, composition, and structure compared to their bulk forms. So, it is necessary to explore their attractive properties in order to use for different technological applications. Ag nanoparticles with different size were prepared by chemical precipitation technique using thioglycolic acid (TGA) as capping agent. The TGA capped Ag nanoparticles were characterized by UV-Visible spectroscopy, which shows surface plasmon resonance, that gives confirmation of formation of Ag nanoparticles. FTIR spectrum proves capping of TGA on Ag nanoparticles. The X-ray diffraction measurement shows that the Ag nanoparticles exhibit face centred cubic structure and estimated particle size is in the range 13 to 16 nm. The Ag nanoparticles are examined by TEM measurement, the Ag nanoparticles are spherical in shape supports the formation of Ag nanoparticles in nanometre range.

1. Introduction:

Metal nanoparticles are applicable in many fields such as photonics, catalysis, data storage, optoelectronic and antibacterial applications, because of their different chemical physical and optical properties from that of their bulk counterpart [1-4]. Size, shape and composition of metal nanomaterial decides the properties of metal nanomaterials needed for different applications. Because of their exceptional properties like high resistance to oxidation, high electrical and thermal conductivity for the application in electronic industries in integrated circuits. Silver nanoparticles are well known for their outstanding antibacterial property because of their high surface area and direct interaction of bacterial cell wall, membranes, and nucleic acids by attaching to negative side of protein and nucleic acid and change structure which attacks the viability [5-7].

Silver nanoparticles has been synthesized in various methods such as, laser ablation [8], microwave processing [9], UV irradiation reduction [10] thermal decomposition [11], ion implantation [12], electrolysis methods [13], chemical reduction [14,15] etc. here we have chosen chemical reduction method, which easy and possible with minimum laboratory conditions [16,17]. To get particles in nanometer scale it is necessary to stabilize the surface of the particle while preparing, to prevent aggregation which leads bulk size. So, we have to use capping agents to remove surface defects of metal particles by forming coordinate bonds with metal atoms or ions [18-21]. Thiols are one type of the best capping agents. Ag+ ions are readily attached to the thiol group [22-25] in the TGA and forms coordinate bond and stops further attachment of silver particles keeps the particle size in nanometer. Here, we report the synthesis of silver nanoparticles by chemical reduction method using thioglycolic acid as passivating molecules. Sodium borohydrate ($NaBH_4$) is used to reduce the Ag+.

2. MATERIALS AND EXPERIMENTAL METHODS:

2.1 Materials:

All chemicals and reagents we used are of analytical grade. Silver nitrate ($AgNO_3$), Sodium borohydrate ($NaBH_4$), Thioglycolic acid (TGA) were obtained from sd-Fine Chemicals, India.

2.2Experimental Methods:

Here silver nanoparticles were synthesized in aqueous route at room temperature. $AgNO_3$ is used as silver source and sodium borohydrate is used for reducing $AgNO_3$. 0.05M of $AgNO_3$ solution is prepared in 60 ml of distilled water. 0.01M of $NaBH_4$ solutions prepared in water separately. 0.4 mM of TGA is added to the silver solution on stirring, then colorless solution turns to yellow turbidity. Then added 17 ml of sodium borohydrate on stirring, color of the solution turns yellow to brown and settled within 5minutes (Sample S1). The same procedure has followed by changing the quantity of sodium borohydrate by 12 ml and 8 ml, named as S2 and S3 respectively. By keeping the molarity of $AgNO_3$ and TGA constant and color of the solution become much darker as the increase the quantity of sodium borohydrate added. The settled precipitate was washed with distilled until it reaches pH 7. The collected sample was dried under incandescent lamp.

Optical absorption measurements were made using UV-Visible-NIR Spectrometer model JASCO V-670 and PL spectra were recorded using Horibha fluomax-4 Fluorspectrometer. The FTIR measurements on powdered samples were made using a Nicolet iN10 FTIR spectrometer in transmission mode. These measurements were carried out in the spectral range of 500-4000 cm^{-1} with a linear scan velocity of 0.632 cm/s, and each spectrum is an average of 100 scans. Powder X-ray diffraction (XRD) measurements were carried out using a Philip X'Pert powder diffractometer with Cu KR1 radiation (λ = 1.54056 A˚) with a scan step of 0.016 deg/s. Transmission electron

micrographs (TEM) were recorded using a JEOL-2100 electron microscope at 200 kV.

3. RESULTS AND DISCUSSIONS:

Optical properties of silver nanoparticles have its own significance to study, which reveals the wavelengths of incident light with which Ag nanoparticles have strong coupling. Absorption spectrum of Ag nanoparticle is examined by UV-Visible spectroscopy study. The absorption spectra show surface plasmon resonance peak (λ_{max}) at 358 nm (S1), 371 nm (S2) and 378 nm (S3), on which size, shape and scattering color of Ag nanoparticle are depended [26-28]. Particle size are found to be large as surface plasmon resonance (SPR) peak take red shift, width of the SPR band is relevant to size distribution of Ag nanoparticles, wide SPR band depicts the wide size distribution [29]. Ag nanoparticle having greater the sharpness and enhancement in the magnitude of the SPR band, provides superior sensing resolution even with a similar plasmon response [30]. Comparably SPR peak observed for prepared Ag particles shows good sharpness, so it is expected to have good sensing resolution and less size distribution as shown in Figure-1.

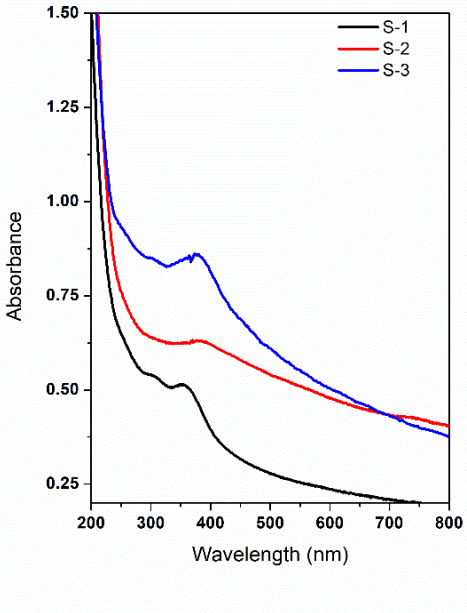

Figure 1: Optical absorption spectra of Ag nanoparticles.

Photoluminescence (PL) spectra of Ag nanoparticles are shown in the figure-2, the PL emission at 433 nm, 435 nm and 438 nm for S1, S2 and S3 samples with excitation wavelength 360 nm, 370 nm and 380 nm respectively for the samples S1, S2 and S3. The Ag nanoparticles exhibit size dependent SPR and radiative emission nature. The incident light excites the interband

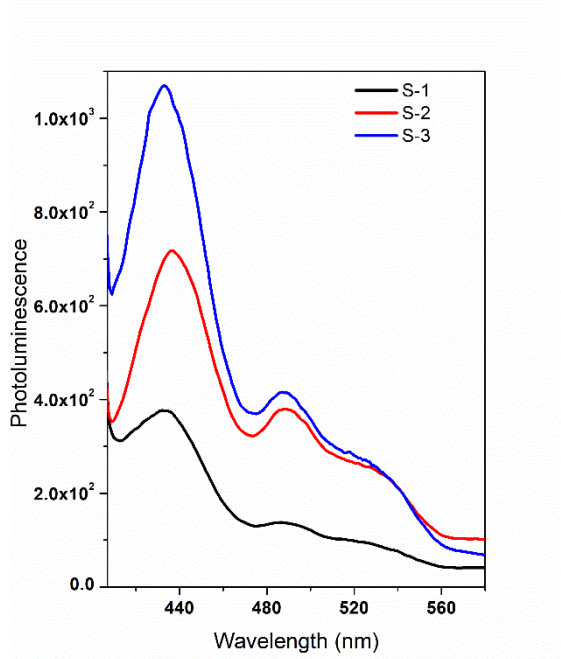

Figure 2: Photoluminescence spectra of Ag nanoparticles.

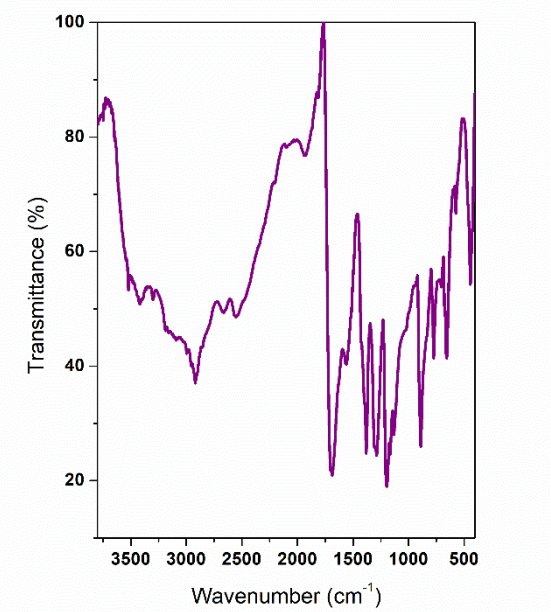

Figure 3: FTIR spectrum of Ag nanoparticles.

transition within short interval of time excited electrons relax to SPR mode. Then they

undergo radiative deexcitation which gives emission spectra. So, as SPR is size dependent, the radiative emission is also dependent on size [31-33].

FTIR spectral analysis gives the information about functional groups present in the material. Figure 3 shows FTIR stpectrum of TGA capped Ag nanoparticle (S1). The standard FTIR spectrum of TGA shows vibrations at 1114, 1346, 1782 and 2562 cm^{-1} assigned to -C-S, -C-H, C=O and -S-H functional groups [34]. In the FTIR spectrum, there is no peak shown at 2562 cm^{-1} confirms the binding of -SH group to the Ag nanoparticles. This confirms the capping of TGA on Ag nanoparticles by forming Ag-SH bond. XRD pattern of TGA capped Ag is shown in the figure 4. Diffraction peaks are

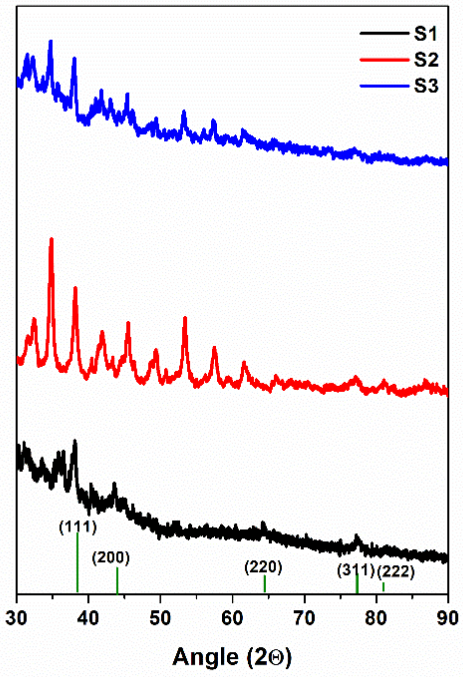

Figure 4: X-ray powder pattern of Ag nanoparticles.

appeared at 2θ angles 38°, 45°, 62°, 77° and 81° represents the Bragg's planes of reflection (111), (200), (220) and (311) based on the FCC (JCPDS, file No. 65-2871). And size of the nanoparticles is calculated using Debye sherrer's equation.

$$D = (0.89\ \lambda)/\beta \cos\theta$$

λ is the wavelength of X-ray radiation, θ is half of angle between incident ray and diffracted ray, β is the full width at half maximum (FWHW) of the peak. Average size of the particles is found to be 13 nm 15 nm and 16 nm for samples S1, S2 and S3 respectively. TEM measurements were carried out for S1 sample. The estimated size of Ag nanoparticles is 15 nm as shown in figure 6. The calculated size matches with the size estimated by XRD measurement. Figure 6.b shows the HRTEM image, crystal lattice of spherical Ag nanoparticle can be clearly seen in the inset image. The details of the particles size are shown in table 1.

Sample	SPR Wavelength (nm)	Emission Wavelength (nm)	Particle size (nm)	
			XRD	TEM
S1	358	433	13	15
S2	371	435	15	-
S3	378	438	16	

Table 1: optical absorption, emission wavelength and particle size estimated by XRD and TEM.

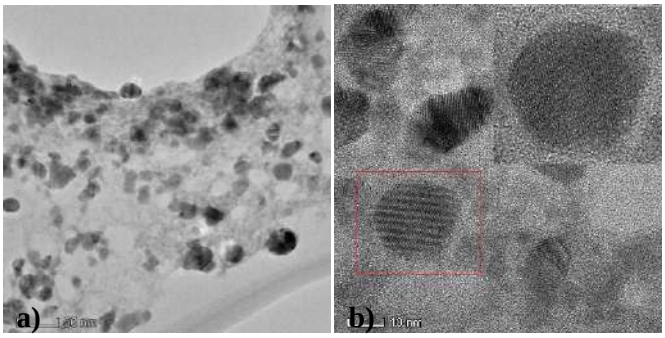

Figure 5: a) TEM image of Ag nanoparticles (S1). b) HRTEM image of Ag nanoparticles, inset image shows crystal lattice.

4. Conclusions:

Ag nanoparticles are prepared by chemical reduction method in open air condition using TGA as capping agent. Efficient capping of TGA molecule is confirmed by FTIR pattern. Particle size has been tuned, that was confirmed by XRD and TEM reports. Shifting in the SPR peak evident the particle size tuning as well as formation of Ag nanoparticles. The present method of preparation is simple and feasible, can be carried out with minimum laboratory setup.

References

[1] R. Janardhanan, M. Karuppaiah, N. Hebalkar, T. N. Rao, Synthesis and surface chemistry of nano silver particles. Polyhedron (Elsevier),28, 2522–2530, (2009).

[2] M. C. Daniel, D. Astru, Gold Nanoparticles: Assembly, Supramolecular Chemistry, Quantum-Size-Related Properties, and Applications toward Biology, Catalysis, and Nanotechnology. Chem. Rev. (ACS), 104, 293−346, (2004).

[3] N. Satoh, T. Nakashima, K. Kamikura, K. Yamamoto, Quantum size effect in TiO_2 nanoparticles prepared by finely controlled metal assembly on dendrimer templates. Nat. Nanotech. (Nature Publ.), 3, 106−111, (2008).

[4] Wells, A. F. Structural Inorganic Chemistry, 6th ed.; Oxford University Press: New York, (1987).

[5] S. Matussin, M. H. Harunsani, A.L. Tan, M.M. Khan, Plant-Extract-Mediated SnO_2 Nanoparticles: Synthesis and Applications, ACS Sustainable Chemistry & Engineering, (ACS) 8, 3040-3054,(2020).

[6] X. Pang, L. Zhao, Z. Lin, A general and robust strategy for the synthesis of nearly monodisperse colloidal nanocrystals. Nat. Nanotech. (Nature Publ.), 8,426-431, (2013).

[7] L. J. Schierholz, A. Lucas, A. Rump and G. Pulverer, J. Hosp. Infect., 40, 257, (1998).

[8] R. Molavi, M. H. Sheikhi, Facile wet chemical synthesis of Al doped CuOnanoleaves for carbon monoxide gas sensor applications. Materials Science in Semiconductor Processing (Elsevier) 106, 104767, (2020).

[9] M. N. Kalasad, M. K. Rabinal and B. G. Mulimani, Ambient synthesis and characterization of high-quality CdSe quantum dots by an aqueous route. Langmuir (ACS), 25, 12729–12735, (2009).

[10] B. C. Zhu, P. F. Xia, Y. Li, W.K. Ho, J.G. Yu, Fabrication and photocatalytic activity enhanced mechanism of direct Z-scheme g-C_3N_4/Ag_2WO_4 photocatalyst, Appl. Surf. Sci. 391, 175–183, (2017).

[11] M. Mohammed, Rahman, S. B. Khan, A. Jamal, M. Faisal, A. M. Asiri, Fabrication of highly sensitive acetone sensor based on sonochemically prepared as-grown Ag_2O nanostructures. Chemical Engineering Journal. (Elsevier), 192, 122-128, (2012).

[12] Y. Li, X.Y. Xiao, Z. H. Ye, Fabrication of $BiVO_4$/RGO/Ag_3PO4 ternary composite photocatalysts with enhanced photocatalytic performance. Appl. Surf. Sci. (Elsevier) 467-468, 902–911, (2019).

[13] L. N. Ma, G. H. Wang, C. J. Jiang, H. L. Bao, Q. C. Xu, Synthesis of core-shell TiO_2@gC_3N_4 hollow microspheres for efficient photocatalytic degradation of rhodamine B under visible light, Appl. Surf. Sci. (Elsevier), 430, 263–272, (2018).

[14] J.X. Low, B. Cheng, J.G. Yu, Surface modification and enhanced photocatalytic CO_2 reduction performance of TiO_2: a review, Appl. Surf. Sci. (Elsevier), 392, 658–686, (2017).

[15] A. Ito, M. Shinkai, H. Honda, and T. Kobayashi, J. Biosci. Bioeng. Medical application of functionalized magnetic nanoparticles. (Elsevier), 100, 1-11, (2005).

[16] S. Guo and E. Wang, Synthesis and electrochemical applications of gold nanoparticles. Anal. Chim. Acta (Elsevier), 598, 181-192, (2007).

[17] C. Fang, A.V. Ellis and N. H. Voelcker, Graphene masks as passivation layers in the electrochemical etching of silicon.Electrochimica Acta (Elsevier), 59, 346-353, (2012).

[18] S. Jradi, L. Balan, X. H. Zeng, J. Plain, D. J. Lougnot, P. Royer, R. Bachelot, S. Akil, O. Soppera and L. Vidal, Spatially controlled synthesis of silver nanoparticles and nanowires by photosensitized reduction. Nanotechnology (IOP), 21, 95605, (2010).

[19] K. K. Caswell, C. M. Bender and C. J. Murphy, Seedless, surfactantless wet chemical synthesis of silver nanowires. Nano Lett. (ACS), 3, 667-669, (2003).

[20] R. J. Chimentao, I. Kirm, F. Medina, X. Rodriguez, Y. Cesteros, P. Salagre, J.E. Sueiras, Different morphologies of silver nanoparticles as catalysts for the selective oxidation of styrene in the gas phase, Chem. Comm. (RSC), 846–847, (2004).

[21] M. Hasanpoor, M. Aliofkhazraei, M. Hosseinali, Electrophoretic deposition of ZnO–CeO_2 mixed oxide nanoparticles, J. Am. Ceram. Soc. (ACS), 100, 901–910, (2017).
[22] M. Hasanpoor, H. Liu, H. Liu, X. Han,Core–shell CeO_2 micro/nanospheres prepared by microwave assisted solvothermal process as high-stability anodes for Li-ion batteries. J. Solid State Electrochem. (Springer), 21, 291–295, (2017).

Karnatak University Journal of Science 53 (2022) 105-113

Karnatak University Journal of Science

ISSN: 0075-5168

Study of ground and excited state dipole moment of chalcones in different organic alcohols by using solvatochromic shift method

Shilpa Nayak[a], Netravati Khanapurmath[b], Chittidi Nagaraju[b] , Susmita Rayawgol B[b] ,Sujatha K[b*]

[a*] P.G Department of Chemistry, JSS College, Dharwad-580003, Karnataka, India.

[b] Department of Chemistry, Karnatak University Dharwad-580003, Karnataka, India.

Corresponding author: sujathakorganic@gmail.com

ARTICLE INFO

Article history:
Received: 30 June 2022
Revised: 26 July 2022;
Accepted: 27 July 2022

Keywords:
Chalcones;
Dipole moment;
Solvatochromism;
Stokes shift;
Solvent – solute interactions

ABSTRACT

Electronic absorption and fluorescence spectra of substituted chalcones have been studied comprehensively in several organic alcohols at room temperature. A reasonable agreement has been observed with change in ground and excited state dipole moments which have been determined using solvatochromic shift method based on the solvent polarity properties $f_1(\varepsilon, n)$ and $f_2(\varepsilon, n)$.

1. Introduction

Chalcones are a class of compounds in which two aromatic planar rings are connected through α, β-unsaturated carbonyl system exerting strong electron donor-acceptor interactions depending on the substituent attached to the aromatic rings. Chalcones have found to be versatile synthetic intermediates in the synthesis of novel heterocycles with good pharmaceutical profile [1]. These are main precursor of flavonoids and isoflavonoids which show a diverse range of pharmacological activities like cytotoxicity, anti-tumour, anti-inflammatory, anti-plasmodial and anti-oxidant [2].

Apart from very important biological and pharmaceutical applications, the photo physical properties of chalcones have attracted considerable research attention including metal sensing, optical materials, laser dyes, etc. [3-5].These molecules usually show strong polarity-dependent Stokes shifts, large changes in dipole moments on excitation, and very high fluorescence quantum yields [6].

Solvatochromism dependence of absorption and emission maxima with the polarity of solvents. Excited state properties of the molecules are quite sensitive due to intermolecular solute-media interactions and in turn affect the energy of the electronic states thus gives rise to variation in the spectral shifts [7,8]. The influence of the solvents on the absorption and emission spectra has been extensively used to determine the magnitude as well as direction of dipole moment in ground and excited states [9,10].

2. Experimental

2.1 Materials and method

Chalcone derivatives (**Figure 1**) are prepared according to the literature methods [11, 12]. Solvents used during the present investigation were methanol, ethanol, propanol, butanol, pentanol, hexanol, heptanol and octanol, these are of spectroscopic grade. The concentrations chosen were 10^{-5} M in all the cases. UV-Vis and fluorescence measurements are carried out at room temperature. The absorption and emission spectra were recorded on a U-3310 UV-Vis and fluorescence spectrophotometer (Hitachi F-7000, Japan) respectively.

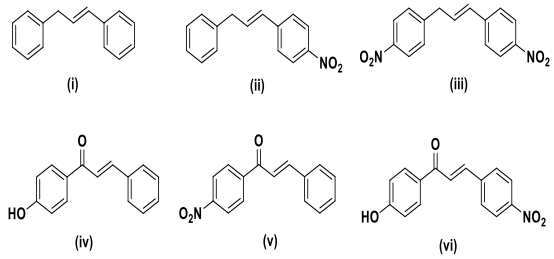

Figure 1. Structure of the compounds studied

2.2 Determination of dipole moments

Method 1:

The method which employed depends on the internal electric field for studying the effect of substituted groups $–NO_2$ and -OH on the dipole moments of chalcones. This method makes use of dependence of absorption and emission band maxima on refractive index and dielectric constant to estimate the excited state dipole moments of organic compounds. Knowing the excited-state dipole moment of organic molecules having large polarizability is important in designing efficient non-linear optical materials. For a chromophore, the tunablity range of the emission energy (as a function of the polarity of the medium) is also determined by excited-state dipole moment. Further, the experimental data on dipole moments are useful in parameterization in quantum chemical methods. Among the techniques available for the determination of the excited state dipole moments, the most popular is that based on the Bakshiev and Kawski-ChammaViallet equations which afford good results for the estimation of excited state dipole moments of organic compounds.

According to Bakhshiev correlation between the solvent spectral shifts and solvent polarity function f_1 is given by [13]

$$\bar{\upsilon}_a - \bar{\upsilon}_f = S_1 f_1(\varepsilon, n) + \text{constant} \quad (1)$$

According to Chamma and Viallet [13]

$$(\bar{\upsilon}_a + \bar{\upsilon}_f)/2 = S_2 f_2(\varepsilon, n) + \text{constant} \quad (2)$$

Where, $\bar{\upsilon}_a$ is absorption maxima and $\bar{\upsilon}_f$ is emission maxima expressed in (cm^{-1}).

$$S_1 = 2(\mu_e - \mu_g)^2/a_0^3 hc \quad (3)$$

$$f_1(\varepsilon, n) = \frac{2n^2+1}{n^2+2}\left(\frac{\varepsilon-1}{\varepsilon+2} - \frac{n^2-1}{n^2+2}\right) \quad (4)$$

$S_2 = -2(\mu_e^2-\mu_g^2)/a_0^3hc$ (5)

$f_2(\varepsilon, n) = \frac{2n^2+1}{2(n^2+2)}\left(\frac{\varepsilon-1}{\varepsilon+2}-\frac{n^2-1}{n^2+2}\right)+\frac{(n^4-1)}{2(n^2+2)^2}$ (6)

Where 'n' is refractive index, ' ε ' is dielectric constant of the solvents. Calculated values of solvents polarity parameter are listed in **Table-1**. The ground and excited state dipole moments are estimated by means of the following equations assuming that the symmetry of the investigated solute molecule remains unchanged upon electronic transitions and the ground and excited state dipole moments are parallel [15].

$$\mu_g = \frac{s_2-s_1}{2}\left[\frac{hca_\circ^3}{2s_1}\right]^{\frac{1}{2}} \quad (7)$$

$$\mu_e = \frac{s_1+s_2}{2}\left[\frac{hca_\circ^3}{2s_1}\right]^{\frac{1}{2}} \quad (8)$$

Where $\mu_g$and μ_e are ground and excited state dipole moments respectively, 'h' is Plank's constant, 'c' is the velocity of light, 'a_o' is Onsagar cavity radius, evaluated by calculating the Vanderwaal's volumes (V=4/3 πa^3) according to Edwards method. The ratio of excited state dipole moment to the ground state dipole moment can be expressed as,

$$\Delta\mu = \frac{|\mu_g|}{|\mu_e|} = \frac{|s_1-s_2|}{|s_1+s_2|} \quad (9)$$

The slopes s_1 and s_2 have been determined by plotting the stoke's shifts **(**$\bar{\upsilon}_a$-$\bar{\upsilon}_f$) and ½($\bar{\upsilon}_a$+$\bar{\upsilon}_f$**)** against the bulk solvent polarity functions $f_1(\varepsilon, n)$ and $f_2(\varepsilon, n)$ respectively for different solvents.

Method 2:

For understanding polarization dependence or hydrogen bonding effects in solvents it is useful to use E_T (30) function, which is an empirical measure of solvent polarity and is based on solvatochromic behavior of betaine dye as a probe solute [3]. On this scale each solvent gives a quantitative expression for polarity. However, to avoid dimensionality problems, normalized values of E_T (30) namely E_T^N are employed which includes not only solvent polarity but also the protic hydrogen bond effect.

The change in dipole moment can be determined by Eq. (10) [14]

$$\Delta\mu = \mu_e - \mu_g = \sqrt{\frac{81\ m}{(6.2/a_0)^3 11307.6}} \quad (10)$$

Where, m is the slope obtained from a linear plot of Stokes shift ($\bar{\upsilon}_a$-$\bar{\upsilon}_e$) against E_T^N.

Further, excited state dipole moment can also be determined by using following expression

$$(\bar{\upsilon}a - \bar{\upsilon}f) = 11307.6\left[\left(\frac{\Delta\mu}{\Delta\mu_D}\right)\left(\frac{a_D}{a}\right)\right]E_T^N + \text{constant} \quad (11)$$

where, E_T^N is the microscopic solvent polarity function proposed by Reinhardt based on absorption wave number of a standard betaine dye in the solvent, μ_D and a_D are the change of dipole moment and Onsagar cavity radius, respectiely. Δμ and a are the corresponding quantities of chalcones.

3. Results and discussions

3.1 Electronic spectral properties

Electronic absorption spectra of chalcones exhibited a single band in the range 295-375 nm in the chosen alcohols. Solvent dependent absorption pattern has been observed and which is independent of alcohol polarity.

Solvent effects on the excited and ground states of chalcones investigated by absorption and fluorescence spectroscopy which have been correlated with the dipole moments by Kawski-ChammaViallet equations. In the present work we have demonstrated the application of solvatochromic shift method to the determination of the excited and ground state of chalcones (ii to vi) in comparison with (i).

Owing the applications of chalcones we carried the solvatochromic study of acetophenone- benzaldehyde chalcones and effect of electron withdrawing group –NO_2 On their absorption and emission spectra which was further confirmed by dipole moment calculation following i, ii, iii are the compounds which are under taken for the study. The absorption and emission spectra of **compounds (i) – (vi)** are recorded in various solvents of different solvent parameters of dielectric constant (Ɛ) and refractive index (n). The values of Stokes shift and spectral shift are indicated in **Tables 2,3 and 4**.

3.2 Dipole moment studies

Table 1: Solvent Properties and Polarity functions of Chalcone in different organic alcohols

Solvent	n	ε	$f_1(\varepsilon,n)$	$f_2(\varepsilon,n)$	E_T^N
Methanol	1.329	33.70	0.857	0.652	0.762
Ethanol	1.361	24.30	0.811	0.651	0.654
Propanol	1.385	20.60	0.778	0.6488	0.617
Butanol	1.399	17.40	0.754	0.6448	0.586
Pentanol	1.410	14.80	0.703	0.5779	0.568
Hexanol	1.418	13.00	0.690	0.628	0.559
Heptanol	1.424	11.30	0.651	0.613	0.549
Octanol	1.429	9.80	0.627	0.6045	0.537

Table 2: Wave numbers (cm^{-1}) for the absorption and fluorescence emission maxima of Compounds (i), (ii) and (iii) in different solvents and stokes shift.

Compound	Solvent	λ_a (nm)	λ_f (nm)	$\bar{\upsilon}_a$ (cm^{-1})	$\bar{\upsilon}_f$ (cm^{-1})	$(\bar{\upsilon}_a-\bar{\upsilon}_f)$ (cm^{-1})	$½(\bar{\upsilon}_a+\bar{\upsilon}_f)$ (cm^{-1})
(i)	Methanol	316	410	31645	24390	7255	28010
	Ethanol	304	453	32894	22075	10819	27495
	Propanol	306	406	32679	24630	8049	28654
	Butanol	307	456	32573	21929	10644	27251
	Pentanol	311	368	32154	27123	5031	29638
	Hexanol	312	402	32051	24875	7176	28463
	Heptanol	310	419	32258	23866	8392	28062
	Octanol	311	428	32154	23364	8790	27759
(ii)	Methanol	362	431	27624	23201	4423	25412
	Ethanol	301	404	33222	24752	8470	28987
	Propanol	295	459	33898	2172	11726	28035
	Butanol	375	471	26666	21231	5435	23993
	Pentanol	295	471	33898	21231	12667	27564
	Hexanol	362	404	27624	24752	2872	26188
	Heptanol	301	431	33222	23201	10013	28211
	Octanol	298	453	33557	22075	11482	27816
(iii)	Methanol	302	377	33112	26525	6587	29800
	Ethanol	303	450	33003	22222	10781	27600
	Propanol	309	335	32362	29850	2512	31106
	Butanol	300	375	33333	26666	6667	29999
	Pentanol	300	360	33333	27777	5556	30555
	Hexanol	299	476	33444	21008	12436	27226
	Heptanol	305	469	32786	21321	11465	27050
	Octanol	301	361	33222	27700	5522	30450

The absorption and maximum emission is indication of charge transfer during excitation. Larger magnitude of the Stoke shift indicates that the excited state geometry could be different from that of ground state. The

general observation is that there is an increase in the stoke shift values when there is an increase in the solvent polarity, which shows that there is an increase in the dipole moment on excitation. The fluorescence emission peaks undergoes a red shift, confirming a π-π* transition.

Table 3: Wave numbers (cm^{-1}) for the absorption and fluorescence emission maxima of Compounds (i), (ii) and (iii) in different solvents and stokes shift.

Compound	Solvent	λ_a (nm)	λ_f (nm)	$\bar{\upsilon}_a$ (cm^{-1})	$\bar{\upsilon}_f$ (cm^{-1})	$(\bar{\upsilon}_a-\bar{\upsilon}_f)$ (cm^{-1})	$½(\bar{\upsilon}_a+\bar{\upsilon}_f)$ (cm^{-1})
(iv)	Methanol	315	487	31746	20503	11243	26124
	Ethanol	299	443	33444	22546	10898	27995
	Propanol	300	442	33333	22624	10709	27978
	Butanol	306	442	32679	22624	10055	27651
	Pentanol	318	372	31446	26881	4565	29163
	Hexanol	341	406	29325	24630	4695	26977
	Heptanol	336	403	29761	24813	4948	27287
	Octanol	337	413	29673	24213	5460	26943
(v)	Methanol	306	329	32679	30379	2300	31529
	Ethanol	306	347	32679	28789	3890	30734
	Propanol	340	436	29411	22935	6476	26173
	Butanol	310	413	32258	24213	8045	28235
	Pentanol	318	387	31446	25839	5607	28642
	Hexanol	312	399	32051	25062	6989	28556
	Heptanol	310	411	32258	24330	7928	28294
	Octanol	312	498	32051	20080	11971	26065
(vi)	Methanol	301	516	33222	19379	13843	26300
	Ethanol	301	509	33222	19646	13576	26435
	Propanol	332	403	30120	24813	5307	27466
	Butanol	301	513	33225	19493	13732	26359
	Pentanol	314	364	31847	27472	4375	29659
	Hexanol	346	392	28901	25510	3391	27205
	Heptanol	335	427	29850	23419	6431	26634
	Octanol	310	447	32258	22371	9887	27314

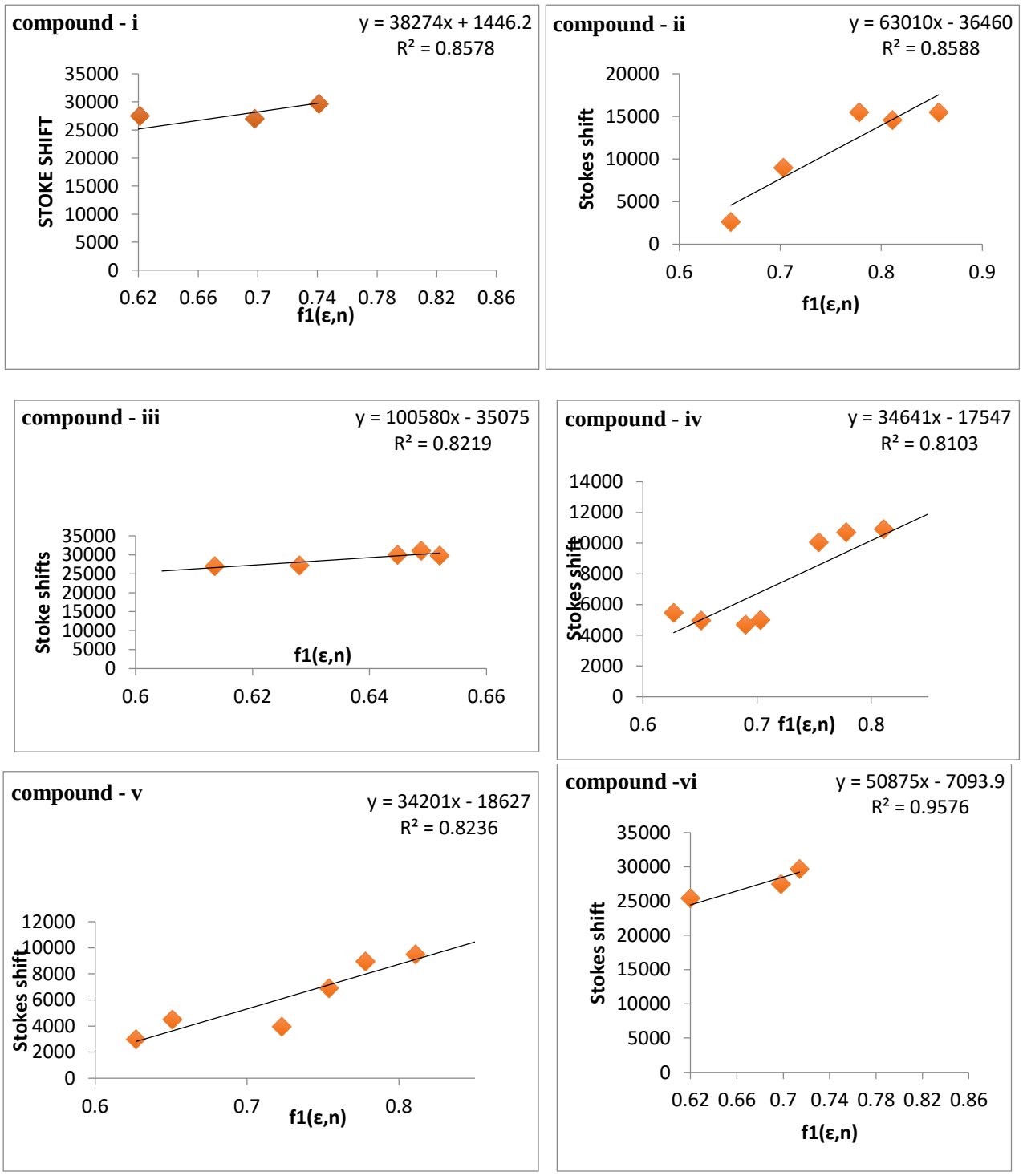

Fig. 2: Variation of stoke shift with $f_1(\varepsilon, n)$ by using Bakhshiev equation in different solvents for compounds (i) to (vi).

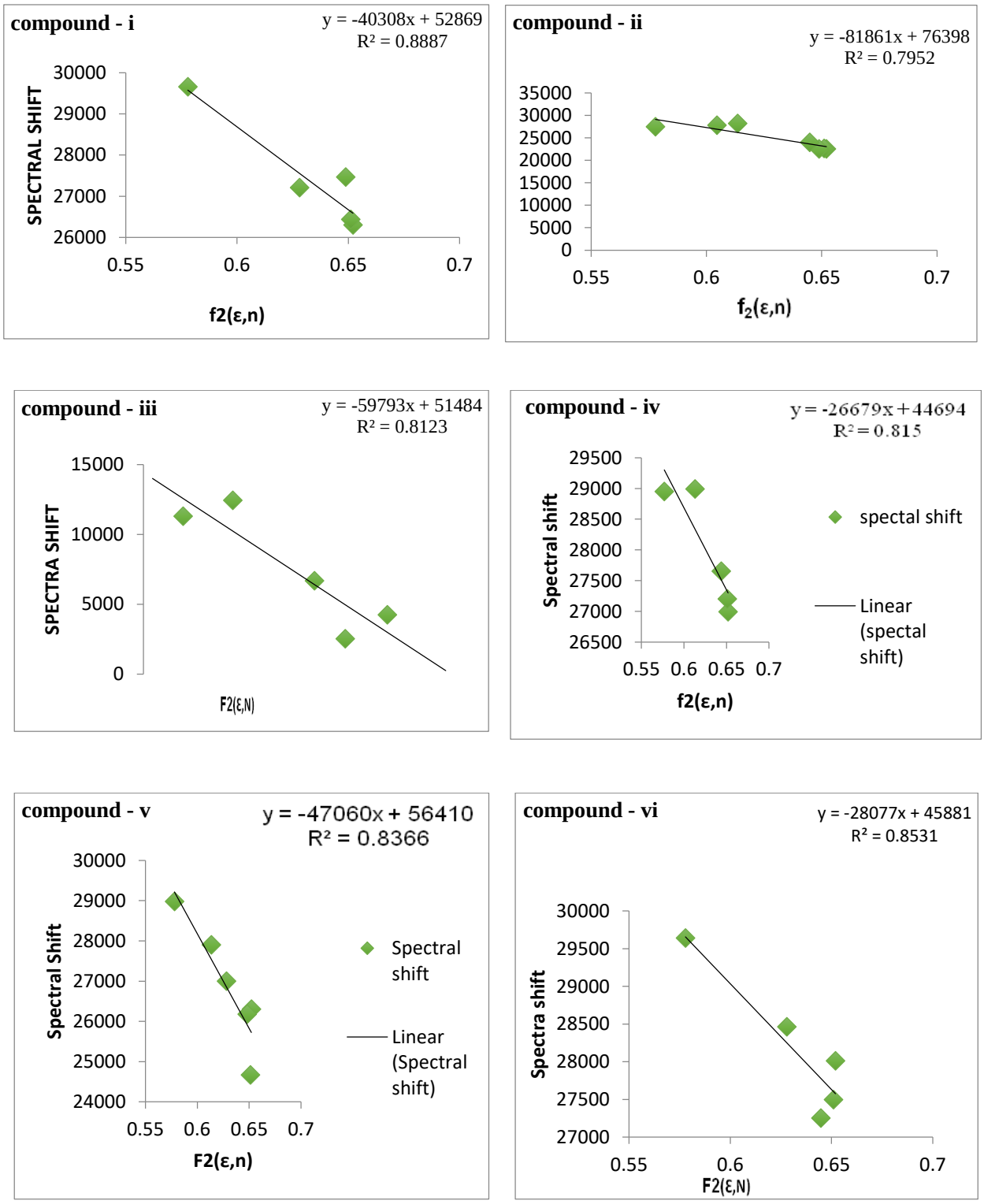

Fig 3: The Variation of the arithmetic mean $\bar{\upsilon}_a$ and $\bar{\upsilon}_f$ with f_2 (ε, n)) by Kawasaki-Chamma Viallet's Equation in different solvents for compounds (i) to (vi).

Table 4: The slopes obtained by plotting stoke's shift **($\bar{\upsilon}_a$-$\bar{\upsilon}_f$)** versus bulk solvent polarity function $f_1(\mathcal{E}, n)(S_1)$ And spectral shift **½($\bar{\upsilon}_a$+$\bar{\upsilon}_f$)** versus bulk solvent polarity function $f_2(\mathcal{E}, n)(S_2)$

Compound	S_1	S_2
i	38274	-40308
ii	63010	-81861
iii	10058	-59793
iv	34641	-26679
v	34201	-47060
vi	50875	-28077

Table 5: Onsagarcavity(a_0), ground state(μ_g), excited state(μ_e) and change in dipole moment($\Delta\mu$) of compounds in (Debye).

Compound	a_0	μ_g(exp) (D)	μ_e(exp) (D)	μ_g/μ_e	$\Delta\mu(\mu_e-\mu_g)$
i	3.513	0.50	1.31	0.38	0.81
ii	4.78	0.25	1.98	0.126	1.73
iii	3.789	1.6	2.28	0.70	0.68
iv	4.30	0.14	1.07	0.129	0.93
v	4.92	0.23	1.53	0.150	1.3
vi	3.707	0.16	1.43	0.11	1.27

CONCLUSIONS

The sufficient difference in the ground and excited state dipole moments of **compound - (i)** shows that $\alpha,\beta-$ unsaturated ketone is resonance stable and due to which the excited state is little stable compared to ground state. Thus the higher value of dipole moment is observed in excited state. Introduction of nitro group on carbonyl side ring in case of **compound-(ii)** increases the excited state dipole moment indicating the increase of $\alpha,\beta-$ unsaturation conjugation extent with the carbonyl as $-NO_2$ withdraws the $\pi-$electron density from the ring than from C=O which is further supported by the decrease in the ground state dipole moment. But in case of **compound - (iii)** ground state as well as excited state dipole moments have been increased which is attributed to the introduction of $-NO_2$ group on alkenyl side ring that results in the more stable charge separated structures by withdrawing the $\pi-$electrons of alkenyl bond into the ring. The difference of around 1 Debye ground and excited state dipole moment of **compound-(iv)** indicates that there is a resonance stable excited state as the μ_e is higher compared to μ_g .

When the –OH group is replaced by $-NO_2$ group carbonyl side ring in **compound-(v)** , μ_e again increases which indicates the more contribution of the α-β unsaturated charge separated systems to the excited state stability. But in case of **compound-(vi)**, where –OH introduced on carbonyl side ring and $-NO_2$ is introduced on alkenyl side ring did not show much variation in μ_g and μ_e which may be because of electron donating and withdrawing groups compensation nature.

REFERENCES

1. L. Santosh Gaonkar, U. N. Vignesh, *Res Chem Intermed* 43:6043–6077 (2017).
2. M.R.Jayapal, N.Y.Sreedhar, Asian *journal of pharmaceutical and clinical research* **vol. 4**, Issue 1, (2011).
3. D.S Chemla, J. Zyss. Non-linear Optical properties of Organic Molecules and Crystals, *Academic press, Newyork*, (1987)
4. P Poornesh, S Shettigar, G Umesh, KB Manjunatha, K Prakash Kamath, BK Sarojini, B Narayana, Nonlinear optical studies on 1, 3-disubstituent chalcones doped polymer films. *Opt Mater* **31(6):**854–859 (2009).
5. B Rajashekara, P Sowmendranb, S Siva SankaraSai, G NageswaraRao Synthesis, characterization and two-photon absorption based broadband optical limiting in diarylideneacetone derivative. *J PhotochemPhotobiol A Chem* **238**:20–23 (2012).
6. Mehboobali Pannipara, M. Abdullah Asiri, A. Khalid Alamry, N Muhammad Arshad, A.

Samy El-Daly, Spectroscopic Investigation, Effect of Solvent Polarity and Fluorescence Quenching of a New D-π-A Type Chalcone Derivative. *J Fluoresc* **24**:1629–1638 (2014).

7. A Kawski, J. F Rabek, *Progress in Photochemistry and Photophysics*, *CRC, Press, Boca Raton* **Vol. 5**, (1992).
8. J. Czekalla, J. W. Sidman and D S. Mc Clurc, J. chem. Physics 24,757 (1956).
9. W Liptay, E. C Lim, Excited states, *Academic press, Newyork* **Vol. 1**, (1974).
10. J Czekalla, Z Electrochem. **64**: 1221 (1960).
11. 11. Y.F Nadaf, V.G Mulimeni, M Gopal, S.R Inamdar, *J. Mol. Struct.(Theochem)* **678**: 177-181 (2004).
12. J.J. Aaron, M. Maafi, C. Kersebet, C.Parkanyi, M.S. Antonious, N.Motohashi, *J. Photochem. Photobiol. A:Chem.* **101:** 127-136 (1996).
13. L.R.Naik, N.N. Math, *Journal of Photoscience* **Vol. 12(2):** 57-61(2005).
14. S.K.Patil, M.N.Wari, C. Yohannan Panicker, S.R.Inamdar, *Spectrochimica acta part A: Molecular and Biomolecular Spectroscopy* **123**: 117-126(2014).

Karnatak University Journal of Science 53 (2022) 114-118

Karnatak University Journal of Science

ISSN: 0075-5168

Gonadal expression of Wnt4 gene in Calotes versicolor embryos incubated at 100% Male-producing and 100% Female-producing temperatures.

Jyothi F. Hiremath and Laxmi S. Inamdar (Doddamani)*

Molecular Endocrinology, Reproduction and Development Laboratory, Department of Zoology, Karnatak University, Dharwad 580 003, India

Corresponding author: ls_doddamani@yahoo.com; Tel: +91-836-2215230 (O); +91-836-2955168 (R)

ARTICLE INFO

Article history:
Received: 4 June 2022;
Revised: 12 July 2022;
Accepted: 19 July 2022;

Keywords:
Adrenal-Kidney-Gonadal complex;
Temperature-dependent sex determination;
Wnt4 gene;
Lizard;
Calotes versicolor;

ABSTRACT

In vertebrates, sex determination and differentiation follows sequential expression of sex-specific genes and many of these genes have evolutionarily conserved expression profiles across the vertebrates. Some have been found to be expressed in reptiles. Wnt4, is a member of Wnt family that found to be involved in ovary differentiation pathway. The tropical oviparous lizard, Calotes versicolor exhibits a novel FMFM pattern of Temperature-dependent sex determination (TSD). We examined the expression pattern of Wnt4 in adrenal-kidney-gonadal complex during different stages of embryonic development in C. versicolor. Expression of Wnt4 was studied at both 100% Female-producing temperature (FPT) and 100% Male-producing temperature (MPT). The eggs of this lizard were collected during breeding season and incubated at 31.5 ± 0.5oC (FPT) and 25.5± 0.5oC (MPT). The Adrenal– Kidney–Gonadal complex (AKG) was collected during different stages of development and subjected to semiquantitative RT-PCR. The results reveal very faint expression of Wnt4 during Pre-TSP (pre-Thermo- sensitive Period) and TSP stages in the embryos incubated at both FPT and MPT. Further, robust expression of Wnt4 was noticed during sex differentiation in the embryos incubated at FPT. Thereafter the expression was more or less same during post-gonadal differentiation stages. However, in the embryos incubated at MPT, a decline in the expression of Wnt4 was noticed after gonadal differentiation. These results unveil the dimorphic expression pattern of Wnt4 during sex differentiation in C. versicolor. The present study is in consistent with the expression pattern of Wnt4 that found in other vertebrates.

1. Introduction

Sex determination is a process by which organisms' sexual fate is determined. In most of the organisms sex of an individual is determined at the time of fertilisation by genes hence the name genetic sex determination (GSD). Various environmental factors, including photoperiod, social environment and temperature influence sex determination across the animal kingdom (1). However, temperature is the only environmental variable that has been conclusively shown to determine sex in reptiles. This form of ESD is called temperature-dependent sex determination (TSD) (2). All species of Crocodiles exhibits TSD (3). The two extant species of tuatara also have TSD (4). In contrast, all snakes have GSD (5). In Lizards, some are TSD species, some exhibit GSD and in some both GSD and TSD co-occurs. Phylogenetic and molecular analyses suggest that sex-determining mechanisms can evolve quite rapidly in this group (6). Virtually all studies of the molecular biology of sex determination in reptiles have examined homologs of sex-determining genes first identified in mammals. The general approach is to clone partial or full-length cDNAs of these genes in TSD species. mRNA expression is characterized in the gonads or adrenal-kidney-gonad complexes (AKGs) of embryos that have been incubated at male and female-producing temperatures. Expression differences are taken as evidence that the gene of interest is involved in TSD.

A number of transcription factors and signalling molecules are now known to play a role in testicular differentiation. In contrast, the molecular control of ovarian development is less well understood. Several important players in ovarian differentiation and development have been identified. One requirement for proper ovarian development is *Wnt* signalling. *Wnt* proteins are a family of locally acting signalling molecules required in diverse developmental events, including gastrulation, axis formation, cell polarity, stem cell differentiation, and organ development (7)**.** *Wnt4* deficiency leads to abnormal development of kidneys, pituitary gland, mammary gland and both the male and female reproductive systems**.** Analysis of mutant mice showed that lack of Wnt4 leads to the masculinization of the XX embryo and in normal embryonic XX gonads, *Wnt4* expression is up-regulated (8). In the ovary, *Wnt4* acts via Follistatin to prevent the formation of a testis-specific coelomic blood vessel (9). In Wnt4-/- XY mice, gonadal expression of *Sox9, Mis, Dhh*, and *Sf1* is decreased but can be rescued by ectopic Wnt4, suggesting an active role for *Wnt4* in testicular development as well (10). It has been shown that *Wnt4* is expressed in the mesonephros, gonad and in close association with the Mullerian-duct indicated that Wnt4 may be important for mediating the initial formation of the Mullerian ducts, regulating the migration of steroidogenic mesonephric cells into the developing gonad, oocyte maintenance and repression of steroidogenesis in mice (11). In reptiles *Wnt4* expression has been studied in *Calotes versicolor* (12,13), *Trachemys scripta* (14) and *Chelonia mydas* (15)

2. Materials and methods:

2.1 *Animal collection*:

Calotes versicolor is a poly autochronic multi-clutched lizard that has extended breeding phase (May-Oct) and retains its eggs in the oviduct for 2 weeks. It usually lays 6-32 eggs in a clutch. Gravid females possessing oviductal eggs were caught from the areas around Dharwad (15^{o},17'N,75^{o},3'E) Karnataka, India. Fertilization was confirmed by observing the matured yolky follicles with stigmata. All the gravid females collected from the area contains almost alike embryonic stages for that particular time. They were maintained in reptile dwelling cages 20'x20'x10' covered with mesh and they were maintained for about 10 days quarantine period. Food (grasshoppers/silkworms/ cockroaches) and water were supplied *ad libitum*.

2.2 *Egg incubation and tissue collection:*

Eggs collected from gravid females were randomly assigned and incubated in the incubator at the female-producing temperature

of 31.5 ± 0.5ºC and at Male-producing temp 25.5± 0.5ºC. Care was taken to ensure that the fluctuation in the incubation temperature did not exceed 0.5ºC and a relative humidity of 62%. Other incubation methods have already been described in elsewhere (16). The eggs were incubated from stage 27 to stage 42. Developmental progress was monitored regularly and the stages of embryonic development were determined as per the criteria previously described for *C. versicolor* (17). Sexual dimorphism is absent in adult *C. versicolor*. The hemipenis that can be seen clearly in male embryos during embryonic period gets resorbed in one-day-old male hatchlings. Hence, the cloacal sexing was performed prior to experimentation to distinguish the sex of the embryo (18). The Adrenal-kidney-gonadal (AKG) complexes (n = 10) were collected from the embryos incubated at FPT and MPT during different stages of development.

2.3 *RNA extraction and cDNA synthesis:*

Adrenal- kidney -gonadal (AKG) complexes (n = 10) were excised in ice cold PBS under stereozoom binocular (Leica MZ6, Wetzlar, Germany) during different stages of embryonic development incubated at both FPT and MPT and stored in RNAlater (Sigma-Aldrich, USA) at -20ºC. Total RNA was isolated from pooled AKGS using TRI reagent (Sigma-Aldrich, USA) as per the manufacturer's instructions and the concentration of total RNA was measured using Nanodrop-1000. About 1-2 µg of RNA treated with DNase-I (Fermentas) to remove DNA contamination. The cDNA synthesis was done by using oligo-dT primers and MMULV Reverse-Transcriptase (Fermentas) in 20 µl volume at 42°C for 1 hour.

2.4 *Semiquantitative RT-PCR:*

The primer set -*Wnt4* F:5'-CAACTGGCTGTACCTGGCCAA-3' and *Wnt4* R:5'-GAAGGCTACGCCATAGGCGAT-3' utilised for the current study was same as utilised for *C. versicolor* by Tripathi and Raman (12) and *Actin*-β F:5'-GGCTACAGCTTCACCACCAC-3' and *Actin*-β R:5'-AGATGGCTGGAAGAGGGCT-3' at 94 °C for 30 s, 60 °C for 1 min and 72 °C for 1 min. 40 cycles were carried out. PCR products (25 µl) were analysed on a 2% agarose gel containing 0.5 µg /ml ethidium bromide.

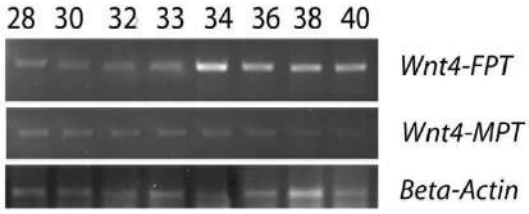

Fig 1. Semiquantitave RT-PCR analysis of *Wnt4* expression in AKGs of *Calotes versicolor* embryos from stages 28-40 incubated at 100% female-producing temperature (FPT) and 100% Male-producing temperature (MPT). β-*Actin* was used as positive control.

3. Results and discussion:

The AKG expression pattern for *Wnt4* was studied for all the embryonic stages (stages 27-42) incubated at FPT and MPT. However, the emphasis was given to Pre-TSP (stages 27-30), TSP (Stages 30-33), Gonadal differentiation (Stage 34) and Post–gonadal differentiation stages (Stages 36-42). The results reveal that RT-PCR analysis of the *Wnt4* yielded a 429 bp fragment (Fig 1). A faint *Wnt4* expression was observed in Pre-TSP embryos and TSP embryos irrespective of the incubation Temperature. The expression becomes strong during sex differentiation stage in embryos incubated at FPT, thus indicating its role in sex determination. However, the expression was downregulated in embryos incubated at MPT during post-gonadal sex differentiation stages. Thus, the observed results indicate the expression of *Wnt4* in AKG becomes sexually dimorphic only after gonadal sex differentiation. These results are consistent with the expression pattern found in mice (8). In reptiles, *Wnt4* was studied in two TSD turtles, *T. scripta* (14) and *C. mydas* (15) and in the lizard, *Calotes versicolor* which is inhabiting northern-region of India (12). In *T. scripta*, *Wnt4* is expressed at comparable levels

throughout the TSP as measured by qPCR between gonads developing at FPT and MPT. However, during ovarian differentiation, expression at FPT significantly rises above MPT by up to 4-fold and only becomes dimorphic during later ovarian differentiation**.** Strong *Wnt4* expression is observed in the mesonephros, dorsal metanephric tissues and Mullerian ducts of both sexes. The expression at MPT begins to localize in a striped pattern indicative of developing sex cords at the end of the TSP. The expression in the ovary becomes concentrated in the cortical region (14). The observed results on the expression pattern of *Wnt4* in the present study on *C. versicolor* are consistent with the pattern observed in *Trachemys scripta.* In contrast, qPCR of the *Wnt4* gene in embryonic gonads of *Chelonia mydas* showed a different expression pattern with *T. Scripta* and *Calotes versicolor* species. In *C. mydas Wnt4* expression increased in embryos incubated at MPT indicating its role in sexual differentiation rather than sex determination (15). In northern species of *C. versicolor Wnt4* expression is nowhere found in early stages. Its expression was first detectable on day 20 of incubation (12) which is expressed much later than other female and male pathway genes and even at later stages, there is no strict correlation in the expression patterns with other genes (13).

The expression pattern of *Wnt4* observed in the present study on southern species of *C. versicolor* and that of *T. scripta* (14) can be comparable with the expression pattern of *Wnt4* in mice (8). In mice *Wnt4 is* expressed in the mesenchyme of the indifferent gonad of both sexes and expression is downregulated in the embryonic male gonad but is maintained in the female gonad and sexually dimorphic expression continues over the period in which the sexes become morphologically distinct (8). Whereas studies on human embryonic gonads do not detect sex differences in *Wnt4* expression during the sex-determining period (19). Whole mount in situ hybridisation of embryonic chicken gonads, *Wnt4* was expressed in the gonads of both sexes from E4.5, prior to gonadal sex differentiation. Expression became sexually dimorphic during gonadal sex differentiation (E6.5 – 8.5), being upregulated in females and downregulated in males. Little expression was observed in the adjoining mesonephros (20). The observed results of *Wnt4* expression in the present study on *C. versicolor* is in agreement with *T. scripta* (14), chicken (20) and mice (8). Based on the above results its inferred that the expression of *Wnt4* in *C. versicolor* divulges a dimorphic pattern during gonadal sex differentiation and post gonadal differentiation stages.

Acknowledgement:

All procedures used in this experiment adhere to CPCSEA guidelines for the care and use of laboratory animals approved by the Institutional Animal Ethical Committee No. 639/02 at Department of Zoology, Karnataka University, Dharwad, Karnataka. The Corresponding author (LSI) thanks Indian National Science Academy, New Delhi for the Award of INSA Visiting Scientistship to visit MRDG Division, Indian Institute of science Bangalore, Bangalore.

***References*:**

1. Bull JJ: Evolution of Sex Determining Mechanisms, Benjamin-Cummings, Menlo Park, C A (1983).
2. Bull JJ: Sex determination in reptiles. The Quarterly Review of Biology, 55:3–21 (1980).
3. Deeming DC: Prevalence of TSD in crocodilians, in Valenzuela N, Lance VA (eds): Temperature-Dependent Sex Determination in Vertebrates, pp 33–41, Smithsonian Institution, Washington (2004).
4. Nelson N J, Cree A, Thompson M B, Keall S N, Daucherty C H: Temperature dependent sex determination in tuatara, in Valenzuela N, Lance VA (eds): Temperature- Dependent Sex Determination in Vertebrates, pp 53–58, Smithsonian Institution, Washington (2004).
5. Matsubara K, Tarui H, Toriba M, Yamada K, Nishida-Umehara C, et al: Evidence for

different origin of sex chromosomes in snakes, birds, and mammals and step-wise differentiation of snake sex chromosomes, Genetics, Proc National Academy of Sciences USA, 103:18190–18195 (2006).

6. Ezaz T, Quinn A E, Sarre S D, O 'Meally D, Georges A, Marshall Graves J A: Molecular marker suggests rapid changes of sex-determining mechanisms in Australian dragon lizards. Chromosome Research, 17: 91–98 (2009).
7. Cadigan, K. M. & Nusse, R. Wnt signaling: a common theme in animal development. Genes and Development.11, 3286-3305 (1997).
8. Vainio S, Heikkila M, Kispert A, Chin N, McMahon AP: Female development in mammals is regulated by Wnt-4 signalling. (Nature) 397,6718: 405-409, (1999).
9. Yao HH, Di Napoli L, Capel B. Cellular mechanisms of sex determination in the red- eared slider turtle, Trachemys scripta. Mechanisms of Development, 121: 1393 1401, (2004).
10. Jeays-Ward K, Dandonneau M, Swain A: Wnt4 is required for proper male as well as female sexual development. Developmental Biology, 276(2):431-440 (2004).
11. Bernard P, Harley VR Wnt4 action in gonadal development and sex determination. Int J Biochem, Cell Biology, 39: 31–43 (2007).
12. Tripathi V, Raman R: Identification of Wnt4 as the ovary pathway gene and temporal disparity of its expression vis-à-vis the testis genes in the garden lizard, *Calotes versicolor*. Gene: 449: 77–84 (2010).
13. Priyanka, Vidisha Tripathi, Rajiva Raman: Conservation of Ovary-Specific Genes, Foxl2, Aromatase, and Rspo1, in the Common Indian Garden Lizard, *Calotes versicolor*, That Lacks Chromosomal or Temperature- Dependent Sex Determination: Sexual Development (2018).
14. Shoemaker C M, Queen J, Crews D: Response of candidate sex determining genes to changes in temperature reveals their involvement in the molecular network underlying temperature-dependent sex determination. Molecular Endocrinology , 21(11):2750-2763 (2007).
15. Anggraini Barlian, Noviana Vanawati, Fitria D. Ayuningtyas: The patterns of sex determination and differentiation genes in green sea turtle (*Chelonia mydas*). Journal of Biological Researches: 20: 15-20, (2015).
16. Laxmi S. Inamdar (Doddamani), Vani V and Polani B. Seshagiri: Tropical Oviparous Lizard, *Calotes versicolor*, Exhibiting a Potentially Novel FMFM Pattern of Temperature-Dependent Sex Determination Journal of Experimental. Zoology. 317:32–46, (2012a).
17. Muthukkaruppan V R, Kanakambika P, Manickavel V, Veeraraghavan K: Analysis of development of the lizard, *Calotes versicolor*. A series of normal stages in the embryonic development. Journal of Morphology, 130:479–489 (1970).
18. Inamdar Doddamani L S, Vani V, Advi Rao G M: Dimorphic hemipenis correlates the pathways of gonadal sex differentiation in the lizard *Calotes versicolor* (Daud.). Journal of Advanced Zoology 33: 31–37 (2012b).
19. Cardoso-Moreira M, Sarropoulos I, Velten B, Mort M, Cooper D N, Huber W, et al. Developmental gene expression differences between humans and mammalian models. Cell Reports; 33(4):108308 (2020).
20. Smith C A, Shoemaker C M, Roeszler K N, Queen J, Crews D, Sinclair A H: Cloning and expression of R-Spondin1 in different vertebrates suggests a conserved role in ovarian development. BMC Developmental Biology, 8:72 (2008b).

Diligent Activities of SPIE. Karnatak University, Student Chapter, under LASER Spectroscopy Programme.

SPIE.(Society of Photographic Instrumentation Engineers,USA, founded in1955) is now the international society for optics and photonics. Its main objective is to advance light-based technologies. It is serving 255,000 constituents from 183 countries across the world. SPIE publishes the SPIE Digital Library, the world's largest collection of optics and photonics applied research with more than 500,000 papers from SPIE journals, conference proceedings and presentations, and eBooks. SPIE affiliated student groups are studying optics and photonics at universities around the world.

SPIE. Karnatak Univ. Student Chapter, established on 8th February 2019 under Laser Spectroscopy Programme, Department of Physics, Karnatak University Dharwad, includes student members from Physics, Chemistry and Life science departments, itscurrent strength is 27. Prof. Sanjeev R. Inamdar is the founder Faculty Advisor and encourages all members to enhance the knowledge in field of light and photonics and invigorate all of us by his tremendous achievements and hard work.

Inauguration of the academic activities of the SPIE. Karnatak University Student Chapter, at Dharwad Regional Science Centre, in May 2019.

Prof.Vasudev K. Aatre, Renowned defence scientist and former Scientific Advisor to the Defence Minister, Govt. of India inaugurated the academic activities of the SPIE.Karnatak University Student Chapter in May 2019.

The main purpose of SPIE Karnatak University Student Chapter is to inspire the Science Faculty students to take up laser and photonics (optics) related research activity by providing information to them on emerging technologies in photonics through interdisciplinary information exchange, career development programme and also taking this topic of study of light to the general public.

Our Student Chapter strives to create awareness about current developments in Photonics. Henceour chapter has been organizing seminar/talks, by all the members periodically once in fortnight on current trends inPhotonics and applications. Several seminars and guest lectures by eminent scientists of premier institutes of India as well as abroad are also conducted, During COVID-19 lockdown period also webinars and online lectures are conducted. Here's a glimpse of the Chapter accomplishments.

1. *International Day of Light*

Our Student Chapter has been celebrating International Day of Light (May 16) every year since 2019 by organizing special lectures/talks by eminent scientists working in the area of photonics.

2019: Organized a special lecture by Prof.Vasudev K. Aatre (A Renowned Defence Scientist and Former Scientific Advisor to the Defence Minister, Govt. of India) on ***"Can India become a super power in science & technology?"***

2021: Conducted two Light related lectures in online mode by speakers are

i. Sr. Physics Professor Dr.Kuldeep Raina (Vice Chancellor, M S Ramaiah University of Applied Sciences, Bangalore. Former VC, DIT University, Dehradun) on ***"Display Technology and its Evolution: An overview".***

ii. Dr. Rajesh V. Nair (Associate Professor, IIT Ropar) on ***"Spatial and Temporal Manipulation of light emission".***

2022: A special lecture by Prof. Sharathanantha murthy (Univ. of Hyderabad),on ***"Modern Optics and its various applications".***

2. *Conducted several Webinars by well-known scientists of the country:*

- Dr. Dharmendra Pratap Singh, Maître de Conférences (Associate Professor), Université du Littoral Côte d'Opale (ULCO), Calais, France, on ***"Indian Contribution In The Research Of Discotic Liquid Crystalline Materials And Their Modern Electro-Optical And Photonic Applications".***
- Dr. M. G. Kotresh, Assistant Professor, Department of Physics, VSKD University, Bellary, Karnataka, India, on ***"Analysis of Nano-Bio Interaction Using Absorption and Fluorescence Spectroscopic Methods".***
- Prof. Shreedhar A Joshi, SDM college of Engineering and Technology, Dharwad, Karnataka, India, on ***"Basics of Optical Fiber Communications and Its Future Networks".***
- Dr. M. N. Kalasad, Associate Professor & Chairman, Department of Physics Davangere University, Davangere, Karnataka, India, on ***"Nanomaterials".***
- Dr. Ajeetkumar Patil, Associate Professor, Department of Atomic & Molecular Physics, Manipal University, Manipal, India, on ***"Hue Imaging System for Field Applications".***
- Prof. SharatAnantamurthy, Professor, School of Physics, University of Hyderabad, Hyderabad, India, on ***"Light as A Handle and Stretcher to Investigate The Biomechanics of Microscopic Matter".***

- Prof. Prem Bisht, Professor, Department of Physics, IIT Madras, Chennai, India, on ***"Role of Photonics in Sensing and Imaging"***

- Prof. B. N. Jagatap, Department of Physics, IIT Bombay, Mumbai, India, ***on "Future of Education".***

1. Invited Lectures:

Prof. Pramod S. Patil, Professor and Head, Department of Physics, Shivaji University Kolhapur, Maharastra, India, on ***'Perovskite Solar Cells'.***

Dr. B. N Jagatap, Senior Professor of Physics, IIT Bombay, India, has delivered Lecture on ***'The Road to Bose Einstein Condensation'.*** The lecture was on August 5, 2019.

Dr. C.H. Bhosale. Shivaji University, Kolhapur, has delivered lecture on ***"Solar energy assisted purification of water thin films",*** on June 9, 2022.

Dr. B. N Jagatap, Senior Professor of Physics, IIT Bombay, India, has delivered Lecture on ***"Photonics for Sustainable Development",*** on June 9. 2022.

1. One-Day Workshop on Foldscope Microscopy:

Several students from schools and colleges in and around Dharwad were given skill development training on Foldscope (Foldable Paper Microscopy).

- Conducted One-day Workshop and Hands on Trainingon January 7, 2022, at Dharwad Regional Science Centre for 150 secondary school students and includes 20 high schools.
- Conducted One-day workshop and Hands on Training for P.U. and B.Sc. students, on 25 March, 2022, at Prism Science College, Dharwad.
- Conducted One-day workshop and Hands on Training, on 9th June, 2022, for 69 M.Sc. Physics Students.
- Skill Development Training & One-Day Workshop on 16 July, 2022, in P C Jabin Science College Hubballi, for 45 B.Sc and M.Sc students.
- Skill Development Training & One-Day Workshop for 55 B.Sc Students of Karnatak Science College, Dharwad, on 25th July 2022.

Training Session for secondary school students at Dharwad Regional Science Centre.

Inauguration of Hands-on Training for B.Sc. & M.Sc. students in P. C. Jabin Science College, Hubli.

SPIE. Chapter members with M.Sc. students of Department of Physics, K.U. Dharwad.

SPIE. Chapter members with B.Sc. students of Karnatak Science College, Dharwad.

Visit to Low Power Transmission Centre, All India Radio station, Dharwad.

Prof. Laxmi S. Inamdar demonstrating live cell imaging to secondary school students.

Outreach Programme :

Arranged a study tour for SPIE Members and M.Sc.(E&C) students to All India Radio station Dharwad as a part of outreach programme on May 13, 2022. All the 25 Members got first-hand experience with working of advanced digital communication equipment at the Low Power Transmitter Centre. They also visited the audio recording studio facility.

Presently our SPIE. K U Chapter is 27 members strong. We have the wonderful guidance, and outright support of Prof. Sanjeev R. Inamdar in spreading the knowledge of Photonics to the general public. Department of Physics is really supportive for our chapter, in conducting workshops, Lecture series and outreach activities.

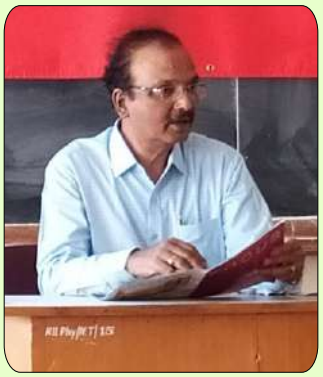

Faculty advisor-
Prof. Sanjeev R. Inamdar *FRSC, FKSTA*

Office Bearers of SPIE.Karnatak Univ., Student Chapter 2019-20

President - Mr. Mallikarjun Patil
Vice President - Mr. Manjunath Wari
Secretary - Mr. Madivalagouda Sannaikar
Treasurer - Mr. Shivaraj Patil

Office Bearers of SPIE.Karnatak Univ., Student Chapter 2020-21

President - Mr. Mallikarjun Patil
Vice President - Mr. Shivaraj Patil
Secretary - Mr. T. S. Tilakraj
Treasurer - Mr. Vikram Pujari

Office Bearers of SPIE.Karnatak Univ., Student Chapter 2021-22

President - Mr. T. S. Tilakraj
Vice President - Mr. Vikram Pujari
Secretory - Mr. Altafhusain Makandar
Treasurer - Mr. Vighneshwar S. Bhat

Office Bearers of SPIE.Karnatak Univ., Student Chapter 2022-23

President - Mr. Vikram Pujari
Vice President - Miss Shrikrupa Chavan
Secretory - Mr. Altafhusain Makandar
Treasurer - Mr. Vighneshwar S. Bhat

World Environment Day 2022

SPIE. Karnatak University Student Chapter 2022-2023

OBITUARY

Prof. Bassappa B. Kaliwal

Department of Zoology, Karnatak University Dharwad

(1954-2021)

Professor Bassappa B. Kaliwal, a distinguished academician, able administrator and a compassionate gentleman was born in 1954, at Narayanpur, Shiggaon Taluk of Haveri District, Karnataka, India. After completing his school education, he completed B.Sc. (1974), M.Sc. (1976) and Ph.D. (1981) in Zoology from Karnatak University, Dharwad. His fields of research were Reproductive Biology, Reproductive toxicology, Physiology, Microbiology and Biotechnology.

Dr. Kaliwal began his academic journey as a Lecturer in Zoology at Karnatak Science College, Dharwad (1979-88), became Senior Lecturer (1988-90), Reader (1990-99) and Professor (1999-2002) in the Department of Zoology, Karnatak University. He established and nurtured two new departments in the University: Microbiology (1999) and Biotechnology (2001) and served as Chairman for 12 years. He guided 30 students for Ph.D. and 34 for M.Phil. degrees. With 36 years of research and teaching experience, Dr B. B. Kaliwal contributed significantly to scientific research. For the first time he showed that there is a co-localisation of Fos containing neurons within SON of the hypothalamus also express nNOS. The progesterone-induced implantation delay and nidation model shown by Prof. Kaliwal's team has been used to understand the mechanisms of anti-implantation activity in rats.

Prof. Kaliwal published more than 175 research papers in National and International journals of repute. He completed 15 research projects funded by UGC, DST, DBT, etc. He received Special Grant of Rs.12 Crores from Department of Biotechnology, New Delhi. He was awarded the Prestigious Post-doctoral Commonwealth Fellowship to work with Dr. David Murphy, Professor of Experimental Medicine at the University of Bristol, UK (2003-2004). Besides academic distinction, he was president of Research Forum for 4 years, President of Karnatak University Post Graduate Teachers Association for 6 years and President of Council of University Teachers Associations of Karnataka State for 13 years. He held many important positions in Karnatak University such as Chairman, Board of Studies in Zoology, Applied Genetics, Bioinformatics, Biotechnology and Microbiology and also of different universities in Karnataka and other States. He conducted several short-term courses in Photobiology, Biological Sciences,

Chronobiology, Zoology, Bioscience, Biotechnology, Microbiology, Bioinformatics, etc. Prof. Kaliwal excelled as the Vice Chancellor of Davangere University by drawing the path for the growth of the young University in academic and research activities in all faculties of the University by creating the state-of-art infrastructure and motivating the young faculty members. Prof. Kaliwal was Fellow of the Society for Reproductive Biology and Comparative Endocrinology (SRBCE), one of the dynamic scientific Societies in India since 1992, elected as President of the Society in 2019 and effectively served in that coveted post from 1st April 2019 till his departure to the Heavenly Abode on 9th December 2021.

Prof. Kaliwal, who began his journey from a village and excelled in academic, research and administration, is one such great soul.

Prof. M. Michael Aruldhas **M.Sc., M.Phil.,Ph.D.,F.R.E., FNASc.**
Secretary, Society for Reproductive Biology and Comparative Endocrinology,
Department of Endocrinology,Dr.ALM PG Institute of Basic Medical Sciences,
University of Madras,Taramani Campus,Taramani- Chennai-600113,India

.

Dr. M.A. Akbarsha
Biomedical Scientist & Research Coordinator,
National College (Autonomous), Tiruchirappalli,
Editor-in-Chief, Journal of Endocrinology and Reproduction (JER) of SRBCE,
General Secretary, Society for Alternatives to Animal Experiments (SAAE-I)
Founder & Gandhi-Gruber- Doerenkamp Chair,
Mahatma Gandhi – Doerenkamp Center for Alternatives,
Bharathidasan University, Tiruchirappalli, India

Prof. Laxmi S. Inamdar **M.Sc.Ph.D., FKSTA**
Department of Zoology, Karnatak University, Dharwad

KARNATAK UNIVERSITY JOURNAL OF SCIENCE
INSRTUCTIONS TO THE AUTHORS

General Information

Manuscript must be submitted as Microsoft Word document with text in Times New Roman font with size 12. The manuscript be structured as: Abstract, Introduction, Materials and Methods, Results and Discussions, Conclusions, Acknowledgment followed by References. The length of MS should not exceed 12 typed pages.

1. Title of research article should be centered and followed by authors, their affiliation, along with contact e-mail ID of the corresponding author.
2. Name of the corresponding author should be identified by an asterisk (*).
3. Abstract not exceeding 250 words be included on Title page followed by 4-5 key words. Each key word must be separated by a semicolon (;).
4. The references should be cited in text with a square bracket [21] and be limited to 30.
5. Subtitles used in the manuscript must be in bold, and follow the numbering order as: 1, 1.1, 1.2; 2, 2.1, 2,2; etc.
6. Text after the subtitle should follow directly without paragraph, whereas subsequent paragraphs must start with paragraphs.
7. Coloured figures will be included in print copy, if necessary.
8. Representation of figure, scheme and table should be in the body of the text as **Fig. 1, Scheme 1** and **Table1,** respectively. If the sentence starts with the indication of any Figure then it should be written as **Figure 1** (For example). The examples of figure, scheme and table captions are to be represented as:

Figure1. Fluorescence spectra of ternary quantum dots.

Scheme1. Synthesis of chromophores.

Table 1. Physical and thermal properties of NLO materials.

9. Style of references

a. Books

i. W. J. Koros, B. T.Chen, R. T. Chem, Handbook of Separation Process Technology, Wiley-Interscience: New York, USA, p67 (1987)

b. Book Chapter

i. M. Zhu, T. Y. Jhab, K. K. Sirkar, Optical plastics – a wonderful material, In: Basics of Non-linear Optics, T. Brouse, R. A. Huggins, eds. Elsevier: New York, USA, p54 (2001)

c. Journals

i. Photophysics and rotational diffusion dynamics of large prolate non-polar laser dyes Sanjeev R. Inamdar, J.R. Mannekutla, M.S. Sannaikar, M.N. Wari, B.G. Mulimani and M.I. Savadatti J. Mol. Liquids (Elsevier), 268C, 66-76 (2018)

ii. P. M. Patil, Monisha Roy, A. Shashikant, S. Roy and E. Momoniat (2018): Triple diffusive mixed convection from an exponentially decreasing mainstream velocity, International Journal of Heat and Mass Transfer (Elsevier) 124, 298-306 (2018)

iii. S. Sebastian, N. Sundaraganesan, Spectrochim. Acta (Elsevier), A75, 941-952 (2010).

d. Conference Proceedings

i. K.P. Medium, A.S.R. Usha, C.K. Menon, Proc. 5th Annual Conference on Polymers, Istanbul, Turkey, Sept. 5-21, p. 47 (1997).

10. You may submit the manuscript as a single MS word file containing all the figures, tables, schemes, figure captions. Include a cover letter addressed to Chief Editor, KU J Science, Department of Physics, Karnatak University, Dharwad 580003 (e-mail: srinamdar@kud.ac.in; him_lax3@yahoo.com) that must contain the names and contact details of at least two potential reviewers.